



Provided by the author(s) and University of Galway in accordance with publisher policies. Please cite the published version when available.

Title	Experimental and numerical characterisation of materials for biomass co-firing
Author(s)	O'Hagan, Conor
Publication Date	2017-02-23
Item record	http://hdl.handle.net/10379/6354

Downloaded 2024-04-26T04:36:46Z

Some rights reserved. For more information, please see the item record link above.



Experimental and Numerical Characterisation of Materials for Biomass Co-Firing

Conor P. O'Hagan B.E. (2012)

Supervisors: Dr. Rory Monaghan and Prof. Sean Leen



A thesis submitted to the National University of Ireland, Galway
as fulfilment of the requirements for the Degree of Doctor of Philosophy

December 2016

Mechanical Engineering, National University of Ireland, Galway

Abstract

As Europe continues to decarbonize its electricity generation capacity, operators of thermal power plants face challenges to which they must adapt including increasingly transient operation and co-firing with biomass. This research focuses on peat-fired power plants and the response of superheater tube materials to the altered deposit composition formed during peat-biomass co-firing. Both experimental and multi-physics modelling studies on the effects of biomass deposit compositions on boiler tube material properties are presented.

The addition of biomass to peat has been shown to result in increased levels of corrosion on heat exchanger tubes in plants. An experimental methodology has been developed at NUI Galway for representative corrosion testing of power plant materials for different levels of biomass-peat mixtures. Synthetic salts, representative of deposits formed during biomass co-firing are produced and their compositions are compared to compositions of deposits obtained from operational plants. These salts are applied to candidate materials and exposed to temperatures in the range of 540 °C to 600 °C for up to 1 month. The corrosion layer of each sample is then measured using scanning electron microscopy (SEM) and optical microscopy. Energy dispersive X-ray spectroscopy (EDX) elemental analysis is also carried out; this provides information regarding chemical composition at different depths.

A novel physically based corrosion model (PCM) to describe the accelerated corrosion process active oxidation which occurs beneath alkali-halide-containing deposits, which form on heat exchanger tubes during biomass firing was developed. This model uses measurements of porosity and pore radius, coupled with a physically based corrosion mechanism, to predict corrosion rates. Results from this model are validated with experimental results and published models that make use of a fitting factor.

A finite-element (FE) methodology which combines corrosion effects with creep damage in pressurised tubes is presented. Experiments are carried out to obtain a corrosion rate for P91 steel. This corrosion rate is then used to simulate corrosion in the FE model via adaptive meshing. This is combined with creep damage models to investigate the effect of corrosion tube wall loss and creep damage on tube stresses and creep rupture life. Experimental results allowed initial characterisation of the complex, multi-layered nature of oxides formed during the active oxidation of P91.

Computational results quantify the detrimental effect of uniform corrosion on creep rupture life for a range of internal steam pressures. These results will be of significant interest to plant operators who are concerned with the impact of corrosion on creep life of plant components.

An in-depth experimental microstructural characterisation of P91 and 347SS following exposure to salts representative of deposits formed during biomass co-firing is presented. Samples have been etched allowing for a comprehensive evaluation of the microstructural degradation of samples. Several key processes have been identified which would contribute to a reduced life expectancy of tubes. The detrimental effect of impurities in materials, such as inclusions, on the corrosion process is identified. Pitting corrosion is found to initiate at sites of near-surface inclusions and its mechanism is discussed. Measurements of pits taken from in-situ tubes are compared with experimental measurements and the results are found to agree. Localised intergranular corrosion was detected at numerous locations across the samples. Results indicate that the corrosion mechanism and rate at which it occurs depend on the Cl and K content of the salts applied to the samples.

The surface topography of samples has been analysed to determine the effect of corrosion on surface finish. Results from testing on P91 and 347SS are compared to determine the material with a greater corrosion resistance. 347SS is found to offer significantly higher corrosion resistance than P91. This is primarily attributed to the higher Cr content in 347SS, which results in more protective oxide scales forming closer to the substrate surface.

FE models have been developed which investigate the effect of differential thermal expansion coefficients between material impurities, such as inclusions and base metal. The detrimental effect of such inclusions, which lead to localised stress concentrations, is shown. FE models which investigate the effect of pitting corrosion on stress levels in pressurised tubes are also presented. Stress levels are shown to increase with increasing pit depth, size and frequency.

Table of contents

Abstract	ii
Acknowledgements	ix
List of Publications	x
Nomenclature	xi
1. Introduction.....	1
1.1. Energy & the environment.....	1
1.2. Biomass as a fuel	6
1.2.1. Composition of biomass	7
1.2.2. Differences between fossil fuels and biomass	12
1.2.3. Sources of biomass	13
1.2.4. Conversion techniques for woody biomass	15
1.3. Combustion technology	16
1.3.1. Grate combustion.....	17
1.3.2. Pulverised fuel combustion.....	17
1.3.3. Fluidised bed combustion	18
1.4. Challenges for biomass combustion	20
1.5. Aims and objectives.....	24
1.6. Thesis overview	26
2. Literature Review	28
2.1. Chapter overview	28
2.2. Solid Fuel Combustion	29
2.3. Ash formation in fuels	30
2.4. Corrosion of materials	32
2.4.1. Thermodynamics of metal oxidation	33
2.4.2. Kinetic modelling of metal oxidation	34
2.4.3. Forms of Corrosion.....	35

2.4.4.	Oxide scale structure.....	36
2.4.5.	Corrosion Modelling.....	38
2.5.	Mechanical damage	41
2.5.1.	Creep.....	42
2.5.2.	Creep Damage.....	46
2.5.3.	Fatigue	46
2.6.	Material macro and micro structures	48
2.6.1.	Structure of materials.....	50
2.6.2.	P91 Microstructure	51
2.6.3.	347SS Microstructure	53
2.6.4.	Inclusions	54
2.7.	Fireside corrosion	59
2.7.1.	Active oxidation process.....	59
2.7.2.	Thermodynamic stability of metal oxides and chlorides	62
2.7.3.	General structure of oxides	63
2.7.4.	Formation of low temperature eutectics	65
2.7.5.	Sulphation of deposits.....	68
2.7.6.	Reaction of Cl-species with oxide scale	68
2.7.7.	Chromate formation.....	68
2.7.8.	Reaction between Cl-species and carbides	70
2.7.9.	Molten sulphate corrosion	70
2.7.10.	Corrosion associated with gaseous Cl-species.....	72
2.7.11.	Solid phase reaction with Cl-species in deposits.	74
2.7.12.	Active Oxidation Modelling	77
2.8.	Summary	78
3.	Experimental Methods.....	80
3.1.	Chapter Overview	80

3.2.	Synthetic Salt Calculation and Preparation	82
3.3.	Sample Preparation and Exposure	86
3.4.	Post-Exposure Work	87
3.5.	Analytical Tools.....	90
3.5.1.	Optical Microscopy.....	90
3.5.2.	Scanning Electron Microscopy	91
3.5.3.	Energy-dispersive X-Ray Spectroscopy	93
3.5.4.	White Light Interferometry.....	94
3.6.	Deposit and fuel characterisation.....	96
3.6.1.	Methodology	97
3.6.2.	Deposit composition analysis	97
3.6.3.	Fuel composition analysis.....	101
3.6.4.	Deposit and fuel composition characterisation conclusions	104
3.7.	Summary	105
4.	Porosity-Based Corrosion Model.....	106
4.1.	Introduction.....	106
4.2.	Modelling.....	107
4.2.1.	Labyrinth Factor Method (LFM)	114
4.2.2.	Porosity-based Corrosion Method (PCM)	116
4.3.	Results and Discussion	118
4.3.1.	Experimental – 540 °C.....	118
4.3.2.	Experimental – 600 °C.....	129
4.3.3.	Modelling – Labyrinth Factor Method (LFM)	131
4.3.4.	Modelling – Porosity Based Corrosion Model (PCM)	133
4.4.	Conclusions.....	139
5.	Effect of Corrosion on the Service Life of P91 Piping.....	141
5.1.	Introduction.....	141

5.2.	Methodology	142
5.2.1.	Creep Model	142
5.2.2.	Finite Element Model	143
5.2.3.	Corrosion Model	144
5.3.	Results.....	148
5.3.1.	Experimental.....	148
5.3.2.	Computational.....	153
5.4.	Discussion.....	163
5.5.	Conclusions.....	165
6.	Microstructural Investigation into the Corrosion Response of P91 Steel.....	166
6.1.	Introduction.....	166
6.2.	Methodology.....	167
6.2.1.	Experimental.....	167
6.2.2.	Computational.....	167
6.3.	Results.....	169
6.3.1.	Experimental.....	169
6.3.2.	Modelling.....	182
6.4.	Discussion.....	184
6.5.	Conclusions.....	185
7.	Microstructural Investigation into the Corrosion Response of 347SS	187
7.1.	Introduction.....	187
7.2.	Methodology.....	188
7.2.1.	Experimental.....	188
7.2.2.	RepliSet samples.....	188
7.2.3.	Computational.....	189
7.3.	Results.....	191
7.3.1.	Experimental.....	191

7.3.2.	RepliSet samples.....	201
7.3.3.	Modelling.....	203
7.4.	Discussion.....	207
7.5.	Conclusions.....	209
8.	Discussion and Conclusions.....	211
8.1.	Chapter Overview	211
8.2.	Discussion of Thesis	211
8.3.	Recommendations for Future Work	214
8.4.	Conclusions	217
	References	219

Acknowledgements

Firstly I would like to thank my supervisors Dr. Rory Monaghan and Prof. Sean Leen for their support, expertise and enthusiasm for this research over the past number of years.

Next I would like to acknowledge the Irish Research Council (IRC) for co-funding this project with ESB and Bord na Móna under the Enterprise Partnership Scheme, grant number EPSPG/2012/466. Thanks in particular to my industrial supervisors Dr. Fionn Griffin from ESB and Mr. Barry Hooper from Bord na Móna.

I would like to thank the NUI Galway technical staff Mr. William Kelly, Mr. Pat Kelly and Mr. Bonaventure Kennedy. I would also like to thank Dr. Éadaoin Timmins for training me in the use of the SEM and EDX.

Thanks to Dr. Richard Barrett for his discussions regarding component life in operational plants. Thanks to Dr. Barry O'Brien, who provided many useful insights into the corrosion of metals and the field of metallurgy. Thanks also to Eimear O'Hara for the many exciting conversations regarding material microstructure and oxidation.

I would like to thank my friends and colleagues in the engineering building, including, Donnacha, Enda, Sinéad, Paddy, Tarek, Eoin, the 10.30 tea crowd and the wider PhD research group. Thanks also to my friends outside of college in particular Con, Liam, Daire, Mike, Brendan, Dave and the extended Maree basketball crew for the many adventures throughout the years.

Finally, I would like to thank my parents Brendan and Mary and my siblings Sinead, Niamh and Colm for their continued support throughout my studies.

List of Publications

The work presented in this thesis has resulted in the following publications:

- C.P. O’Hagan, B.J. O’Brien, F. Griffin, B. Hooper, S.B. Leen, R.F.D. Monaghan, Porosity-Based Corrosion Model for Alkali Halide Ash Deposits during Biomass Co-firing, *Energy & Fuels*. 29 (2015) 3082–3095. doi:10.1021/ef502275j. (**Chapter 3 & 4**)
- C.P. O’Hagan, R.A. Barrett, S.B. Leen, R.F.D. Monaghan, Effect of High-Temperature Corrosion on the Service Life of P91 Piping in Biomass Co-firing, *J. Press. Vessel Technol.* 138 (2016) 21407. <http://dx.doi.org/10.1115/1.4032648> (**Chapter 5**)
- O’Hagan, C. P., O’Brien, B. J., Leen, S. B., & Monaghan, R. F. D. (2016). A microstructural investigation into accelerated corrosion of P91 steel during biomass co-firing. *Corrosion Science*. <http://doi.org/10.1016/j.corsci.2016.03.028> (**Chapter 3 & 6**)
- O’Hagan, C. P., Leen, S. B., & Monaghan, R. F. D. (2017). A microstructural investigation and computational model of the accelerated corrosion of 347SS during biomass co-firing. *Corrosion Science*. Under review (**Chapter 7**)
- O’Hagan, C. P., O’Brien, B. J., Leen, S. B., & Monaghan, R. F. D. (2014). Experimental Characterisation of Materials for Biomass Co-Firing. In *Proceedings of the 22nd European Biomass Conference and Exhibition* (pp. 23–26), June 2014, Hamburg, Germany. (**Chapter 3 & 4**)
- O’Hagan, C.P., Barrett, R.A., Leen, S.B., Monaghan, R.F.D. Effect of high temperature corrosion on the service life of P91 piping in biomass co-firing. *ASME Pressure Vessels and Piping Conference*, 19-23rd July 2015, Boston, US (**Chapter 5**)
- O’Hagan, C. P., Leen, S. B., & Monaghan, R. F. D. (2014). An experimental and numerical characterisation of materials for use in biomass co-firing. In *1st International Conference on Materials Design and Applications*, 30th June - 1st July 2016, Porto, Portugal. (**Chapter 7**)

Nomenclature

Symbol	Definition
HHV	Higher heating value
A	Creep material coefficient
A'	Creep material constant
A_0	Creep material constant
A_L	Linear Arrhenius coefficient
A_P	Parabolic Arrhenius coefficient
B'	Creep material constant
C	Material specific Larson Miller constant
C_A	Gas-phase concentration of A
D_e	Damage
D_{eff}	Effective diffusivity
$D_{i,x}$	Diffusion coefficient of x
$D_{K,x}$	Knudsen diffusivity of x
$D_{M,x}$	Molecular diffusivity of x
j_x	Diffusional flow of x
J_x	Flux of x
k_L	Linear oxidation constant
k_P	Parabolic oxidation constant
k_U	Corrosion kinetic parameter
L_e	FE model characteristic length
m	Creep material constant
m	Mass
MW_i	Molecular weight of an individual element
n	Creep material constant
n	Norton creep exponent
N_x	Number of moles produced/ consumed
P	Pressure
P_{LM}	Larson Miller Parameter
P_x	Partial pressure of x
Q_{Cr}	Creep activation energy
Q_L	Linear activation energy
Q_P	Parabolic activation energy
r	Radius
\bar{r}	Average pore radius
R_A	Specific gas constant
R_a	Surface roughness value
R_i	Inner tube radius
R_o	Outer tube radius

\bar{R}	Ideal gas constant
S_{ij}	Deviatoric stress
t	Time
T	Temperature
T_m	Melting temperature
t_R	Time to rupture
Y_i	Mass fraction of individual element
α	Creep material constant
β	Pit growth parameter
γ	Distribution shape factor
δ_U	Material characteristic length
ε	Labyrinth factor
ε	Porosity
ε_c	Creep strain
$\dot{\varepsilon}_{ss}$	Steady state creep strain
λ_n	Pitting parameter
ρ_x	Density of x
σ	Stress
σ_A	Axial stress
σ_{Creep}	Creep stress
σ_{eq}	Equivalent (von Mises) stress
$\sigma_{GeomGrth}$	Geometric growth stress
σ_H	Hoop stress
$\sigma_{IntrGrth}$	Intrinsic growth stress
σ_{Mech}	Mechanical stress
$\sigma_{Microcrck}$	Microcrack stress
σ_r	Rupture stress
σ_R	Radial stress
σ_{Therm}	Thermal stress
$\sigma_{x,y}$	Mean collision diameter of gas x and gas y
τ	Tortuosity
ϕ	Creep material constant
χ	Creep material constant
ω_c	Creep damage (void volume fraction)
$\Omega_{x,y}$	Temperature dependent collision integral of gas x and y

1. Introduction

1.1. Energy & the environment

Fossil fuels, such as oil, coal and natural gas are traditionally known as the prime sources of energy in the modern world. However, such fuels are now in limited supply; furthermore, these fuels cause severe environmental and health damage, such as global warming, acid rain and urban smog as a result of emissions. Due to these factors, there is a worldwide effort to reduce the use of fossil fuels in energy production. Figure 1.1 shows the energy balance for Ireland during 2014 in units of kilotonnes of oil equivalent (ktoe). The left hand side shows the inputs to Ireland's energy system. The right hand side shows the end-use sectors in which the energy is used. It is clear from Figure 1.1 that oil is still the dominant fuel (47% of total requirement), primarily due to its demand in the transport sector.

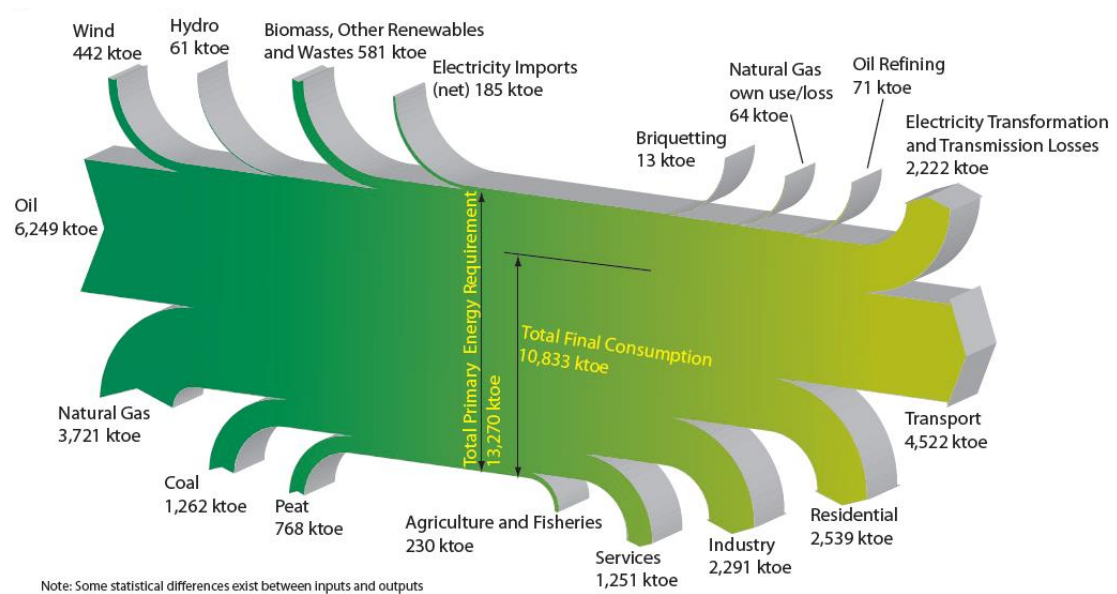


Figure 1.1: Energy flow in Ireland in 2014 [1].

The primary uses of peat in Ireland is shown in Figure 1.2, split into the portions used for electricity generation in power plants, and residential heating. An overall declining trend in peat used was observed from 1,377 ktoe in 1990 to 768 ktoe in 2014, a 44% decrease in use. Direct peat use in households decreased by 72% over this period, while that for power plants decreased by 8% [1].

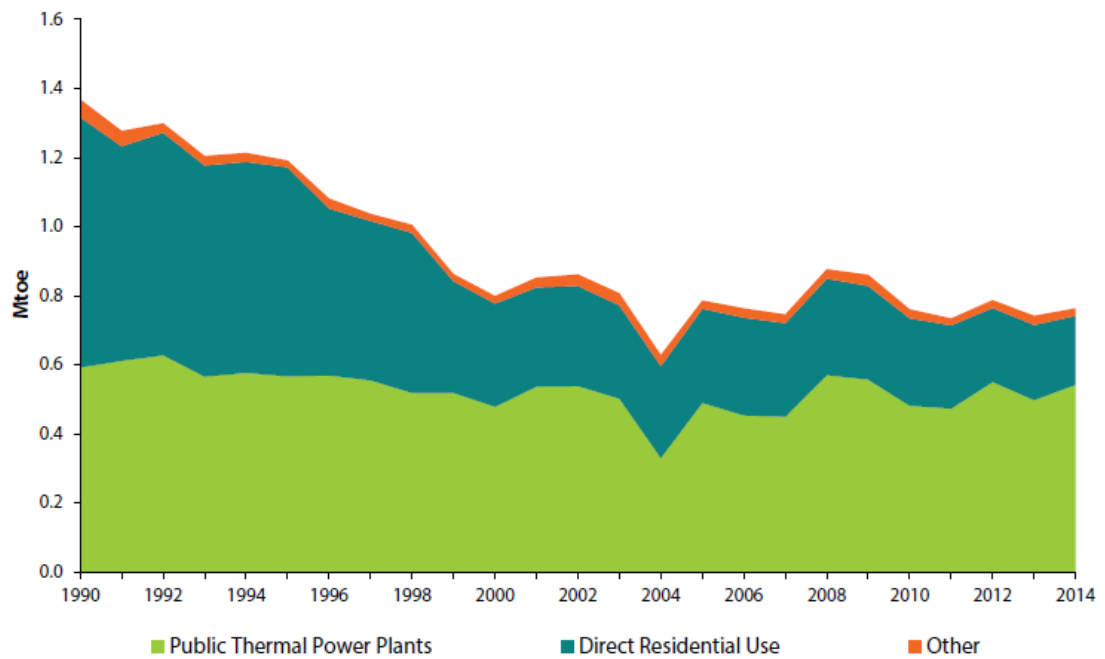


Figure 1.2: Peat use in Ireland 1990 – 2014 [1].

Table 1.1 shows the percentage shares of fuel used in electricity generation in Ireland from 1990 to 2014. The trend away from fossil fuels is visible in this table with fossil fuels dropping from providing 98.1% of Ireland’s electricity generation capacity in 1990 to 80.8% in 2014. Peat consumption accounted for 12.6% of fuel inputs to electricity generation for 2014 [2]. It must be noted that these figures are shares of fuel energy used to produce electricity. Direct renewable electricity sources, such as wind and hydroelectric are assumed to have efficiencies of 100% (e.g. that there are no electrical losses), resulting in their relatively low shares in Table 1.1. Data for the total electricity generation shows that wind accounts for 24% of the electrical energy generated in Ireland, as of 2015 [3].

Table 1.1: Percentage shares of energy sources used in electricity generation in Ireland [2].

Energy Source	1990 (% Share)	2014 (% Share)
Fossil Fuels (Total)	98.1	80.8
<i>Coal</i>	40.2	21.6
<i>Peat</i>	19.5	12.6
<i>Oil (Total)</i>	11.1	1.4
<i>Gas</i>	27.2	45.2
Renewables (Total)	1.9	14.5
<i>Hydro</i>	1.9	1.4
<i>Wind</i>	-	10.1
<i>Biomass</i>	-	1.2
<i>Other Renewables</i>	-	1.7
Non-Renewables (Wastes)	-	0.6
Combustible Fuels (Total)	98.1	84.2
Electricity Import (net)	-	4.2

The focus of this work is on the use of peat and biomass as fuels for large scale electricity generation. The use of peat as a fuel for electricity generation has been supported for years by a public service obligation (PSO) levy, which is charged to all electricity customers. The proceeds of this levy are used to recoup additional costs associated with supplying electricity from such generators. This maintained the use of an indigenous fuel source and sustained employment in peat-producing areas of Ireland. However, due to recent EU legislation, this practice will change and the PSO system is being phased out between now and 2019.

Peat is currently burned at three state-of-the-art power plants in Ireland, summarised in Table 1.2. The PSO for Edenderry power station expired in 2015, while those for West Offaly Power (WOP) and Lough Ree Power (LRP) will expire in 2019 [1,4].

While peat-fired plants operators had been given a target of 30% biomass co-firing by the year 2030, this has recently been changed and plants must now cease the burning of peat entirely by 2030. This will result in the restoration of Ireland's natural boglands. It is envisaged that the loss of up to 2,500 peat harvesting jobs will be avoided by the establishment of willow plantations to provide biomass to plants in Ireland [5]. Biomass can typically be defined as any organic matter which comes from living or recently living organisms.

Tariff levels and structures which were designed to encourage the efficient use of biomass, and have higher tariffs rewarding high efficiency cogeneration, came into effect from 2016. The market certainty provided by this scheme allows plant operators to enter into long-term supply contracts for biomass stimulating demand for a range of energy crops [6]. These tariffs combined with the end of the PSO's for peat by 2020 will result in biomass becoming a more attractive fuel than peat from an economic point of view for plant operators [7].

Table 1.2: Overview of peat-fired power plants in Ireland.

Plant	Edenderry	West Offaly	Lough Ree
			
Operator	Bord na Móna	ESB	ESB
Technology	Bubbling fluidised bed (BFB)	Circulating fluidised bed (CFB)	Circulating fluidised bed (CFB)
Capacity (MW_e)	120	150	100
Year opened	2005	2005	2004
Year PSO expires	2015	2019	2019
Superheater tube material	P91	347SS	347SS
Max steam temperature	540 °C	563 °C	563 °C

All three plants of interest to this study make use of fluidised bed technology. Fluidised bed combustion is typically regarded as one of the most flexible for burning a wide variety of solid fuels of variable or unpredictable quality, while maintaining low emissions. Fluidised bed boilers designed for a single fossil fuel input can be modified to make use of a combination of fossil fuels and renewables with a relatively low investment; this is known as co-firing. Typically a fluidised bed boiler can obtain fuel-to-steam efficiencies of over 90% even with challenging low-grade fuels [8]. CFB plants are typically able to operate at higher steam temperatures than BFB plants due to their operating mechanisms, which are discussed in more detail in Section 1.3.

1.2. Biomass as a fuel

Biomass is a carbon-based fuel that is developed from organic matter and is generally considered to be a renewable source of energy. It can be burned to produce heat, power and/or electricity. Examples of materials classified as biomass fuels include woodchip, forest debris, miscanthus, willow, manure and certain types of waste. As biomass can be burned at any time it does not have the intermittency issues associated with other renewable energy sources, such as solar, tidal or wind energy.

Biomass is often considered a carbon-neutral fuel, as the material used to generate electricity, would otherwise be dumped in landfills, openly burned, or left as fodder for forest fires [9]. In reality there is an addition of CO₂ to the environment due to harvesting, transportation and processing of the biomass [10].

Fossil fuels such as coal, oil and gas are derived from biological material that has absorbed CO₂ from the atmosphere millions of years ago. Over this time oxygen and moisture is driven out of the materials. As such they offer high energy density, however burning of these fuels results in the release of the combustion products to the atmosphere. Therefore when we burn coal, we make a net addition of CO₂ to the atmosphere [9]. It can thus be said that the primary difference between biomass and fossil fuels is the time scale of atmospheric carbon fixation.

A table showing the major advantages and disadvantages of biomass fuels has been produced by Saidur et al. [9], which has been reproduced here in Table 1.3.

Table 1.3: Major advantages and disadvantages of biomass fuels [9].

Advantages	Disadvantages
Is a renewable and inexhaustible fuel source	Incomplete renewable energy resource with respect to the complete life cycle
Can be co-fired with conventional fuels (reducing emissions and achieving economic benefits)	Commonly contains high contents of moisture, Cl, K, Na, Mn and trace elements
Leads to a reduction in hazardous emissions	Has low energy density
Reduces biomass-containing wastes	There is potential competition with food and feed products
Maintains employment in rural areas	If directly burned without planting new crops, will contribute to global warming
Provides indigenous energy source	Would require an uptake in purpose-grown crops to meet quantities required to make a global effect.
Feeding systems can be easily adapted to deal with biomass fuels	Can be expensive if large quantities are required May need to be pre-treated before use as a fuel

1.2.1. Composition of biomass

Composition of a biomass fuel is typically described in three different ways; (1) its constituent components, (2) proximate analysis and (3) ultimate analysis.

Biomass consists of three main constituents; cellulose, hemicellulose and lignin with varying amounts of lipids, proteins, sugars, starches, water and inorganic components making up the balance [11]. Typically, the heating values of the fuel are strongly

related to the lignin content of the fuel. The heating values of lignin are typically reported to be higher than cellulose and hemicellulose.

Heating value or calorific value (CV) of a fuel is an expression of the chemical energy content, released as heat when a material is burnt. Heating values are typically expressed as higher heating value (HHV) or lower heating value (LHV). HHV is the total energy released when the fuel is burnt, including the latent heat contained in the released water vapour, and represents the maximum energy recoverable from a biomass source. As the latent heat in the water vapour is not normally used effectively, the LHV is the appropriate value to use to obtain values for the energy available [10].

Proximate analysis is used to determine the percentage of volatile matter (VM), fixed carbon (FC), moisture and ash content of various biomass feedstocks. VM of a solid fuel is the portion driven off as a gas, by heating (to 950 °C for 7 minutes under ASTM standards). FC is the portion of the fuel consumed during combustion with ash remaining as the residue. This is important information for the combustion of biomass, as high ash contents will lead to ignition and combustion problems.

The chemical composition of the ash can present significant operational problems for plant operators [10]. If the melting point of the dissolved ash is low, fouling and slagging problems will occur. High FC and VM result in a higher HHV of the biomass fuel [9,12]. As the focus of this work is on problems related to ash content it is discussed in detail in Chapter 2.

The proximate analysis, on a dry basis, for a selection of solid biomass and fossil fuels is shown in Table 1.4, with coal and peat also shown for comparative purposes. As can be clearly seen the FC content of coal is far higher than any of the biomass fuels and the VM content is far lower. Bark and willow offer the highest FC content of the biomass fuels presented.

Table 1.4: Proximate analysis, (dry basis) for a selection of solid biomass and fossil fuels.

Fuel	Fixed Carbon	Volatile Matter	Ash	Ref.
Coal	79.6	12.0	8.4	[13]
Peat	28.5	67.7	3.8	[14]
Bark	17.1	78.1	4.8	[14]
Willow	15.9	82.5	1.6	[9]
Wood Pellets	13.7	79.6	6.78	[15]
Straw	13.6	80.5	5.9	[14]

Ultimate analysis of biomass is used to determine the percentages of C, H, O, N and S present in biomass fuels. The ratio of H to C and O to C can then be used to estimate the heating value of these fuels as will be discussed in the section on the combustion of biomass [9]. The ultimate analysis for a selection of solid biomass and fuels of interest is shown in Table 1.5.

Values of the ultimate analysis of a fuel can be combined with formulae, such as Dulong's, Boie's, Chang's or Demirbas' equation to provide the gross calorific value [16,17]. This is done based on the weight fractions of carbon, hydrogen, oxygen and sulphur.

$$HHV = 33.86C + 144.4 \left(H - \frac{O}{8} \right) + 9.428S \quad (1-1)$$

Dulong's equation is shown in Equation 1-1 with results given in MJ/kg. The effect of different O:C and H:C ratios on a fuel's HHV can be seen in Table 1.5.

Table 1.5: Ultimate analysis for selection of dry solid biomass and fossil fuels [15].

Fuel	C	H	O	N	S	H:C X 10	O:C	HHV (MJ/kg)
Coal	76.73	4.69	10.52	1.41	0.40	0.61	0.14	30.89
Peat	55.00	5.50	32.60	1.70	0.20	1.00	0.59	18.64
Bark	50.40	5.64	40.07	0.55	0.03	1.12	0.79	17.07
Willow	50.19	5.90	42.22	0.10	<0.01	1.18	0.84	16.99
Wood Pellets	50.80	7.51	41.67	0.03	<0.01	1.48	0.82	17.20
Straw	46.00	6.28	43.01	0.51	0.09	1.37	0.94	15.58

The effects of O:C and H:C ratios on the CV of solid fuels can be qualitatively shown via a Van Krevelen diagram as shown in Figure 1.3. This shows that higher O:C and H:C ratios reduce the energy value of a fuel. There are a number of pre-treatment procedures which a material can undergo in order to reduce its O content, thus increasing its CV, such as torrefaction.

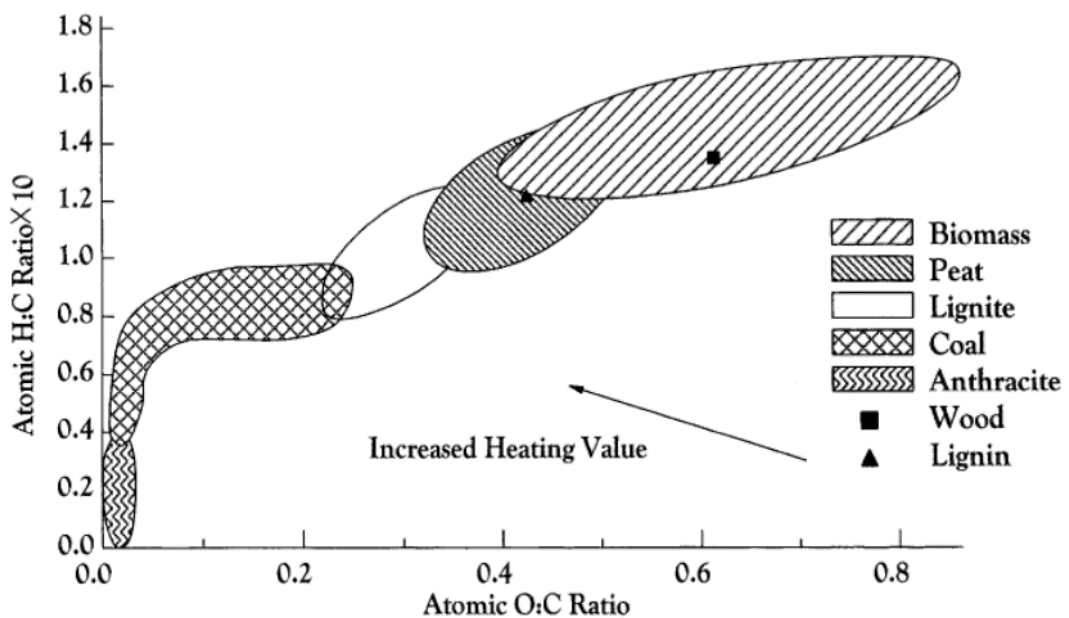


Figure 1.3: Van Krevelen diagram for various solid fuels, adapted from [18].

Torrefaction removes moisture and oxygen-containing volatiles from the material by exposing it to temperatures typically between 200 – 320 °C. This results in a change in the properties of the material, resulting in a higher quality fuel for combustion applications. The benefits of torrefaction include increased HHV, improved homogeneity of composition, improved handling and making the fuel more hydrophobic. The effects of torrefaction on the composition and HHV of miscanthus and wheat straw are shown in Table 1.6 [19].

Table 1.6: Ultimate analysis showing effect of torrefaction on miscanthus and wheat straw composition (% dry fuel) [19].

Material	Torrefaction temperature	C	H	N	S	O	HHV (MJ/kg)
Miscanthus	Raw	46.66	6.00	0.21	0.00	45.34	15.79
	200 °C	48.16	5.81	0.15	0.00	43.87	16.31
	300 °C	55.33	5.22	0.10	0.00	34.77	18.73
Wheat straw	Raw	45.54	5.59	0.00	0.00	43.71	15.42
	200 °C	46.56	5.36	0.00	0.00	41.40	15.77
	300 °C	55.86	4.88	0.00	0.00	29.49	18.91

Further material properties of interest during processing as an energy source include moisture content, alkali metal content and the material bulk density. Moisture content can be defined as intrinsic or extrinsic. Intrinsic moisture is the inherent moisture content of material regardless of the influence of weather effects. Extrinsic moisture includes the influence of prevailing weather conditions during harvesting and storage on overall biomass content [10].

Alkali metals in the ash fraction (Na, K, Mg, P and Ca) can react with silica during combustion forming a sticky, mobile liquid which can cause blockages of airways in the furnace and boiler plant, due to accumulation on plant components. This is discussed in more detail in Chapter 2. The bulk density of a material to be used as an

energy source is important in relation to the transportation, handling and storage of biomass fuels.

1.2.2. Differences between fossil fuels and biomass

There are a number of differences in key characteristics between biomass and coal. The content of volatile matter in biomass is typically around 80% compared to 30% for coal [8]. There are significant variations in the physical structure, composition and properties of the various biomass fuels which are of potential use for co-firing. Biomass can be said to behave in a similar manner to low-rank (lower energy content and carbon content) coals.

Biomass fuels differ from standard fossil fuels used in fluidised bed combustion (FBC) in a number of ways. They typically have: higher moisture contents, lower heating values, higher hydrogen content, higher volatile matter content, less carbon and more oxygen [20]. As there is more volatile matter available for reaction in biomass it is more likely that homogeneous ignition will occur for biomass fuels [9]. A summary of some of the different physical, chemical and fuel properties of biomass and coal fuels is given in Table 1.7.

Table 1.7: Physical, chemical and fuel properties of biomass and coal fuels [9,15]. daf = dry ash free.

Property	Coal	Wood Pellets	Palm Kernels	Straw
Bulk density (kg/m³)	1300	500	500	500
Carbon content (% daf)	68.80	47.91	44.20	38.46
Ash content (% dry)	17.70	1.10	4.38	8.90
Volatile content (% daf)	32.50	79.16	71.63	72.00
Calorific value (kJ/kg)	27443.5	18710.5	18719.0	15353.5

1.2.3. Sources of biomass

The two main sources of biomass are purpose-grown energy crops and waste. Energy crops encompass purpose-grown crops. Waste include wood residues, forestry residues, sewage, municipal solid waste and animal waste [8,21]. In general the characteristics of the ideal energy crop are [10]:

- High yield
- Low energy input to produce
- Low cost
- Composition with least contaminants
- Low nutrient requirements

The capacity to grow perennial energy crops willow SRC (short rotation coppice) and miscanthus on land in Ireland currently in grassland is substantial. Up to 250,000 ha of grassland could be converted to produce energy crops at acceptable yields without significant effect on existing farm enterprises or food and feed production [22].

Figure 1.4 shows the domestic supply curves for direct combustion of biomass in Ireland for (a) 2012, and projected curves for (b) 2020 and (c) 2030. They depict the quantity of each biomass resources that could be available (width of each block) and the price at which it is available (height) to be sold by farmers [22]. The majority of the resources are shown to be woody types of biomass. There is significant potential for both willow and miscanthus from 2012 to 2030 due to the high market price and the tariffs set by the government [6] . Note the change in the x-axis for table a – c in Figure 1.4. The disposal costs associated with waste, such as Biodegradable Municipal Solid Waste (BMSW) and Post Consumer Recovered Wood (PCRW) mean these resources are typically available to bioenergy installations at a negative/zero price and thus they appear below the zero price line.

In 2012, Ireland had a total primary energy requirement of 13,270 ktoe [1], of which direct combustion of biomass contributed approximately 350 ktoe (2.6%) of this. In 2020, the Sustainable Energy Authority of Ireland (SEAI) project that Ireland will have a primary energy requirement of 15,324 ktoe [23], with direct combustion of biomass potentially accounting for 4.7%. If an increase to 17,000 ktoe is assumed for 2030, the market share of direct combustion of biomass could increase to 17.7%.

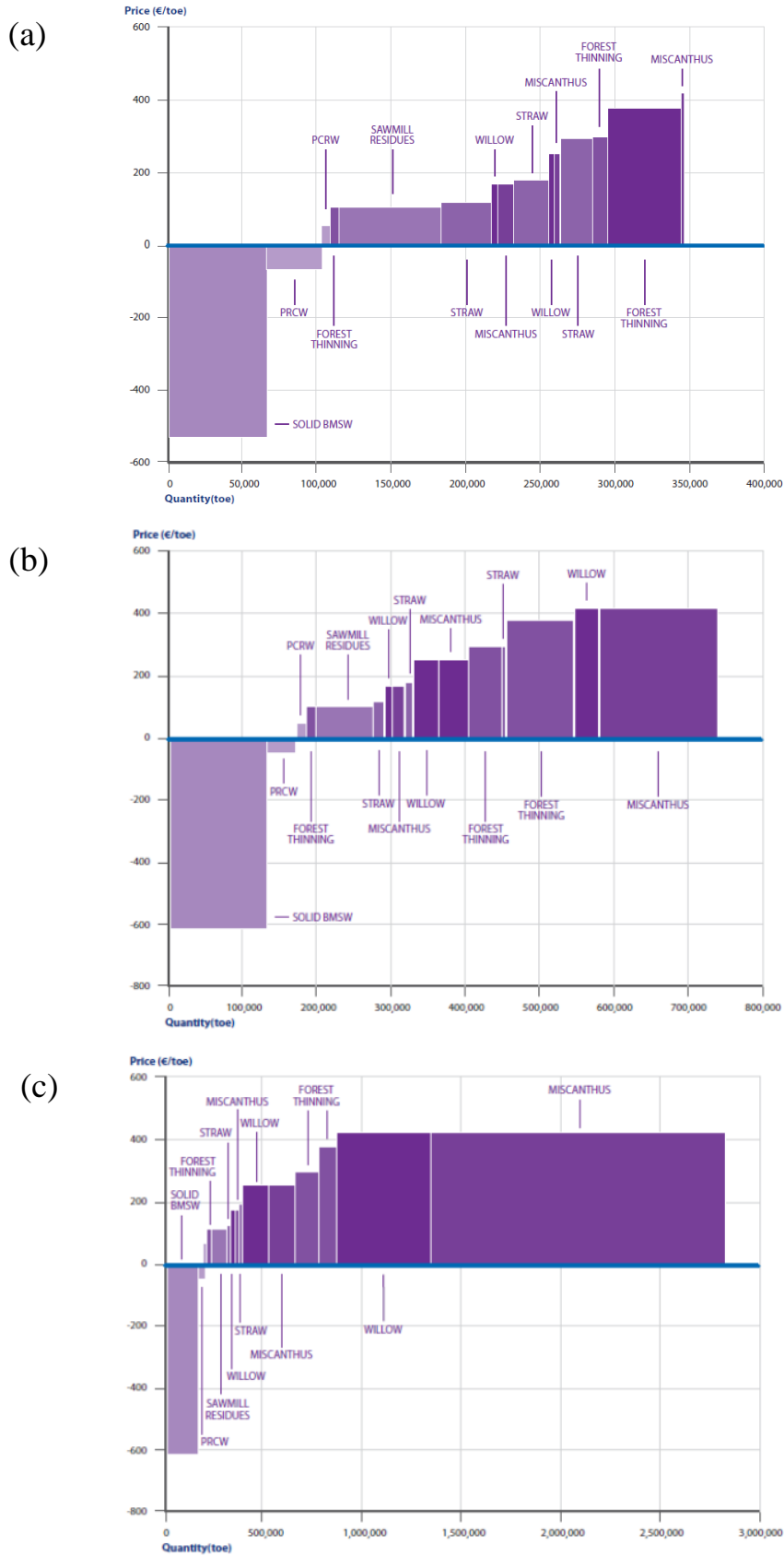


Figure 1.4: Domestic biomass resource supply curves for direct combustion for (a) 2012, (b) 2020 and (c) 2030 [22]. Note the change in the x-axis for table a – c.

1.2.4. Conversion techniques for woody biomass

There are a number of methods by which woody biomass can be converted to useful energy. Thermal conversion of biomass is the primary mechanism of retrieving energy, with combustion, gasification and pyrolysis the main methods used [24]. In addition to thermal conversion techniques, solid biomass can be converted into bio-fuels via bio-chemical conversions, such as fermentation and anaerobic digestion, but these are beyond the scope of this work [24].

A brief overview of the thermal methods used to produce solid, liquid and gaseous biofuels is given, followed by a section on the preparation required for the direct combustion of biomass. An overview of the different thermal conversion processes and the products produced from these processes is shown in Figure 1.5 [25].

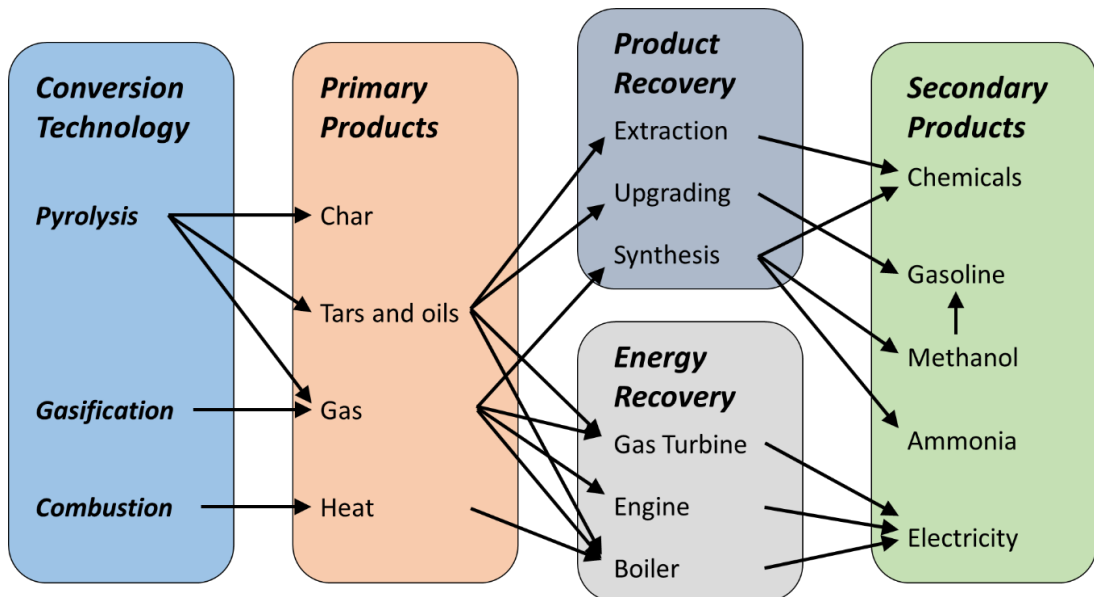


Figure 1.5: Biomass thermal conversion processes and different applications, adapted from [25].

Solid biomass can be converted into useful biofuels via number of conversion techniques. Pyrolysis is the thermal decomposition of biomass in the absence of oxygen. It occurs at relatively low temperatures ($\approx 300 - 650$ °C) and converts biomass to more useful fuels, such as a hydrocarbon rich gas, carbon rich solid residue and bio-oil [18,24]. Torrefaction is considered a mild form of pyrolysis, occurring at approximately $200 - 320$ °C. The purpose of torrefaction is to reduce moisture and oxygen content of biomass, thereby increasing its heating value [18].

Gasification is the thermo-chemical conversion of biomass into gaseous fuels (syngas) by the partial oxidation of the biomass at high temperatures. It is used to produce both low and high calorific value syngases.

Biomass can be burned directly in dedicated biomass combustion systems, waste-to-energy plants, and alongside fossil fuels in existing power plants (co-firing). Co-firing with peat for electricity production has been found to be a promising practice and is the focus of this work. The products that form during the combustion of biomass are the focus of this work and are discussed further in Chapter 2.

1.3. Combustion technology

Three main technologies are currently used in the combustion of biomass: grate bed combustion, pulverised fuel combustion and fluidised bed combustion. The purpose of combustion is to produce high-temperature flue gas, which heats water in heat exchanger (boiler or superheater) tubes to produce a superheated and pressurised steam. This steam then enters a turbine and drives an electric generator. This low pressure steam then condenses to water and the cycle, which is known as the Rankine cycle, is closed.

The efficiency of the Rankine cycle depends on the pressure and temperature of the steam entering the turbine. Hence, there is a need for materials capable of withstanding high temperatures and pressures. A diagram showing an ideal Rankine cycle is shown in Figure 1.6.

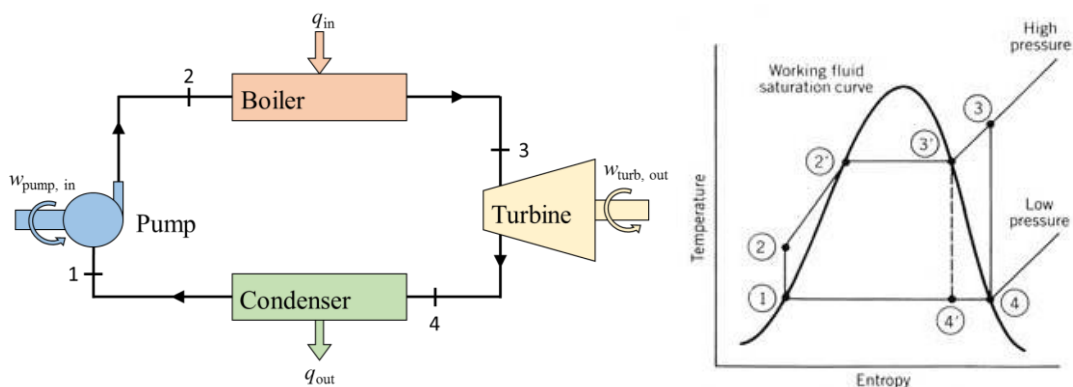


Figure 1.6: Diagram and graph showing the key stages of Rankine cycle.

1.3.1. Grate combustion

Grate boilers are the traditional boiler of choice for small scale solid fuel combustion with a wide operating size ranging from 15 kW_e to 500 MW_e. Grate boilers have the ability to burn a range of fuel types including, coal, peat and biomass. In this technology, drying, pyrolysis, char gasification and char oxidation take place on a grate, with combustion air distributed throughout the furnace [26].

The drawback with grate combustion technology is the relatively low boiler efficiency and high greenhouse gas emissions. However due to the simple structure, the cost of investment, operation and maintenance are typically low, making them favourable for small-scale applications [8].

1.3.2. Pulverised fuel combustion

In pulverised fuel plants, fuel is ground to a fine size (diameter < 2 mm), to facilitate continuous entrainment in the gas flow [26]. There are three ways in which biomass can be added to a fossil-fuel-burning pulverised boiler.

- 1) If the proportion of biomass is kept low, it can be fed with the fossil fuel through the mills to the boiler. However if the biomass proportion exceeds a certain limit issues will arise with the feeding system due to the different physical properties of biomass [27,28].
- 2) Separate handling, and grinding of the biomass, before injection into the pulverised fuel; which is then fed into the boilers. This involves significant changes to the operation of the boiler and creates difficulties in controlling operating conditions. Separate preparation of the biomass ensures it can be fed into the boiler through the normal feeding lines without problems [29].
- 3) Separate handling and grinding of the biomass in addition to separate combustion in dedicated boilers. This involves a high cost to operators. The benefits of this system is that it allow for both the biomass and fossil fuel to operate at optimal conditions for the individual fuel source [29].

All three options will likely result in a loss of net power output so the proportion of biomass in the mixture is therefore limited. This is due to the lower calorific value of biomass compared to fossil fuels or power used to prepare the biomass fuel for

combustion. The main motivation for using biomass in pulverised fuel combustion is the need to reduce emissions in existing plants [8] and subsidies and regulations which are currently in place [2,4].

1.3.3. Fluidised bed combustion

In this technology, fuel enters the combustion chamber via feed lines and mix with the bed material, which is typically sand or limestone. Up to 90 – 98 % of the total solid mass entering the combustion chamber is bed material. Primary combustion air enters the chamber from below a perforated bed plate or via tubes which protrude from the bed of the boiler and causes the individual particle to become suspended in the air stream, and the bed is known as fluidised [30]. As the air velocity increases, there is bubble formation, vigorous turbulence and rapid mixing of the particles. This allows for intense heat transfer, which provides good conditions for complete combustion [31].

There are two main boiler types that make use of fluidised bed technology, bubbling fluidised bed (BFB) and circulating fluidised bed (CFB). A schematic of a circulating fluidised bed boiler is shown in Figure 1.7 (a) and a bubbling fluidised bed boiler in Figure 1.7 (b).

The choice between BFB and CFB is typically linked to the choice of fuels being burnt. BFB is typically thought of as simpler and cheaper and hence it is favoured in plants that exclusively burn biomass or similar low-grade fuels that contain highly volatile substances to keep costs down. Recently, new CFB designs have provided a competitive alternative to BFB for use in biomass fired plants [8].

In a bubbling fluidized bed the fuel particle sizes are typically large and the velocity of air and overall temperature are lower, as shown in Table 1.8 [26,29,32]. This is done to ensure that fuel does not escape the combustion chamber prior to combustion. In a circulating fluidized bed, the material passes through a cyclone separator, which then returns the unburnt fuel particles and bed material to the combustion chamber. Further information on both bubbling and circulating fluidized bed technology can be found in references [33,34].

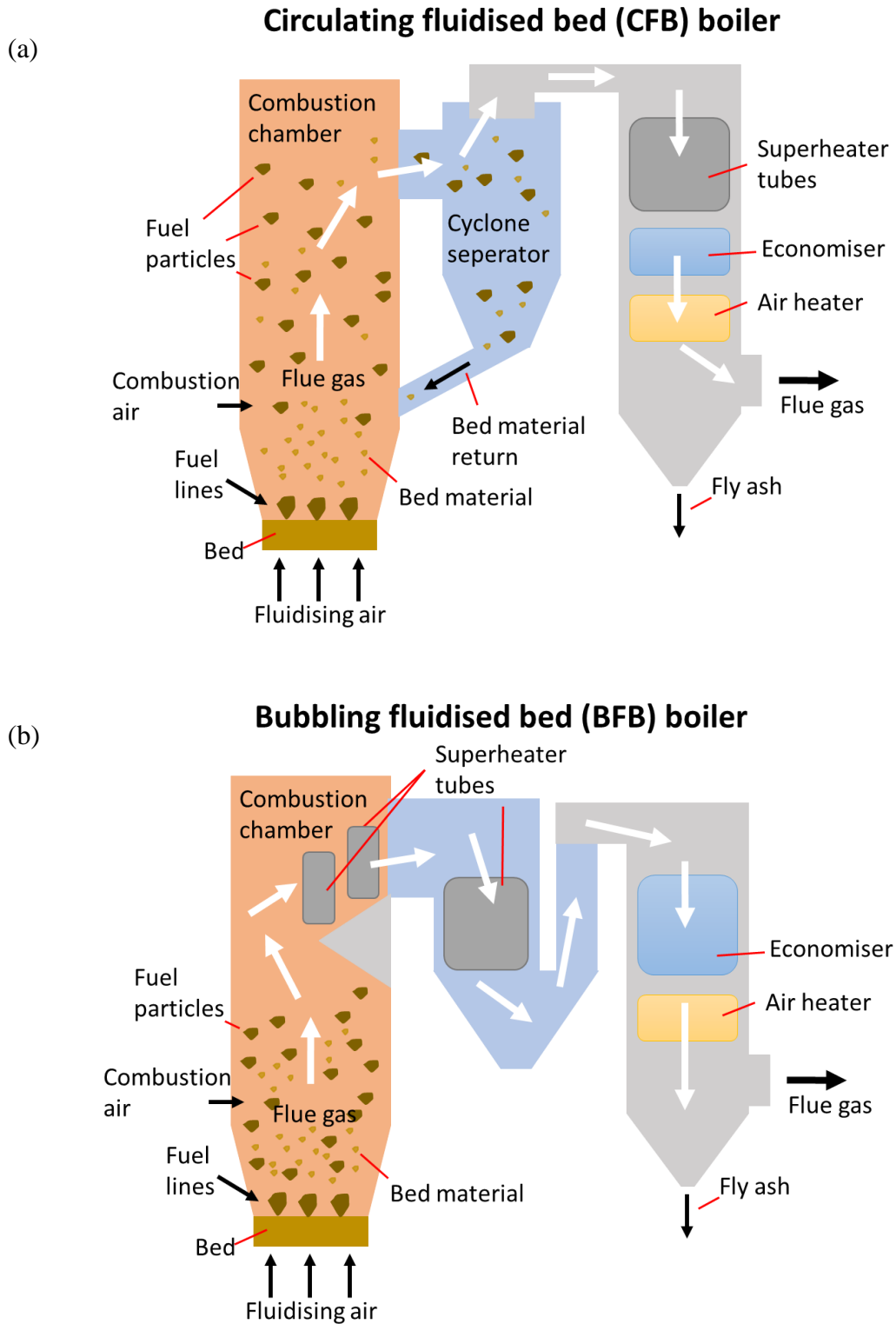


Figure 1.7: Schematic of a (a) circulating fluidised bed boiler and (b) bubbling fluidised bed boiler.

Table 1.8: Characteristics of bubbling and circulating fluidised bed technology [26,29,32].

Technology	Bubbling	Circulating
Fuel particle size (mm)	< 80	< 40
Bed particle diameter (mm)	0.5 – 1.0	0.2 – 0.4
Fluidization velocity of air (m/s)	1 – 2	5-10
Bed temperature (°C)	650 – 850	750 – 900

1.4. Challenges for biomass combustion

A number of challenges have been identified in the use of biomass as a fuel in power plants. If biomass is to replace a fossil fuel at a large scale this will require the use of large areas of land to cultivate suitable biomass fuels in sufficient quantities. It must be ensured that sufficient farmland exists for the production of both food and energy crops for use in plants. A problem also exists in relation to the cost of producing and harvesting biomass fuels. The most significant cost in the production of biomass is in the transport of the biomass, which is largely a function of the distance between the plant and the biomass production site and the fuel HHV [10].

Importation of biomass via shipping is an alternative means of obtaining sufficient quantities of biomass. The economic feasibility of this will depend on the quantities required via shipping and the distance travelled [29,35]. From an environmental view it was found that the emissions from long range transportation ≥ 1200 km, via shipping are of negligible importance [36].

In addition to these production issues of biomass, problems occur during combustion of the fuel. Fouling, slagging, agglomeration, trace metal emissions, the low heating value of biomass fuels, as well as the high temperature corrosion of heat exchanger tubes [9,20], are all significant challenges in the use of biomass as a fuel in plants

Trace elements (e.g. Cu, Pb, Zn, etc.) present in some biomass fuels can cause environmental and health problems. Due to this, plant operators must take measures

to reduce the presence of these harmful metals, such as cleanup by adsorbent materials [9,37].

Biomass fuels typically have a high moisture content relative to fossil fuels. As a result of this their heating value is typically lower, leading to potential flame stability problems. Blending biomass with higher quality fuels can overcome this problem [9,38,39].

Fouling and slagging are terms used to describe the accumulation of ash on the surface of heat transfer equipment. The high levels of chlorine and alkalis in biomass result in low melting temperature eutectics forming which cause highly-adherent melts to form on tube surfaces leading to enhanced deposition. The degree of fouling and slagging varies throughout the boiler depending on local gas temperature, tube temperature, temperature gradients, gas velocities, tube orientation and fuel composition [40–42].

Agglomeration is when bed particles adhere to each other forming larger entities (agglomerates). In biomass fired plants it can occur due to two phenomena: (i) the accumulation of low-temperature-melting salts of potassium and phosphorous, and (ii) with silica from sand and calcium from fuel initiating a reaction with potassium phosphate leading to the formation of low temperature melting silicates of potassium and calcium. Agglomeration is a leading cause of de-fluidization in boilers, which can result in costly shutdown periods [43]. Fuel particles burning in the defluidized zone will fail to dissipate their heat leading to the formation of a localised hot spot. The temperatures of particles in this region increase, leading to particles sticking to one another, further restricting mobility in the zone. This also results in the formation of clinkers in this region which can cause damage to plant components [30].

Sintering of the bed is caused by changes in bed particle chemistry due to reaction with ash-forming matter. Sand, gravel, ash from coal, and limestone are commonly used as bed materials, leading to the formation of potassium and calcium silicates when burning biomass fuels [30]. These can in turn form a molten viscous glassy phase on the particle surfaces, making the particles highly-adherent. Nonetheless, quartz is still the dominant bed material used for economic reasons. Limestone is sometimes added to the bed material to reduce SO₂ emissions. In co-firing agglomerates of particles from the different fuels, will form, in addition to the particles formed from

each individual fuel, making the prediction of sintering in a multi-component bed difficult [44–46].

High temperature fireside corrosion of heat exchangers is a well-known issue in the power generation industry and can result in early tube failures leading to costly plant shutdown and repair. The high levels of alkali chlorides induce an accelerated corrosion rate of the tube walls. The focus of this work is on high temperature corrosion and as such this is discussed briefly here with a more in-depth review in Section 2.7.

Fireside corrosion occurs as a result of exposure of tube-wall material to the gaseous, molten and/or solid products of the combustion process. Flue gases, which contain O₂, N₂, CO₂, SO₂, HCl and other minor gaseous species, can result in a harmful environment for plant components. In addition to gaseous species, fractions of non-combustible materials (ash), such as alkali salts (e.g. K₂SO₄, NaCl, KBr), which form as a product of the combustion process, can be transported to heat exchangers, where they can form deposits on tube walls.

It has been found that the co-firing of biomass results in the formation of ash with different properties from those of peat and coal individually. Specifically, biomass ash contains elevated levels of alkali halides, mainly potassium and sodium chloride, which cause accelerated corrosion of heat exchanger tubes. The focus of this work is the corrosion process that occurs during biomass co-firing and the associated effects on structural integrity of in-situ pipes. An example of heavy fouling and corrosion of superheater tubes taken from an operational plant with steam conditions of 563 °C and 16.8 MPa is shown in Figure 1.8 (Courtesy of ESB).



Figure 1.8: An example of in-situ deposits on superheater tubes and tubes showing heavy corrosion following removal (Courtesy of ESB).

Change in compositions of flue gas and ash formed during co-firing and subsequent high-temperature corrosion is the main reason why steam temperature, and hence, plant efficiency in biomass plants is lower than in coal plants [47]. The extent of fireside corrosion of heat exchanger tubes in co-firing plants depends primarily on (i) composition of the gas and ash combustion products, (ii) the flue gas temperature and (iii) the material of the tube walls.

Biomass typically contains lower levels of sulphur, relative to fossil fuels, while the content of alkali metals and chlorine can vary. The Cl:S ratio of biomass fuels is generally found to be higher in biomass fuels due to the lower sulphur levels. Potassium and chlorine are both known to affect corrosion rates. The presence of chlorine typically causes the formation of loosely adherent, non-protective oxide layers. Failure of superheater tubes in a bubbling fluidized bed boiler has been reported, following just six months of combustion of a high-Cl bark-biosludge mixture [48]. This highlights the need for improved understanding of the biomass corrosion process.

A large amount of work has been carried out on the corrosion potential of chlorides in deposits [49–54]. The consensus is that alkali chloride-containing deposits result in very high corrosion rates, even when the tube surface temperatures are well below the melting points of the salts. This is primarily due to a corrosion mechanism known as

active oxidation, which is described in detail in Chapter 2 [51,55–58]. It has been shown that the most severe corrosion problems occur due to the formation of Cl-rich deposits on the superheater tubes [59–61]. This can be partly attributed to the formation of liquid phases in deposits. It has been shown that corrosion rates accelerate if Cl₂, HCl or alkali chlorides are present in the atmosphere [51,53,62–64].

1.5. Aims and objectives

The aim of this research is to characterise and accurately predict the co-firing induced corrosion of superheater tube materials and the effect of this corrosion on tube mechanical performance.

A combined experimental and modelling approach has been adopted. The experimental aspect investigates the corrosion rate caused by salts formed by synthetic peat-biomass ash on different candidate tube materials at a range of temperatures. The modelling aspect adopts a multi-physics approach, based on solid mechanics modelling, to predict the effect of material corrosion on the mechanical performance and structural integrity of plant components. A porosity-based diffusion model is also developed to provide a physical model for the corrosion process.

The main objectives for this project can be split into experimental and computational aspects respectively, experimentally the objectives are as follows:

- Determine the chemical composition of deposits forming on heat exchanger tubes and prepare representative synthetic salts.
- Assess the response of candidate tube materials to the synthetic salts at representative temperatures.
- Investigate the effect of inclusions formed during the manufacturing of materials on corrosion rates and mechanisms.

From a computational viewpoint the objectives of this work are the following:

- Develop a physically-based model for the active oxidation corrosion process.
- Investigate the effect of uniform corrosion on tube rupture life.
- Investigate the effect of sub-surface inclusions on localised stresses.

- Investigate the effect of pitting corrosion on tube stresses in a pressurised tube.

The key activities, each of which address an objective, which have been carried out during this research are detailed in Table 1.9.

Table 1.9: Key activities discussed in thesis.

Experimental	
Identification of deposit composition and preparation of synthetic salts	Chapter 3
Elemental analysis of a range of biomass fuels and deposits obtained from operational plants	Chapter 3
Exposure of boiler tube material to synthetic salts at temperatures representative of plant operating temperatures	Chapter 4, 5, 6 and 7
Examination of oxide scales and assessment of subsurface material damage	Chapter 4, 5, 6 and 7
Investigation on the effect of inclusions on corrosion rates of materials	Chapter 6 and 7
Examination of samples taken from in-situ heat exchanger tubes	Chapter 7
Computational Modelling	
Identification of key limiting phenomena in corrosion process	Chapter 4
Determination of corrosion rates based on experiments and first principles	Chapter 4 and 5
Development of a porosity-based model for corrosion rate	Chapter 4
Incorporation of a uniform corrosion sub-model into mechanically loaded finite element models	Chapter 5
Investigation into the effect of inclusions on localised stresses of samples via finite element modelling	Chapter 6
Development of a pitting corrosion model and investigation of the effect on localised stresses via finite element analysis	Chapter 7

1.6. Thesis overview

Chapter 2 contains a review of literature relevant to this research. It details: (1) how the biomass decomposes during combustion leading to the formation of ash, (2) the science behind the corrosion of materials, (3) the materials of interest to this work, and (4) an in-depth review into previous work done on the fireside corrosion caused by co-firing biomass.

Chapter 3 presents the experimental methodology, which has been developed at NUI Galway, to investigate the accelerated corrosion which is observed during biomass co-firing. The method behind producing synthetic salts to replicate in-situ deposits is detailed, along with the conditions at which samples were exposed. Results of energy dispersive X-ray spectroscopy (EDX) carried out on samples of raw and torrefied biomass materials are presented, and their suitability for use as a fuel is discussed. Additionally samples of deposits have been obtained from super-heater tubes and analysed to determine the composition of the deposits which accumulate for different plants. The analytical equipment used in the examination of test samples is discussed and the theory that they operate under is briefly described.

A novel physically-based model to predict the accelerated corrosion under salt deposits subject to active oxidation for pure iron is presented in Chapter 4. This newly-developed model uses measurements of oxide layer porosity and pore radius to obtain an effective diffusion coefficient to predict corrosion rates. Comparisons are made between results obtained from this model and previously developed empirical models.

Chapter 5 presents experimental results for the corrosion rate of P91 steel when exposed to salt deposits. These are combined with creep damage models to assess creep-corrosion of pressurized tubes using the finite element program Abaqus. The effects of uniform tube wall material loss and creep damage on tube stresses and creep rupture life is investigated.

A microstructural study into the corrosion process of P91 during co-firing is presented in Chapter 6. The effects of inclusions as potential sites for pit initiation in pitting corrosion is discussed. The potential of inclusions to act as sites for stress concentrations is studied using finite-element models and the results are discussed.

These stress concentrations can result in localised plastic strains which may lead to crack initiation points.

A microstructural study into the corrosion process of 347SS during co-firing is presented in Chapter 7. Comparisons are made between the corrosion rates and mechanism of 347SS and P91, from Chapter 6. The effect of pitting corrosion on tube stresses is investigated in Chapter 7. Experiments have been carried out to determine the frequency and severity of pits that form during biomass co-firing. Finite-element models of pipes have been developed with pit formation based on the experimental data, as well as data on pit formation from in-situ tubes.

Chapter 8 summarizes the main outcomes and conclusions from the previous chapters. This leads to recommendations for potential future work.

2. Literature Review

2.1. Chapter overview

In order to characterise materials for use in power plants during biomass co-firing a number of significant factors should be considered. These can be broken into the following key topics; (i) the biomass fuel, (ii) the combustion technology used, (iii) the heat exchanger materials used, (iv) the mechanical loading to which the material is subjected and (v) the corrosion mechanism to which the materials are subjected.

Knowledge of biomass as a fuel is essential in order to appreciate the benefits of co-firing biomass in large scale power generation. The use of biomass as a fuel and the combustion technology currently used for co-firing was presented in Chapter 1.

Section 2.2 details the decomposition of a fuel particle as it undergoes combustion. The details behind ash formation and deposition on heat exchangers is discussed in Section 2.3. A background on corrosion as a general damage mechanism is given in Section 2.4. The different forms of corrosion are discussed and a number of corrosion models are reviewed.

The mechanical damage mechanisms associated with heat exchanger tubes at high temperatures, is reviewed in Section 2.5. The material microstructure of interest to this research are reviewed in Section 2.6. A detailed review of previous work on the accelerated corrosion due to biomass co-firing is presented in Section 2.7. Finally, an overall summary of the literature review is given in Section 2.8.

2.2. Solid Fuel Combustion

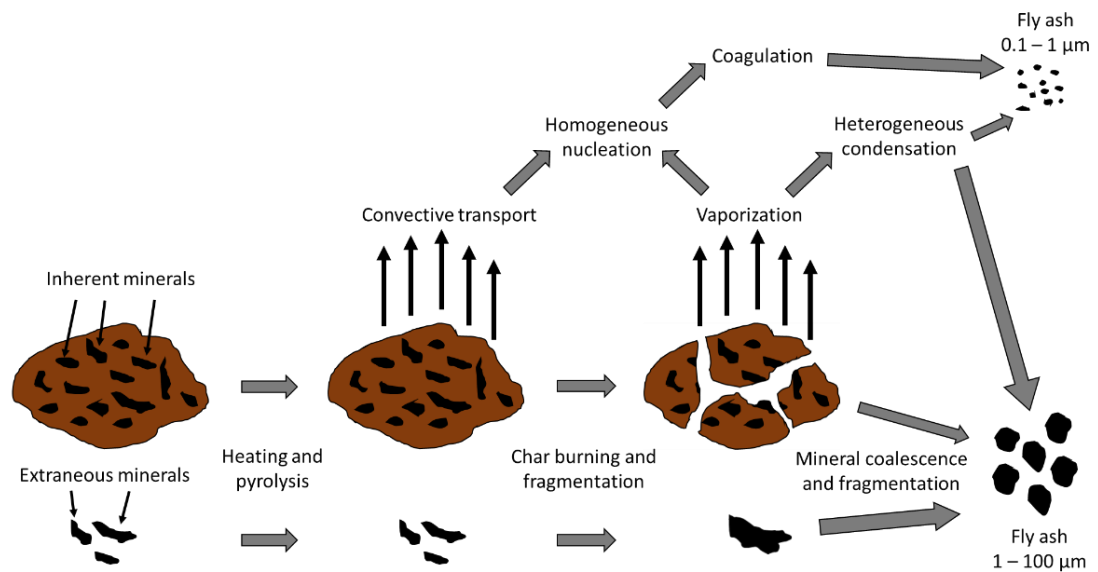


Figure 2.1: Schematic showing thermal decomposition of fuel and ash formation, adapted from [65,66].

In a combustion chamber, a particle of fuel undergoes heating and drying, devolatilisation and volatile combustion, swelling and primary fragmentation, combustion of char with secondary fragmentation. These processes are shown schematically in Figure 2.1. Both organic and inorganic components of the fuel undergo devolatilisation, which leads to the release of gases stored in the pores of the fuel, with the remaining solid called char [67–70].

Char consists of carbon, organic substances and ash. Char oxidation is typically the rate-limiting step in the combustion process [71]. The combustion of a char particle proceeds via the diffusion of oxygen to the surface of the particle, and then through the pores of the particle to the internal surface. Once there, it reacts with carbon on the inner and outer surfaces of the particle. Products of this reaction then diffuse to the outer surface and to the bulk gas surrounding the particle. A number of models have been developed to describe this process [71,72].

2.3. Ash formation in fuels

Very little ash-forming matter is expected to be produced during the drying stage which takes place at temperatures of around 100 °C [73]. During high temperature devolatilisation, the fuel particles release large amounts of vapours and gases. For most biomasses, between 70-90% of combustible matter will be released as vapours during this stage, with some ash-forming elements being released during this stage. During the following char burning step, particle temperature can reach 850 – 1000 °C and the easily-volatilised ash-forming metals form gaseous compounds such as chlorides. The extent of this release of gases depends upon the burning conditions, such as temperature and oxygen content [20].

Inherent mineral matter is considered the most important source of ash-forming elements responsible for high temperature corrosion of heat exchanger tubes. Inherent minerals form in the fuel matrix as an oxygen-containing compound, which does not separate from organic particles before combustion. As biomass contains higher levels of oxygen than fossil fuels, the potential for inherent minerals is larger in biomass. Typical examples of inherent materials are combinations of alkali and alkaline earth metals such as sodium or potassium compounds [72,74].

There are a number of sources of biomass fuel property data available both in the literature and in online data banks which show analyses of the ash-forming matter of fuels [15,39,75,76]. Table 2.1 shows the ash elemental analysis (major elements) for a number of important biomass materials. It is clear from the data presented that while the composition varies biomass fuels tend to be rich in similar elements, i.e. calcium, potassium and phosphorous. While the ash chemistries of other biomass materials vary significantly they are all dominated by Ca, K or P [29]. This information is extremely important when related to the melting temperature of biomass ash, as is discussed in more detail in Section 2.7.4.

Table 2.1: Typical ash elemental analysis (major elements) for a number of biomass fuels [29].

Biomass type	Forestry residue	SRC willow	Miscanthus	Olive residue	Palm kernel
S content (wt%, dry ash-free basis)	0.04	0.05	0.20	0.20	0.20
Cl content (wt%, dry ash-free basis)	0.01	0.03	0.20	0.20	0.10
Ash content (wt%, dry basis)	2	2	4	7	4
Elemental analysis (mg/kg of ash, dry basis)					
Al	0	0	0	1500	750
Ca	5000	5000	2000	6000	3000
Fe	0	100	100	900	2500
K	2000	3000	7000	23,000	3000
Mg	800	500	600	2000	3000
Na	200	0	0	100	200
P	500	800	700	1500	7000
Si	3000	0	0	5000	3000

There are five main mechanisms which contribute to deposit growth on heat exchangers: condensation, thermophoresis, brownian and eddy diffusion, impaction and chemical reactions [77–79]. Impaction is typically considered the main contributor to deposit build up on heat exchanger walls [72]. A number of computational models have been produced using CFD (computational fluid dynamics), among other techniques, to predict deposit formation on tubes [80–84].

2.4. Corrosion of materials

Corrosion is the irreversible degradation of materials via chemical reaction with their environment. There are several consequences of corrosion, the majority of which result in detrimental effects on the safe, reliable operation of equipment. This can lead to costly plant shutdowns and the repair or replacement of corroded materials. Oxidation is the most common form of corrosion, and occurs via the chemical reaction of a material with oxygen. Other types of corrosion include sulphidation and chlorination.

Corrosion can occur in reducing (low oxygen containing) environments, via the reaction of a material with other elements, such as chlorine (chlorination) or sulphur (sulphidation) [85–87]. If the combustion process is not carried out in sufficient levels of oxygen (lower P_{O_2}), a reducing environment will form. However, it is more likely that a mixed gaseous environment, consisting of SO_x , CO_2 , NO_x and HCl, will be present during combustion [88].

Different materials react with oxygen (oxidise) at different rates due to their material properties. Alkali and alkaline earth metals, such as sodium, magnesium and calcium, oxidise quickly. Noble metals, such as silver or gold, have a high resistance to corrosion, while transition metals, such as iron, nickel and chromium, have a moderate corrosion resistance [89]. Alloys of transition metals are commonly used for heat resistant materials by boiler manufacturers due to their relatively low cost.

The addition of different alloying elements is employed to promote enhanced corrosion resistance and improved mechanical performance. The addition of chromium, for example, increases oxidation resistance, due to the formation of chromium oxide on the substrate surface [87]. This oxide layer acts as a barrier against further oxidation, by preventing additional oxygen reaching the substrate. This is discussed in further detail in Section 2.6.

2.4.1. Thermodynamics of metal oxidation

It is well known that metals are thermodynamically unstable and form different oxides, sulphides, etc. easily, particularly at high temperatures [87]. The most stable phase of a material under different conditions can be expressed in the form of phase equilibrium diagrams. The most stable phases for a metal M at a given temperature are shown in Figure 2.2, as functions of partial pressures of sulphur (P_{S_2}) and oxygen (P_{O_2}).

From this we can see that at a low P_{S_2} an increase in P_{O_2} , will lead to the formation of metal oxide (MO). Similarly when P_{O_2} is low and P_{S_2} , high, metal sulphide (MS) will form. If both P_{O_2} and P_{S_2} are high, a metal sulphate (MSO_4) will form [90]. If the temperature changes, the phase equilibrium will change to represent the new stable phase locations.

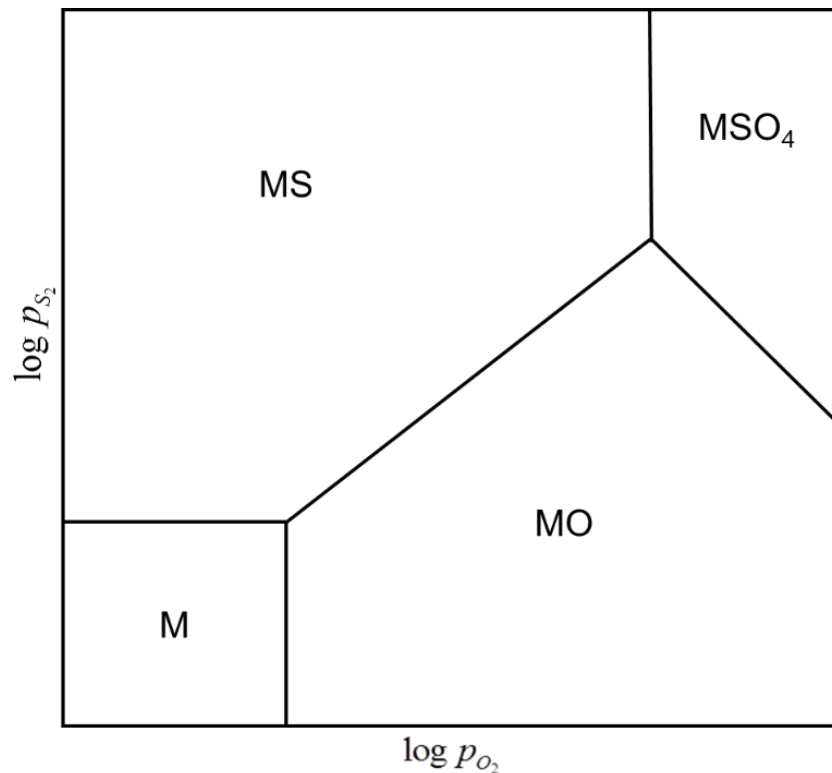


Figure 2.2: A typical metal sulphur-oxygen phase diagram at a given temperature, adapted from [90].

2.4.2. Kinetic modelling of metal oxidation

The extent of oxidation is often measured by the mass increase of a material, since oxidation is the addition of oxygen atoms to a material the weight of the material usually increases. Oxidation behaviour, in terms of time history of mass increase, Δm , at high temperatures, is typically classified as linear or parabolic, as follows, respectively:

$$\Delta m = k_L t + C \quad (2-1)$$

$$\Delta m^2 = k_P t + C \quad (2-2)$$

where k_L and k_P are kinetic coefficients and C is the constant of integration. k_L is usually positive but can be negative, indicating that the oxide evaporates once formed, causing the material to lose weight. k_P is always found to be positive [87]. The applicability of either model depends on oxidation behaviour observed during testing.

The effects of temperature on kinetic coefficients of oxidation can be represented using Arrhenius equations, as follows:

$$k_L = A_L e^{-Q_L/\bar{R}T} \quad (2-3)$$

$$k_P = A_P e^{-Q_P/\bar{R}T} \quad (2-4)$$

where A_L and A_P , are Arrhenius coefficients, Q_L and Q_P are activation energies for oxidation and \bar{R} is the ideal gas constant [87].

2.4.3. Forms of Corrosion

The different forms of corrosion are briefly reviewed in this section [91–94]. A schematic showing the different forms of corrosion is shown in Figure 2.3.

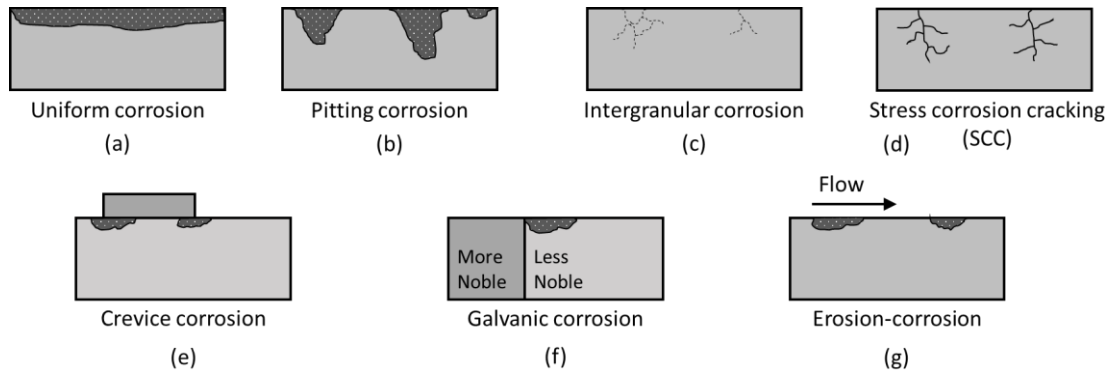


Figure 2.3: Schematic showing different types of corrosion, adapted from [95].

Uniform corrosion, which is the most common form of corrosion spreads uniformly over a wide surface area, resulting in a relatively predictable corrosion rate [94] (Figure 2.3 (a)). It is caused by chemical or electrochemical reaction and results in the deterioration of the entire exposed surface of a metal. It is considered the safest form of corrosion due to its predictable, manageable and often preventable nature. It can be limited via inhibitors or protective coatings, which prevent harmful elements reaching the metal surface [92].

Pitting corrosion is the most destructive of all corrosion types; it is localised, resulting in the formation of numerous small irregularly shaped cavities (pits) in the metal (Figure 2.3 (b)). It can be initiated from surface defects and it may be covered and hidden by compound corrosion products. When a small pit forms, the area becomes anodic, while the remaining metal becomes cathodic resulting in a localized galvanic reaction. It is difficult to predict pitting and failure can result from a relatively small area of corrosion [91,92].

Intergranular corrosion is a localised chemical or electrochemical attack of the grain boundaries of metals, with little corrosion of the grains (Figure 2.3 (c)). This can be caused by impurities in metals, which tend to be present in higher contents near grain boundaries. Intergranular corrosion leads to weakening of the metal and increased potential for dislocation of grains. It is only detectable using microscopic observation at high magnification [89,92].

Stress corrosion cracking (SCC) occurs due to the combination of mechanical stress and a corrosive environment. This leads to the crack formation at the metal surface. SCC, is typically localised, with fine cracks progressing through the metal [94]. Typically the corrosive environment that causes SCC is only mildly corrosive in the absence of mechanical stress. Due to this the metal surface can appear healthy, while being filled with microscopic cracks. This makes early detection of SCC difficult and can result in the unexpected failure of metals (Figure 2.3 (d)) [89,92].

Crevice corrosion (Figure 2.3 (e)) is an intensely localised corrosion, which occurs within the crevices and other shielded areas of metals. The crevice can be a gap between two metals or a metal and a non-metallic material. It is similar to pitting corrosion and is caused by acidic conditions or a depletion of oxygen [89,92].

Galvanic corrosion occurs when electrochemically dissimilar materials come in contact with one another in a corrosive environment. This results in the flow of electrons from one material to another due to the electrochemical potential difference developed between two different metals and occurs due to poor design (Figure 2.3 (f)). The difference in electrode potentials of the metals leads to one metal acting as an anode and the other as a cathode leading to the accelerated attack on the anode member of the metals. The corrosion damage is highly localised in the contact zone with the other metal [89,92].

Erosion-corrosion is the acceleration of a corrosion rate due to the flow of the surrounding fluid or fluidised material around a metal surface. The increased turbulence caused by corrosion of the metal surface results in a rapidly increasing erosion rate. A combination of erosion and corrosion can lead to very high pitting rates. Typically waves and grooves form on metal surfaces following erosion-corrosion which exhibit a directional pattern (Figure 2.3 (g)) [94].

2.4.4. Oxide scale structure

Different materials form oxides at different distances from the substrate. This occurs as they have different diffusion coefficients. Materials with lower diffusion coefficients will form oxides close to the surface than those with high diffusion coefficients as they will not diffuse as far before oxidising [87].

In certain cases an initial oxide layer is desirable as it forms close to the substrate, resulting in a protective oxide scale. These oxides have lower vapour pressures than materials which form oxides which are detached from the substrate. Oxides which form further from the substrate offer little protection against further oxidation.

Oxide scales develop stresses, which can result in their breakdown. The stress in an oxide has been described as a superposition of six individual stress terms as follows [96]:

$$\sigma_{Total} = \sigma_{IntrGrth} + \sigma_{GeomGrth} + \sigma_{Therm} + \sigma_{Creep} + \sigma_{Microcrck} + \sigma_{Mech} \quad (2-5)$$

$\sigma_{IntrGrth}$ corresponds to the stresses which occur during oxide growth and relate to the formation of new oxides within the oxide layer. $\sigma_{GeomGrth}$ correspond to the stresses which occur during oxide growth and relate to the surface geometry (e.g. curvature, roughness). σ_{Therm} represents the thermally-induced stresses due to the difference in thermal expansion coefficients of the oxides and the metal; σ_{Creep} and $\sigma_{Microcrck}$, are stress associated with oxide creep and oxide damage, respectively; σ_{Mech} , is stress due to mechanical loading, e.g. internal pressure. Sabau et al. [97] have presented critical strain criteria for crack initiation, delamination and separation of oxide scales. Based on this criteria, failure of the oxide scales can be predicted.

Figure 2.4 shows two possible mechanisms for the breakdown of oxide scales. As the oxide scale thickens, cracks can develop or detachment from the substrate can occur. If the volume of the oxide is less than the volume of the parent material, it will crack in order to relieve the strain as shown in Figure 2.4 (a). If the volume of the oxide is greater than that of the parent material, the oxide will break the adhesion between the oxide and substrate resulting in the release of the strain energy as shown in Figure 2.4 (b) [87]. The volume change occurs as a result of the addition of oxygen atoms to the material and the growth of the oxide.

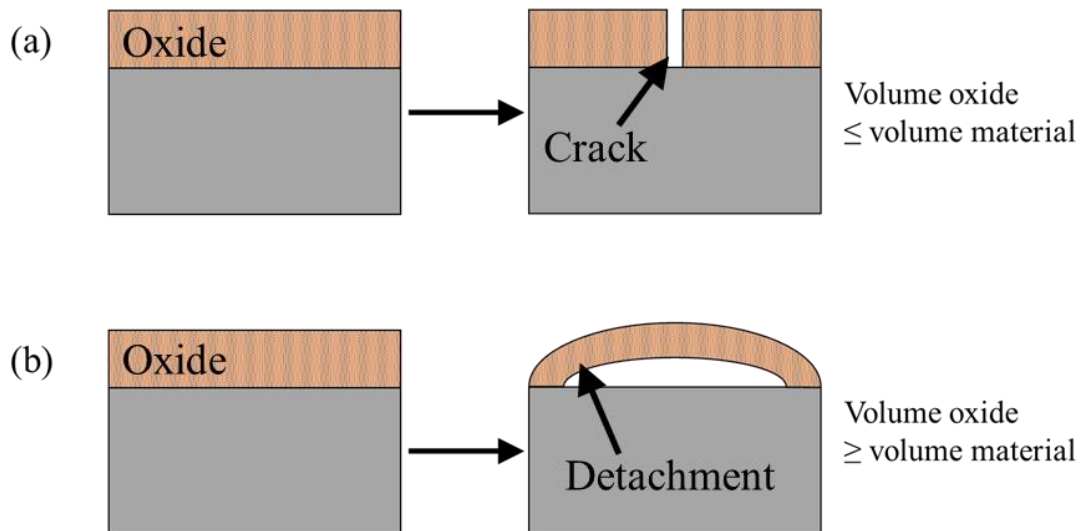


Figure 2.4: Schematic showing oxide scale breakdown if (a) volume of oxide is less than the material or (b) the volume of the oxide is greater than the material, adapted from [87].

2.4.5. Corrosion Modelling

There have been a number of efforts to model corrosion in previous work. A brief discussion on these is presented in this section with the functionality and results obtained shown. As this work focuses on the implementation of corrosion damage in finite element models these are the focus of this section. There are several other examples of incorporating corrosion damage into life calculations, such as the work by Neu and Sehitoglu [98,99] amongst others [100–103].

Wenman et al. [104] modelled pitting corrosion and stress corrosion cracking (SCC) of a 2D cross sectional pipe via element removal in the finite element (FE) code Abaqus. The model was based on the assumption that cracks grow from the base of surface pits, under mechanical control. Results of the model correspond well with stress-corrosion cracking which was observed in a boiling MgCl_2 environment. In this model, pit formation was limited in favour of crack growth. This allowed the model to simulate crack initiation at the base of pits. Crack growth was then controlled by stress redistribution around the deleted elements in contact with the free surface. Figure 2.5 shows some typical pit morphologies which were created via deletion of computational elements [104].

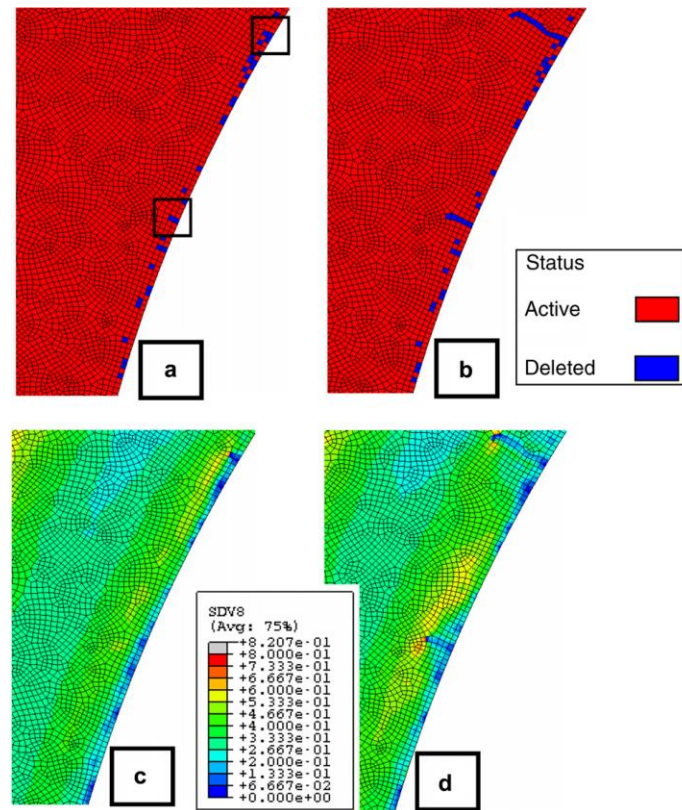


Figure 2.5: (a) Pits showing varying depths and morphologies created by element deletion based on a critical plastic strain and random number generator, (b) following time increments showing pits transitioning to cracks in marked boxes in (a). (c) and (d) show corresponding fraction of yield stress [104].

Steam-side oxide scale growth on heat exchanger tubes has been modelled in work by Purbolaskono et al. [105] using the finite element program ANSYS. This work investigated different oxide growth rates and resultant changes in temperatures at the scale-metal interfaces. The effect of different design temperatures for steam and different heat transfer properties were investigated. Scale growths were shown to be influenced by tube geometry and heat transfer parameters such as steam temperatures, mass flow rates of steam, flue gas temperatures and convection coefficients on the outer surface of the tubes [105].

Turnbull et al., [106,107] modelled the evolution of pits, pit-to-crack transition and early stage crack growth using the finite element program Abaqus. This model accurately captured the early stages of crack growth.

Grogan et al., [108] developed a numerical model to predict the effects of corrosion on the mechanical integrity of bio-absorbable metallic stents. Experimental work was

carried out to determine the effects of corrosion on the integrity of metallic foils in addition to the effects of mechanical loading on the corrosion behaviour of the foils. The model was then applied to a complex stent in an idealized arterial geometry.

A second corrosion model has been developed by Grogan et al. [109] to model corrosion of stents making use of an adaptive meshing technique. This method was more efficient than previous methods and as it does not depend on element deletion it was less sensitive to mesh resolution.

Biglari and Nikbin [110] developed a sub-grain size finite element meshing technique which has been applied to a combined creep-corrosion damage and crack growth model. The model allowed for crack paths to cause failures from intergranular and transgranular cracking in addition to surface oxidation and depletion due to corrosion. A probabilistic random crack extension criterion was deployed to allow for the statistically varying random damage and crack growth development during a model run.

This takes into account the scatter which occurs in test data and oxide/crack growth measurements. A model of a simple block under tension subjected to creep and corrosion damage and the relative extent of creep to corrosion damage under different loading conditions was investigated. A result showing crack growth and oxide scale is shown in Figure 2.6.

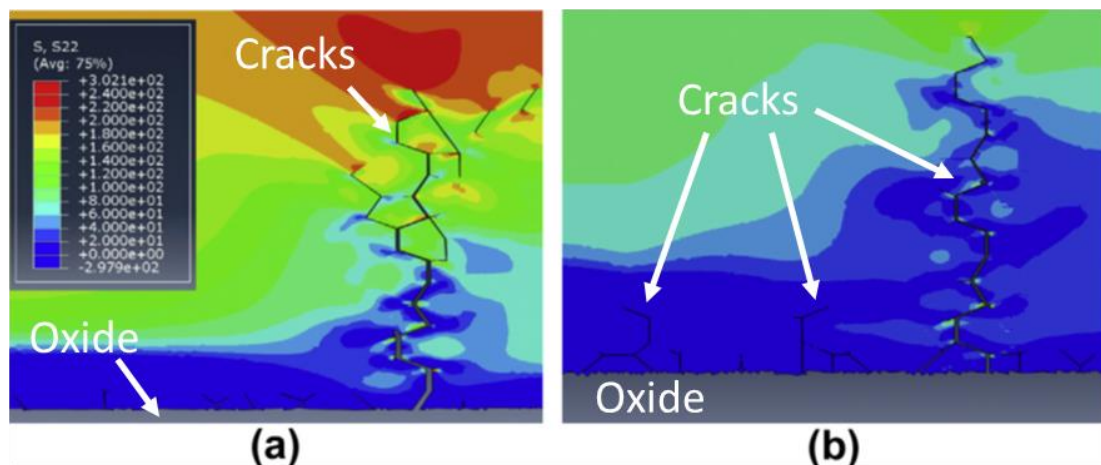


Figure 2.6: Tensile stress distributions under (a) load of 150 MPa after 1980 h with oxide of 20 μm and (b) load of 70 MPa after 158 kh and oxide of 120 μm showing numerous cracks [110], oxide scale is shown as grey area.

Additionally, work by Fournier et al. [101–103] attempted to combine creep, fatigue and oxidation effects in order to obtain lifetime predictions. Fournier et al, found that the environment played a major role both in crack initiation and propagation [101].

A summary of the different finite element models developed for corrosion damage is shown in Table 2.2.

Table 2.2: Summary of finite element modelling work on corrosion carried out to date.

Corrosion type	Geometry modelled	Authors	Ref.
Pitting and SCC	2D heat exchanger tube	Wenman et al.	[104]
Pitting and SCC	2D and 3D cylinder	Turnbull et al.	[106,107]
Pitting	3D Bio-absorbable metallic stent	Grogan et al.	[108]
Uniform	3D heat exchanger tube	Purbolaskono et al.	[105]
Uniform	3D Bio-absorbable metallic stent	Grogan et al.	[109]
Uniform and SCC	2D polycrystalline plate	Biglari and Nikbin	[110]

2.5. Mechanical damage

Heat exchanger tubes are subjected to mechanical as well as chemical and thermal damage, potentially leading to failure of tubes. This section will discuss creep and fatigue damage to which tubes are subjected under operating conditions.

Tube rupture occurs due to microstructural and metallurgical changes, such as grain boundary separation in addition to the formation of internal cracks, cavities and voids. Creep is the main source of failure in steam generating boilers, accounting for 23% of all failures, as shown in Figure 2.7 [72,111]. Ash related corrosion accounts for 12% of all failures, highlighting its importance to plant operators.

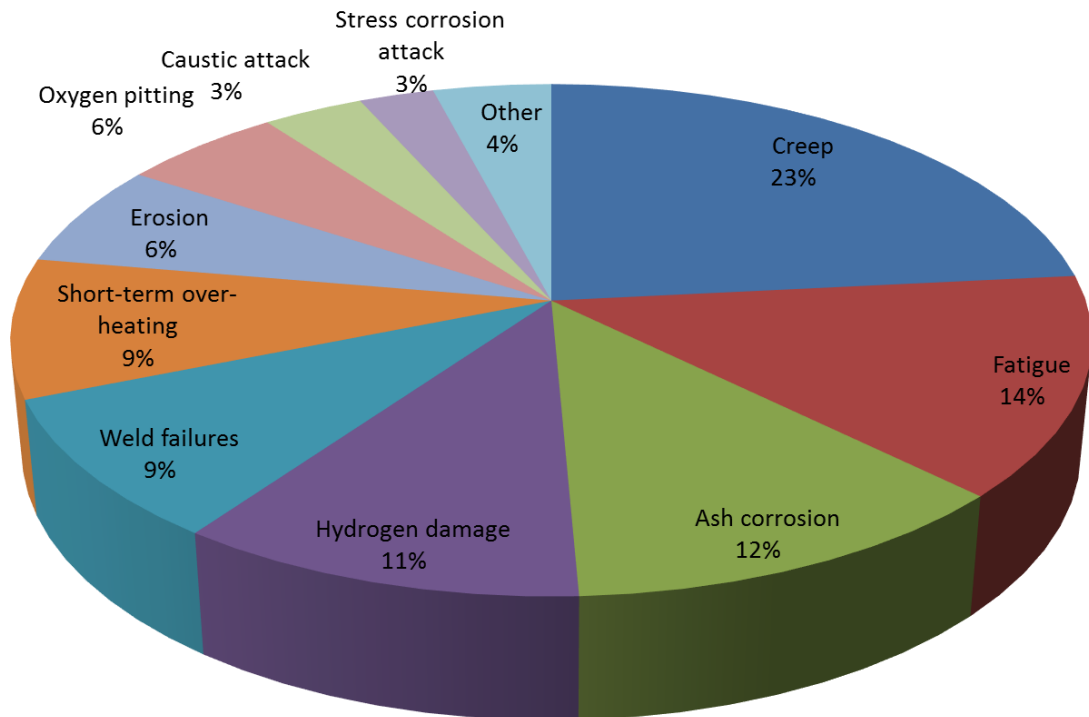


Figure 2.7: Causes of failure in steam generating boilers, based on studies carried out in the USA [72,111].

2.5.1. Creep

Creep is the slow, continuous deformation of a material, at elevated temperatures under a constant applied load over an extended period of time. Typically metals experience creep deformation at temperatures greater than 0.3 to 0.4 T_m , where T_m is the melting temperature of the metal in Kelvin. Creep failure is said to have occurred when a component is no longer fit for purpose, due to excessive deformation, or when a component has suffered fracture [87]. Creep rate has been shown to increase with increasing temperature and increasing stress, as shown in Figure 2.8. Creep strain, ϵ_c , can be expressed as a function of stress σ , time t , and temperature T , as follows:

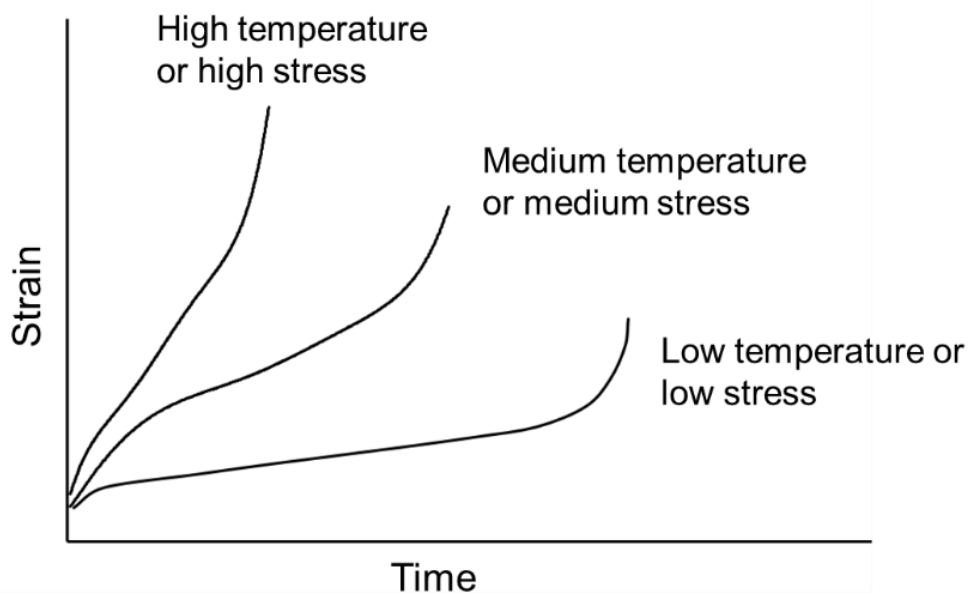


Figure 2.8: The effect of stress and temperature on creep strain rate, adapted from [112].

$$\varepsilon_c = f(\sigma, t, T) \tag{2-6}$$

Creep deformation is typically broken into three distinct stages: primary, secondary and tertiary creep, as shown in Figure 2.9 for a uniaxial constant load test.

Primary creep shows a steady decrease in creep rate and occurs at the early stages of creep lifetime. In this step rapid dislocation multiplication occurs, with consequent rapid increases of the dislocation density. As a result of this, the creep rate decreases due to strain hardening [113].

Secondary creep shows an approximately constant creep rate. This can be attributed to a balancing of dislocation annihilation and accumulation, which results in the dislocation density remaining constant, thus providing a constant creep rate.

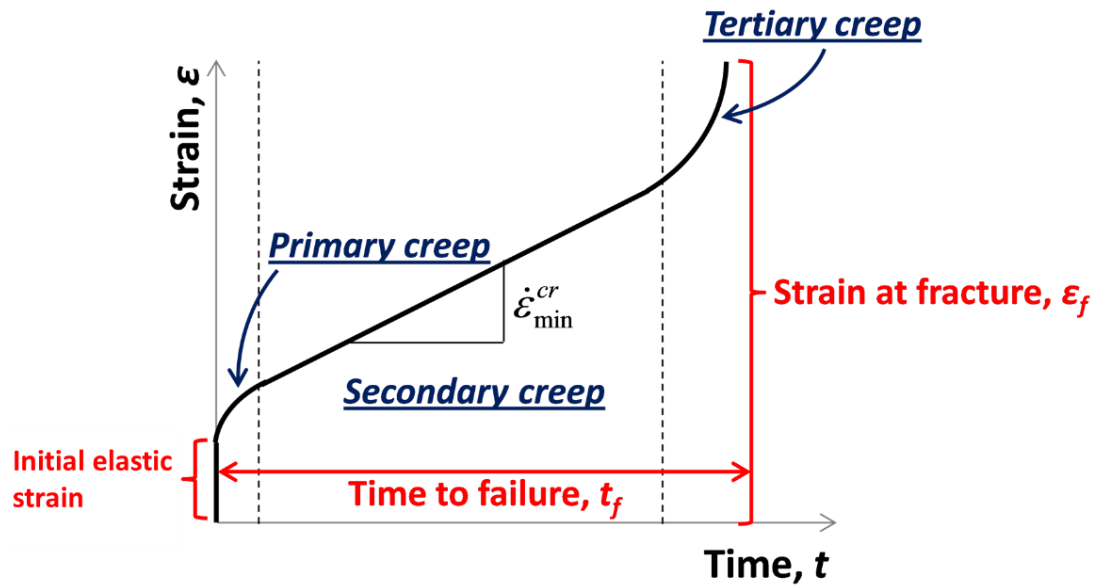


Figure 2.9: Typical creep curve displaying the three distinct regions of creep, adapted from [114].

Finally tertiary creep is associated with accentuation of damage accumulation due to void nucleation and growth along the grain boundaries [115], as shown in Figure 2.10. This causes the material to weaken and leads to an increasing creep rate. Coarsening of carbides and nitrides, in addition to the predominance of dislocation annihilation also occurs in this stage leading to an increased creep rate [116].

Voids continue to nucleate, grow and accumulate before finally forming cracks along the grain boundaries, resulting in rupture. If necking occurs, stress levels will increase over the decreasing cross sectional area, shortening time to rupture. Final rupture occurs due to metallurgical/micro-structural changes, such as grain boundary separation, formation of internal cracks, decreased cross sectional area and coalescence of the voids leading to the formation of small cracks which propagate and cause rapid failure [112]. A schematic showing the formation and coalescence of creep voids on a test specimen is shown in Figure 2.10.

When designing components to resist creep a number of factors, in particular stress and temperature, must be considered. If the temperature is high, stress must be kept low and if stress is high, temperature must be kept low. As the thermal efficiency of plants increase at higher temperatures, creep represents a key challenge for next generation materials to obtain higher plant efficiency [112].

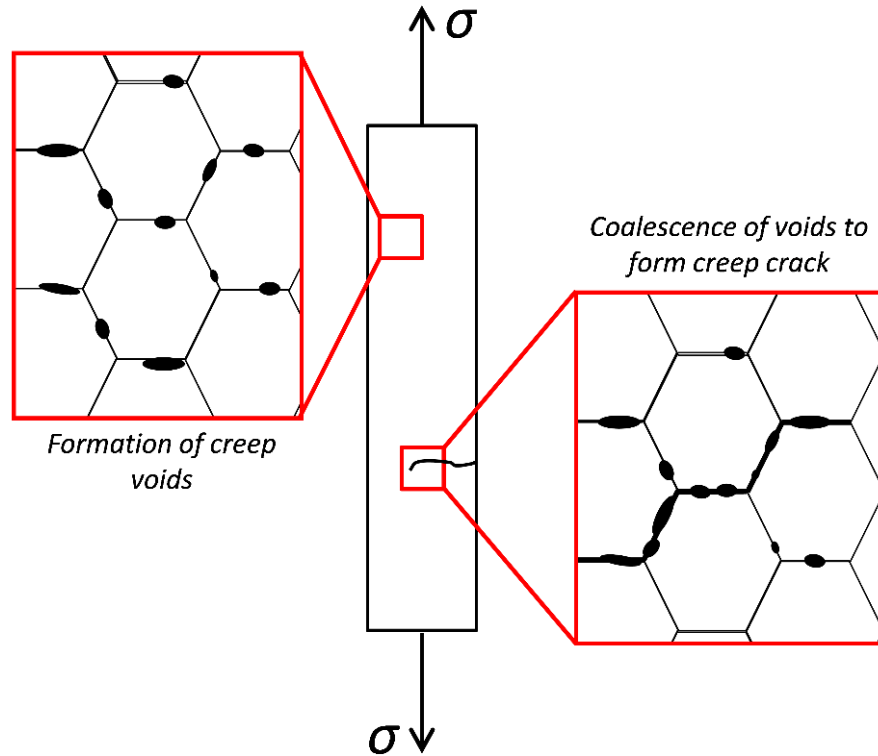


Figure 2.10: Creep void formation and coalescence of voids from creep crack in test specimen [114].

The rate of steady-state creep, $\dot{\epsilon}_{SS}$, can be described by the Norton power law, as follows:

$$\dot{\epsilon}_{SS} = A\sigma^n \quad (2-7)$$

where A is a material coefficient, σ is stress and n is the Norton creep exponent, which typically takes a value between about 3 and 8.

Temperature-dependence can be added as follows:

$$A = A_0 e^{-(Q_{Cr}/\bar{R}T)} \quad (2-8)$$

where A_0 is a material constant, Q_{Cr} is creep activation energy, \bar{R} is the universal gas constant and T is temperature in Kelvin.

2.5.2. Creep Damage

The Norton creep equation has been generalised to include the effects of creep damage [117]. A major benefit of damage models is their ability to accurately capture the tertiary stages of a creep curve. The Kachanov damage evolution model [118] represents growth of voids and cavities as a function of time and stress. The Kachanov model is based on a creep damage variable ω_c , where ω_c is defined as the void volume fraction.

The Kachanov model has been extended to multi-axial form by numerous authors, e.g. Hyde et al. [119], as follows:

$$\frac{d\varepsilon_{ij}^c}{dt} = \frac{3}{2} A' \left(\frac{\sigma_{eq}}{1-\omega_c} \right)^n \frac{S_{ij}}{\sigma_{eq}} t^m \quad (2-9)$$

$$\frac{d\omega_c}{dt} = B' \frac{\sigma_r^\chi}{(1-\omega_c)^\phi} t^m \quad (2-10)$$

$$\sigma_r = \alpha \sigma_1 + (1-\alpha) \sigma_{eq} \quad (2-11)$$

where ε_{ij}^c is creep strain, t is time, σ_{eq} is equivalent (von Mises) stress, σ_r is rupture stress, σ_1 is maximum principal stress, S_{ij} is the deviatoric stress and A' , m , n , B' , χ , ϕ and α are material constants [120]. In the Kachanov model, failure is assumed to occur when damage reaches a value of 1, i.e. when the void volume fraction reaches 1. Clearly, for high temperature applications, there will be an interaction between creep and corrosion. Work has been carried out by Fournier et al. which has investigated the interaction of creep, corrosion and fatigue [101–103]. It was found that the environment plays a major role both in the initiation and propagation of cracks.

2.5.3. Fatigue

Fatigue is the progressive degradation of a material subjected to cyclic loading. It is currently of increasing interest to plant operators due to an increased demand for flexible operation of plants. Fatigue failure can occur at stress values lower than the yield stress of a material. Fatigue proceeds via the generation of micro-cracks. These

micro-cracks gradually grow as cyclic loading continues until they reach a critical size, at which stage the crack will propagate rapidly, leading to fracture of the material.

Fatigue can be classified into low cycle fatigue (LCF) and high cycle fatigue (HCF). The threshold from LCF to HCF is normally taken at approximately 10,000 cycles to failure. One key difference between HCF and LCF relates to the relative proportions of crack initiation and crack growth. For LCF, crack initiation occurs early in the fatigue life, as low as 3 to 10 % of the fatigue life, with a long crack growth period [121]. Conversely, HCF failures have a long fatigue crack initiation period.

LCF occurs when the material undergoes cyclic elastic and plastic strain, whereas in HCF only cyclic elastic strain occurs at a mesoscale (although it does exist on a microscale). LCF occurs when structures are subjected to heavy cyclic loadings which induce irreversible strains causing damage up to crack initiation and propagation. From a physical point of view, the repeated variations of stress induce alternate plastic strains which produce internal micro-stresses which lead to the initiation of microcracks [122].

HCF is one of the most difficult phenomena to handle in solid mechanics and as a result is one of the main causes of failure of mechanical components in service. The difficulty occurs as defects form at the early stages of damage at a very small micro or nanoscale under cyclic stresses which are below the engineering yield stress. From the physical point of view, the cyclic variations in elastic stresses induce micro-internal stresses above local yield stresses. This causes the formation of permanent micro slip bands which lead to the formation of microcracks [122]. In power plant environments, materials are also subjected to thermal fluctuations which can cause fatigue damage, even in the absence of mechanical loading. Combined mechanical and thermal loading leads to thermo-mechanical fatigue.

This is an area of significant research in recent years as fossil fuel power plants no longer operate at a constant base load due to an increased reliance on renewable energy [102,103,123,124]. Their components are subjected to more transitions from base load to intermittent mode operation. This causes significant cyclic thermal gradients and mechanical loads during start-up and shut down cycles. In the present work, the effects of corrosion-fatigue are not explicitly investigated.

2.6. Material macro and micro structures

For higher operating efficiencies, materials must be assessed for mechanical performance and corrosion resistance at higher temperatures. Material performance depends on many factors, including material composition, microstructure and manufacturing. Heat treatment and alloying of metals allows control of properties by controlling the microstructure and phases of the metal. For heat-resistant steels, operating at high temperatures and under mechanical loading (e.g. steam pressure), mechanical properties, corrosion resistance, cost and ease of fabrication must all be considered.

Creep strength is one of the most important issues when considering a material in plants as they traditionally operate under steady state at high temperatures and pressures. Recently due to the desire for flexible operation, fatigue strength is also becoming of interest to operators.

Figure 2.11 shows a comparison of the relative costs and allowable temperatures of a range of candidate high temperature materials, including plain carbon steel, at an allowable stress of 49 MPa to provide a creep rupture life of 100,000 hours. The allowable stress of a material at a given temperature provides a good representation of the ranking of heat resistant steels [125]. P91 and 347SS are the materials of interest to this work and they fit into the 9 – 12% Cr Steel and the 18% Cr – 8% Steel groups respectively. It is clear that both steels offer a good compromise of cost and high temperature performance for the relevant temperature range of approximately 600 °C.

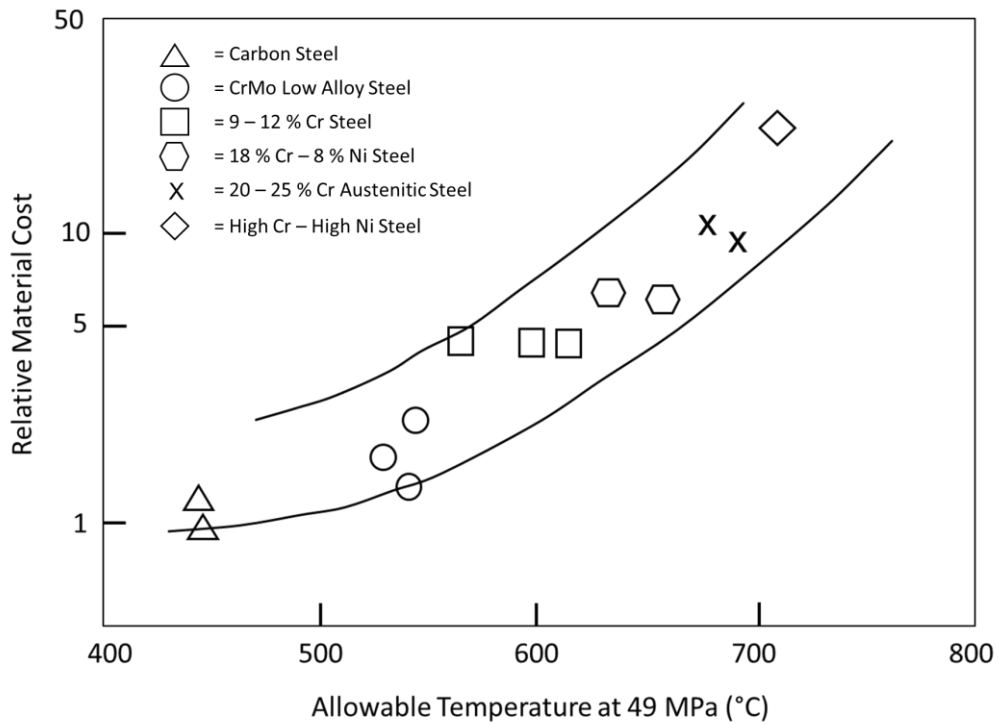


Figure 2.11: Relationship between the allowable metal temperature at 49 MPa of allowable stress and relative material cost to provide a life of 100,000 hours, adapted from [125].

Fireside corrosion is a major life-limiting requirement for heat exchanger tubes. In general, increasing the chromium (Cr) content of a material will increase its corrosion resistance [125]. If the material is to be used at temperatures of 650 °C, 12% Cr is the minimum required to provide oxidation resistance. When the Cr level is above 20%, steam-side oxidation has been shown to be fully stopped. However to maintain creep strength a Ni content of at least 30% is required, which is costly. Oxide scale growth has also been found to be much slower in fine grained Cr steels even following long term exposure [125].

A brief review on the structures of materials is provided in Section 2.6.1, followed by a review of the microstructure of P91 and 347SS, two materials of specific interest to this study. The effects of impurities, such as inclusions, which form during the manufacturing process, are also discussed.

2.6.1. Structure of materials

Table 2.3 shows a summary of material structures across the range of length-scales from Ashby and Jones [126], with asterisks indicating the range of structures which can be controlled during manufacturing in order to adjust material properties.

Table 2.3: Size scale of material structure properties [126]. * denotes structures which can be controlled to alter material properties.

Structural feature	Typical scale (m)
Nuclear structure	10^{-15}
Atom structure	10^{-10}
Crystal / glass structure	10^{-9} *
Structure of solutions / compounds	10^{-9} *
Structure of grains and phase boundaries	10^{-8} *
Shapes of grains and phases	10^{-7} to 10^{-3} *
Aggregates of grains	10^{-5} to 10^{-2} *
Engineering structures	10^{-3} to 10^3 *

The smallest controllable structural feature of a metal is the crystal structure. This is the way in which atoms pack together to form the crystalline structure. These atoms are held together by metallic bonds. Typically pure metals at room temperatures pack into one of three simple crystal structures; (i) face-centred cubic (FCC), (ii) body-centred cubic (BCC) and (iii) close-packed hexagonal (CPH.). The crystal structure of metals can change due to phase transformation, as controlled by heat treatment, for example. For example, iron changes from BCC (ferrite) to FCC (austenite) at 914 °C but back to BCC (ferrite) at 1391 °C [126].

Phases are regions of a material of uniform physical and chemical properties. Metal crystals and solid solutions are examples of phases. A pure metal, or a solid solution will be single-phase, and while it is possible to make single crystal metal alloys, it is

prohibitively expensive, except in the case of jet engines and gas turbines, where the high cost can be justified. Normally single-phase metals are polycrystalline, meaning they are made up of crystals or grains which are connected via grain boundaries, that have special properties of their own [126].

Grains consist of packed atoms and are connected via metal and covalent bonds at grain boundaries [87]. Grains can come in various shapes and sizes, all of which will have an effect on the performance of the material. By decreasing the grain size of a mild steel by a factor of ten its strength can be doubled. A smaller grain size will also result in lower internal degradation under corrosive conditions. Fine grain structure is beneficial in forming protective chromium oxide as the higher grain boundary area promotes diffusion along the grains [47,127].

The processing of a metal will strongly influence the shape of grains. For example, rolling will result in stretched-out grains, while casting will result in the solidifying grains being elongated in the direction of easiest heat loss.

2.6.2. P91 Microstructure

P91 steel is a modified 9Cr-1Mo steel which contains additional vanadium, niobium and nitrogen. P91 standards has a narrower range for the content of carbon, chromium, silicon, molybdenum, phosphorous, sulphur, nickel and aluminium [128]. The composition of P91 composition is given in Table 2.4, as reported by ThyssenKrupp Materials International and ASTM standards [129,130].

Table 2.4: Chemical composition of P91 steel (mass %) [129,130].

C	Si	Mn	P	S	Cr	Mo	V	Nb	N	Ni	Al
0.08	0.20	0.30			8.00	0.85	0.18	0.06	0.03		
–	–	–			–	–	–	–	–		
0.12	0.50	0.60	≤0.02	≤0.01	9.50	1.05	0.25	0.10	0.07	≤0.40	≤0.04

P91 has a high creep strength and resistance to thermal fatigue relative to earlier Cr-Mo-V steels used for similar applications, e.g. steam headers and tubes. This improved mechanical performance is attributed primarily to its hierarchical microstructure, which consists of prior austenite grains, containing packets, blocks and laths (sub-

grains) and carbide precipitate-strengthening at the lath level. A schematic representation of the microstructure of P91 is shown in Figure 2.12. $M_{23}C_6$ carbides are dispersed along the sub-grain boundaries with NbC and VC precipitates present within the sub-grains. This provides a high dislocation density which inhibits grain movement and creep deformation [116,124,131].

This high dislocation density has been found to decrease following sustained exposure to elevated temperatures [131,132]. Furthermore, laves phase particles (Fe_2Mo) have been found to form in P91 during long term creep [133]. This occurs at the expense of the solid solution strengthening mechanism and its effect on creep life is still under investigation. Laves phases are intermetallic phases, which are classified based on geometry alone, and have composition of AB_2 .

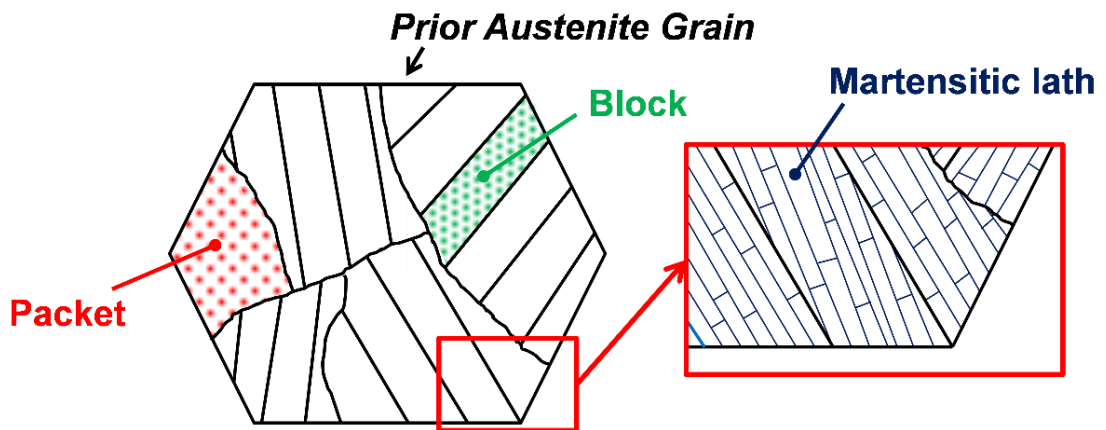


Figure 2.12: Schematic representation of the hierarchical microstructure in P91 steel [114].

Figure 2.13 shows two micrographs of P91 in which the hierarchical microstructure is visible. Figure 2.13 (a) shows the microstructure of as received P91 and (b) shows P91 following creep at 600 °C for approximately 13 years. By comparing Figure 2.13 (a) and Figure 2.13 (b), the coarsening of $M_{23}C_6$ carbides during long term creep is clearly visible. Additionally there is precipitation of Laves phases and identification of small scale precipitates in the specimen following creep. A loss of creep strength occurs due to these microstructural changes, viz. coarsening of $M_{23}C_6$ carbides, precipitation and coarsening of Laves phases and recovery of the matrix [134].

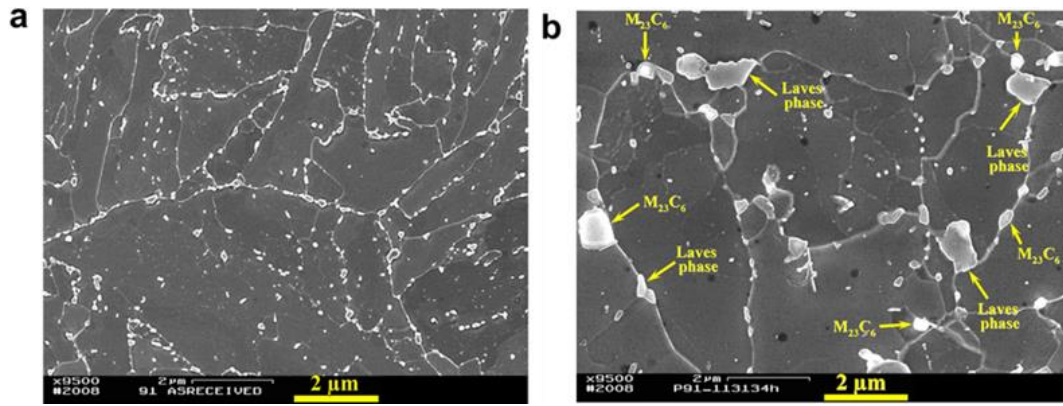


Figure 2.13: Microstructure of (a) as-received P91, (b) following creep at 600 °C for 113,341 hours [134].

2.6.3. 347SS Microstructure

347SS is a niobium-stabilised austenitic stainless steel, consisting of fine grains and small and uniformly-distributed NbC precipitates. 347SS has a high steam-side corrosion resistance. This is attributed to the fine grain structure and high chromium content, which promotes the generation of a uniform adherent chromium rich oxide layer between the base metal and environment. The protective Cr₂O₃ oxide scale formation is favoured as the effective diffusion coefficient of chromium along grain boundaries is more than two orders of magnitude greater than that of lattice diffusion at 500 °C. This effect decreases with increasing temperature [127]. The chemical composition for 347SS is shown in Table 2.5.

Table 2.5: Chemical composition of 347SS (mass %) [135].

<i>C</i>	<i>Si</i>	<i>Mn</i>	<i>P</i>	<i>S</i>	<i>Cr</i>	<i>Nb</i>	<i>N</i>	<i>Ni</i>
0.04 –	0.75	2.00	0.045	0.03	17.0 –	10×C min	0.02	9.0 –
0.08					19.0	1.0 max		13.0

The presence of niobium, which forms carbides easily, suppresses the formation of the chromium-rich M₂₃C₆ carbides at grain boundaries. This in turn protects against the formation of a chromium-depleted zone which would be susceptible to accelerated corrosion. Fine secondary precipitation leads to improved creep resistance during service. An SEM image showing the microstructure and intergranular precipitates of 347SS is shown in Figure 2.14.

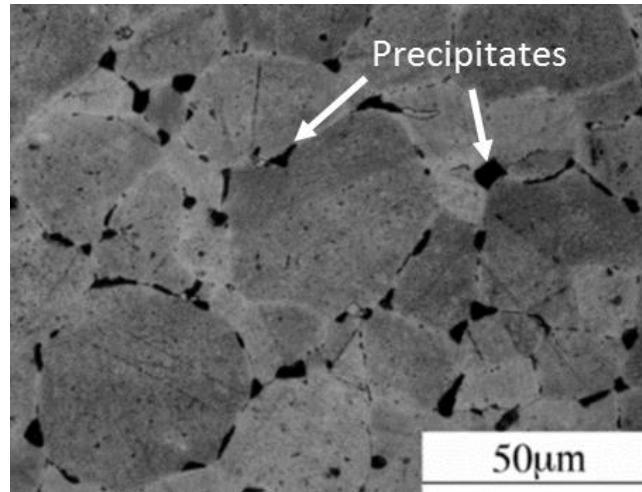


Figure 2.14: Intergranular precipitates present in 347SS [136].

Despite its stabilization with niobium, which provides good corrosion resistance at high temperatures, chromium carbide precipitates can form at temperatures in the range of 450 to 900 °C along grain boundaries, leaving them susceptible to intergranular corrosion.

2.6.4. Inclusions

During the manufacturing process of steels, impurities known as inclusions commonly form in the steel. This occurs due to chemical reactions with the environment, contamination and other factors. These are generally regarded as unavoidable and typically form as oxides, silicates or sulphides.

Sulphide inclusions have been found to be the most deleterious for corrosion resistance and can lead to localised attack in aggressive environments. Inclusions are also well known to lead to the deterioration of mechanical properties of materials, especially fatigue strength [137].

Inclusions have a higher thermal expansion coefficient than metals. Due to this thermal mismatch, localised stress concentrations are often found at the interface of inclusions and steel, at high temperatures. When sufficient chloride has accumulated in the metal-oxide interface, the higher molar volume of metal chloride compared to oxide causes the oxide film to rupture mechanically [138].

2.6.4.1. Effect of inclusions on pitting corrosion

It is well established that sulphide inclusions, if present, will act as pit nucleation sites [138–142]. Calcium and manganese sulphates in particular have been shown to affect the corrosion resistance of steel, by reducing resistance to pitting corrosion and stress corrosion cracking [143,144].

Pitting of stainless steels in aggressive environments is generally accepted to occur through an initiation step and a propagation step, as shown schematically in Figure 2.15 [145]. The initiation step occurs with the dissolution of the inclusion in a Cl-containing environment, with very small quantities of chlorine needed to initiate pitting. The dissolution of the sulphides has been observed to occur initially at the inclusion edges, with micro-crevices appearing at the periphery of the inclusions [140,146,147]. Specifically, it has been reported previously that the sequence of events for pitting corrosion at sulphides, as shown in Figure 2.15, is as follows:

- 1) The composition in and around sulphide inclusions changes, taking in chromium from the metal matrix, resulting in a chromium-depleted zone around the inclusion;
- 2) The chromium-depleted zone provides a region of high-rate metal dissolution resulting in the formation of a narrow trench at the inclusion edges;
- 3) The inclusion dissolves in this new environment;
- 4) Sulphur products form a crust over the former inclusion providing a closed environment resulting in pitting.

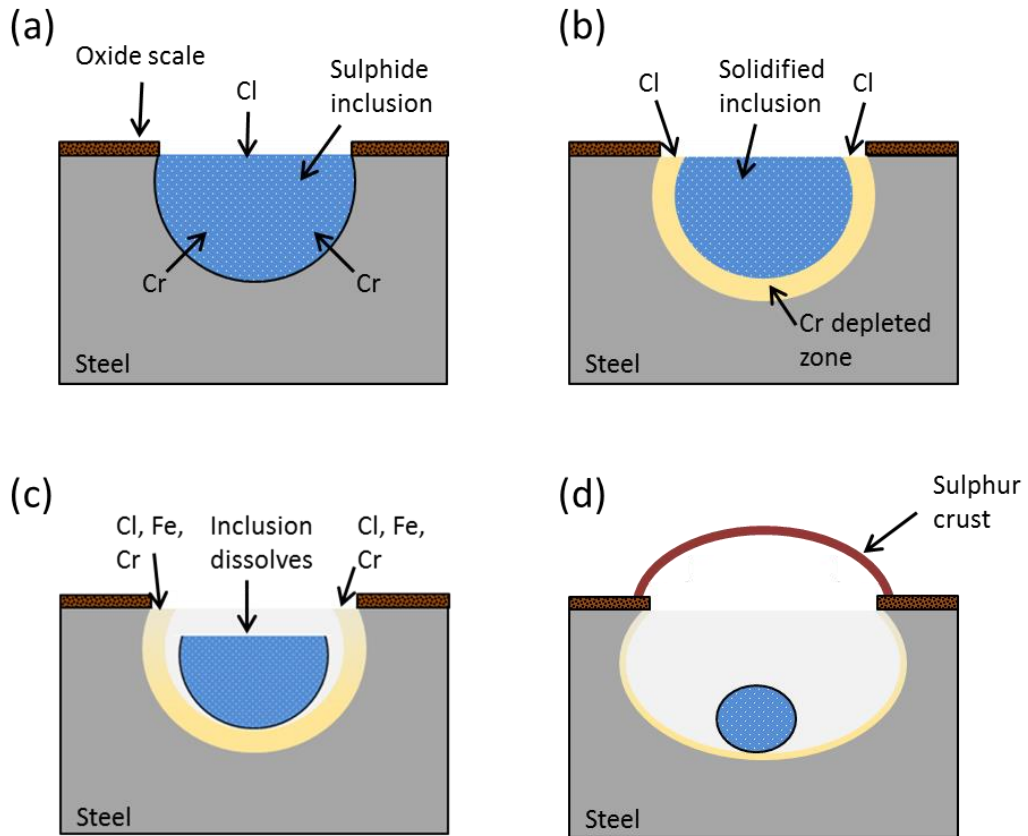


Figure 2.15: Schematic showing the mechanism by which pitting corrosion proceeds in the presence of an inclusion, adapted from [147].

It has been found that even small quantities of chlorine present in the environment will result in the initiation of pitting [147]. When samples containing inclusions have been exposed to NaCl, it has been observed that pitting occurs almost instantly [148]. Dissolution of the sulphides has been reported to initially occur at the inclusion edges with micro-crevices appearing at the periphery of inclusions [140,148].

The critical zone of chromium depletion is a region of just 200 to 400 nm width, yet it can result in catastrophic failure of metallic structures [147]. This proposed mechanism is supported by results that show the chromium depletion from the metal matrix around inclusions, as presented in Figure 2.16. It is further supported by results showing that a number of inclusions have been found to be significantly Cr-enriched [148]. Chlorine-containing species have been found to become concentrated in the pit further accelerating the metal dissolution [140].

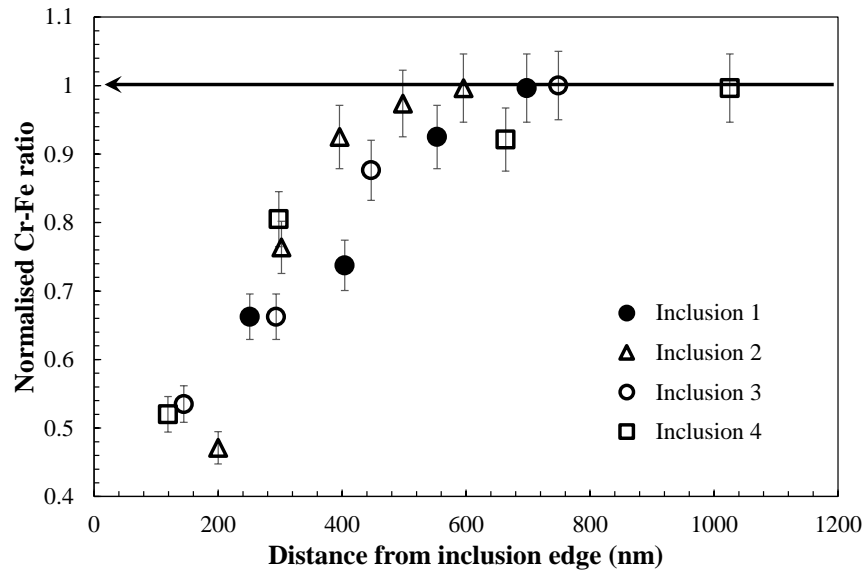


Figure 2.16: Normalised Cr/Fe ratio as a function of proximity to a sulphide inclusions, 4 inclusion sites on surface are shown and trend was evident from many other sites [147].

In addition to the composition of inclusions, the shape and size have significant effects on whether or not propagating pits will develop [148]. Sulphide inclusions will not operate as sites for corrosion initiation if they are sufficiently small. This is because a small open cavity formed by the initial triggering cannot retain a solution which is sufficiently aggressive to continue the corrosion [147]. This size has previously been reported to be below approximately 0.7 μm in diameter [140]. As stress corrosion cracking (SCC) often initiates at pits, this is a significant issue for plant operators. Although the overall material loss may be minimal, cracks from SCC can penetrate deeply and result in early failure of components.

2.6.4.2. Effect of inclusions on fatigue

In addition to acting as pit initiation sites, it has been found that inclusions have a detrimental effect on the mechanical properties of a material, especially the fatigue properties of metals [149]. Inclusions are well known to lead to the nucleation of cracks, with numerous reports identifying crack initiation points at inclusions [150–154].

A critical inclusion size exists, below which inclusions tend not to initiate cracks in fatigue [151,153]. In the presence of inclusions greater than 10 μm a detrimental effect under cyclic loading was observed. Additionally, inclusions aligned in a cluster caused a detrimental effect [153]. It has been shown that as the inclusion size increases, the

fatigue life of a metal decreases [149]. Stresses that develop at particle-matrix interfaces due to the differences in thermal expansion play an important part; the inclusions with the highest thermal mismatch with the metal were found to be the most detrimental on fatigue life [151].

Voids form by cracking of the particles or by de-cohesion at the particle-matrix interface, showing the importance of volume fractions, distribution and morphology of inclusions. For inclusions in steel, the particle-matrix bonding is generally weak, so that voids form at low plastic strains. These elongate under the influence of tensile stress and can link with adjacent voids to form micro-necks. These progressively crack, leading to ductile fracture surfaces with highly dimpled appearances [87,151].

Figure 2.17 shows results from in-situ SEM tension tests where an inclusion has been manufactured into the sample [149]. As loading increases, the cracks widen, coalesce and propagate into the matrix. As the specimen fails the cracks widen and portions of the inclusion fall out of the matrix. Subsurface inclusion effects are also significant. When a cluster of Al_2O_3 inclusions exist near, but not on, the surface they will act as the crack initiation site.

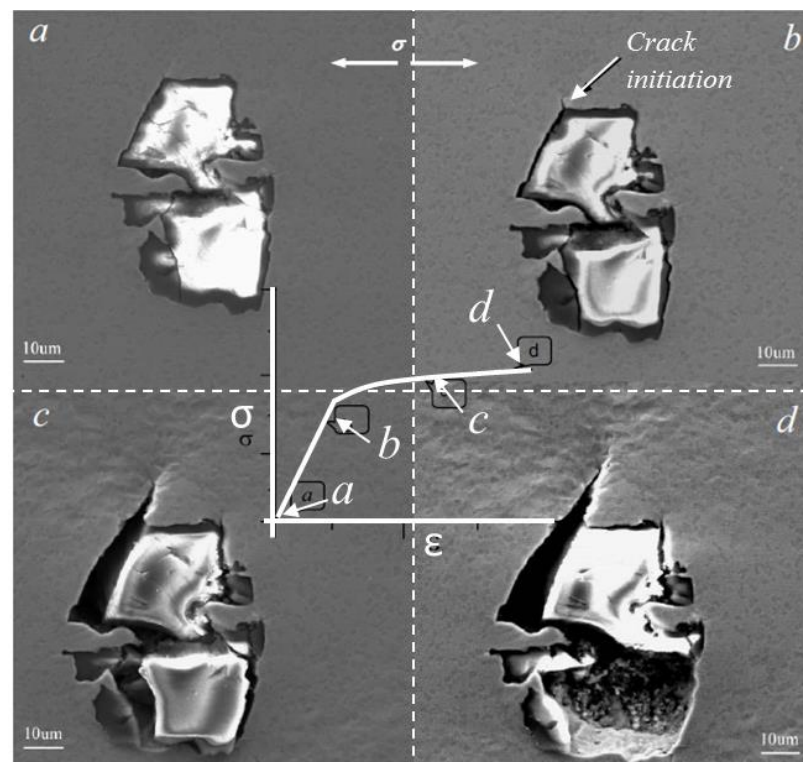


Figure 2.17: SEM in-situ tension test of Al_2O_3 inclusion in parent metal Rene '95, (a) before loading, (d) after specimen fracture [149].

2.7. Fireside corrosion

A specific focus of this work is on accelerated fireside corrosion during biomass co-firing. This section presents a review of the corrosion mechanisms that occur during co-firing and the factors that influence these mechanisms.

It has been shown that the most severe corrosion problems in biomass-fired systems occur due to the formation of Cl-rich deposits on the superheater tubes [59–61]. Depending on deposit composition, metal temperature and composition of gaseous atmosphere, the corrosion process proceeds via a number of mechanisms, as discussed in detail here.

Severe gas-phase corrosion attacks will not occur as the partial pressure of HCl in biomass-derived flue gas is typically not sufficiently high, although the concentration will vary for different biomass fuels. It may however cause oxide scale failure and increased sulphidation of water walls [59]. Alkali-chloride-containing deposits have been shown to cause accelerated corrosion far below the melting point of the deposits [50]. The corrosion can be severe in air but can be further enhanced by SO₂, causing intra-deposit sulphidation of the alkali chlorides, liberating HCl or Cl₂ gas close to the metal surface [51,155]. In certain cases, if the metal surface temperature is high enough, molten phases can form in the deposit, resulting in a further enhanced corrosion rate [59].

All of the corrosion mechanisms discussed above can take place in combustion systems. The dominant mechanism will depend on the combustion environment, combustion temperature, metal temperature and the presence of elements, such as alkali metals, sulphur etc. However as this work is focused on biomass-fired boilers, it focuses on the corrosion associated with alkali chloride containing deposits.

2.7.1. Active oxidation process

One of the most commonly observed mechanisms for accelerated corrosion in biomass-fired boilers is known as active oxidation [47,51,60,85,155,156]. Figure 2.18 shows a schematic of active oxidation as it proceeds for superheater tubes in-situ.

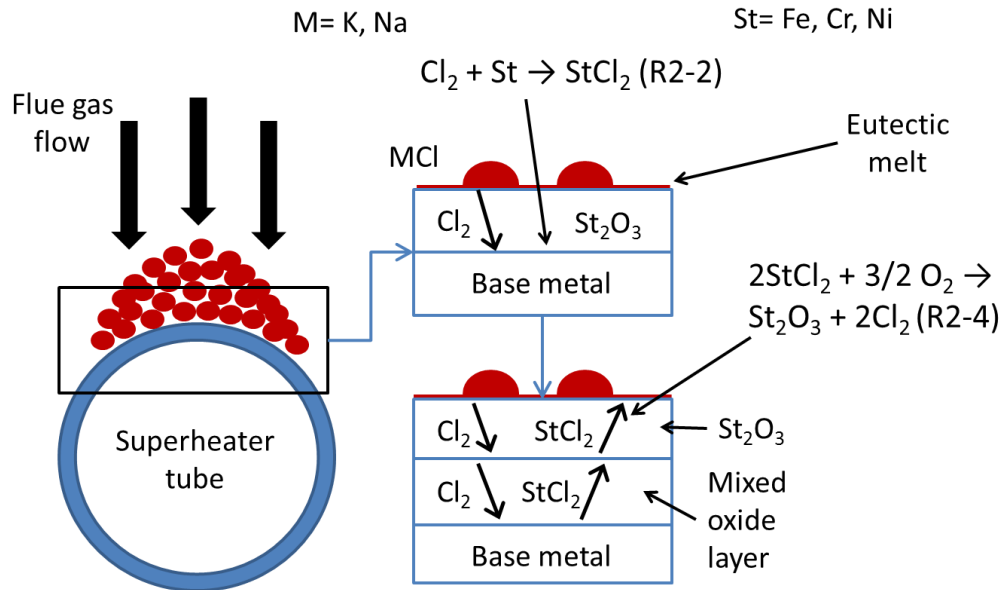
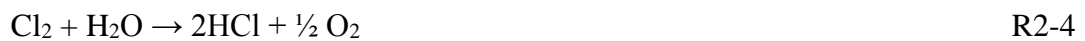


Figure 2.18: Schematic of tube wall corrosion via active oxidation.

In order for active oxidation to occur, chlorine must be present as Cl_2 or HCl in the flue gas or the deposit. This chlorine penetrates the protective oxide scale and migrates to the metal surface. Once there, it reacts with the unoxidised metal alloy (St) to form metal chlorides (StCl_2), via reaction R2-1. At the metal-oxide interface, there is very little molecular oxygen as it is assumed to have been consumed to produce the initial protective oxide layers. The chloride initially forms as a solid; however due to the high volatility of metal chlorides, it soon evaporates (R2-2) [51].



Due to the high vapour pressure of the StCl_2 , the chloride diffuses outward through the oxide scale to regions of higher oxygen concentration. Once it has reached a sufficiently-high oxygen concentration, reaction R2-3 occurs resulting in the formation of a poorly adherent, non-protective oxide (St_2O_3) layer [157]. In addition to the passive nature of the oxide formed, the chlorine released as a product of R2-3 is

then free to travel back through the oxide scale and repeat the cycle, resulting in the continuous loss of metal, with little net consumption of chlorine.

Additionally this chlorine can itself be oxidised in the high moisture flue gas resulting in the formation of HCl (R2-4) [51]. Grabke et al. [51] suggest that the rate is controlled by the outward diffusion of metal chlorides through the porous scale.

There have been a number of proposals for how the chlorine is released including (1) reaction of sulphidation of alkali chlorides in deposits and, (2) reactions between alkali chlorides and the metal oxide scale. These are discussed in detail in the coming sections. In addition, it has been proposed that the chlorine can penetrate the oxide layer as HCl and/or Cl₂ initially, as per reaction R2-2 and R2-5, thus forming the metal chlorides and initiating the active oxidation cycle via this step. However work by Abel et al. [158] and others [157,159] suggests that Cl₂, and not HCl, is the main aggressive species in this form of corrosion, for short term exposure at least.

The active oxidation process starts with almost no incubation time following introduction of a chlorine component, with the penetration of chlorine through the oxide scale still not being fully understood. It is believed that the chlorine must itself cause the formation of fast diffusion paths, possibly through grooves and fissures at grain boundaries, as it occurs so quickly [51].

A number of challenges have been raised to the active oxidation theory. The main argument against this theory is that if the pores and cracks are open to diffusion of Cl₂ or HCl then it must also be open to diffusion of smaller O₂ molecules [58,160]. It can therefore be argued that the low oxygen potential at the metal-oxide interface should be difficult to maintain. Additionally it has been questioned why highly reactive Cl₂ molecules would not react with Fe ions in the oxide scale prior to reaching the metal-oxide interface. A possible solution to these challenges was proposed by Grabke et al. [51] who state that chlorine must effect the creation of fast diffusion paths, possibly through grooves which occur at grain boundaries. A similar effect has been observed in the growth of Fe₃O₄ in steam at 200 – 300 °C under the influence of chlorides [161]. Based on the evidence observed to date it appears likely that active oxidation plays a significant role in the accelerated corrosion due to co-firing.

2.7.2. Thermodynamic stability of metal oxides and chlorides

As discussed previously in Section 2.4.1. the thermodynamic stability of a material in a multi-component gaseous environment can be visualised using a phase diagram. Figure 2.19 shows the phase diagram for pure iron in a chlorine and oxygen-containing environment (Fe-O-Cl system) at 540 and 600 °C respectively, and was obtained using chemical reaction and equilibrium software [61]. At low partial pressures of Cl_2 and moderate to high pressures of oxygen, various oxides of iron (Fe_3O_4 and Fe_2O_3) are stable. At high partial pressures of Cl_2 and low partial pressures of oxygen, metal chlorides (FeCl_2 and FeCl_3) are stable. When partial pressures of both chlorine and oxygen are low, pure iron (Fe) remains stable. The impact of temperature on the stable phases can be seen from comparison of Figure 2.19 (a) and (b).

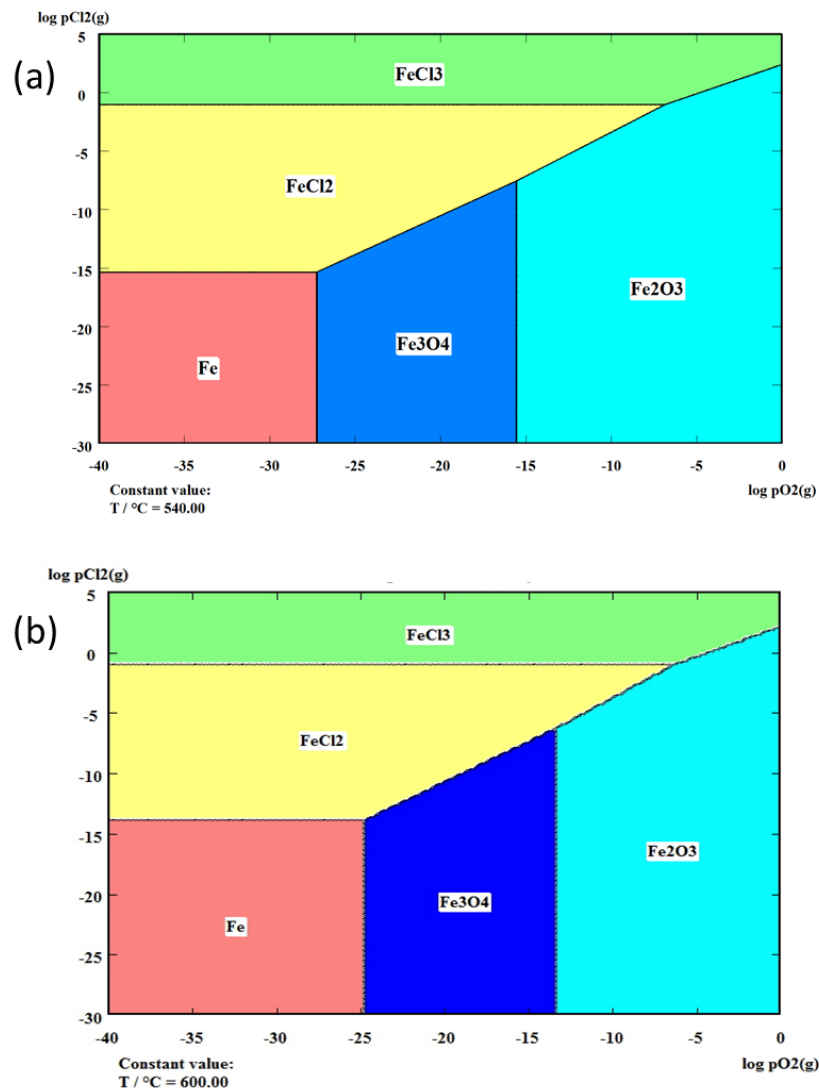


Figure 2.19: Phase stability diagram of Fe-O-Cl system at (a) 540 °C and (b) 600 °C.

Due to the high vapour pressures of metal chlorides they can evaporate even at low temperatures resulting in rapid loss of metal from the surface. When investigating the vapour pressures of chlorides, it must be considered that mixed chlorides ((Fe, Cr) Cl₂) also form, whose vapour pressures can be estimated from binary gaseous vapour pressures. It must also be noted that if liquid chlorides form, the rate of corrosion will likely increase significantly due to fluxing of the oxide scale. These liquid metal chlorides will only be present for a narrow temperature range, just above the melting point of the chlorides, as at higher temperatures they will evaporate.

2.7.3. General structure of oxides

Typically the oxide scales formed during co-firing are regarded as passive and offer little or no protection against further corrosion, due to their detached nature. Provided the temperature reached is high enough, multiple layers of poorly adherent oxides form [85,162]. For an iron-based chromium alloy the outer portion will primarily consist of iron oxide with a mixed chromium, iron spinel oxide in the middle portion of the scale [53,85]. The oxide closest to the substrate surface is found to consist primarily of chromium oxide. Iron oxide forms further from the surface due to the higher vapour pressure of iron chloride compared to chromium chloride as seen in Figure 2.20, thus it diffuses further from the surface before converting to oxide. Traces of iron and chromium chlorides can often be detected at the corrosion front between the base metal and the oxide scales [53].

During active oxidation, cupolas (domes) of iron oxide often form over the sample, the shape of which correspond to the stagnant diffusion boundary layer of FeCl₂(g) as it travels to areas of higher oxygen concentration [85].

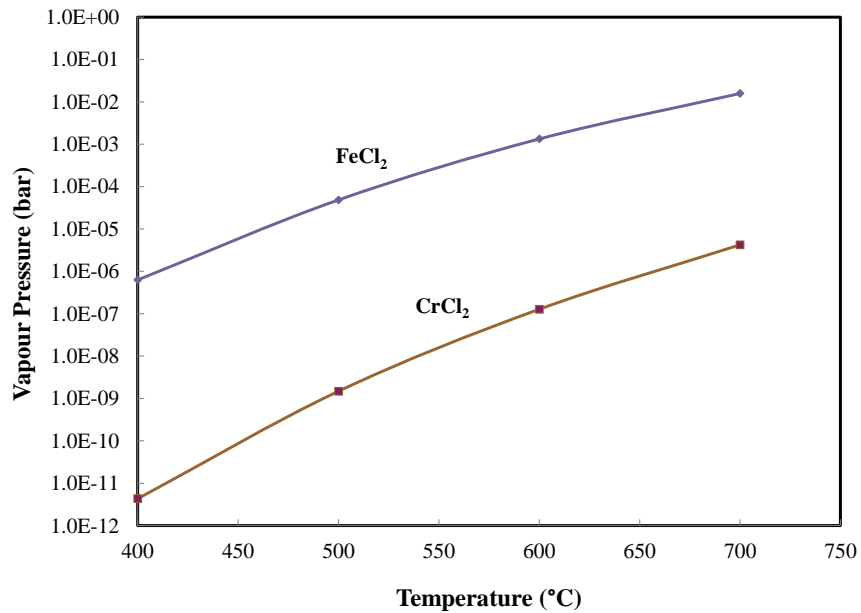


Figure 2.20: Equilibrium vapour pressures of Cr and Fe chlorides at 400 to 700 °C.

During oxidation, stress accumulates in the oxide scale. This stress can be attributed to three distinct sources: 1) growth stresses, which are induced during oxidation, 2) stress due to thermal mismatch between the oxide and substrate, and 3) phase transformation of the oxide layer [163]. This stress can then be relaxed via several mechanisms, such as spallation and cracking of the oxide scale [164].

Poorly-adhered layers of oxides form due to high growth stresses in the oxides which cause repeated cracking and spalling of the scales, resulting in voids forming between the layers [85,165,166]. Buckling of the outer layer, due to stresses in the scale results in delamination from the inner layers, which remain attached to the substrate [167]. An SEM image showing multiple layers of oxide which have detached from the substrate is shown in Figure 2.21.

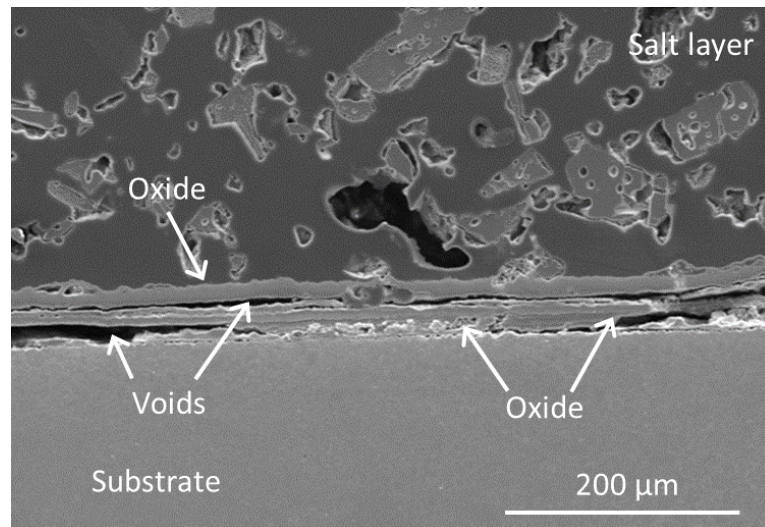


Figure 2.21: SEM image showing multiple layers of oxide above substrate following delamination.

2.7.4. Formation of low temperature eutectics

It is well known that potassium chloride, which has a melting temperature of 774 °C, forms low-melting-temperature eutectics when mixed with other substances. For example the eutectic melt temperatures of potassium chloride with FeCl_2 and CrCl_2 can be just 355 °C and 470 °C respectively, dependent on relative quantities. While the melt temperature of a sodium chloride and sodium chromate mixture can reach 557 °C. The lowest point of a mixed alkali chloride-sulphate melt temperature is approximately 517 °C [92].

This is of great relevance since corrosion rates typically increase in the presence of a molten phase, as chemical reactions occur quicker when a liquid phase is involved in comparison to a solid-solid phase reaction. The melting points of pure substances and eutectic points of binary systems have been tabulated by Nielsen et al. [59], based on data published by Shinata et al. [168] and Janz et al. [169]. A selection of this data is given in Table 2.6.

Table 2.6: Selection of melting temperatures for mixtures of alkali chlorides, metal chlorides, alkali sulphates and alkali chromates, adapted from [59].

System	Melting temperature (°C)	eutectic point (mol% alkali)
NaCl	801	
KCl	772	
FeCl₂	677	
NaCl – FeCl₂	370 – 374	≈ 56
KCl – FeCl₂	340 – 393	45.8 – 91.8
CrCl₂	845	
NaCl – CrCl₂	437	53.7
KCl – CrCl₂	462 – 475	36 – 70
Na₂CrO₄	792	
NaCl – Na₂CrO₄	557	
K₂CrO₄	980	
KCl – K₂CrO₄	650	68.4
K₂SO₄ – Na₂SO₄	834	

Work by Nielsen et al., [53] deposited salts consisting of KCl and K₂SO₄ and deposits taken from a 10 MW straw-fired grate boiler on metal samples. These were then exposed to a synthetic flue gas (6 vol% O₂, 12 vol% CO₂, 400 ppmv HCl, 60 ppmv SO₂, balance N₂) at 550 °C. A molten phase was identified in contact with the metal interface. In similar tests, Lith et al., [64] identified eutectic melts forming at 560 °C, with the amount of melt present depending on the composition of the deposit.

Cha et al., [170] studied the local reactions of KCl particles with iron, nickel and chromium surfaces. KCl was deposited on samples using a custom built alkali chloride depositor. These were then exposed to a gas consisting of 20 vol% O₂, balance N₂ with and without 0.05 vol% HCl between 300 – 500 °C. It was found that at 500 °C, for the gas containing HCl and the chromium sample, a local eutectic melt had formed between KCl and CrCl₂. The eutectic melting temperature was found to be in the range of 462 – 475 °C.

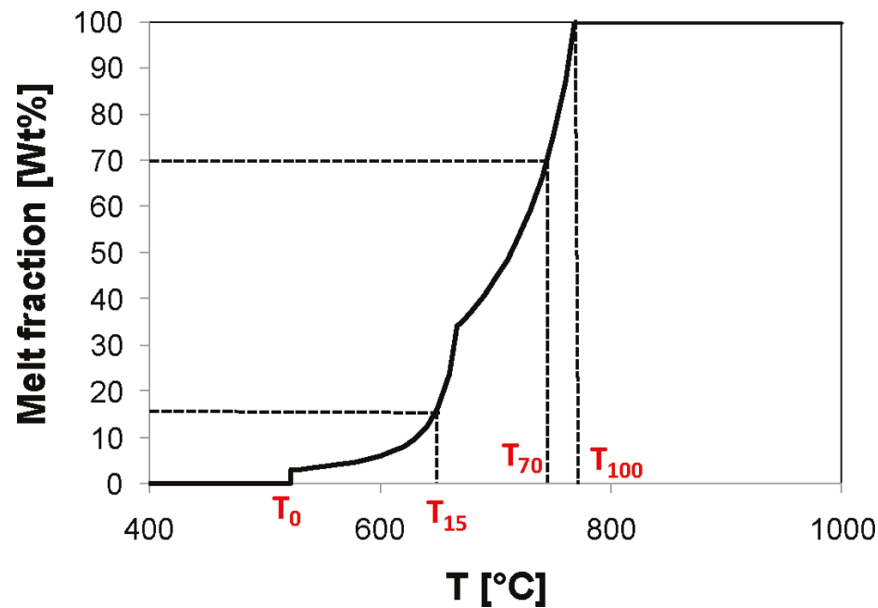


Figure 2.22: Melt fraction as a function of temperature for a salt consisting of a mixture of alkali sulphates and chlorides with the four characteristic melt temperatures indicated [20].

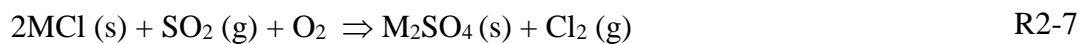
Salt mixtures such as those which form in fly ash are found to melt in stages. Figure 2.22 shows the melting curve for a salt consisting of a mixture of sulphates, and alkali (K and Na) chlorides based on the Abo Akademi thermodynamic multi-component melt model [171,172]. Based on such curves, Backman et al. [172] defined four characteristic temperatures. T₀, the temperature at which the first molten phase occurs, T₁₅, the temperatures at which 15% of the mixtures is molten, T₇₀, the temperature at which the mixture is so molten it loses any previous shape, T₁₀₀ is the temperature at which the entire mixture is in its molten phase.

If the superheater tube temperature is higher than T₀ of the deposited salt, the heat exchanger steel will be directly exposed to a molten phase, which will result in higher rates of corrosion. At temperatures above T₁₅, it has been found that almost all particles which hit the melt will stick to surface; therefore this is known as the ‘sticky

temperature'. In this case the amount of deposit forming on the tube is limited solely by the amount of particles that hit the molten surface [20,172].

2.7.5. Sulphation of deposits

It has been proposed in literature that accelerated corrosion can be initiated by the sulphation of alkali chloride containing deposits [51,155,173–175]. It is suggested that gaseous SO₂ reacts with chlorides forming alkali sulphates, with HCl or Cl₂ being produced, as shown in reactions R2-6 and R2-7, in which M = K, Na. The reaction that corrosion will proceed via is based on the exposure conditions, such as the presence of H₂O.



This chlorine can then be used in active oxidation, resulting in the continuous transport of metal from the metal-scale interface toward the higher oxygen partial pressure in the bulk gas. However, other work has proposed that the SO₂ in the flue gas can convert the corrosive KCl to the less corrosive K₂SO₄ [176].

Okoro et al., [177] tested samples exposed to a KCl deposit in a gaseous atmosphere containing N₂, O₂, CO₂, SO₂ and HCl and suggest that the sulphation of KCl in addition to the formation of a KCl-iron chloride melt within the sulphate will lead to the production of chlorine for use in active oxidation.

2.7.6. Reaction of Cl-species with oxide scale

Grabke et al. [51] have proposed that the chlorides in the deposit will react with the metal oxide scale, producing a detached oxide with chlorine being released, as per reaction R2-8. This reaction provides high partial pressures of Cl₂, and corrosion proceeds via active oxidation. St= Fe, Cr, Ni.

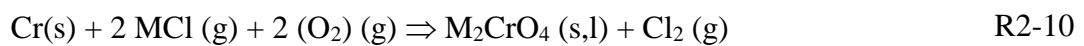


2.7.7. Chromate formation

In addition to causing the formation of lower melt temperature eutectics, the presence of alkalis in deposits has been found to result in the formation of alkali chromates. The

oxide scale is thus destroyed, resulting in a loss of its protective properties. This releases chlorine, which initiates active oxidation [49,50]. This has been identified for both gaseous alkali chlorides and solid alkali chlorides in deposits.

Hossain and Saunders among others [178–181] have found that gaseous alkali chlorides cause a breakdown of protective Cr₂O₃ oxide layers [182]. A mechanism is suggested where M₂CrO₄ (alkali chromates) form, with chlorine being released by reactions R2-9 and R2-10, where M = K, Na.



Chromate formation via the reaction of alkali chlorides with the oxide scale has been described as acting like a chromium sink, removing the protectiveness of the chromium oxide layer. This results in a rapidly growing scale with chlorine being released to initiate active oxidation [58].

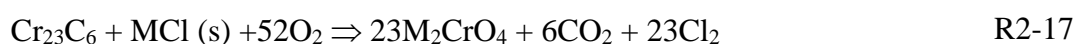
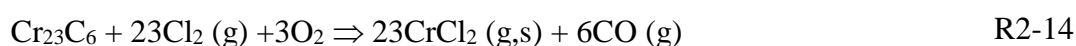
A number of authors have identified the formation of alkali chromates, and subsequent destruction of oxide scale and release of chlorine as important contributors to accelerated corrosion identified under alkali-chloride-containing deposits [47,85,183,184]. Reactions R2-11, R2-12 and R2-13 show the proposed reactions for alkali chlorides present in deposits with the oxides.



Pettersson et al., [58] among others [179–181,185,186] found that in dry conditions, KCl reacts with chromium oxide in the scale forming potassium chromates. If sufficient water vapour is present the formation of hydrogen chloride is thermodynamically favoured over Cl₂ via reaction R2-11. The presence of KCl (s) causes a breakdown of most of the protective scale following just 1 hour of exposure [185].

2.7.8. Reaction between Cl-species and carbides

Several authors have shown that chromium carbides are preferentially attacked by alkali chlorides, resulting in voids forming in the metal matrix. This occurs when carbides are exposed to gaseous and/or solid alkali chlorides [56,85,156,165,183,187]. If these carbides are located along grain boundaries, cavities will form along the boundary. Work by Grabke et al. [165] shows that other carbides such as Mo₆C, TiC and NbC have better corrosion resistance than the metal matrix. Therefore it can be said that chromium carbides are weak spots in the corrosion of alloys in oxidising-chlorinating environments. [85,156,165]. The proposed reactions are shown in reactions R2-14, R2-15, R2-16 and R2-17.



The preferential attack of carbides is of significant interest when considering the effect on the mechanical performance of material. As the pinning effect of carbides at grain boundaries is a major strengthening mechanism for high temperature materials, the preferential corrosion of these carbides may result in a significant loss of mechanical performance, while not affecting the outward appearance of the material.

2.7.9. Molten sulphate corrosion

Deposits formed in traditional coal-fired boilers contain less chlorine than that found in biomass-fired boilers. The most common form of corrosion in coal-fired boilers is caused by the presence of molten alkali-metal-tri-sulphates [188,189]. Fouling deposits containing alkali sulphates form on the tubes and react with SO₃ in the gaseous environment and iron oxide to form liquid alkali-iron-tri-sulphates, reaction R2-18.



This form of corrosion has been well described in literature [190–194] and is described by a simple fluxing model which involves a sulphate melt forming causing the dissolution of the protective oxide layer. Formation of the alkali–iron-trisulphates requires a relatively high concentration of SO_3 , which is generated by heterogeneous catalytic oxidation of SO_2 within the deposit by iron oxide.

The temperature dependence of this form of corrosion typically follows a bell shaped curve as shown in Figure 2.23. At relatively low temperatures, below $550\text{ }^\circ\text{C}$ (823 K), the corrosion rate is modest and occurs via gas diffusion between the tube material and bulk flue gas through the deposit. As the temperatures reach the deposit melting temperature, the corrosion rate increases dramatically. The molten layer dissolves the protective oxide scale, with metal sulphates forming at the oxide scale-melt interface, and diffuse outward in the melt. This continuous fluxing is promoted due to the temperature gradient across the molten sulphate layer, with solubility decreasing outward in the melt, leading to the metals being precipitated as metal oxides [57,195].

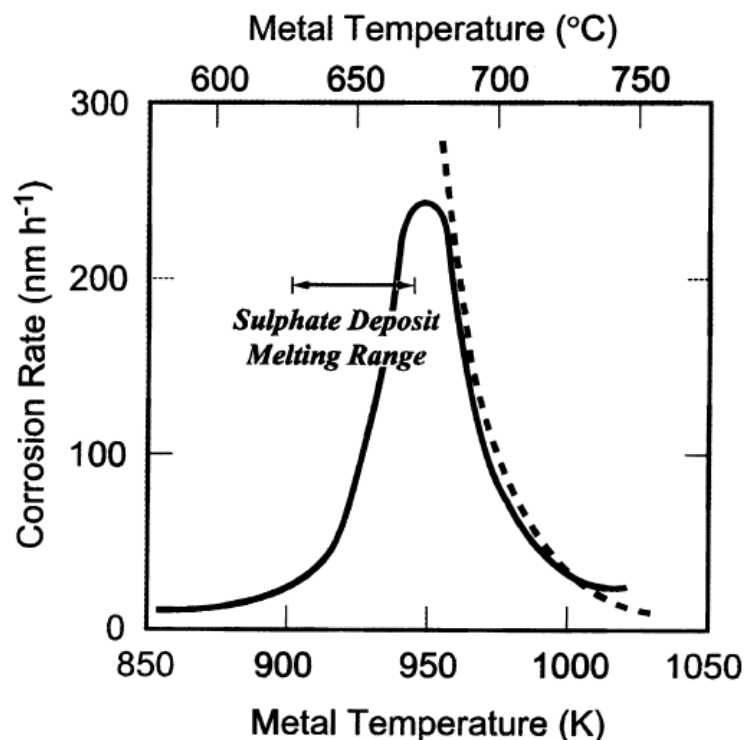


Figure 2.23: Bell-shaped curve showing temperature dependence of corrosion via molten sulphate deposits [59]. The dotted line is a theoretical prediction.

The corrosion rate is shown to decrease with increasing temperatures above a peak point (approximately $670\text{ }^\circ\text{C}$ (943 K) for coal combustion) due to decreasing stability

of iron and chromium sulphates at higher temperatures [86,167]. Additionally pyrosulphates, e.g. $M_2S_2O_7$, where $M=Na, K$, can form due to the interaction of SO_2 with deposits. These are typically molten at operating temperatures. These pyrosulphates can proceed to react with the oxide layer forming alkali-iron-trisulphates, consuming the oxide scale by reactions R2-19 and R2-20.



2.7.10. Corrosion associated with gaseous Cl-species

When HCl and/or Cl_2 are present in the gas phase, the corrosion rate of superheater alloys has been shown to be strongly accelerated [62,63]. This accelerated corrosion proceeds via active oxidation. It is generally accepted that chlorides cause the breakdown of oxide scales, destroying their protective properties. HCl is typically expected to be the dominant Cl-species in the bulk gas.

A number of experiments have been carried out in HCl-containing atmospheres, with the results showing an accelerated corrosion rate at higher levels of HCl [85,156,160]. In addition to the proposed mechanism of HCl reacting directly with the steel and initiating active oxidation, it has been suggested that HCl could react with O_2 in the atmosphere, releasing Cl_2 via reaction R2-21. A schematic of corrosion caused by Cl_2 is shown in Figure 2.24.



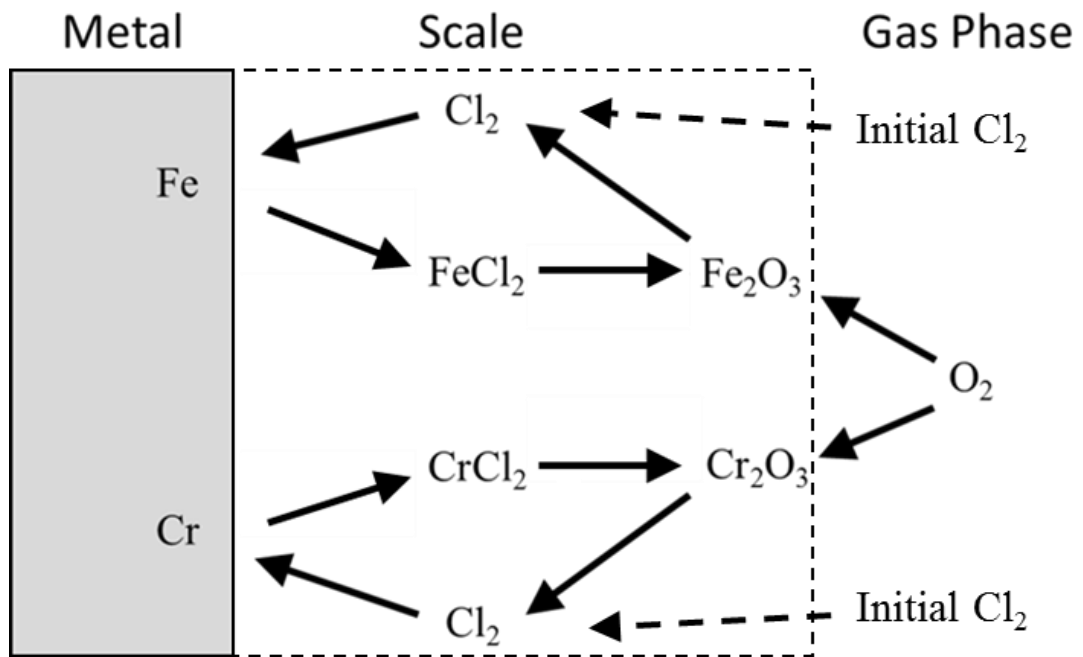


Figure 2.24: Schematic drawing of corrosion caused by $\text{Cl}_2(\text{g})$, adapted from [59].

The influence of increasing amounts of HCl in flue gas on the morphology of the oxide layer formed was investigated by Mayer and Manolescu [62] and their results are summarised in Table 2.7.

Table 2.7: Results from increasing HCl content on oxide formed on metal [62].

Flue gas HCl content (vol. %)	Oxide scale morphology
0.0	Continuous non-porous oxide layer forms
0.1	Blisters form in oxide but layer remains continuous
0.2	Porous, non-continuous oxide layer forms
0.8	Second irregular and porous oxide forms, initial oxide disintegrates entirely
2.0	Continuity of all layers is destroyed and corrosive gases have free access to Fe

Asteman and Spiegel report that pure Cr and 304 steel can fully resist HCl (g) attack, with pure Fe undergoing severe corrosion when exposed [157]. However these tests were carried out at 400 °C, and it is likely that the temperature was not high enough for active oxidation to occur. Work by Viklund and Pettersson [196] shows that at 400 °C, oxide layers that form prior to testing offer protection against further corrosion. However, when the temperature was raised to 700 °C the protection from pre-oxidation was lost and any oxide formed was passive.

In reducing environments, metal chlorides form directly on the metal surface, as oxide layers will not form. The rate of corrosion strongly depends on temperature in this case, as it is governed by the volatilisation of metal chlorides [59]. At temperatures below 500 °C, the corrosion rate will be parabolic with time, as a protective chloride layer will form on the metal. At higher temperatures, the corrosion will initially increase at a parabolic rate, followed by a linear decrease with time. This occurs when the scale will no longer grow, as the growth of the chloride layer will no longer be fast enough to supply the amount of metal chloride required for volatilisation. The time taken to this shift, when the chloride reaches what is known as the critical thickness, depends on temperature, atmosphere and metal properties. At further elevated temperatures, above 800 °C, the high volatility of the chloride results in complete evaporation leading to a linear weight loss [59].

2.7.11. Solid phase reaction with Cl-species in deposits.

Skrifvars et al. [49,50] exposed six steels of varying compositions to six synthetic salts containing various levels of Na, K, S, Cl and O in air. The compositions and melt temperatures of these salts are shown in Table 2.8. From Table 2.8 the effect that chlorine, and in particular KCl, has on the melt temperature is evident. With the addition of 0.3 wt % Cl to salt 1 the melt temperature drops from 884 °C to 625 °C (Salt 3), while if K is added to this mixture (Salt 4) the melt temperature drops to 526 °C.

Table 2.8: Compositions and first melt temperatures T_0 of synthetic salts of synthetic salt mixtures [50].

Salt (wt-%)	1	2	3	4	5	6
Na	32.4	24.8	32.4	24.8	32.5	24.9
K	0.0	10.5	0.0	10.5	0.0	10.5
S	22.6	21.6	22.5	21.5	22.1	21.1
Cl	0.0	0.0	0.3	0.3	1.3	1.3
O	45.0	43.1	44.8	42.9	44.1	42.2
T_0 (°C)	884	834	625	526	621	522
Description	No K, No Cl	K, No Cl	No K, Low Cl	K, Low Cl	No K, High Cl	K, High Cl

For Salt 1, almost no oxide layer growth was observed for temperatures ranging from 450 – 600 °C. Salt 2 displayed a slight increase in corrosion rate compared to Salt 1. Increased corrosion rates were observed for samples exposed to Salt 3 despite the fact that the temperatures tested did not exceed the melt temperature of the deposit (625°C).

Samples exposed to Salt 4 experienced a sharp increase in the corrosion rate, which can be attributed to chromate formation and the fact that salt melt temperature was exceeded during testing. An increase in chlorine content results in an increased corrosion rate for samples exposed to Salt 5 compared to Salt 3. The corrosion rate is however, lower than Salt 4. This is expected as the melt temperature of Salt 5 was not exceeded. As expected the highest corrosion rate was observed for Salt 6. It has the highest level of chlorine and potassium and the melt temperature of the deposit is exceeded during testing.

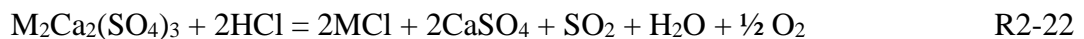
With the addition of chlorine, corrosion occurred, even below melting temperatures of the deposits, although this was greatly accelerated when melt temperature was exceeded. These results show that it is not necessary to have a chlorine, water or SO_2

containing gaseous environment to have accelerated corrosion [49,50]. Pure alkali sulphates does not increase the corrosion rate to any notable degree. However when chlorine was added to the deposit the corrosion rate increased severely [20,50].

Enestam et al. [47] exposed samples of 347SS and Sanicro 28 to pure NaCl and KCl deposits at temperatures varying from 400-600 °C. Internal degradation of Sanicro 28 was substantial; affecting both grain boundaries and grains. The difference in grain boundary attack between 347SS and Sanicro 28 was attributed to different grain size, as 347SS consists of grains of 42 µm while Sanicro 28 consists of grains of 125µm. Fine grain structure is beneficial in forming protective chromium oxide due to the higher grain boundary area, which promotes diffusion along the grains [47].

Lehmusto et al. [181] found that deposits containing K₂SO₄ do not result in an accelerated corrosion rate. This is attributed to the fact that the reaction of K₂SO₄ with the protective oxide is not thermodynamically favoured.

Grabke et al. and Lith et al. [51,64] have shown that when HCl is present in the atmosphere, the corrosion rate beneath deposits is accelerated. It is suggested that in the presence of HCl, sulphates in the deposit are converted to mixed chlorides as per R2-22, where M = Na, K. These proceed to react with the oxide scale, as shown previously, resulting in the release of Cl₂ leading to active oxidation.



When HCl and SO₂ are both present in the atmosphere, less corrosion was measured [51]. This was attributed to enhanced stability of the sulphates in the deposits, resulting in less chlorine being released for the active oxidation mechanism.

Work by Nielsen et al. [53] exposed samples to KCl in a gas consisting of 6 vol% O₂, 12 vol % CO₂, 400 ppmv HCl, 60 ppmv SO₂, balance N₂ at 550°C. Internal corrosion was identified in localised areas reaching up to 50 µm at points. The nature of the internal corrosion was varied, with cracks, voids and internal attack through grain boundaries all detected. A number of pits were also detected in the samples with depths reaching up to 200 µm. Chlorine was found in pits indicating that chlorine plays a role in the localised pitting attack.

2.7.12. Active Oxidation Modelling

A number of models have been developed in previous work to determine the growth of corrosion layers on metals due to active oxidation [51,53,159]. Grabke et al. [51] showed that the rate limiting step of the active oxidation process was the outward diffusion of FeCl₂ gas through the porous oxide scale. Based on this, an equation was developed for the diffusional flow of FeCl₂ gas, as follows:

$$j_{FeCl_2} = \varepsilon \left(\frac{D_{i,FeCl_2}}{d} \right) (p_{i,FeCl_2} - p_{s,FeCl_2}) \quad (2-12)$$

where ε , is a labyrinth factor which accounts for the open space available for FeCl₂ diffusion in the porous oxide scale, j_{FeCl_2} is the diffusional flow of FeCl₂, d is the thickness of the oxide scale (m), $D_{i,FeCl_2}$ is the molecular diffusion coefficient of FeCl₂ through the porous oxide layer (m²/s), p_{FeCl_2} is the partial pressure of the FeCl₂ gas (Pa), with (*i*) and (*s*) designating the interface of substrate and oxide and the surface of the oxide, respectively. Partial pressure at the surface is found to be negligible. The labyrinth factor ε is determined based on experimental data for the formation of iron oxide in active oxidation.

Stott and Shih [159] developed a similar equation for the flux of FeCl₂ through the scale; it differs only in terms of the units used to describe diffusivity:

$$J_{FeCl_2} = \varepsilon \left(\frac{D_{FeCl_2}}{dRT} \right) (P_{i,FeCl_2} - P_{s,FeCl_2}) \quad (2-13)$$

where J_{FeCl_2} is the outward flux of FeCl₂, R is the ideal gas constant (J/KgK) and T is the temperature (T) with all other terms the same as developed by Grabke et al.

Nielsen et al. [53] defined the growth of an oxide layer via a parabolic law to represent the diffusion of gas-phase reactants through the oxide layer as follows:

$$x = \sqrt{k_p(T)t} \quad (2-14)$$

where x is the corrosion depth, t is the exposure time, T is the temperature and k_p is a constant which is dependent on the chemical reaction rate. k_p , the parabolic rate constant can be written as follows for a reaction of the type R2-23:



$$k_p(T) = \frac{2bD_e C_{Ag}}{\rho_b} \quad (2-15)$$

where D_e is the effective diffusivity of gas A through the porous layer (m^2/s), ρ_b is the molar density of B in the material (mol/m^3), C_{Ag} is the gas-phase concentration of gas A (mol/m^3) and b is the stoichiometric coefficient. Results from Equation 2-15 are shown in Figure 2.25. All of the current models make use of experimental data to provide fitting constants to match experimental results.

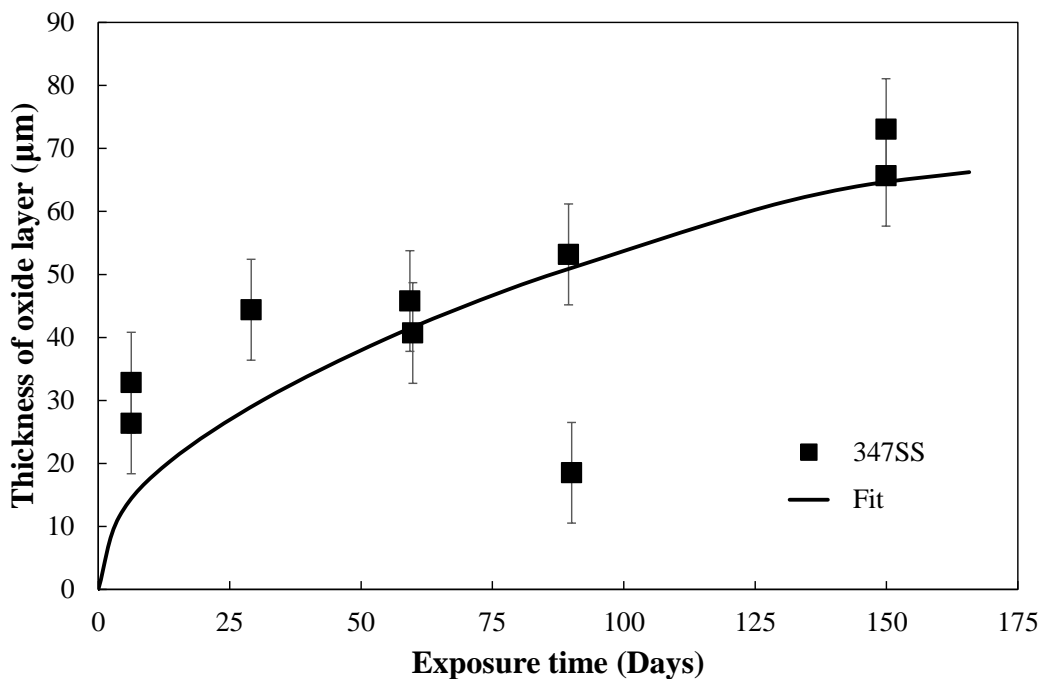


Figure 2.25: Oxide layer thickness for AISI 347 SS covered with KCl [53].

2.8. Summary

It is clear that the elevated levels of alkali chlorides produced during biomass co-firing result in accelerated corrosion of heat exchanger tubes in plants. Multiple layers of non-adherent oxides form, with metal wastage, void formation, pitting corrosion and grain boundary corrosion all detected on samples. It has been determined from work carried out by several authors that alkali chlorides present in deposits, particularly at temperatures above the deposit melt temperature, cause the most severe corrosion of tube material. This corrosion rate can then be further accelerated by gases present in the environment in which the tubes are situated.

Tests have previously been carried out using synthetic salts to study the accelerated corrosion process which occurs during biomass co-firing. However, this work typically ignores the calcium content, which forms approximately 40% of the deposit content. This calcium content will affect the melting temperature of the deposit, which, will in turn, affects the corrosion rate and mechanism. This is due to the fact that the presence of a molten phase causes an increased corrosion rate.

Limited work on microstructural analysis of biomass corrosion samples has been presented to date. Pitting corrosion can often be hidden from the naked eye by corrosion products and may therefore not be visible without etching.

Relatively little work has been done to date on the effect of inclusions, that form as impurities during the manufacturing of materials. Near-surface inclusions cause pit formation if present in chlorine-containing environments, which leads to a detrimental effect on component integrity. Inclusions are well known to act as crack initiation sites and can cause decreased life expectancy.

Studies have attempted to develop models to predict the corrosion rate for active oxidation. Typically they use an empirical constant, known as a 'labyrinth factor', to fit the model to experimental data. As laboratory experiments are typically short-term, caution must be taken when extrapolating these results to long-term prediction of corrosion and life times of heat exchanger tubes. Hence, there is a need for a more physically-based model to extrapolate from short term data to long term corrosion prediction.

Although there has been a significant amount of work on the corrosion rates and mechanisms relevant to biomass co-firing, the effect of corrosion on the mechanical performance and structural integrity of plant components has received relatively little attention. In uniform corrosion, the loss of material is expected to decrease creep rupture life and allowable stress. However, this has not been previously investigated for corrosion rates experience during biomass co-firing. If pitting corrosion occurs, the material is at risk of stress corrosion cracking (SCC). Stress concentrations will occur at pits, which may lead to crack initiation points.

3. Experimental Methods

3.1. Chapter Overview

Chapter 3 presents the experimental programme that was undertaken as part of this research. The specific sample preparation and experimental methodology is detailed. The analytical techniques used are introduced and a brief review of their operational theory is presented. A method for determining the elemental composition of biomass fuels and ash produced during combustion is introduced.

This chapter is divided into four main sub-sections, Section 3.2 details the preparation technique for the synthetic salts, which were produced to replicate in-situ deposit compositions taken from tests at different levels of biomass co-firing at operational plants. Section 3.3 describes the preparation of the metal specimens and the conditions at which they were exposed.

The post-exposure work carried out on samples is described in Section 3.4. The tools used in analysing samples and brief descriptions of their operating theories are shown in Section 3.5. Section 3.6 describes a method, developed through this work, for characterising in-situ deposit compositions. This method was also extended to determine the elemental composition of biomass samples.

During the course of this work an experimental test program was carried out in order to investigate the corrosion of materials when exposed to deposits representative of those formed during biomass co-firing. Descriptions of the tests carried out are shown in Table 3.1.

Three materials were exposed to two synthetic salts, A and B, whose compositions are given in Table 3.2. These salts are representative of different levels of biomass co-firing in peat fuelled plants, based on in-situ tests carried out by industrial collaborators. Two of the materials tested, P91 and 347SS, are currently used in operational plants and are thus of interest to industrial collaborators. Pure iron (99.5% purity), henceforth referred to as iron, was also investigated in order to gain an understanding of the corrosion process at its most fundamental level.

Table 3.1: Experimental test matrix carried out to investigate performance of materials in co-firing plants.

Test	Temperature (°C)	Material	Synthetic Salt	Time Exposed (Days)
1	540	Iron	A	1, 4, 7, 14, 21, 28
2	540	Iron	No salt	1, 4, 7, 14, 21, 28
3	540	P91	A	1, 4, 7, 14, 21, 28
4	540	P91	No salt	1, 4, 7, 14, 21, 28
5	600	Iron	A	1, 4, 7, 14, 21, 28
6	600	Iron	B	1, 4, 7, 14, 21, 28
7	600	Iron	No salt	1, 14, 28
8	600	P91	A	1, 4, 7, 14, 21, 28
9	600	P91	B	1, 4, 7, 14, 21, 28
10	600	P91	No salt	1, 14, 28
11	600	347SS	A	1, 4, 7, 14, 21, 28
12	600	347SS	B	1, 4, 7, 14, 21, 28
13	600	347SS	No salt	1, 14, 28

The experimental method used in the present work is a modified version of that of Skrifvars et al. [49,50] in which synthetic salts are deposited on metal specimens and placed in high temperature furnaces. This method was chosen as industrial collaborators in the project had previously obtained results from this method which could be used to validate our method. A schematic of the method used here is shown in Figure 3.1. A more detailed description of the experimental procedure is provided in the coming sub-sections.

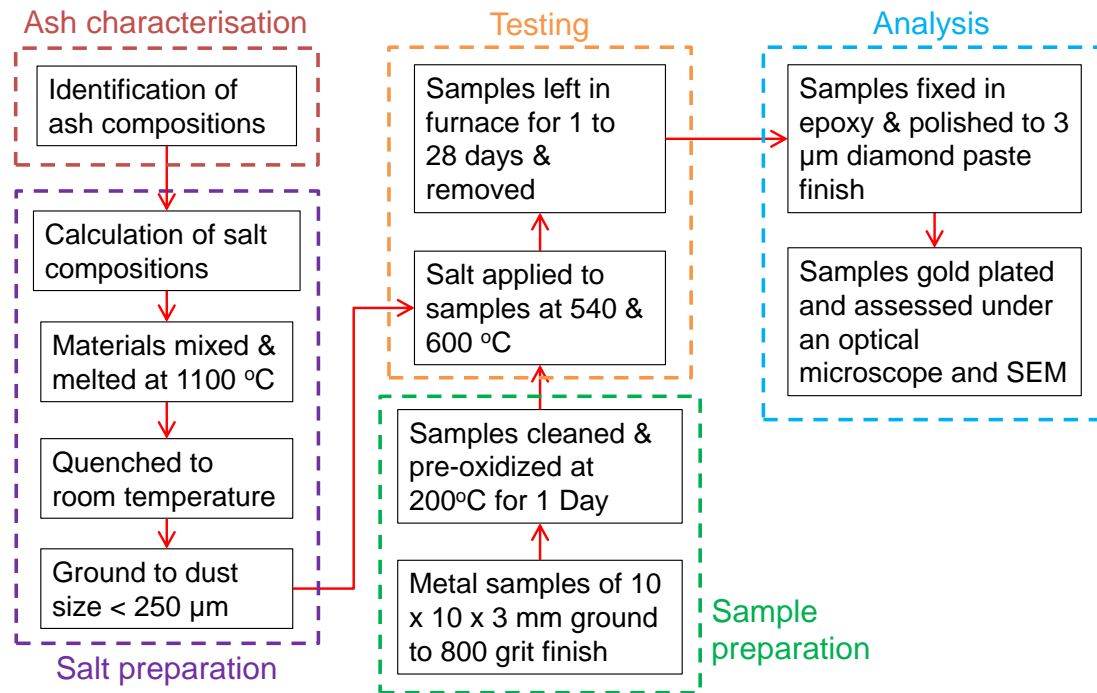


Figure 3.1: Flowchart detailing experimental methodology.

3.2. Synthetic Salt Calculation and Preparation

Deposit compositions shown in Table 3.2 were obtained from in-situ tests carried out by industrial collaborators for various levels of co-firing. These are presented in elemental form as it is common practice to provide the percentage of the elements analysed as if they were all oxides [20]. It is noted that this is very seldom the case, and it is more likely that the elements will be present as more complex compounds. A method for obtaining deposit compositions has been developed as part of this work and is described in Section 3.6.

Following identification of the target composition, a range of starting compounds including NaCl, KCl, Na₂SO₄, K₂SO₄, NaBr, KBr, MgSO₄ and CaSO₄ were obtained from Sigma-Aldrich. In addition SiO₂, Fe₂O₃, Al₂O₃ and NiO were initially considered, however due to the extremely high melt temperatures of these compounds (1566 – 2072 °C) it was deemed unfeasible to include them in mixtures. This was due to both the capabilities of the ovens at NUIG and the melting temperature of the container ($T_{\text{Max}} = 1750 \text{ °C}$) used to hold the mixture.

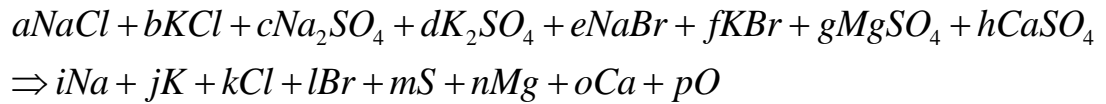
The in-situ deposit compositions chosen to produce representative salts were a 30% woodchip, 70% peat mixture, named salt A and a 60% willow, 40% peat mixture, named salt B. These compositions were chosen in order to evaluate the effect of a high-Cl, low-K containing fuel (salt A) and a low-Cl, high-K containing fuel (salt B). This is significant as Cl and K are two of the most important elements in the high temperature corrosion during biomass co-firing, as was discussed in Chapter 2.

Table 3.2: Chemical composition of deposits from in-situ tests and representative synthetic salts produced.

Element (wt. %)	30% Woodchip, 70% Peat		60% Willow, 40% Peat	
	In-situ composition	Synthetic Salt A	In-situ composition	Synthetic Salt B
Na	2.09	2.12	1.61	1.51
K	5.21	5.27	13.97	13.34
Cl	2.18	2.29	0.23	0.23
Br	0.07	0.07	0.19	0.21
S	21.59	42.52	22.57	42.19
Mg	3.54	3.36	3.46	3.46
Ca	44.35	44.37	39.17	39.06
Si	5.87	-	6.84	-
Fe	9.70	-	0.48	-
Al	1.7	-	1.88	-
Ni	0.94	-	6.67	-
P	1.51	-	2.36	-
Ti	0.00	-	0.32	-
Cr	1.23	-	0.24	-

The quantities of the starting compounds to be mixed to obtain a similar composition to the deposits were identified using stoichiometric calculations, as is detailed below. The starting compounds were mechanically mixed together, melted at 1100 °C in an alumina crucible, quenched to room temperature, ground and screened to a particle size of less than 250 µm.

Taking the 30% woodchip, 70% peat deposit measurements and synthetic salt A as an example, the following technique was carried out to determine the starting quantities of each material. These equations were developed based on knowledge of the compositions of the starting compounds. The chemical reaction below shows contribution of all the starting compounds to the final individual molar fractions of the elements.



where *a-h* are the amount of the starting compounds which are used to produce the synthetic salt and *i-n* are the number of moles of the individual elements in the final mixture. This was used to determine the individual molar fraction of each element, *X_i*, via elemental balance equations, as follows:

$$Na \quad \quad \quad i = a + 2c + e \quad \quad \quad (3-1)$$

$$K \quad \quad \quad j = b + 2d + f \quad \quad \quad (3-2)$$

$$Cl \quad \quad \quad k = a + b \quad \quad \quad (3-3)$$

$$Br \quad \quad \quad l = e + f \quad \quad \quad (3-4)$$

$$S \quad \quad \quad m = c + d + g + h \quad \quad \quad (3-5)$$

$$Mg \quad \quad \quad n = g \quad \quad \quad (3-6)$$

$$Ca \quad \quad \quad o = h \quad \quad \quad (3-7)$$

$$O \quad \quad \quad p = 4c + 4d + 4g + 4h \quad \quad \quad (3-8)$$

Equation 3-1 shows that the number of moles of Na in the mixture (i) is equal to the amount of NaCl (a), NaBr (e) and twice the Na₂SO₄ (c) added to the starting mixture. From this the output mass fraction, Y_i of each element in the mixture was obtained as follows:

$$Y_i = \frac{X_i MW_i}{MW_{mix}} \quad (3-9)$$

where the atomic weights of the individual elements (MW_i) are shown in Table 3.3 and $MW_{i,mix}$ is found, as follows:

$$MW_{i,mix} = \sum_{i=1} X_i MW \quad (3-10)$$

The moles of each salt in the starting mixture was then changed iteratively until a synthetic salt which is representative of the in-situ tests is obtained. For example the composition of synthetic salt A by molar percentage is 4.64% KCl, 3.31% Na₂SO₄, 2.49% K₂SO₄, 0.07% KBr, 9.94% MgSO₄, and 79.55% CaSO₄. It is noted that the majority of the error between the synthetic salt and in-situ is present as S. This is due to the fact that the majority of the starting elements were sulphates. This is unavoidable as chlorides or bromides of the respective elements would result in higher levels of Cl or Br, resulting in higher corrosion rates. Oxides of the elements were considered, however the extremely high melt temperatures of the oxides relative to sulphates was deemed impractical.

Table 3.3: Atomic weights of elements in synthetic salt.

Element (i)	Na	K	Cl	Br	S	Mg	Ca	O
Atomic Weight (MW_i)	22.99	39.09	35.45	79.90	32.07	24.31	40.08	15.99

The input quantity of moles then provides starting quantities for the production of the salt. The molecular weights of the starting compounds were used to obtain the mass percentages of each individual starting compound to be used and these are shown in Table 3.4.

Table 3.4: Molecular weights of starting compounds used for synthetic salt.

Chemical (MW_j)	NaCl	KCl	Na₂SO₄	K₂SO₄	NaBr	KBr	MgSO₄	CaSO₄
Molecular Weight	58.44	74.55	142.04	174.26	102.89	119.00	120.37	136.14

The molar percentages of the starting compounds were then obtained and used to determine the mass percentages of starting compounds to use (Y_j), as follows:

$$Y_j = \frac{X_j MW_j}{MW_{j,mix}} \quad (3-12)$$

Following this iterative procedure, the starting quantities to produce salt A and salt B were identified and the values are shown in Table 3.5.

Table 3.5: Salt composition by mass percentage of starting compounds.

Mass Percentage (Y_j)	KCl	Na₂SO₄	K₂SO₄	KBr	MgSO₄	CaSO₄
Salt A	4.64	3.31	2.49	0.07	9.94	79.55
Salt B	0.50	2.50	12.50	0.20	10.74	73.56

3.3. Sample Preparation and Exposure

Iron, P91 and 347SS specimens were cut to size 10 mm × 10 mm × 3 mm and then ground on 240, 320, 400, 600 and 800 grit silicon carbide paper. This was done in order to remove any machining marks, existing oxide layers and to ensure a uniform surface finish for all samples prior to testing. A number of samples were tested using a profilometer to ensure that the surface roughness values, R_a (arithmetic average of absolute values), did not exceed 0.1 μm. Images from optical microscopy showing the difference in surface finish of specimens before and after polishing are shown in Figure 3.2.

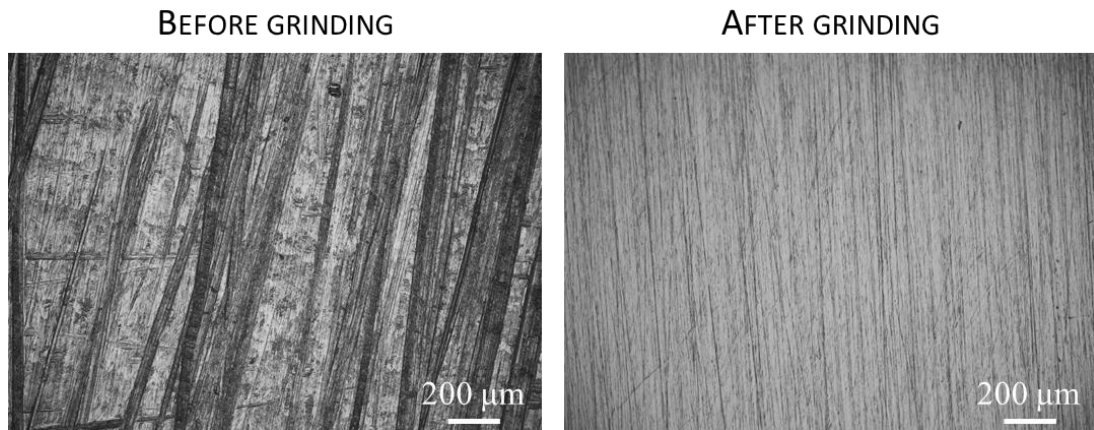


Figure 3.2: Samples of iron before and after grinding prior to exposure to synthetic salt.

Samples were then cleaned and pre-oxidised at 200 °C for 24 hours, in order to produce an initial protective oxide layer on the samples. The synthetic salt was applied to 6 samples of metal and placed in a high temperature furnace at 540 °C and 600 °C. 0.25 ± 0.01 g of salt were applied to each sample using a spatula. A further 6 samples were also placed in the furnace with no salt coverage. Samples were removed from the furnace after 1, 4, 7, 14, 21 and 28 days. Three characterisation techniques were carried out on the sectioned samples; scanning electron microscopy (SEM), optical microscopy (OM) and energy dispersive X-ray spectroscopy (EDX).

3.4. Post-Exposure Work

Figure 3.3 shows a sample of pure iron which was exposed to salt A for 7 days at 540 °C. Following exposure, samples were fixed in epoxy and cut, revealing the cross section of the sample with the arrow indicating the section which is analysed.

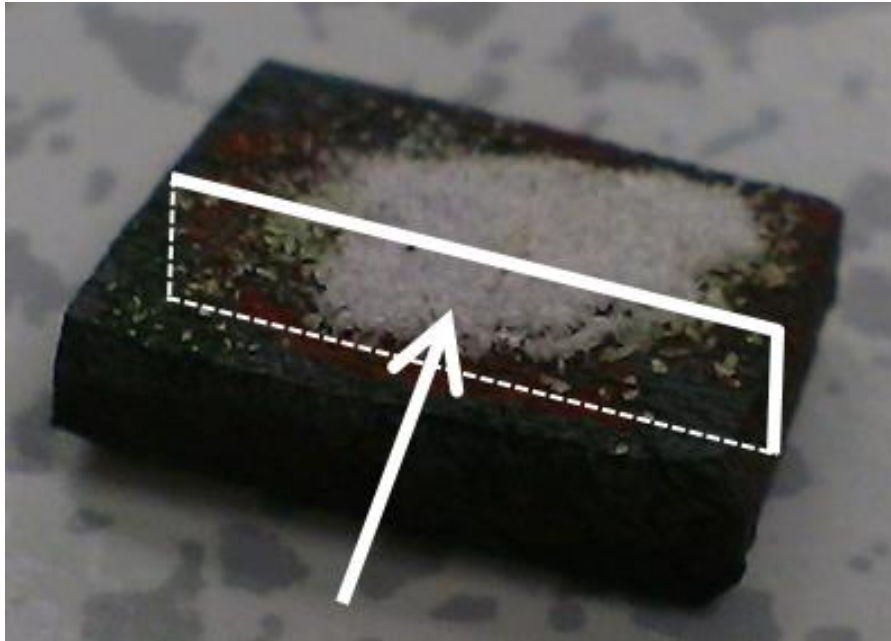


Figure 3.3: Sample following exposure at 540 °C for 7 days with salt coverage, with arrow indicating section to be analysed.

This sectional plane was then ground using 240, 320, 400, 600, 800 and 1200 grit SiC grinding paper and polished progressively using 30, 6 and 3 μm diamond paste. The samples were then examined using an Olympus BX51M optical microscope [197] and a Hitachi S-4700 SEM [198], to measure the depth of corrosion and provide insight into the subsurface material degradation and structure of the corrosion layer.

EDX analysis was also carried out to provide the chemical composition at different depths. Elemental maps were created in order to obtain the complete elemental composition of a section of the sample. Corrosion depth distributions have been quantified using the microscopy techniques in a manner similar to Nielsen et al. [53], Frandsen [199] and Dudziak et al. [192]. The corrosion depth was defined as the sum of the thickness of the oxide layer and the degraded material [50], as illustrated in Figure 3.4. An average thickness was calculated from measurements taken at 15-20 different locations across the specimen width. An example showing the measurement of an oxide layer thickness at four locations across the sample is shown in Figure 3.4.

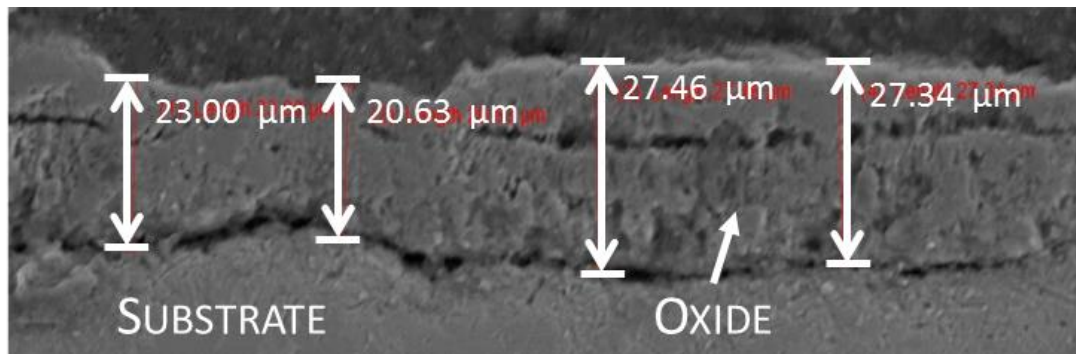


Figure 3.4: SEM image showing oxide layer measurements for sample.

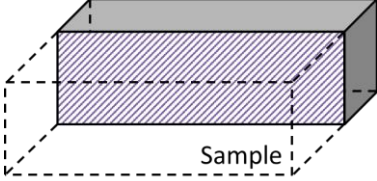
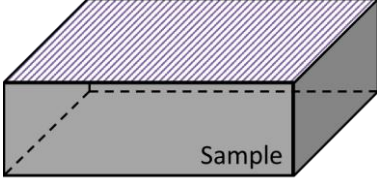
If the effect of the corrosion on the material microstructure is to be investigated then samples were further polished using $0.05 \mu\text{m}$ silica suspension and etched using Vilella's reagent [134]. Samples were then examined under the optical microscope or SEM. Samples were cleaned following each step using an ultrasonic bath. Following initial etching they were re-polished using the silica suspension and re-etched using the same etchant in order to reveal material defects such as inclusions in the steel.

Etchants are used to selectively corrode microstructural features of a sample, creating a contrast between features of the metals microstructure. This occurs as there is a difference in the relative rates of corrosion of microstructural features of a surface. For example grain boundaries can corrode very quickly when exposed to the appropriate etchant, highlighting the edges of the grains. Grain shape and size is then easily identifiable.

Duplicate samples were also placed in the furnace to be used for surface analysis. These samples were not fixed in epoxy and were instead cleaned in an ultrasonic bath and pickled using hydrochloric and nitric acid. Pickling was done to remove any oxide which exists on the sample surface, by submerging the sample in an acidic solution. Mass change measurements were taken to investigate the extent of material loss. Pitting corrosion was identified on the surface of the samples following pickling. The surface of the samples were then analysed using digital elevation modelling (DEM), to reveal the surface profile, which provides depths of the pits.

An overview of the areas analysed is shown in Table 3.6. The preparation techniques required for the analysis to be carried out on this section is shown. The analytical tools used to analyse this area and the information obtained from this analysis is also shown.

Table 3.6: Area of sample examined, preparation techniques required, analytical tools used and information obtained.

View	Section	Surface
Surface examined		
Preparation required	<ol style="list-style-type: none"> 1. Fix in epoxy 2. Section 3. Polish 4. Etch (optional) 	Pickle sample
Analytical tools used	Optical microscopy, SEM, EDX	SEM, EDX, DEM, White light interferometry

3.5. Analytical Tools

The analytical tools used in this work were optical microscopy, SEM, EDX spectroscopy and white light interferometry. Brief explanations of the operational theory of these techniques are included in this chapter.

3.5.1. Optical Microscopy

Optical microscopy makes use of visible light and a system of lenses to magnify the images of samples. A lens close to the object being viewed is used to collect light which focuses a real image of the object inside the microscope. A second lens, or set of lenses then magnifies the image to provide an enlarged image, this allows for higher magnification and interchangeable lenses to adjust magnification. A schematic showing the operating principle of a compound optical microscope is shown in Figure 3.5. The optical microscope used during this work was an Olympus BX51M optical microscope [197].

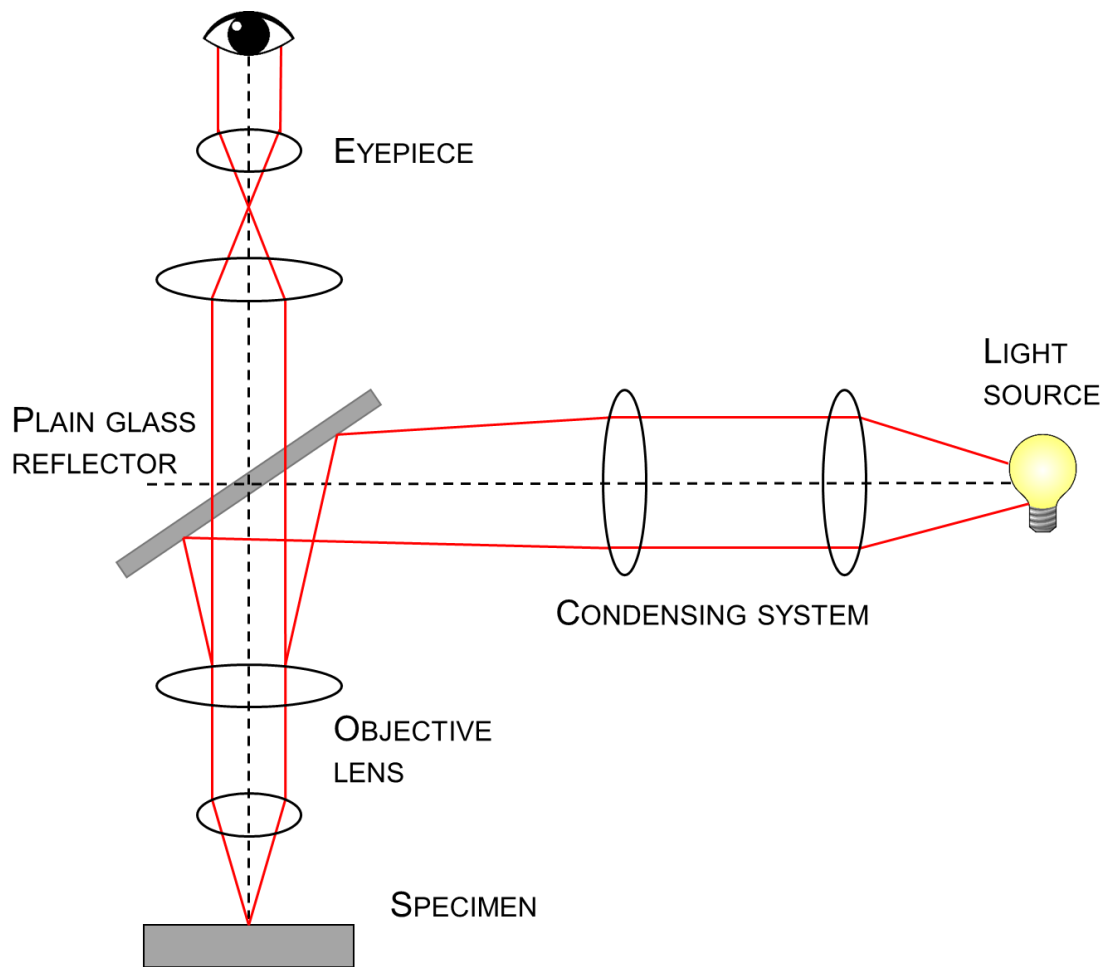


Figure 3.5: Schematic showing operating principle of an optical microscope.

3.5.2. Scanning Electron Microscopy

SEM was used to obtain images of samples at high magnifications. This provides an insight into how the corrosion mechanism proceeds and the products formed. It allows for identification of corrosion damage at a microstructural level, provided samples have been etched. SEM is also used to examine the surface topography of samples and identify areas for EDX analysis.

SEM is in brief a microscopic surface analysis technique which produces images by scanning the surface of a sample with a focused beam of electrons. It operates by emitting an electron beam from an electron gun, which is fitted with a cathode. This electron beam is focused by one or two condenser lenses to an area between 0.4 – 5 nm in diameter. It then passes through scanning coils or deflector plates in the electron column, typically the final lens, which deflect the beam in the x and y axes so it scans

in a raster fashion over a rectangular area of the sample surface. Once the primary electron beam interacts with the sample, the electrons lose energy by repeated random scattering and absorption across the sample. A schematic of this can be seen in Figure 3.6.

If the electrons strike the sample and interact with the nucleus and electrons of the atoms, the electrons produced are called secondary electrons (SEs). If the electrons are reflected back with minimum collision with the surface, then they are called back scattered electrons (BSEs). SEMs can be used to produce very high-resolution images of a sample surface, with details of less than 1 nm in size being visible at a high degree of quality. In addition SEM micrographs have a large depth of field, due to the narrow electron beam. This provides the characteristic three-dimensional appearance which is useful for understanding the surface structure and depths of samples.

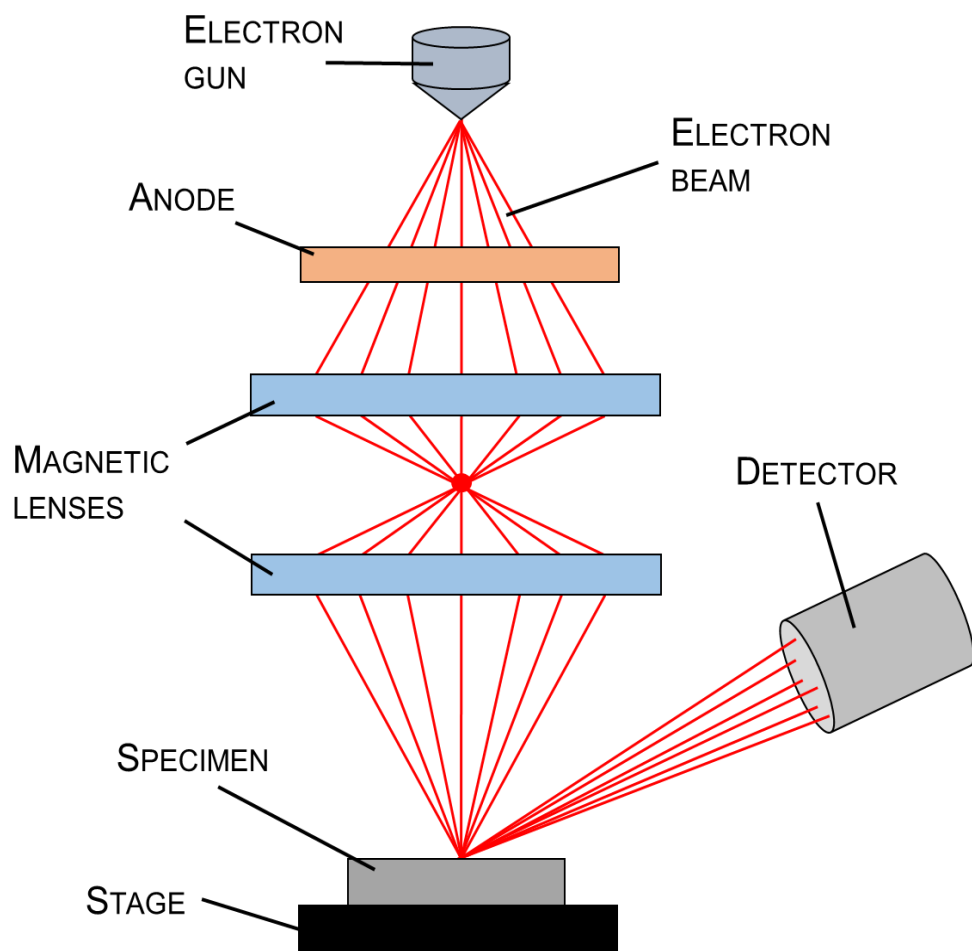


Figure 3.6: Schematic showing operational principle of a scanning electron microscope (SEM).

SEM can typically vary its magnification from 10 to 500,000 times its original size. The ability of a SEM to obtain high magnifications is based entirely on the ability of the electron gun to generate a beam with a small enough diameter.

When a non-conductive specimen is illuminated with an electron beam this causes specimen charging, as electrons collect locally. This causes poor quality imaging, where the electrons can often cause blurry images. Typically non-conductive specimens must be coated with some conductive metal prior to observation. However by reducing the probe current and lowering the accelerating voltage this could be unnecessary. Charging can also cause damage of the sample which is being analysed. The SEM used during this work was a Hitachi S-4700 SEM [198].

3.5.2.1. Digital elevation models

Digital elevation models (DEM) can be produced by taking SEM images after tilting the specimen by small angles. This produces a 3D surface profile of the specimen. This method employs the stereoscopic technique and makes use of the Alicona Mex software which enables an SEM with digital imaging to act as a surface metrology device [200]. The resolution for the Mex software is 3 nm.

3.5.3. Energy-dispersive X-Ray Spectroscopy

Energy-dispersive X-ray spectroscopy (EDX) analysis is used to determine the chemical composition at points of a sample. It is used in this work to define what regions that have converted to oxides or remained unoxidised. EDX point analysis is also used to determine the chemical composition of inclusions. This is necessary as different inclusions will affect the material properties in different ways.

EDX is an analytical technique which is used in the chemical analysis and characterization of a sample. It operates based on the interaction between some form of X-ray excitation and a sample. As each element has a unique atomic structure, they provide unique peaks on its X-ray emission spectrum. To obtain the emission of the X-rays from samples, EDX makes use of electrons which are focused into the sample during SEM. The number and energy of the X-rays emitted from the specimen are then measured using the energy-dispersive spectrometer.

The difference in energies and number of X-rays emitted are unique to each element, allowing for the elemental composition of a sample to be measured. The accuracy of the EDX spectrum can be influenced by the similarity of certain elements' atomic structures. EDX analysis is unable to detect hydrogen in its spectrum due to the fact that hydrogen has no core electrons. The hydrogen electrons are valence electrons and as such participate in chemical bonding, therefore any signal from hydrogen would overlap with signals from excitation of valence electrons from other surface atoms [201].

An example of an EDX spectrum, taken during analysis of salt A is shown in Figure 3.7. This shows the peaks caused by X-rays which are given off as electrons from the element shells. The same element can appear multiple times in a map due to X-rays being emitted from different electron shells of the same element. The data from the EDX analysis was processed using the INCA software from Oxford Instruments.

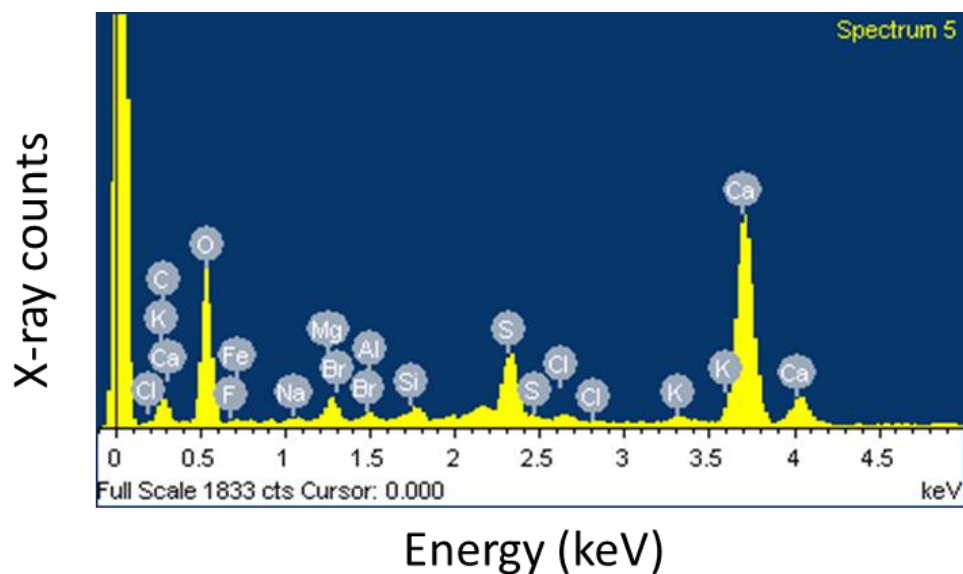


Figure 3.7: EDX spectrum showing numerous peaks from different elements.

3.5.4. White Light Interferometry

White light interferometry was used to examine the RepliSet samples taken from in-situ tubes along the superheater and reheater banks during a planned shutdown. RepliSet is a fast curing, two-part silicone rubber. It is designed to transfer the structure of a solid surface to a highly accurate, stable 3D replica, with a resolution of

0.1 μm [202]. This provides a non-destructive method for microscopic examination and precise measurements of in-situ components. It was necessary to use white light interferometry on these samples due to the material of the samples. Use of a contact profilometer would have resulted in tearing of the samples and inaccurate readings.

The white light interferometer used in this work is a Zygo Newview 100 surface profiler. It can provide surface topography, surface roughness and film thickness measurements to an accuracy of 0.1 nm. The system operates via the generation of an interference pattern (contour lines) which corresponds to the profile (contour map) of the sample surface.

A white light source is used to illuminate test and reference surfaces. A collimating lens collimates the light from the source, with a beam splitter separating the light into reference and measurements beams. These beams then reflect or scatter off the reference mirror and the specimen surface respectively. The reflected beams are then relayed by the beam splitter to the charge-coupled device (CCD) camera, providing the interference pattern. A schematic of this process is shown in Figure 3.8.

The computer then performs fast fourier transformations (FFT) on the collected data to generate the surface profile. The key advantage of white light interferometry over stylus profilometers is its ability to take measurements on soft, easily deformable materials, such as rubbers. This makes it a suitable system for obtaining the surface profile of the Repliset samples.

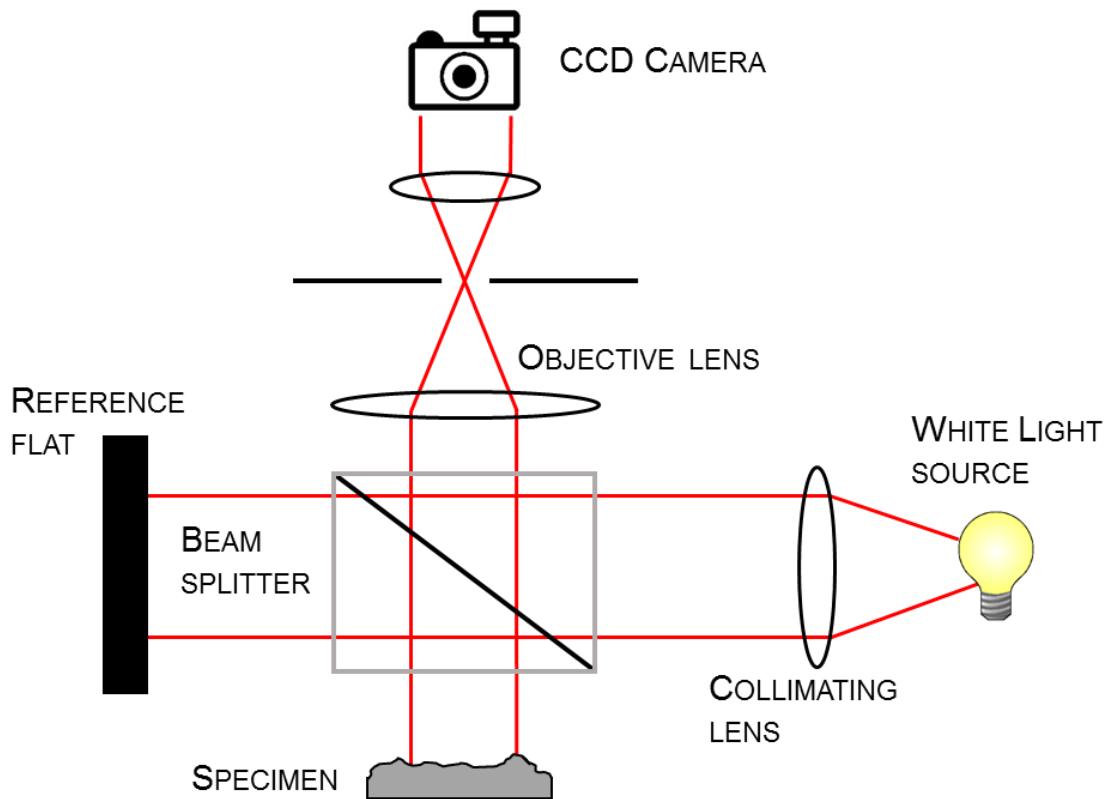


Figure 3.8: Schematic showing operational principle of a white light interferometer.

3.6. Deposit and fuel characterisation

This section presents results from the EDX analysis of deposits obtained from operational power plants and unburnt biomass fuels. Knowledge of the composition of the deposits forming in operational plants is essential to this work, as it is well known that the corrosion rate of the heat exchanger tubes relates primarily to the alkali halide content of the deposits which form on tubes [59–61]. Deposits were obtained from the three plants of interest to this work; (1) West Offaly Power (WOP), (2) Edenderry Power and (3) Lough Ree Power (LRP).

It is noted that at the time of testing WOP and LRP both made use of peat alone as a fuel source, while Edenderry was co-firing approximately 20% biomass with peat. This is expected to have an effect on the deposit compositions measured.

In addition to the deposits analysed this method was extended to obtain the chemical composition of biomass samples obtained from industrial collaborators. As EDX analysis is unable to detect hydrogen, the primary purpose of this analysis was to

determine the O:C ratio of the fuels. The higher proportion of oxygen to carbon will reduce the energy value of a fuel as shown via the Van Krevelen diagram and Dulong equation shown in Chapter 1.

Three different biomass fuels were analysed; (1) olive stone, (2) torrefied olive stone and (3) torrefied wood. Torrefaction is a mild form of pyrolysis and is described briefly in Chapter 1. Torrefaction provides a higher fuel quality for combustion applications by removing moisture and oxygen from the material through exposure to moderately high temperatures in the absence of oxygen.

3.6.1. Methodology

Deposit or fuel samples were fixed on metal stubs by use of carbon tabs. The samples were then gold-plated and examined using a SEM. Using the SEM, the physical appearance of the deposit at a micro-scale was determined. Locations were then identified where EDX could be carried out to determine the chemical composition of the deposit.

Ten to thirteen readings were taken across two locations for each sample. An average of the readings obtained was then found and presented in terms of elemental weight percentages. Results from the deposit analysis are initially presented followed by results from the fuel analysis.

3.6.2. Deposit composition analysis

For the samples of deposits obtained from operational plants, a large spatial variance in elemental composition was observed. This is evident in Figure 3.9, which shows the elemental composition of the deposit at the 12 locations analysed for West Offaly power (WOP). It is clear from the analysis that several different compounds exist in the deposit tested, with areas of high calcium content visible in the first four locations analysed.

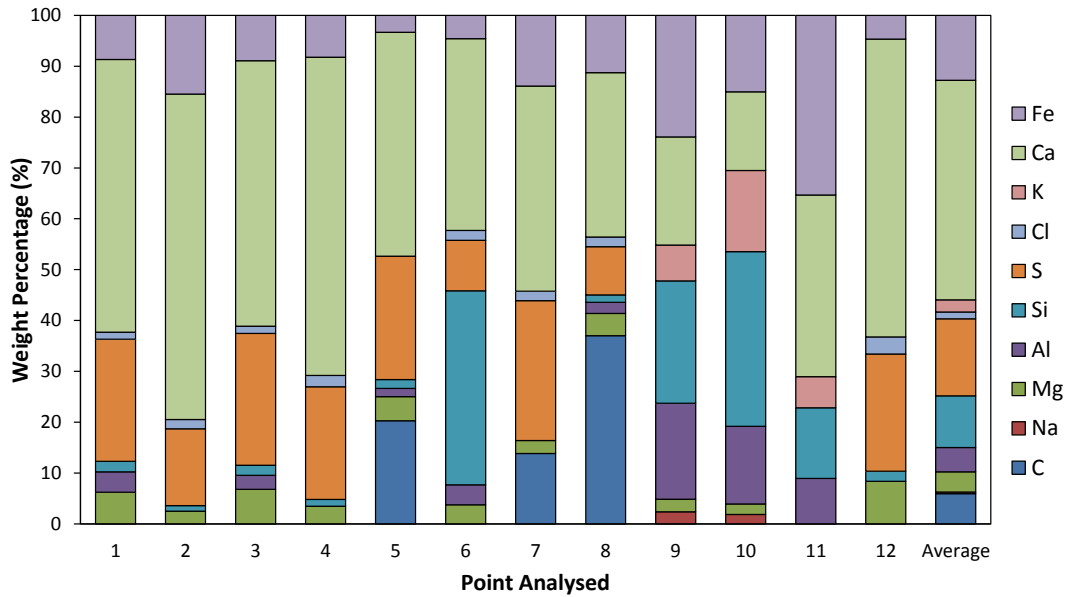


Figure 3.9: Graph showing the non-uniformity of the deposit composition identified at 12 points across a deposit sample for West Offaly power as shown in Figure 3.10.

Figure 3.10 displays the locations on the deposit samples which have been analysed from (a) WOP, (b) Edenderry power and (c) LRP. Points 1-4 analysed on Figure 3.10 (a) appear to be taken from a single large particle in the deposit. These points were found to contain high levels of calcium and sulphur, identifying it as a particle of calcium sulphate. The majority of the other points analysed do not have the appearance of a single particle, the composition obtained at these points could, therefore, be more representative of the deposit as a whole. The possible error in composition readings, could potentially be minimised by passing the deposit through sieves initially to ensure large particles are removed from the deposit. This would likely provide more homogeneous results.

The average deposit compositions from WOP, Edenderry and LRP are shown in Table 3.7. The elements of most interest for this work are Na, K, Cl and Br, as these are traditionally the elements which have the largest effect on the high temperature corrosion of heat exchanger tubes. The results are graphically compared in Figure 3.11, with error bars representing the standard deviation from the different locations analysed.

The variation in deposit composition formed from plants using just peat as a fuel source can be clearly seen from this figure as there is higher levels of Cl and Br found in the deposit from LRP compared with WOP. Higher levels of K and Na were

detected at WOP compared with LRP. Clearly displaying the difference in peat composition when obtained from different locations.

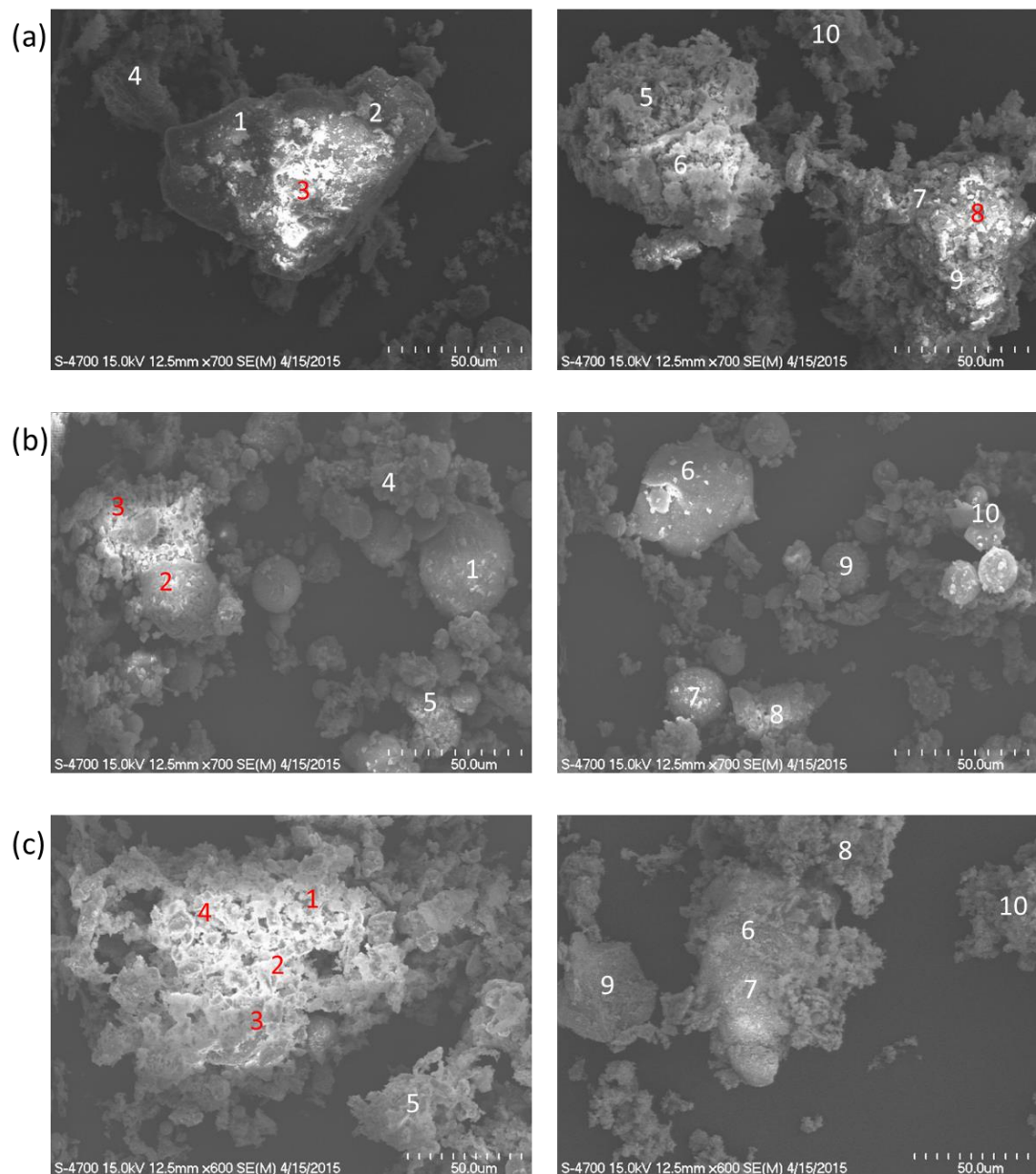


Figure 3.10: SEM images showing locations at which analysis of fuel was performed for (a) WOP, (b) Edenderry and (c) LRP.

When the deposits from LRP and WOP was compared with Edenderry, the effect of biomass is clearly evident, with higher levels of Cl, Br, Na and K all identified in Edenderry. This clearly shows the effect of co-firing in operational plants and the changes it causes to the composition of deposits formed. The deposit formed during co-firing contained elevated levels of elements which are known to cause the accelerated corrosion of heat exchanger tubes.

Table 3.7: Composition of deposits from three operational plants by mass percentage.

	WOP (Peat)	LRP (Peat)	Edenderry (Co-firing)
Ca	43.16	55.56	46.25
S	15.12	16.57	9.41
Si	10.18	4.18	15.28
Fe	12.77	9.57	8.56
K	2.43	0.12	8.92
Mg	3.94	4.84	2.83
Al	4.80	1.66	1.62
C	5.93	2.65	0.00
Cl	1.33	2.78	4.39
Na	0.35	0.04	1.23
Br	0.00	0.28	0.72
F	0.00	1.78	0.77

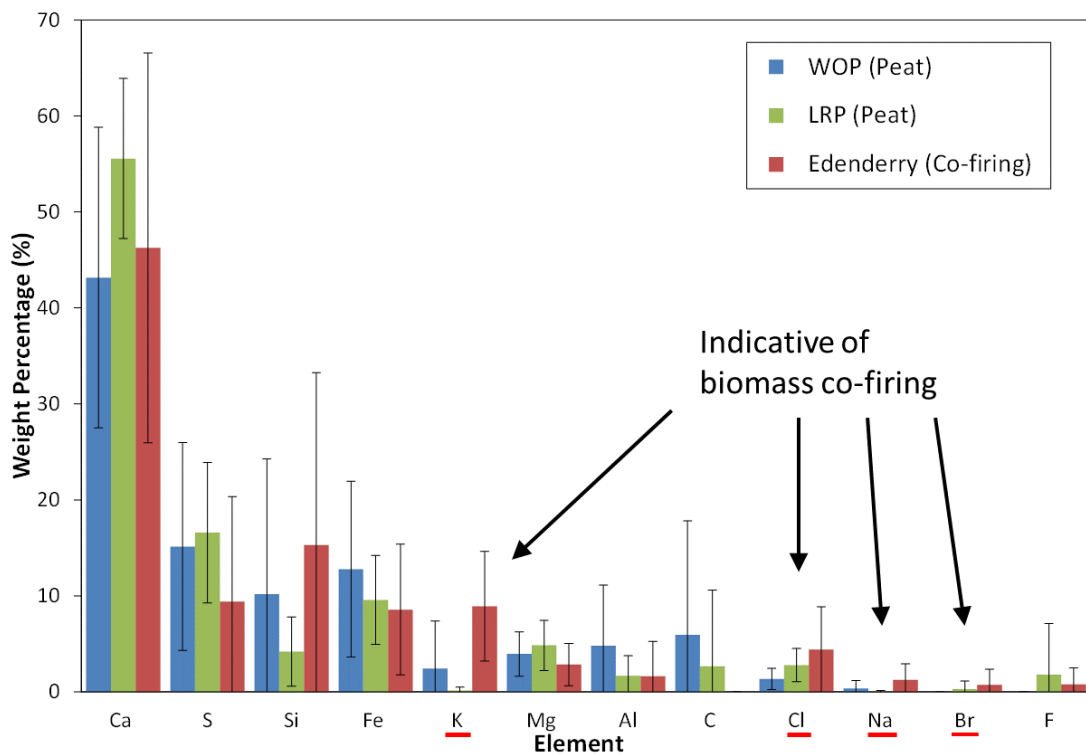


Figure 3.11: Graph comparing composition of samples of deposits obtained from three operational power plants.

3.6.3. Fuel composition analysis

This methodology was then expanded to test a selection of biomass fuels for chemical composition. It was found that for the fuel samples, in contrast to the deposits, the chemical composition was quite spatially uniform. This is evident in Figure 3.12, which shows the chemical composition obtained at each of the 13 points analysed for the olive stone fuel sample.

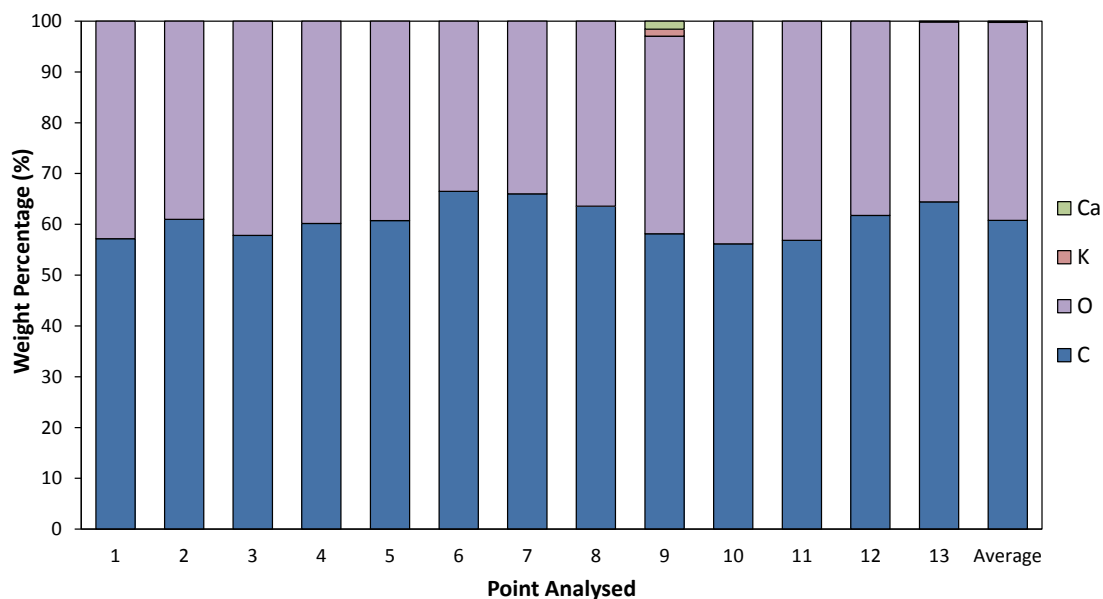


Figure 3.12: Graph showing the composition identified at 13 locations for olive stone.

Figure 3.13 shows SEM images of the fuel samples which were analysed. Figure 3.13 (a) shows the olive stone, Figure 3.13 (b) shows the torrefied olive stone, and Figure 3.13 (c) shows the torrefied wood sample. The locations at which the EDX analysis was carried out for each fuel sample is also shown for each image.

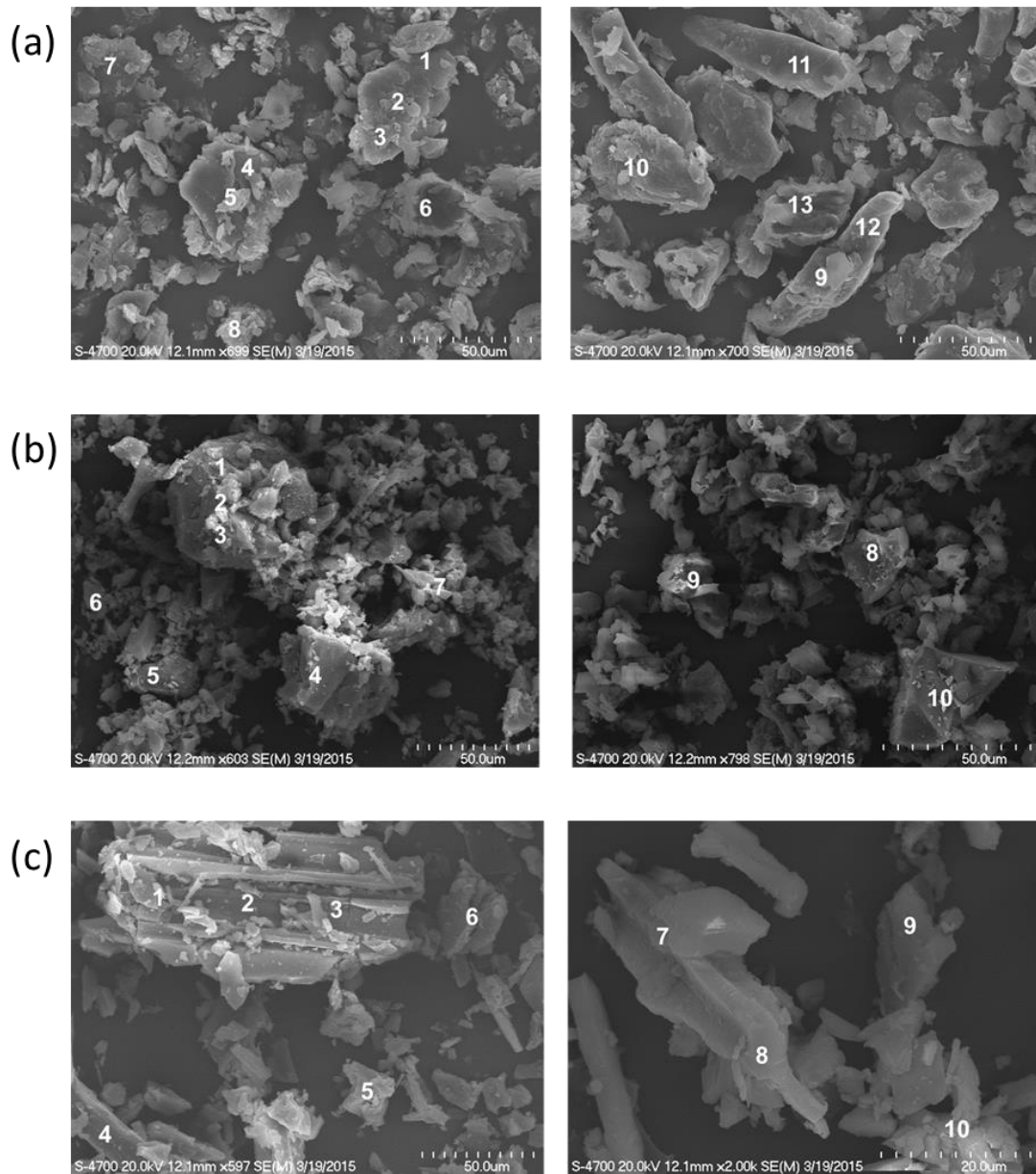


Figure 3.13: SEM images showing locations at which analysis of fuel was performed for (a) olive stone, (b) torrefied olive stone, and (c) torrefied wood.

The results of the analysis for the three fuels are shown in Table 3.8. The olive stone sample was found to consist predominantly of carbon (60.79%). Oxygen makes up 38.97% of the remaining composition, with trace amounts of K and Ca also found. A standard deviation of 3.50% for the C content was identified, with a standard deviation of 3.43% identified for O. The minimum carbon found at a point was 56.17%, while the maximum was found to be 66.48%.

80.72% of the torrefied olive stone consisted of carbon, with 17.97% consisting of oxygen. Additionally, potassium was found in the sample with 1.1% present and trace

amounts of Ca present. A standard deviation of 4.03% was identified for C and O in this sample again showing that the composition does not alter significantly from point to point. A maximum carbon content of 86.07% was identified at a single point with a minimum value of 73.69% identified.

The torrefied wood consisted of 72.29% carbon and 27.43% of oxygen. Trace amounts of Ca and Fe were identified and again the composition does not alter significantly from point to point. A standard deviation of 3.00% was found for C and 3.01% for O. A maximum carbon content of 76.10%, and a minimum carbon content of 67.00% was identified.

The O:C ratio for the three fuels analysed varied significantly. From these results the benefits of the torrefaction process are evident with the O:C ratio changing from 0.64 to 0.22 following the torrefaction of olive stone.

Table 3.8: Composition of three biomass fuels by mass percentage.

(wt.%)	Olive stone	Torrefied olive stone	Torrefied wood
C	60.79	80.72	72.29
O	38.97	17.97	27.43
K	0.12	1.19	0.15
Ca	0.12	0.12	0.12
O:C ratio	0.64	0.22	0.38

Figure 3.14 presents the weight percentages of the olive stone, torrefied olive stone and torrefied wood samples alongside one another for comparison. There is an increase of approximately 25% in the carbon content of the fuel when comparing the pure olive stone composition with that of the torrefied olive stone. This increase in carbon present in the torrefied olive stone is balanced by a decrease in the oxygen present. Torrefied wood was found to have a higher carbon content than olive stone, while having less carbon present than the torrefied olive stone sample. The benefits of the torrefaction process to the O:C ratio of biomass fuels is evident from these results.

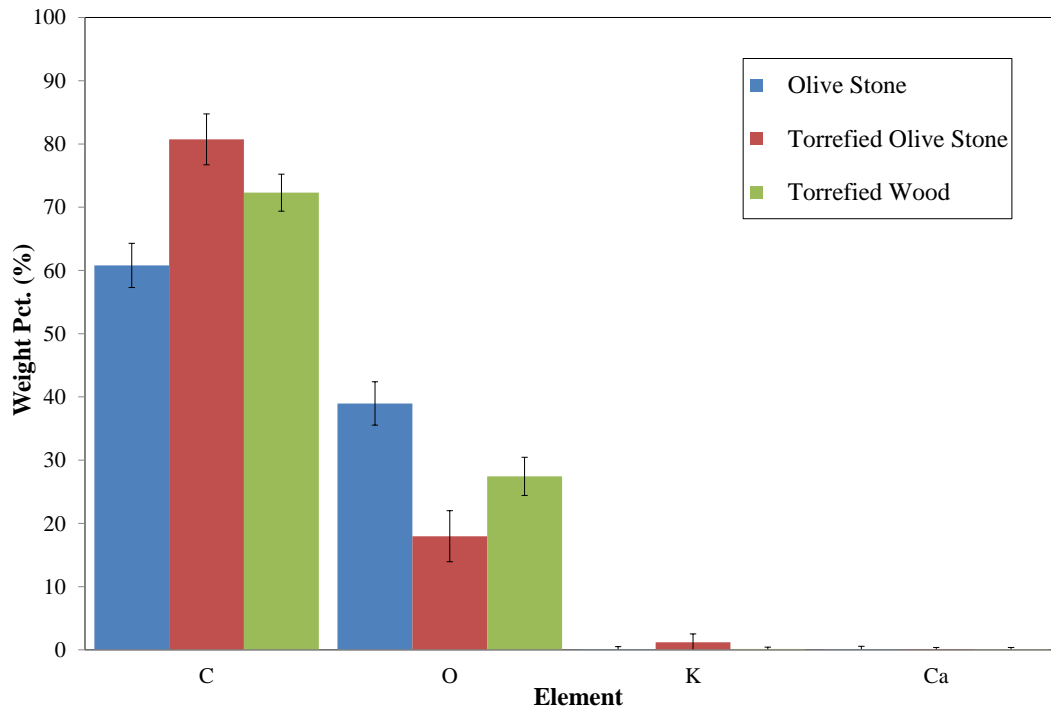


Figure 3.14: Graph comparing composition of three biomass fuels analysed.

3.6.4. Deposit and fuel composition characterisation conclusions

From the analysis of the deposit composition from the operational plants, the effect of co-firing biomass with peat is evident. Higher levels of Cl, Br, Na and K were all detected for the deposit sample which was produced when biomass was co-fired with peat. These are the elements which have been shown to have the greatest effect on the corrosion rate of materials when exposed to the active oxidation corrosion mechanism.

From the composition analysis of the biomass fuels the benefits of the torrefaction process are clear. There is a visible increase in the carbon content when samples have undergone torrefaction.

3.7. Summary

This chapter detailed the experimental programme which was completed during this research. The experimental methodology developed at NUI Galway to investigate the response of materials to deposits produced during biomass co-firing was presented. This method was utilised throughout the research presented.

The procedure used to produce synthetic salt, representative of deposits formed during co-firing was shown. The calculations carried out to determine the starting quantities of compounds used to produce synthetic salt were presented.

The test protocol that all samples underwent both pre and post exposure to the synthetic salt was detailed. The measurement techniques used during this research were presented and examples of samples analysed were shown. The operational theory of the analytical tools used during analysis of samples was detailed.

A test methodology to determine the elemental composition of deposit samples and biomass fuels was presented. From this analysis the effect of co-firing biomass on deposit composition was evident. Deposits from a co-firing plant contained higher levels of K, Cl, Na and Br, all of which are known to contribute to the accelerated corrosion of heat exchanger tubes in operational plants. Analysis of the biomass fuels highlighted the benefits of torrefaction for biomass as an energy source. Torrefied samples were found to contain lower O:C ratio, which relates to a higher HHV.

4. Porosity-Based Corrosion Model

4.1. Introduction

This chapter presents the development of a novel physics-based model to describe accelerated corrosion due to alkali halide-containing deposits, which form on superheater tube walls during biomass co-firing. Synthetic salt A, which represents a 70:30 peat-biomass mix, as described in Chapter 3 has been applied to pure iron samples in air at 540 °C and 600 °C. The corrosion layers were examined using SEM, optical microscopy and EDX elemental mapping to provide insight into the material degradation and structure of the corrosion layer.

Two distinct types of oxide formed on the iron substrate. Initially, a compact, uniform oxide layer formed over the substrate. As the process continued, this oxide layer degraded, leading to spalling which resulted in broken oxide pieces mixing with the salt layer. Additional test samples were examined without deposits as controls to highlight the accelerated rate of corrosion.

Two modelling techniques were examined; the previously-used labyrinth factor method (LFM) and the newly developed porosity-based corrosion method (PCM). The PCM method uses measurements of porosity and pore radius, coupled with a physically-based corrosion mechanism, to predict corrosion rates. Results from the two modelling techniques were compared and both agree with experimental measurements for times of up to 28 days.

These models are based on the assumption that corrosion proceeds via the active oxidation mechanism as discussed in Chapter 2. The chemical reactions which occur during active oxidation are reproduced here as reactions R4-1 to R4-5 [47,51,60,85,155,156]. These correspond directly to reactions R2-1 to R2-5 in Chapter 2. The model also assumes that the rate limiting step of the active oxidation process is the outward diffusion of $\text{FeCl}_2(\text{g})$ as shown in previous work [51].



The PCM is envisioned to be used as a pre-screening method to predict the corrosion depth on superheater tube materials for long term, high temperature tests. It is not expected to eliminate the need for long-term experimental and in-situ testing. The experiments described in Chapter 3 were carried out to gain greater understanding of the corrosion process and for use in the calibration and validation of the models. A number of models have been developed in previous work to determine the growth of corrosion layers on metals [51,53,159] .

The focus of this chapter was on validation of the PCM. For this reason, experiments were performed using pure iron, not materials found in operational plants. Section 4.2 discusses the two modelling methods used and detail the development of the PCM method. Results obtained from the experiments and the modelling are then discussed and compared in Section 4.3, leading to the conclusions in Section 4.4.

4.2. Modelling

Two models are presented for the accelerated corrosion due to alkali halide-containing deposits and active oxidation. These are (1) the previously-used labyrinth factor method (LFM), and (2) the newly-developed porosity-based corrosion method (PCM). The models are compared with each other and with experimental results. A schematic of the corrosion process being modelled is shown in Figure 4.1.

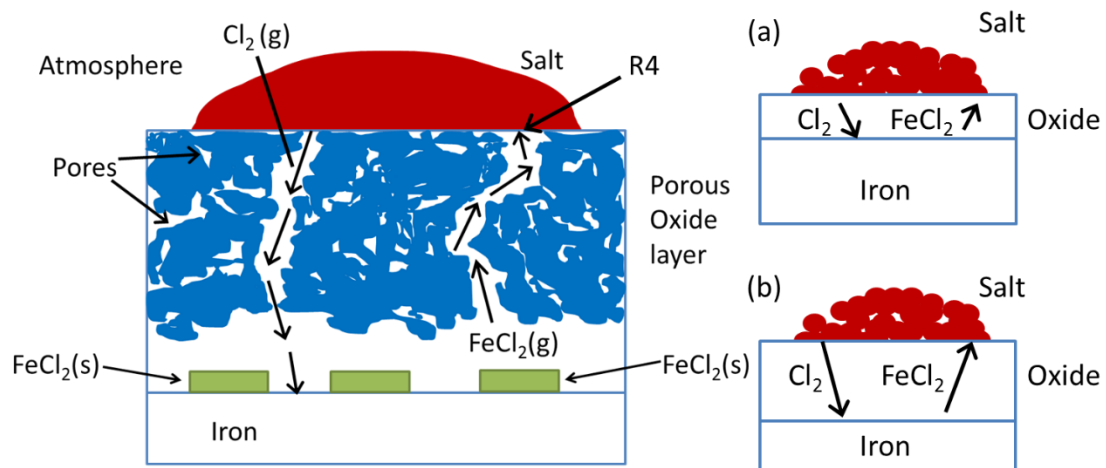


Figure 4.1: Schematic of corrosion process being modelled in which (a) shows the model at an early stage with a small oxide layer and (b) shows a sample following longer term exposure with an oxide layer which has grown thicker and consumed more of the substrate.

This image displays the salt layer resting on top of a porous oxide layer. Cl_2 is released and travels through the oxide until it reaches the iron. Once there, it reacts to form $\text{FeCl}_2(\text{s})$ which then diffuses outwards as $\text{FeCl}_2(\text{g})$. The model assumes a single, porous protective layer of oxide, which continues to grow with time as shown by the growth between (a) and (b). Oxide layer growth is due to (1) degradation of the iron substrate and (2) the lower density of Fe_2O_3 deposited in the oxide layer.

This is a simplification of the plant process, which will in actuality involve the formation and subsequent breakaway from the substrate of multiple layers of oxides, and the deposition of Fe_2O_3 via reaction R4-3 inside the porous oxide layer as opposed to solely on its surface. Deposition of Fe_2O_3 inside the oxide layer leads to retardation of the outward diffusion rate of FeCl_2 by blocking pores [51].

The assumption of deposition of Fe_2O_3 solely on the surface of the porous oxide layer and not within it, gives an upper limit estimate of rate of increase of corrosion depth, therefore providing a conservative estimate of substrate performance. Given this assumption, there is no net flux of O_2 in the porous oxide layer, so it can be modelled as a component of the stationary background gas mixture.

Assuming the rate controlling step of the corrosion process to be the outward diffusion of FeCl_2 gas through the porous oxide layer, as discussed in Chapter 2, Fick's first law forms the basis for the model of the corrosion rate, as follows:

$$J_A = -D_{Eff,A} \frac{dC_A}{dz} \quad (4-1)$$

where J_A is the flux of species A, $D_{Eff,A}$ is the effective diffusion coefficient of A through the porous oxide layer, C_A is the concentration of species A in the gaseous mix and z is the depth into the substrate. The difference between the two models presented, the LFM and PCM is in the calculation of $D_{Eff,A}$, as will be shown in the sections describing the models.

All chemical reactions are assumed to be in chemical equilibrium since they proceed rapidly compared to the diffusion of $FeCl_2$. Therefore, chemical reaction kinetics are neglected. The concentration of species A in the mixture is the driving force for the diffusion rate in this expression. This is related to pressure via the ideal gas law which results in the following expression:

$$J_A = -\frac{D_{Eff,A}}{R_A T} \frac{dP_A}{dz} \quad (4-2)$$

where R_A is the specific gas constant of species A and T is the temperature. In this study, species A is identified as $FeCl_2$. R_{FeCl_2} is the specific gas constant for $FeCl_2$ and is calculated via the following:

$$R_{FeCl_2} = \frac{\mathfrak{R}}{M_{FeCl_2}} \quad (4-3)$$

where \mathfrak{R} is the universal gas constant and M_{FeCl_2} is the molecular weight of $FeCl_2$. $FeCl_2$ partial pressure varies as it diffuses out through the oxide layer and reaches higher concentrations of O_2 . Once it reaches a sufficiently high concentration of O_2 , reaction R4-3 occurs and the $FeCl_2$ converts to Fe_2O_3 , with Cl_2 being released to repeat the process. For this model, temperature-dependent partial pressures are obtained at the metal-oxide interface via calculation of the $FeCl_2$ (g) vapor pressure from reaction R4-2. The partial pressure at the oxide scale surface has previously been found to be negligible [51,159].

By integrating Equation 4-2 through the oxide layer thickness (l_{ox}) and assuming all variables are uniform except P_A , which has been identified as P_{FeCl_2} , the following expression is obtained:

$$J_{FeCl_2} = \left(\frac{D_{Eff, FeCl_2}}{l_{Ox} R_{FeCl_2} T} \right) (p_{i, FeCl_2} - p_{s, FeCl_2}) \quad (4-4)$$

where p_{FeCl_2} is the partial pressure of the $FeCl_2$ gas with (*i*) and (*s*) designating the interface of substrate and oxide, (*i*), and the surface of the oxide, (*s*), respectively. This results in an expression similar to those obtained by Grabke et al. [51] and Stott & Shih [159]. There will potentially be secondary gaseous components, e.g. O_2 and Cl_2 , present in the system.

The constants identified from experimental data are detailed in the results section. Figure 4.2 shows the definitions of key variables used in the model in schematic form and on an SEM image. Experimental samples were polished to a 3 μm diamond paste finish. This provided a good surface finish, while also retaining the visibility of the pores in the oxide scales.

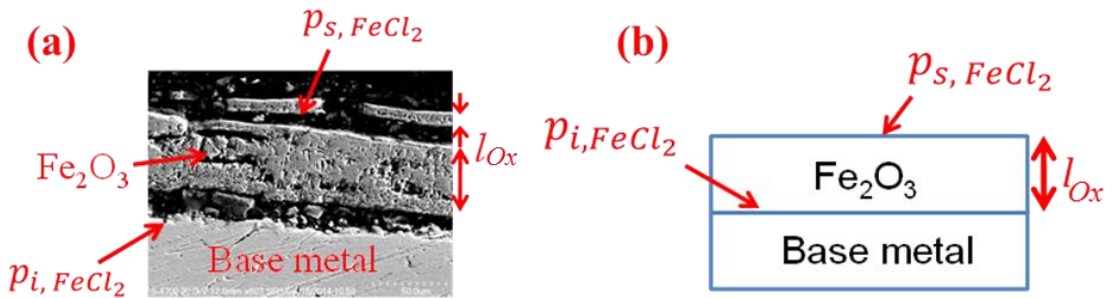


Figure 4.2: Definitions of key variables used in oxide depth calculations on (a) SEM image and (b) and idealised physical model.

From mass conservation the following expression for the amount of iron consumed is obtained:

$$\frac{dl_{Fe}}{dt} = \frac{J_{Fe}}{\rho_{Fe}} \quad (4-5)$$

where l_{Fe} is the depth of the iron which is converted to iron oxide in the sample and ρ_{Fe} is the density of iron. Assuming that all Fe leaves the system as $FeCl_2$, the rate of flux of iron can be related to the flux of iron chloride via the ratio of their respective molecular weights, as follows:

$$J_{Fe} = \frac{M_{Fe}}{M_{FeCl_2}} J_{FeCl_2} \quad (4-6)$$

where M_{Fe} and M_{FeCl_2} are the molecular weights of Fe and $FeCl_2$ respectively. From Equations 4-4 to 4-6, an expression is obtained for the depth of iron which is converted to oxide with respect to time, as follows:

$$\frac{dl_{Fe}}{dt} = \frac{D_{Eff, FeCl_2} M_{Fe} p_{i, FeCl_2}}{M_{FeCl_2} \rho_{Fe} R_{FeCl_2} T l_{Ox}} \quad (4-7)$$

The depth of iron converted to oxide, l_{Fe} must then be related to the depth of oxide formed l_{Ox} . In order to do this it is assumed that for every 2 moles of Fe removed from the substrate 1 mole of Fe_2O_3 is deposited in the oxide layer, from reactions R4-1 and R4-3. The amount of moles of Fe are hence related to the number of moles of oxide, as follows:

$$\frac{dN_{Fe}}{dt} = -2 \frac{dN_{Fe_2O_3}}{dt} \quad (4-8)$$

where N_{Fe} is the number of moles of iron consumed and $N_{Fe_2O_3}$ is the number of moles of oxide produced. This is then related to the mass of the iron consumed and oxide produced via molecular weights, as follows:

$$\frac{1}{M_{Fe}} \frac{dm_{Fe}}{dt} = \frac{-2}{M_{Fe_2O_3}} \frac{m_{Fe_2O_3}}{dt} \quad (4-9)$$

where m_{Fe} is the mass of the iron consumed, $m_{Fe_2O_3}$ is the mass of oxide produced and $M_{Fe_2O_3}$ is the molecular weight of Fe_2O_3 . By relating the volume and density of both the iron consumed and the oxide produced an expression linking the depth of iron with the depth of oxide is produced, as follows:

$$\frac{dl_{Fe}}{dt} = -2 \frac{M_{Fe}}{M_{Fe_2O_3}} \frac{\rho_{Fe_2O_3}}{\rho_{Fe}} \frac{dl_{Ox}}{dt} \quad (4-10)$$

where $\rho_{Fe_2O_3}$ is the bulk density of Fe_2O_3 . The porous nature of the oxide layer which is formed must also be taken into account. The bulk density of porous iron oxide, $\rho_{Fe_2O_3,b}$, can be obtained from the measured porosity and the following expression:

$$\rho_{Fe_2O_3,b} = \rho_{Fe_2O_3} (1 - \varepsilon) \quad (4-11)$$

Then by combining Equation 4-10 and Equation 4-11 the following expression is obtained:

$$\frac{dl_{Fe}}{dt} = -2 \frac{M_{Fe}}{M_{Fe_2O_3}} \frac{\rho_{Fe_2O_3,b}}{\rho_{Fe}} \frac{dl_{Ox}}{dt} \quad (4-12)$$

From the combination of Equation 4-12 with Equation 4-7, an expression for the growth of the oxide layer with time is obtained as follows:

$$\frac{dl_{Ox}}{dt} = \frac{1}{2\rho_{Fe_2O_3,b}} \frac{M_{Fe_2O_3}}{M_{FeCl_2}} \frac{D_{Eff,FeCl_2} p_{i,FeCl_2}}{R_{FeCl_2} T l_{Ox}} \quad (4-13)$$

Following integration an equation for the evolution of the oxide layer depth, l_{Ox} , is obtained, as follows:

$$l_{Ox} = \sqrt{\frac{1}{\rho_{Fe_2O_3,b}} \frac{M_{Fe_2O_3}}{M_{FeCl_2}} \frac{D_{Eff,FeCl_2} p_{i,FeCl_2}}{R_{FeCl_2} T} t} \quad (4-14)$$

where t is time in seconds. The values of the variables and constants used in the calculations are shown in Table 4.1.

Table 4.1: List of variables and constants used in equations.

$M_{Fe_2O_3}$ (g/mol)	159.69	
M_{FeCl_2} (g/mol)	126.751	
M_{O_2} (g/mol)	31.999	
M_{N_2} (g/mol)	28.014	
M_{Cl_2} (g/mol)	70.906	
T (K)	813	873
$p_{i,FeCl_2}$ (Pa)	20.2	133.2
$\rho_{Fe_2O_3}$ (kg/m ³)	5240	
R (J/molK)	8.314	
p (atm)	1	

The difference in methods of dealing with $D_{Eff,FeCl_2}$ is the distinction between the LFM and PCM models. The LFM, which has been used in previous work [51,159,203], does not explicitly calculate $D_{Eff,FeCl_2}$. Instead, it fits a curve to experimental data, and is optimised using least squares. With sufficient data points, the LFM can be used to extrapolate corrosion depth for well-characterised experimental conditions. In order to have reliable predictive capability for a given set of experimental conditions, 7 – 28 days of test data are typically required.

The PCM uses simplified but physically-based modelling to predict $D_{Eff,FeCl_2}$ evolution over time. Determining the duration of test data required for the PCM is one of the objectives of this chapter. The LFM and PCM methods are described in detail in the next sections. Both models assume that the corrosion depth increases uniformly based on the experimental observations.

4.2.1. Labyrinth Factor Method (LFM)

In this method $D_{Eff,FeCl_2}$ is calculated by combining the molecular diffusivity of a diffusing gas through a quiescent mixture of background gases ($D_{FeCl_2,M}$) with a labyrinth factor (λ) as follows:

$$D_{Eff,FeCl_2} = \lambda D_{FeCl_2,M} \quad (4-15)$$

The labyrinth factor accounts for the porosity and tortuosity of the oxide layer and is determined using experimental data [51,159]. The molecular diffusivity through a gaseous mixture, $D_{FeCl_2,M}$, is modelled assuming the background gas is a stationary mixture of N₂ and O₂ in a fixed molar ratio of 79:21 according to the following [204]:

$$\frac{1 - x_{FeCl_2}}{D_{FeCl_2,M}} = \sum_{\substack{j=1 \\ j \neq FeCl_2}}^n \frac{x_j}{D_{FeCl_2,j}} \quad (4-16)$$

where x is mole fraction, n is the number of gaseous species, and $D_{FeCl_2,j}$ is the molecular diffusivity of FeCl₂ through stationary gas j .

The addition of up to 1% (by mole) Cl₂ to the background gas is found to have negligible effect on diffusion properties. O₂ is modelled as being a stationary component under the previously-stated assumption that no Fe₂O₃ deposition, and hence O₂ consumption, occurs inside the porous oxide layer. The values for $D_{FeCl_2,j}$ are calculated using the Chapman-Enskog equation [159,205], as follows and assuming suitable values for the collision diameter, $\sigma_{FeCl_2,j}$ of the gases:

$$D_{FeCl_2,j} = 1.86 \times 10^{-7} T^{\frac{3}{2}} \frac{\left(\frac{1}{M_{FeCl_2}} + \frac{1}{M_j} \right)^{\frac{1}{2}}}{p \sigma_{FeCl_2,j}^2 \Omega_{FeCl_2,j}} \quad (4-17)$$

where $D_{FeCl_2,j}$ is the diffusivity of FeCl₂ through background gas j in m²/sec, M_{FeCl_2} and M_j are the molecular weights of FeCl₂ and background gas j , respectively, p is pressure, $\sigma_{FeCl_2,j}$ is the mean collision diameter of FeCl₂ and background gas j and $\Omega_{FeCl_2,j}$ is the temperature dependent collision integral for FeCl₂ and background gas j at temperature T . The values of the variables used in the Chapman-Enskog equation are shown in Table 4.2.

Table 4.2: List of variables for use in Chapman-Enskog formula.

$\sigma_{FeCl_2}(\text{\AA})$	$\sigma_{N_2}(\text{\AA})$	$\sigma_{O_2}(\text{\AA})$	$\sigma_{Cl_2}(\text{\AA})$	Ω_{FeCl_2,N_2}	Ω_{FeCl_2,O_2}	Ω_{FeCl_2,Cl_2}
3.5	3.798	3.468	4.217	1.1	1.12	1.225

Predictions from the Chapman-Enskog kinetic theory are limited due to the requirement for estimates of the collision diameters and collision integrals. Such estimates are not available for all gases [205]. $\sigma_{FeCl_2,j}$ is the arithmetic average of the values for the two species present, which are tabulated for certain gases [205]. Values of the dimensionless quantity Ω are generally of the order 1 and its calculation depends on an integration of the interaction between two species, which is described by the Lennard-Jones 12-6 potential [205]. Values for iron chloride gas are not yet available, so values are assumed in a manner similar to Stott and Shih [159] and given in Table 4.2.

The labyrinth factor is determined following the analysis of experimental results and optimised using a least squares objective function for a power law, as follows:

$$a = \exp \left(\frac{\sum_{i=1}^n \ln l_i - 0.5 \sum_{i=1}^n \ln t_i}{n} \right) \quad (4-18)$$

where $l = a\sqrt{t}$ in order to accurately describe the square root function as shown in Equation 4-14, n is the number of sample experimental points to be used for the least squares fit. From the combination of $l = a\sqrt{t}$, Equation 4-14 and Equation 4-15 for $D_{Eff,FeCl_2}$ an equation for the labyrinth factor λ is obtained as follows:

$$\lambda = a^2 \left(\frac{M_{FeCl_2} \rho_{Fe_2O_3} R_{FeCl_2} T}{D_{FeCl_2M} M_{Fe_2O_3} P_{i,FeCl_2}} \right) \quad (4-19)$$

Provided there is sufficient experimental data available, the LFM can be used to make predictions for longer exposure times.

4.2.2. Porosity-based Corrosion Method (PCM)

The porosity-based corrosion method (PCM) adopts a physics-based approach to determine values for $D_{Eff,FeCl_2}$, as follows [206,207]:

$$D_{Eff,FeCl_2} = \frac{\varepsilon}{\tau} \left(\frac{1}{D_{FeCl_2,M}} + \frac{1}{D_{K,FeCl_2}} \right)^{-1} \quad (4-20)$$

In this method $D_{Eff,FeCl_2}$ is calculated by combining molecular diffusivity $D_{FeCl_2,M}$ with Knudsen diffusivity $D_{K,FeCl_2}$, the porosity of the oxide layer, ε , found from testing, and τ , the tortuosity of the porous oxide. τ has previously been identified as $1/\varepsilon$ in work by Bhatia and Perlmutter [208] and Smith [207], which provides the following:

$$D_{Eff,FeCl_2} = \varepsilon^2 \left(\frac{1}{D_{FeCl_2,M}} + \frac{1}{D_{K,FeCl_2}} \right)^{-1} \quad (4-21)$$

This model contains contributions from both bulk (molecular) and pore (Knudsen) diffusion to the rate of mass transport through the oxide layer. This allows the PCM to predict the relative contributions of Knudsen and molecular diffusion based on pore characteristics and other measured and calculated variables. For example, for large pore radii, molecular diffusion is predicted to dominate. This would occur as the porosity term tends towards 1 and the $D_{K,FeCl_2}$ value tends towards ∞ (as \bar{r} increases in size), due to cracks forming in the oxide. Knudsen diffusivity is calculated as follows:

$$D_{K,FeCl_2} = 97\bar{r} \left(\frac{T}{M_{FeCl_2}} \right)^{0.5} \quad (4-22)$$

where \bar{r} is the average pore radius in m and $D_{K,FeCl_2}$ is the Knudsen diffusivity in units of m^2/s . $D_{Eff,FeCl_2}$ is then calculated as shown in Equation 4-21 [206].

The oxide layer depth predictions are obtained from Equation 4-14. It is proposed here to determine the value of ε from experimental results. As previously stated, the exact duration required for these experiments is examined in this work. Potential future development of the PCM could involve prediction of ε , so that the need for

experimental characterisation will be further reduced. SEM images are obtained from the samples which have been exposed to the synthetic salt. From these samples an oxide layer is identified. The image is processed as seen in Figure 4.3 (a) using OLYMPUS Stream Motion [197] image analysis software to obtain the total area of the oxide layer on the sample (A_{Total}).

The image is converted to binary via a colour contrast analysis, as shown in Figure 4.3 (b). The pores in the oxide layer can thus be clearly identified and analysed. The area of each individual black and white section in the image is thus quantified and the cumulative area of the pores in the sample (A_{pores}) is obtained. The porosity of the oxide layer is the ratio of the area of the pores to the total area of the oxide, i.e.

$$\varepsilon = \frac{A_{Pores}}{A_{Total}} \quad (4-23)$$

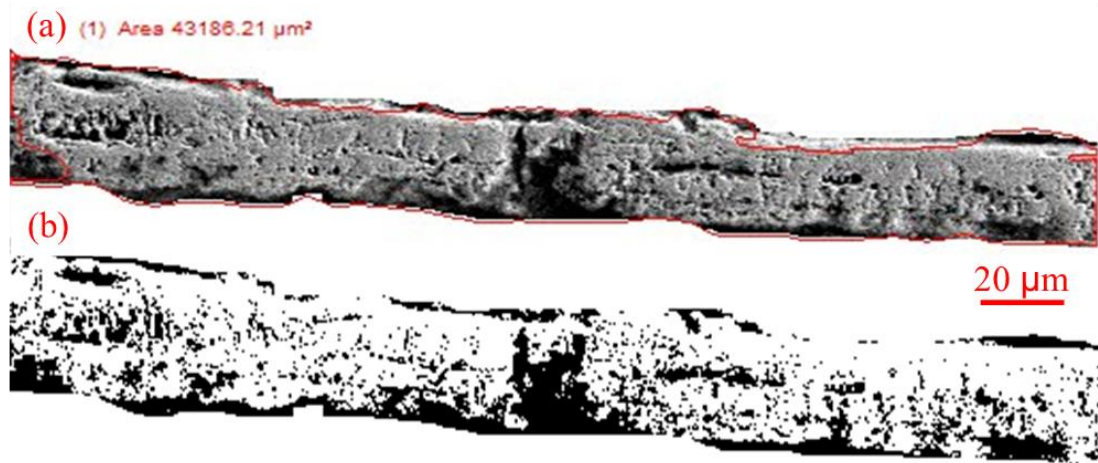


Figure 4.3: Images of a representative porous oxide layer, showing the area used to calculate porosity values (a) SEM image (b) binary version of image.

The Olympus Stream software also provides measurements for the mean radius of the pores detected in the oxide layer. The software obtains measurements for pore radii via the following technique [197]:

- 1) The centre of gravity of each pore is determined.
- 2) Lines are plotted through the centre of gravity at 1° circumferential increments and intercept points with the outer edge of the pore are determined.

3) A local diameter of the pore outer edge is then determined for each circumferential increment. The diameter is defined as the distance between the two intercept points with the outer edges.

4) From this a maximum, minimum and a mean diameter is calculated for that pore.

From these measurements the average pore radius \bar{r} of each pore is obtained and used to determine an overall average pore radius for the sample.

4.3. Results and Discussion

4.3.1. Experimental – 540 °C

This section presents results from the experiments carried out on samples exposed to synthetic salt A at 540 °C for times of 1, 4, 7, 14, 21 and 28 days. SEM results and optical microscopy results are analysed and the mechanism observed is discussed. The experimental methodology followed is detailed in Chapter 3.

Figure 4.4 shows SEM images of the specimen cross section area (see Chapter 3) for exposure times of 1 to 28 days at 540 °C. After 1 day, a cupola (dome of oxide) has formed over a section of the iron (Figure 4.4 (a)). This cupola is formed by evaporating iron chloride and its shape corresponds to that of the stagnant diffusion boundary layer of FeCl₂ entering the bulk gas phase above the sample as described by Zahs et al.[85]. A porous oxide layer has also begun to form on the surface of the sample substrate.

The sample exposed for 4 days shows a cupola, which has completely detached from the substrate and porous oxide layer (Figure 4.4 (b)). A uniform oxide layer has now formed over the substrate and is separated from the substrate. Following 7 days exposure a large void space has appeared below the cupola (Figure 4.4 (c)) and there is evidence of portions of oxide below the cupola, although they appear to have further deteriorated. This breakdown of the protective oxide scale is similar to that discussed by Jonsson et al. [185], which describes an accelerated attack that occurs following breakdown of the initial protective oxide layer.

Examination of the sample exposed for 14 days in Figure 4.4 (d) appears to show uncorroded iron separated from the substrate. This is also seen following examination

of the sample following 21 days exposure. A section of uncorroded iron can be seen detaching from the substrate in Figure 4.4 (e). This undermining of uncorroded iron is of interest and the mechanism behind this process requires further investigation.

Figure 4.4 (f) shows a sample exposed for 28 days. A uniform compact oxide layer has formed over the substrate. This oxide is detached from the substrate and does not provide protection against further attack. Portions of oxide have also mixed with the salt particles. Enestam et al. [47] have defined the uniform compact oxide layer as Type 1 oxide and the porous oxide which is “sprawled around and between salt particles” as Type 2 oxide.

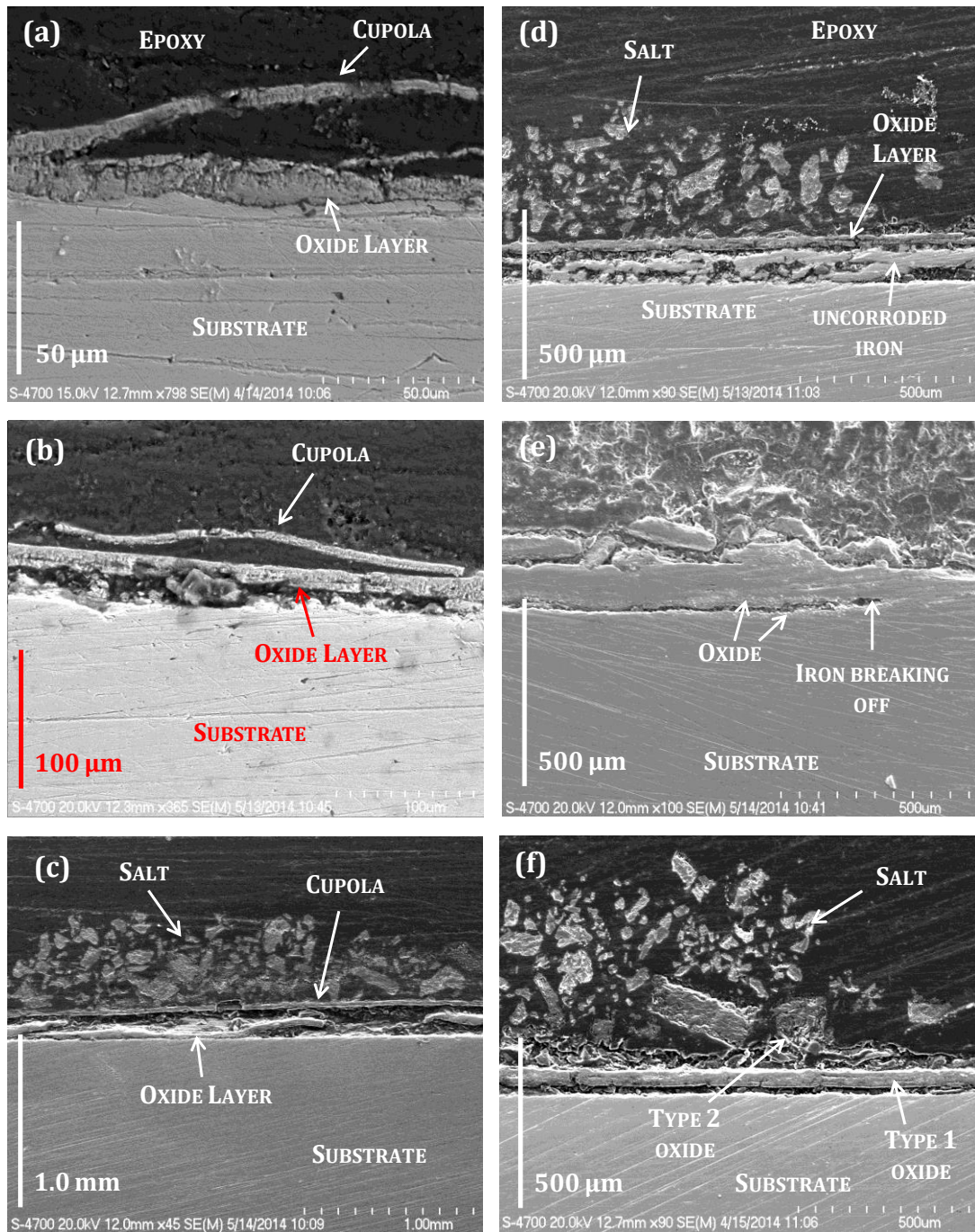


Figure 4.4: SEM images of iron after exposure to synthetic salt A at 540 °C for (a) 1 day; (b) 4 days; (c) 7 days; (d) 14 days; (e) 21 days; (f) 28 days.

Figure 4.5 (a) shows an image of the sample exposed for 28 days at a higher magnification than Figure 4.4 (f). The Type 2 oxide can be seen amongst the salt layer. The uniform Type 1 oxide layer can also be seen as well as the void space between the Type 1 oxide and the substrate.

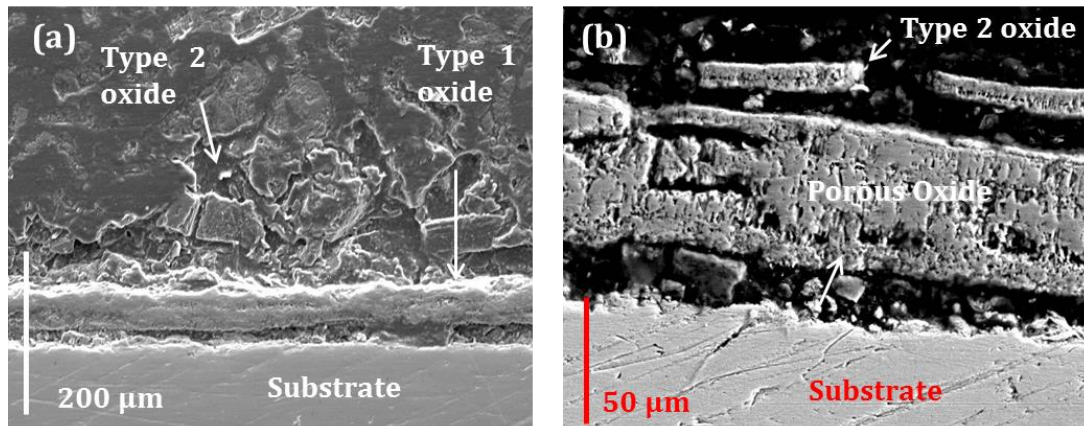


Figure 4.5: SEM image of iron after exposure to salt A at 540 °C for 28 days at (a) 200 μm; (b) 50 μm magnification.

The formation of Type 2 oxide may have occurred following the deterioration of the previous thinner cupolas and porous oxide layers to such an extent that they fragment and mix with the salt layer in a manner similar to spalling. Spalling occurs in corrosion when the substrate sheds particles of corrosion product. The postulation of Type 2 oxide forming from severe deterioration of Type 1 oxide is supported by the fact that these thinner cupolas and oxide layers, which are visible in samples exposed for shorter time periods, can no longer be seen in the longer term tests.

Figure 4.5 (b) shows a further magnified view of the same 28 day sample shown in Figure 4.5 (a). This image reveals the porosity of Type 1 oxide at this stage. A thin broken oxide layer can also be seen above the Type 1 oxide. This is not visible at lower magnification and may be a residue of a previous Type 1 oxide layer. This layer has almost fully broken up and mixed with the salt layer, forming Type 2 oxide.

An optical microscope image is shown for the sample exposed for 21 days in Figure 4.6 under dark light. This image shows uncorroded iron on the top portion, which has separated from the substrate. The bottom portion, closer to the substrate, has been oxidised. This indicates a two-stage mechanism whereby uncorroded iron is undermined by a thin oxide layer before subsequently oxidising. As the iron is subjected to oxidation from two sides, the corrosion rate is expected to increase.

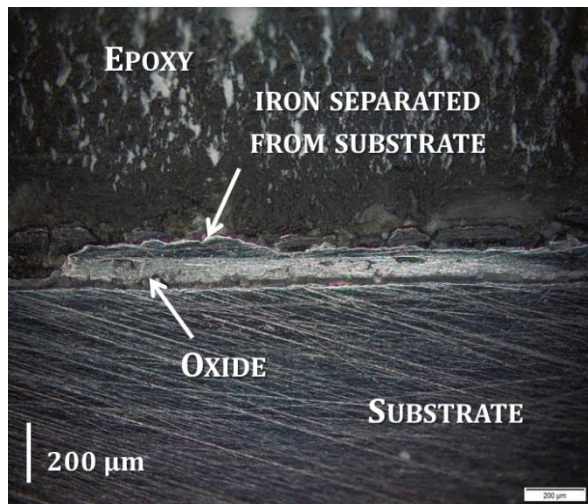


Figure 4.6: Optical microscope image of iron exposed to salt A for 21 days at 540 °C under dark light.

As will be illustrated in Figure 4.7, the chemical composition of the substrate consists of pure iron. The oxide layers consist of both iron and oxygen, uncorroded iron has been shown to consist of pure iron with oxygen present along the edges of the portions which have separated from the substrate.

EDX elemental maps of the cross sectional areas have been obtained to determine the chemical composition of a section of the samples. Maps are presented for samples which were exposed for 14 and 28 days. Figure 4.7 shows the 14 day sample analysed and the corresponding element maps of Fe, O, Ca and S; from this image a uniform, compact, porous oxide layer is visible. A portion of uncorroded iron which has almost fully separated from the substrate is also visible.

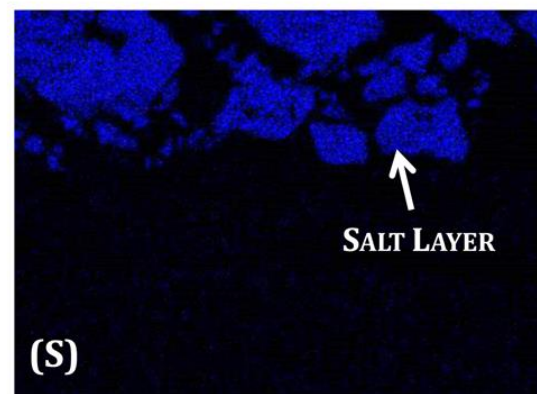
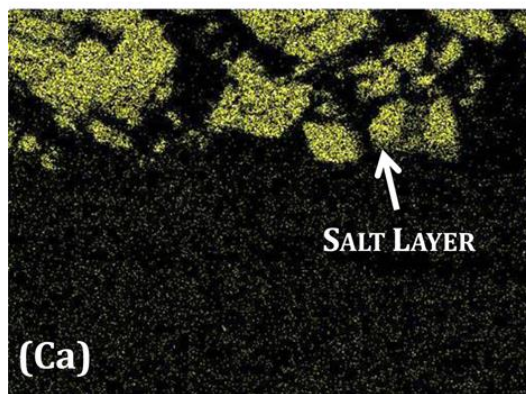
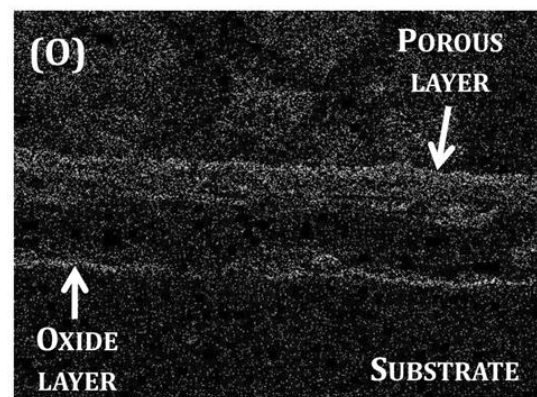
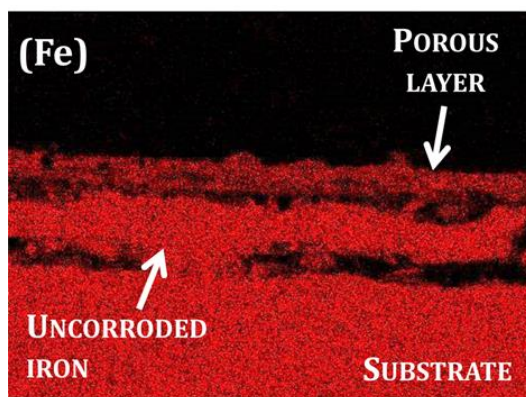
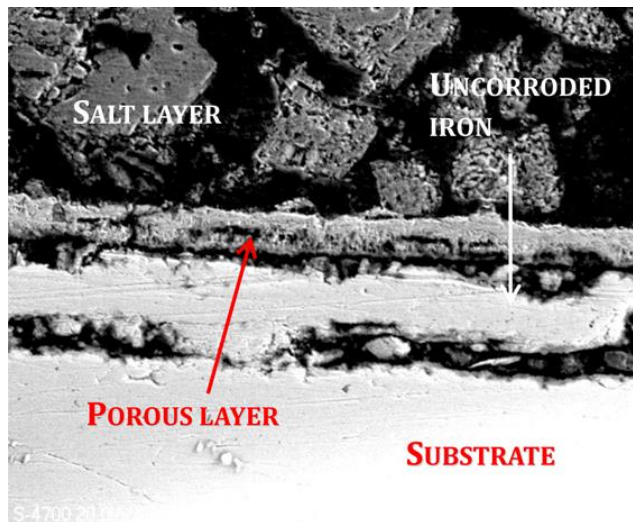


Figure 4.7: SEM image and EDX element maps of the sample following exposure to salt A for 14 days at 540 °C .

The concentration of iron in the porous oxide layer is less than that of the uncorroded iron which has detached from the substrate. The separation between the different layers can be seen in the image. There is no evidence of Type 2 oxide in this image. A layer of oxygen is visible on top of the substrate and on the porous oxide layer with no oxygen present in the uncorroded metal, which has separated from the substrate. Calcium and sulphur are also shown to be present in the salt layer, as expected.

The uncorroded metal, which has detached from the substrate, contains no oxygen except at its edges, confirming that it is not yet fully part of the oxide layer, but is being oxidised from two sides. A layer of oxygen also exists on top of the substrate indicating that the oxidation process has begun at this location.

It is noted that other elements are present, however they do not produce informative maps for a number of reasons. These include low concentrations of the elements, resulting in background elements becoming dominant. Also in the case of Cl_2 , the high volatility of FeCl_2 in the vacuum of the SEM chamber may result in its evaporation.

The 28 day sample analysed using EDX and corresponding elemental maps of Fe, O, Ca and S are shown in Figure 4.8. Both Type 1 and Type 2 oxides are present in this image. A clear void space also exists in this image showing the separation of the oxides from the substrate. Type 1 oxide can be seen in the form of a compact uniform layer over the substrate. Type 2 oxide debris can also be seen mixed with the salt layer in the epoxy.

A layer of oxygen is visible at the top of the substrate and along the entire Type 1 oxide layer. There does not appear to be any uncorroded metal separated from the substrate. Uncorroded metal which had separated may have been fully oxidised following the 28 days exposure. Again the presence of calcium and sulphur in the salt can be seen.

Comparison of the 14 and 28 day results shows the evolution of the corrosion process. After 14 days no Type 2 oxide is present, a porous Type 1 oxide layer is present with a layer of uncorroded iron detached from the substrate beneath it. This uncorroded iron has begun to oxidise from two sides. After 28 days Type 2 oxide is present and there appears to be no uncorroded iron separated from the substrate; there is however a thick porous oxide Type 1 oxide layer.

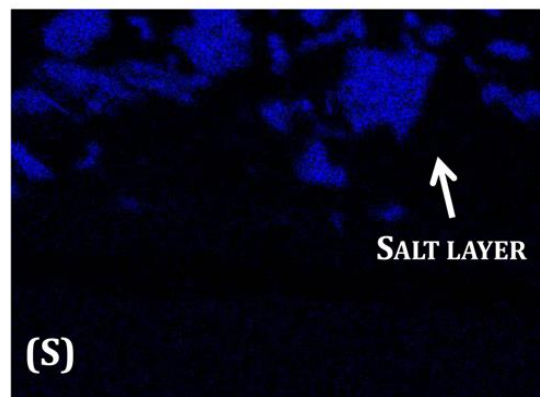
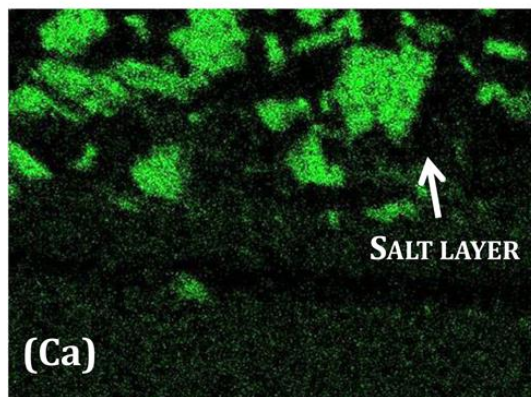
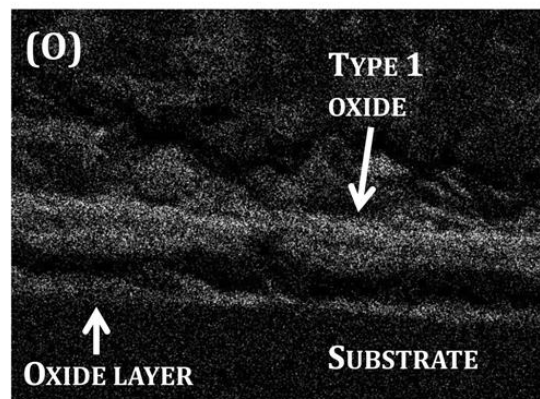
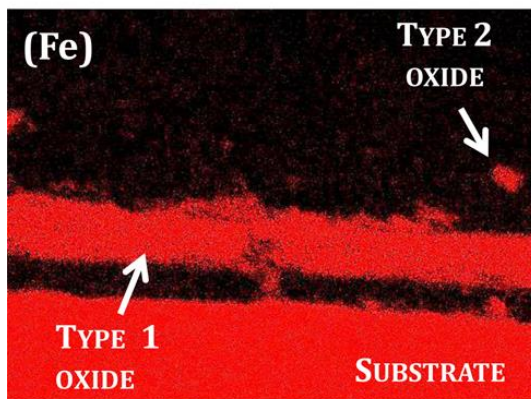
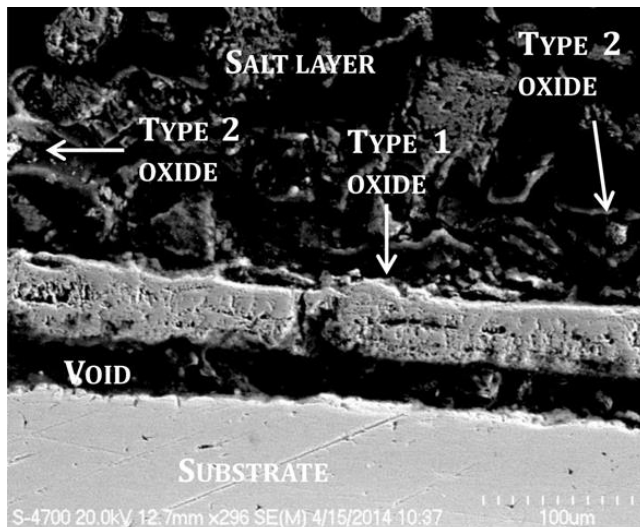


Figure 4.8: SEM image and EDX element maps of the sample following exposure to salt A for 28 days at 540 °C.

Based on observations, the corrosion process is proposed to proceed via the following stages:

1. Initial corrosion of fresh substrate, forming a closely adherent Type 1 oxide layer on substrate surface with a cupola forming over this.
2. Detachment of the oxide layer from the substrate.

3. Fragmentation of the detached layers of oxide leading to formation of Type 2 oxide.
4. Undermining of uncorroded iron, which detaches from substrate
5. Oxidation of detached iron from two sides leading to formation of a new uniform type 1 oxide layer with oxide also forming on substrate surface
6. Detachment of this new oxide formed on substrate surface and fragmentation of the detached layers of oxide leading to formation of Type 2 oxide.

The iron corroded with no salt coverage was also analysed using optical microscopy. A sample of images from these tests are shown in Figure 4.5. After 1 day an initial thin, 11 μm uniform oxide layer has formed on the substrate surface. The sample exposed for 4 days displays a thicker oxide layer, which is still in contact with the substrate, as can be seen in Figure 4.5 (a). This is different to the sample with salt, where the oxide layer is detached from the substrate after 4 days.

Following 7 days of exposure (Figure 4.5 (b)), the porous oxide layer, which has grown in thickness to approximately 28 μm , has begun to detach from the substrate with a void visible between the substrate and oxide. However compared to the sample with salt, which has a thickness of approximately 84 μm (after 7 days), the severity of corrosion is significantly less.

The 14-day, no-salt sample showed clear detachment of the oxide layer from the substrate. After 21 days (Figure 4.5 (c)), this oxide layer has split into two layers which are no longer considered protective. After 28 days (Figure 4.5 (d)), the oxide layer has detached significantly and fresh substrate is again exposed to the atmosphere.

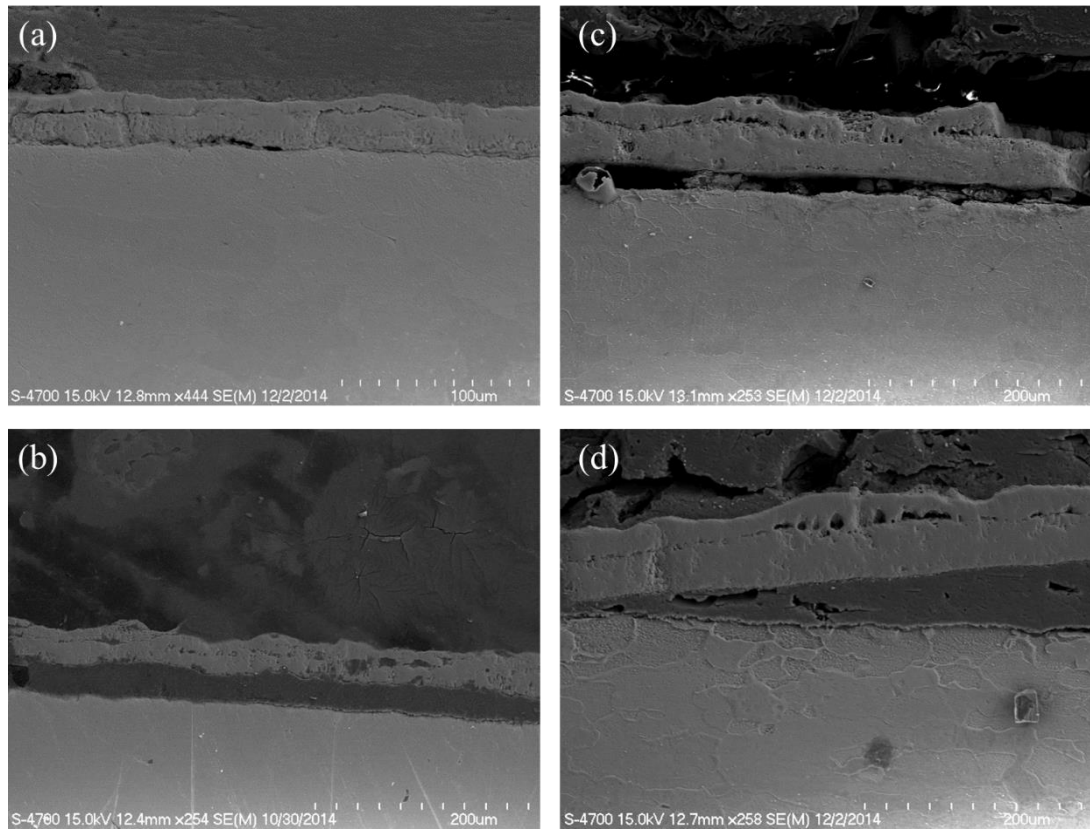


Figure 4.9 SEM images of iron after exposure to no salt at 540 °C for (a) 4 days; (b) 7 days; (c) 21 days; (d) 28 days.

The evolution of corrosion depths was measured using the method previously described in Chapter 3, with between 15 and 20 sample measurements taken across the specimen width. Measurements of corrosion depths are shown in Figure 4.10 for samples with and without the synthetic salt. Of specific interest here is the effect of salt-induced corrosion compared to without salt. Information of the corrosion depth is critical for calibration of the LFM and for validation of both models.

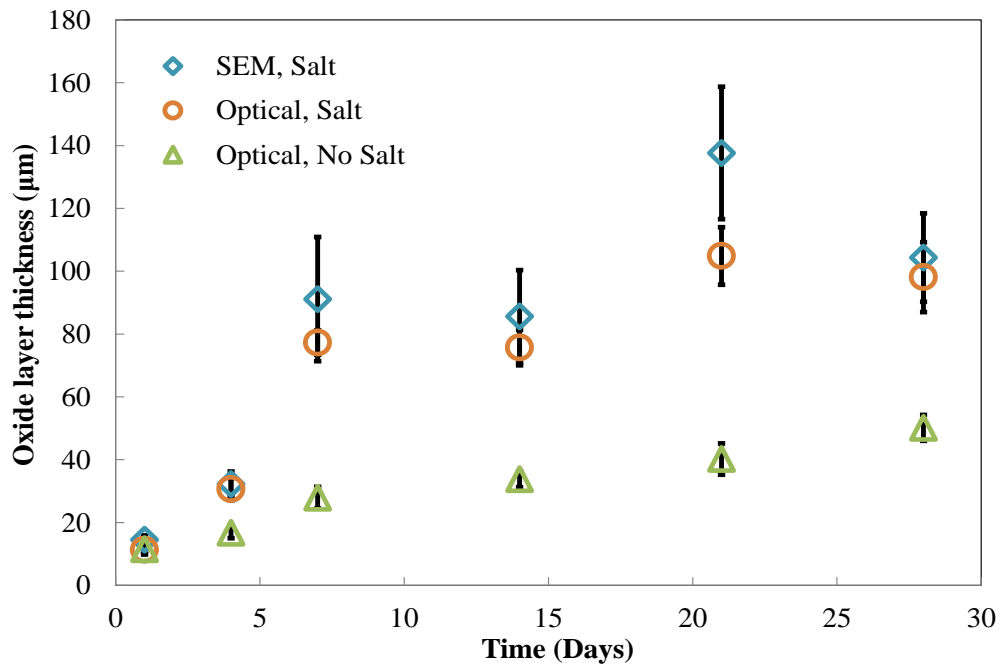


Figure 4.10: Thickness of the oxide layer under optical and SEM with salt A applied and with no salt applied at 540 °C. Uncertainty bars represent a \pm standard deviation.

It was difficult to obtain accurate measurements for samples exposed to the salt for tests beyond seven days due to oxide fragmentation and mixture with the salt. The apparent decrease in corrosion depth seen in Figure 4.10 after 28 days is attributed to this fragmentation process. The SEM provides more detailed information regarding the corrosion layer structure, due to its superior image quality. Pores can be identified from these images if examined at a high enough magnification and therefore these images were used to obtain the porosity data for use in the PCM.

The detrimental effect of the salt on the corrosion rate is clear from Figure 4.10. The samples without salt applied are subject to pure oxidation and display a significantly lower corrosion rate than the samples with synthetic salt at the same conditions. This highlights the accelerated corrosion process due to alkali halide containing deposits and the need to develop a greater understanding of it.

4.3.2. Experimental – 600 °C

Figure 4.11 shows SEM images of the specimen cross section area (see Chapter 3) exposed to salt A for exposure times of 1 to 28 days at 600 °C. As the corrosion mechanisms observed are similar to those found at 540 °C, the analysis of these samples is not as in depth as in the previous section. Again detachment of the oxide from the substrate is visible following just 1 days exposure. There is evidence of cupolas forming on the oxide surface indicating the active oxidation process. Additionally there is visible deterioration of the oxide scale solidity as samples were exposed for longer periods.

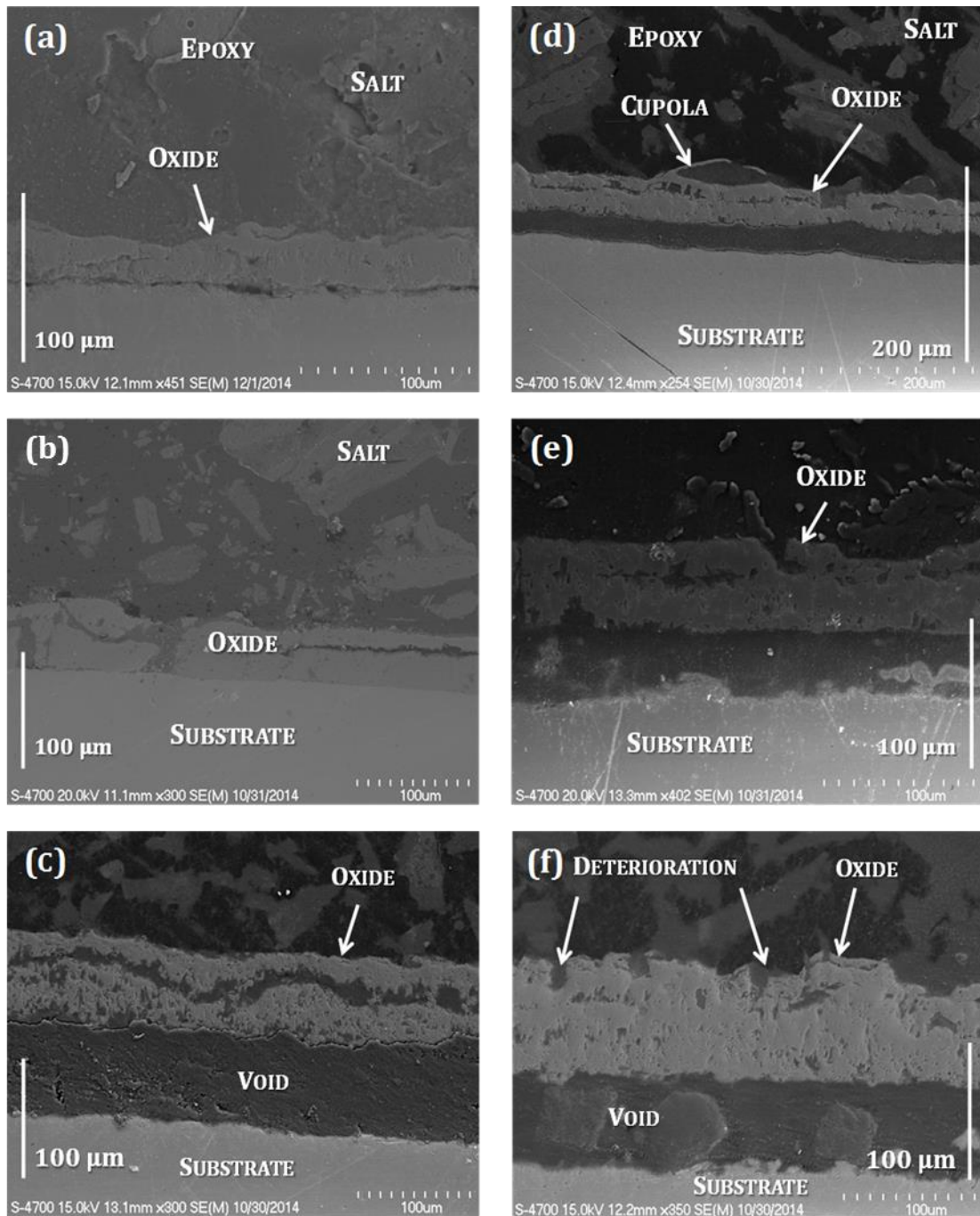


Figure 4.11: SEM images of iron after exposure to salt A at 600 °C for (a) 1 day; (b) 4 days; (c) 7 days; (d) 14 days; (e) 21 days; (f) 28 days.

Figure 4.12 shows EDX elemental maps of samples exposed to salt A at 600 °C for 7 days. Maps of Fe, O, Ca and S are presented which clearly display the oxide region which has formed detached from the substrate surface.

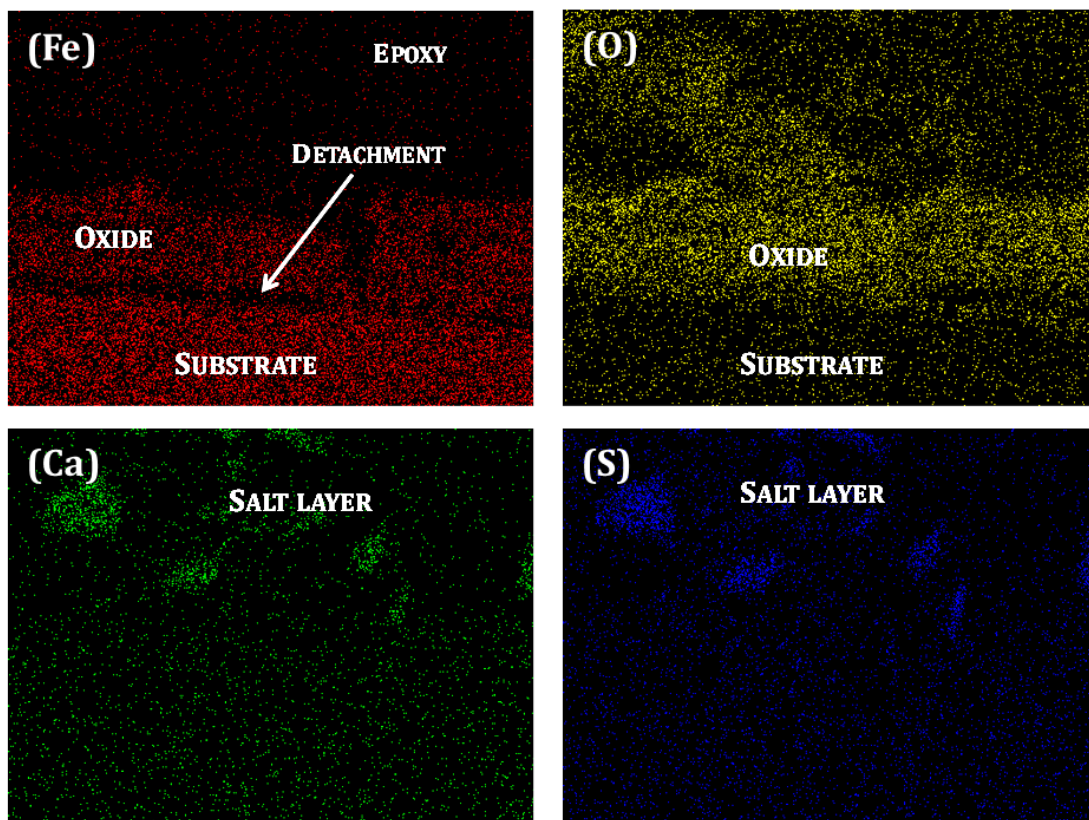
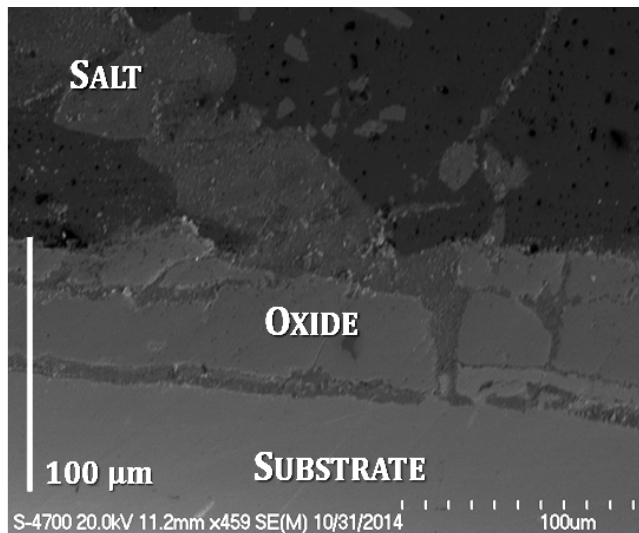


Figure 4.12: SEM image and EDX element maps of the sample following exposure to salt A for 7 days at 600 °C.

4.3.3. Modelling – Labyrinth Factor Method (LFM)

The corrosion depths from the optical microscopy have been used in the least squares fit identification process to obtain the labyrinth factor λ and the corrosion coefficient a for the LFM model; as tabulated in Table 4.3. In order to evaluate the extrapolation capability of the LFM, values for a and λ have been obtained for $n=1$ (1 day), $n=2$ (1,

4 days), $n=3$ (1 to 7 days), $n=4$ (1 to 14 days), $n=5$ (1 to 21 days) and $n=6$ (1 to 28 days).

Table 4.3: Calibrated values of a and λ using least squares fit to experimental data.

n	1 (1 Day)	2 (1 to 4 Days)	3 (1 to 7 Days)	4 (1 to 14 Days)	5 (1 to 21 Days)	6 (1 to 28 Days)
a	2.311×10^{-6}	2.689×10^{-6}	3.507×10^{-6}	3.653×10^{-6}	3.837×10^{-6}	3.829×10^{-6}
λ	2.52×10^{-4}	3.41×10^{-4}	5.81×10^{-4}	6.30×10^{-4}	6.95×10^{-4}	6.92×10^{-4}

Note: For each case all data points up to and including exposure time for that case are included in the least squares fit

The values for a and λ shown in Table 4.3 have been plotted on Figure 4.13. As can be seen the values begin to converge after $n=3$ (1 to 7 days), with the difference being negligible for cases using data after days 21 to 28. Previous work has suggested that data from up to 7 days testing is appropriate for reproducible, relevant information regarding the corrosion tendency of steels [49] and the results shown in Figure 4.13 corroborate this.

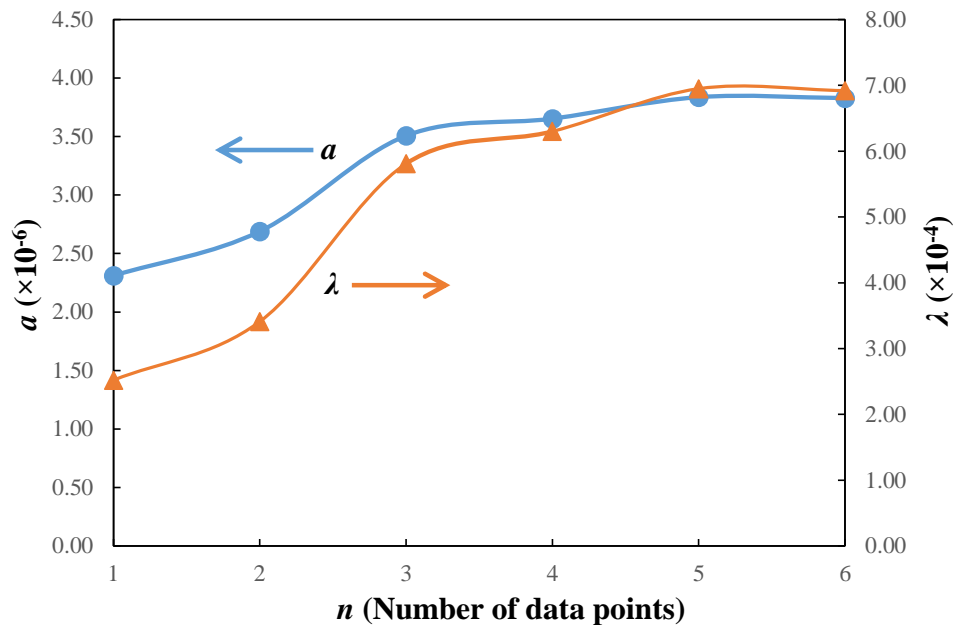


Figure 4.13 Graph showing convergence of a and λ with increasing data points

Figure 4.14 shows the predicted LFM corrosion depth measurements for the values of a and λ identified in Table 4.3, along with the measured experimental data. It is clear that there is sensitivity to the number of days of test data used (n) to fit the data. There appears however to be convergence for $n \geq 5$ (1-21 and 1-28 days), indicating the duration of test data required to calibrate the LFM. It is noted that for models such as the LFM, which use measurements of samples that may contain Type 2 oxide, which is difficult to measure at longer exposure times, an underestimation of the corrosion rate is possible.

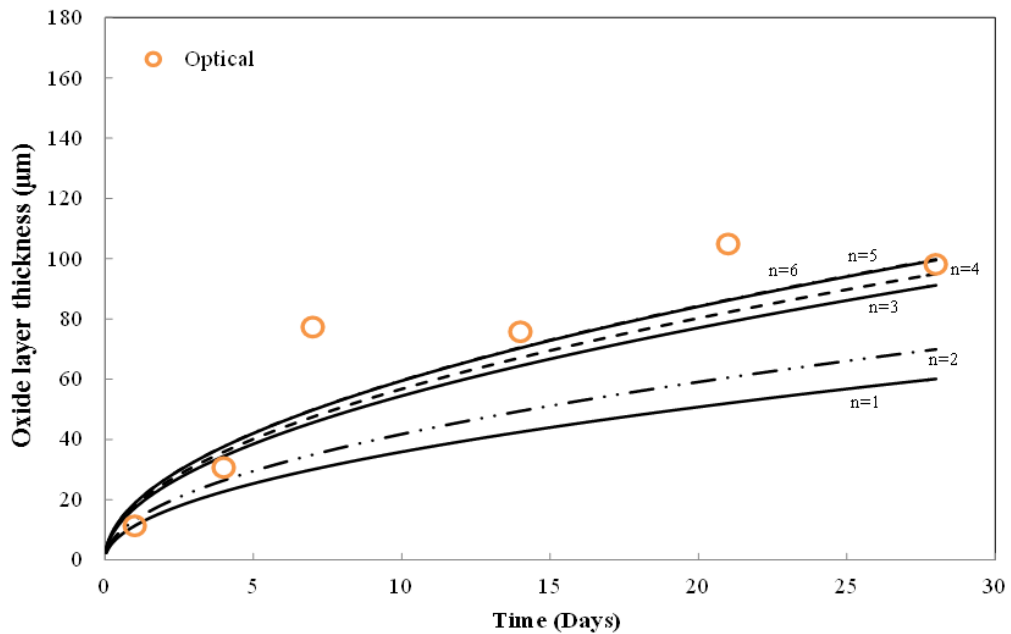


Figure 4.14 Results obtained for LFM method using experimental (optical microscopy) data from 1, 4, 7, 14, 21 & 28 days exposed to salt A at 540 °C and the least squares method

4.3.4. Modelling – Porosity Based Corrosion Model (PCM)

Values of porosity ε and average pore radius \bar{r} of the oxide layer for use in the PCM method have been identified for 6 different exposure times, 1 day only, 4 days only, 7 days only etc. as shown in Table 4.4. These results provide an insight into the evolution of the oxide layer, as shown in Table 4.4. The porosity level is seen to remain relatively constant with respect to exposure time. In contrast, the average pore radius in the sample increases at an almost linear rate. Potential future development of the PCM

could incorporate a theoretical approach for the void/pore growth to obtain values of ε and \bar{r} . This would further reduce the need for experimental characterisation.

Table 4.4: Measured values of porosity ε and average pore radius \bar{r} for different exposure times at 540 °C.

	1 Day	4 Days	7 Days	14 Days	21 Days	28 Days
ε	0.052	0.046	0.060	0.054	0.060	0.058
\bar{r} (μm)	0.341	0.542	0.992	1.124	1.626	2.143

Figure 4.15 shows the change in porosity and pore radius when examined for the test samples exposed for increasing time periods. The porosity remains relatively constant, with the pore radius increasing at an almost linear rate. Using this experimental data and the least squares technique, an equation for pore growth over time can be obtained. In order to further investigate the growth of pore radius with respect to the exposure time, a histogram showing the percentage occurrence of a range of pore radii in the oxide is shown in Figure 4.16.

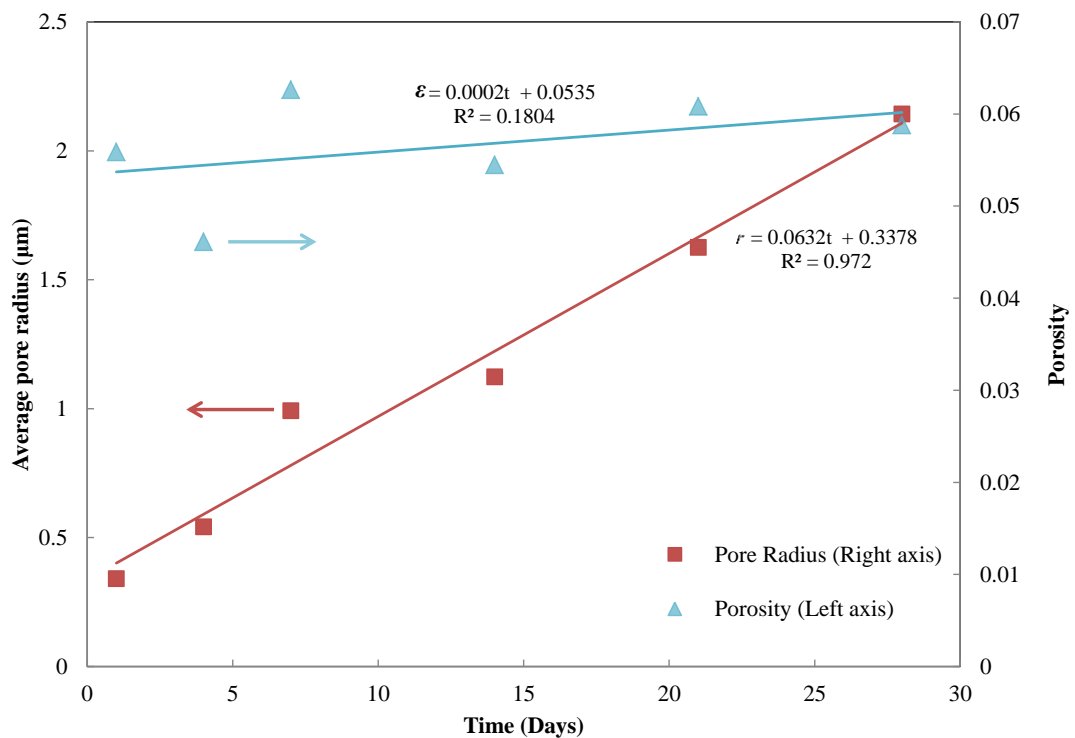


Figure 4.15: Measured evaluations of porosity and average pore radius at 540 °C.

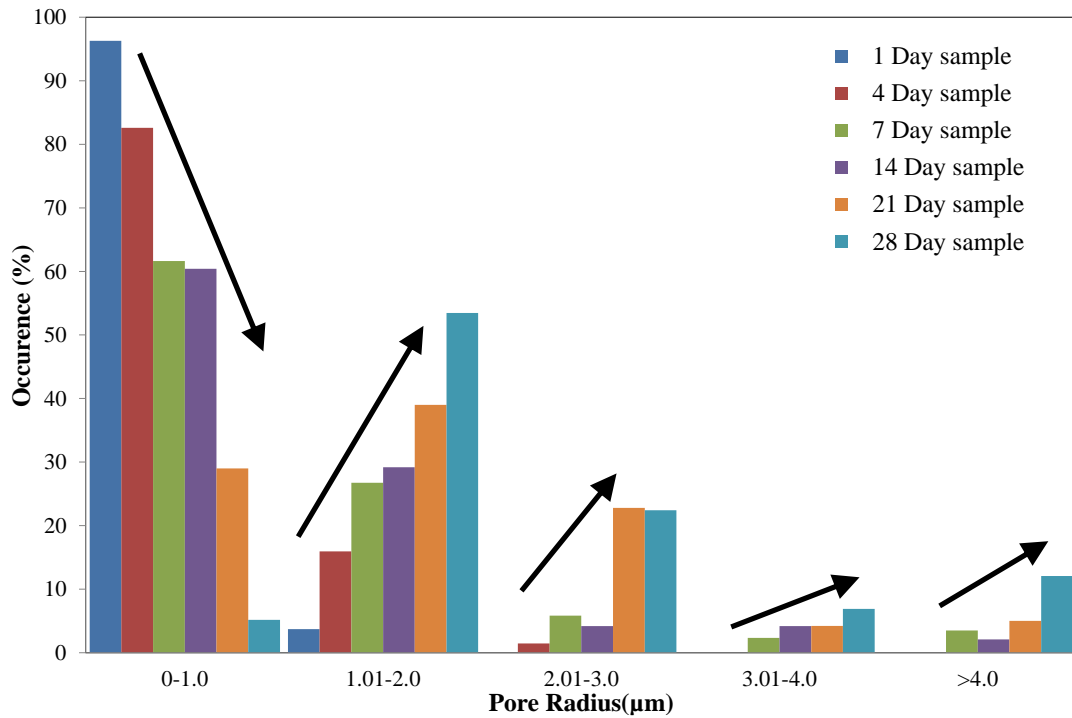


Figure 4.16: Percentage occurrence of pore size ranges in samples after different exposure times at 540 °C.

The vast majority, of pores (> 95%), following 1 day of exposure, are less than 1 µm in radius, with the remaining 5% being in the range of 1 to 2.0 µm. The longer term tests show a continuous trend towards a greater average pore radius. Less than 10% of pores in the sample exposed for 28 days are found to be less than 1 µm in radius with approximately 25% being between 2 to 3 µm and 12% being greater than 4 µm in radius. It appears that as smaller pores grow they coalesce to form larger pores. The porosity remains relatively constant despite this coalescence due to the increasing thickness of the layer, resulting in a larger overall oxide area.

The percentage contributions from the molecular and Knudsen diffusion on the overall effective diffusion has been investigated for varying pore radii, from examination of Equation 4-21. It is expected that as the pore radius increases the influence of molecular diffusion should grow and become dominant at some point. This is shown to occur in pores which have a radius larger than 0.25 µm as shown in Figure 4.17.

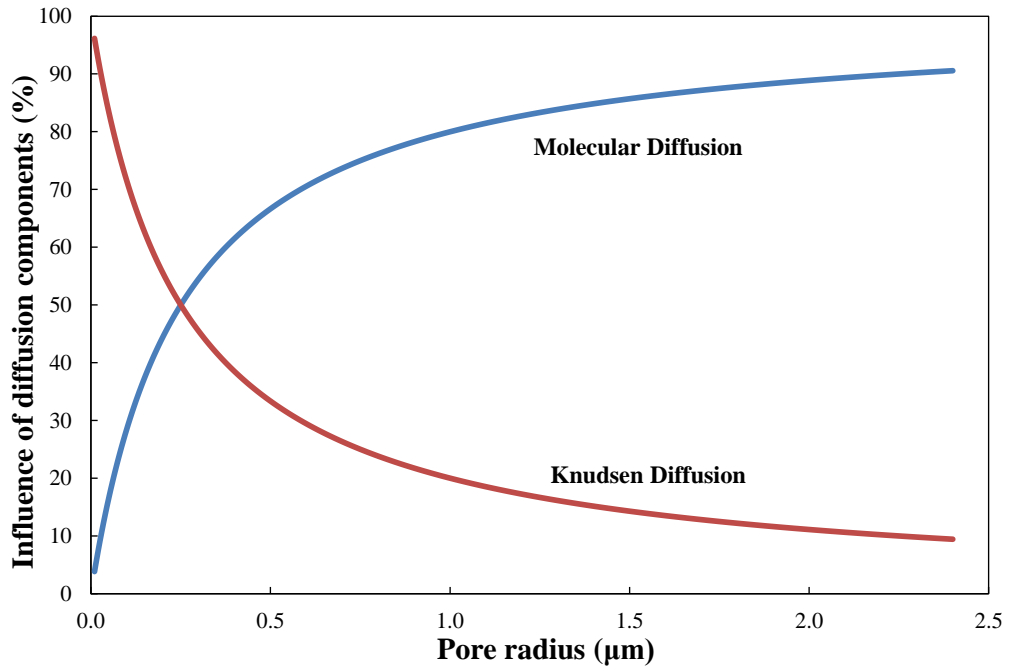


Figure 4.17: Relative contributions of molecular and Knudsen diffusion at test conditions as functions of average pore radius.

For the initial results obtained from the PCM, average values have been taken for both ε and \bar{r} from all values obtained for shorter exposure term tests. The 1 to 7 day sample values for ε and \bar{r} use the average value of the 3 data points obtained from the 1, 4 and 7 day samples. The results are shown in Figure 4.18 and show that the day on which \bar{r} is selected affects predicted corrosion depth. This is to be expected because \bar{r} increases with time, so later values of \bar{r} give greater values of D_K , D_{Eff} and therefore corrosion depth growth. It is noted that an increase in the size of \bar{r} does not result in a linear increase of the corrosion depth. D_K is linearly dependent on \bar{r} , however D_{Eff} , which combines D_K , D_M and ε , is not.

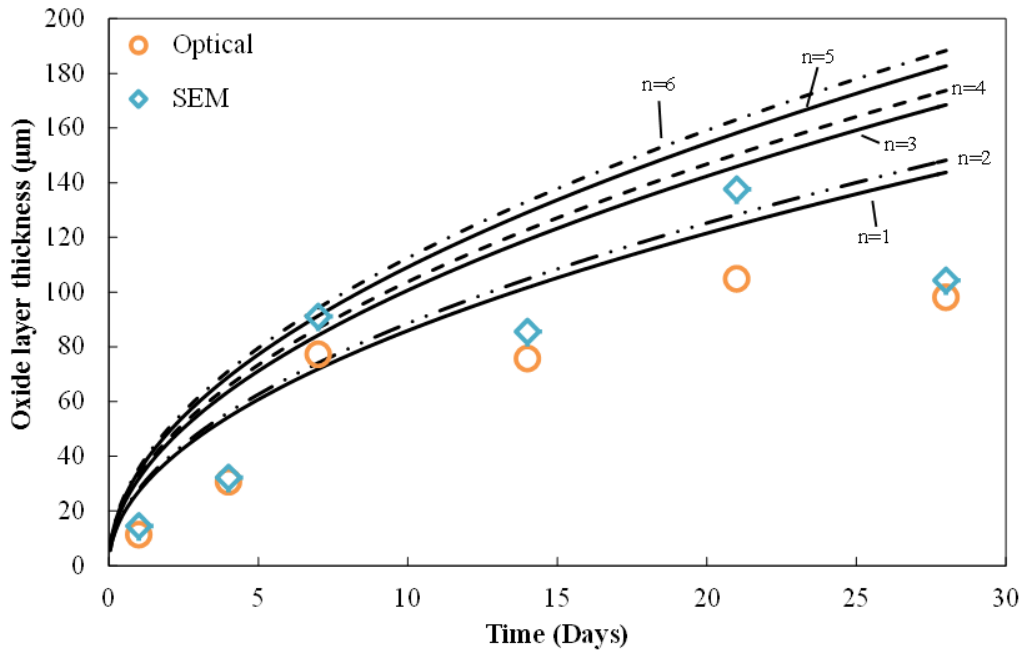


Figure 4.18: Results obtained for PCM predictions using average measured porosity data from different exposure times compared to experimental data at 540 °C.

As previously stated, the PCM does not include a physical sub-model for the evolution of \bar{r} and ε . To observe the effect of an evolving \bar{r} , Figure 4.19 provides PCM predictions for \bar{r} as a function of time. For these curves, n indicates the number of data points used to construct the \bar{r} function. Due to the highly linear nature of \bar{r} evolution, see Figure 4.15, convergence is seen for $n \geq 2$. Figure 4.19 also compares the performance of the LFM calibrated by $n=1$ (1 day) and $n=6$ (28 days) test data and the PCM with \bar{r} growth modelled on $n=1-6$ (1-28 day) test data. In general, the LFM under-predicts the measured trend while the PCM over-predicts it.

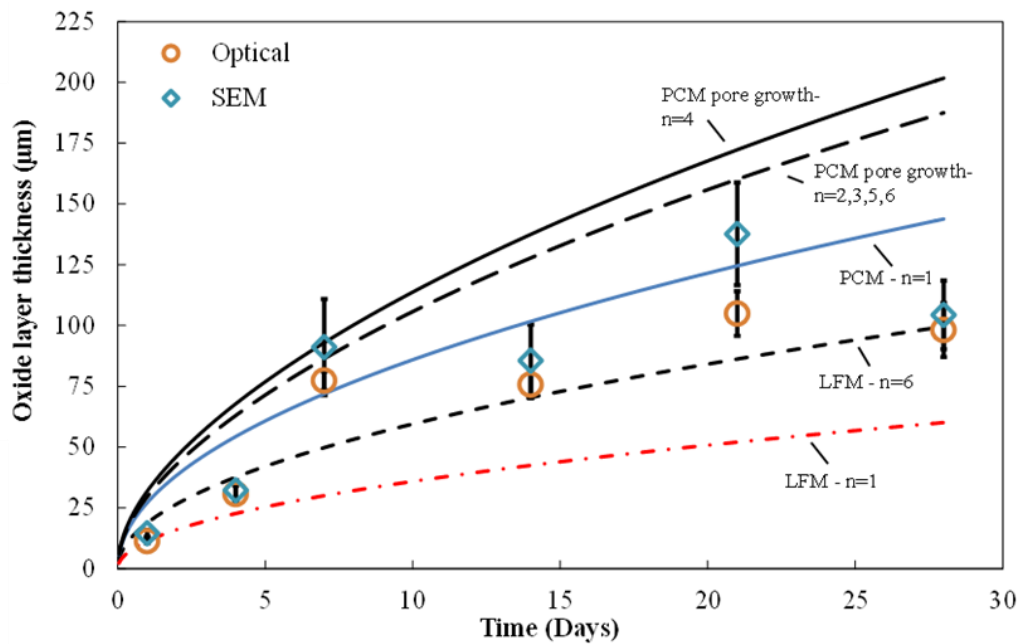


Figure 4.19: Graph comparing results from the LFM, PCM and experimental work at 540 °C.

As highlighted in Figure 4.10, long term test samples show significant degradation, making corrosion depth measurement difficult. Since the LFM requires a least-squares fit from experimental results up to 21 and 28 days, inaccurate measurements can result in inaccurate model predictions. It is therefore suspected that the LFM underestimates the true corrosion depth. Over-prediction compared to experimental data is therefore desirable. The PCM predicts convergence for $n \geq 2$.

A comparison of both the LFM and PCM methods with corrosion measurements from the tests carried out at 600 °C are displayed in Figure 4.20. It is noted that the corrosion depth does not appear significantly different than that seen at 540 °C as shown in Figure 4.10. It is possible that not all corrosion is captured using the current measurement methods at 600 °C. The partial pressure of the FeCl_2 gas diffusing outwards at 600 °C is approximately an order of magnitude higher than that at 540 °C (133 Pa at 600 °C, 20.2 Pa at 540 °C). It is possible that as FeCl_2 diffuses outwards very rapidly, it is not converted to Fe_2O_3 (reaction R4-3) until it travels further from the substrate and is thus not captured in the oxide layer measured.

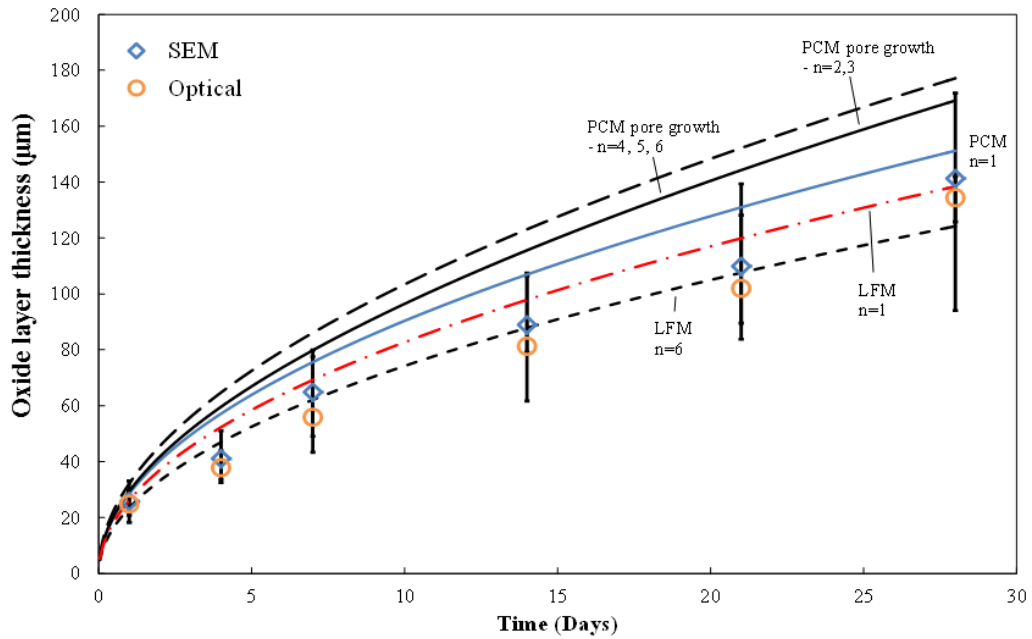


Figure 4.20: Graph comparing results from the LFM, PCM and experimental work at 600 °C.

For potential future studies, initial porosity measurements, which have been incorporated into the PCM, could be modelled by a theoretical approach for pore growth. This would replace the need for measured data for ε and \bar{r} . For application to more complex alloys a number of additional aspects would need to be considered. Additional oxides and chlorides such as chromium oxide/chloride and mixed oxides/chlorides would need to be taken into consideration. The oxides would thus be more complex, with a number of layers of different oxides expected. Future work could also examine the role of inter-granular penetration of Cl_2 in the overall process [166,209].

4.4. Conclusions

The physical process and mechanisms of corrosion of pure iron were studied for different exposure times from 1 to 28 days at temperatures of 540 °C and 600 °C, both with and without deposition of alkali-halide containing synthetic salt, representative of the deposits formed during the biomass co-firing combustion process. Optical microscopy, SEM and EDX has revealed the key stages in the corrosion process. These are: (1) initial corrosion of fresh substrate producing Type 1 oxide, (2) detachment of oxide from substrate, (3) fragmentation of detached layers due to pore coalescence

resulting in formation of Type 2 oxide, (4) undermining of uncorroded iron, (5) oxidation of uncorroded iron and fresh substrate, (6) detachment of oxides, continued oxidation and fragmentation.

The key physical role played by the porous oxide layer, vis-à-vis the rate-limiting, outward diffusion of FeCl_2 , is thus identified as the basis for a novel corrosion model for the accelerated corrosion due to alkali halide-containing deposits. This model is thus called the porosity-based corrosion model (PCM) and is based on observations of porosity and pore radius of the oxide layer, which are used to calculate an effective diffusivity for FeCl_2 gas diffusing through the porous oxide layer.

The porosity of the oxide layer remains relatively constant for different exposure terms, while the pore radius was found to grow at an almost linear rate. This provides the further opportunity for future development of a model incorporating pore growth, such as the random pore model [208,210]. It is postulated that smaller pores coalesce to form larger pores as time passes, leading ultimately to fragmentation of the oxide.

Comparison of the PCM to the previously-used LFM indicates that the PCM provides a conservative estimate of corrosion depth. This is not an undesirable outcome as the long-term test data needed to calibrate the LFM can be difficult to obtain due to significant degradation of oxide layers. Future work will focus on the incorporation of a pore-growth model into the PCM and an examination of the role of inter-granular Cl_2 penetration.

5. Effect of Corrosion on the Service Life of P91 Piping

5.1. Introduction

This chapter presents a finite element methodology which investigates the effect of corrosion on creep rupture life in high-temperature pressurized tubes. Experiments have been carried out in order to determine a corrosion rate of P91 for tube wall loss in operational plants co-firing peat and biomass. The more complex composition and microstructure of P91 steel resulted in a more complex corrosion mechanism than was observed for iron. SEM images and EDX element maps are presented and help to gain an insight into the corrosion process and material deterioration. These results provide data for the calibration of a user defined subroutine to model the corrosion rate on tube walls. This model was then combined with finite element models of pressurised tubes and creep damage models to produce a combined creep-corrosion model, which was used to predict tube rupture life for a range of internal tube pressures.

Superheater tubes typically carry the highest pressure and temperature steam, while also being exposed to high temperature combustion flue gases. Due to this, superheater tubes are more susceptible to high-temperature creep and corrosion failures than furnace walls and economizer tubes, which operate at lower temperatures [211]. Approximately 90% of failures due to high-temperature creep or long-term overheating occur in the superheater and reheater tubes [105]. Creep rupture failure of the superheater and reheater tubes is a primary cause ($\approx 30\%$) of forced outages at coal and biomass fired boilers [212].

Finite-element (FE) analysis of pipes subjected to creep damage has previously been carried out by Hyde et al. [120,213], among others. Separate FE models were also developed to model corrosion of tube walls. Wenman et al. [104] modelled pitting corrosion and stress corrosion cracking via element removal in the FE code Abaqus, thus allowing for prediction of stress redistribution and subsequent crack growth.

Sawada et al. [214] have investigated the effect of oxidation on the creep strength of T23 steel in air and in helium and found that at 625 °C there was no noticeable effect of oxidation; however at 650 °C oxide scales contributed to creep strength degradation. As these tests were carried out in air, without deposits, it is expected that

they would have lower corrosion rates than those carried out exposed to harmful deposits.

5.2. Methodology

Experimental tests have been carried out in order to obtain a realistic corrosion rate for the superheater tube wall loss. The experimental methodology carried out is presented in detail in Chapter 3. A synthetic salt, termed salt A, representative of deposits formed during co-firing of a 70:30 peat: woodchip mixture was applied to samples of P91 steel at 540 °C for up to 28 days. The chemical composition of this salt is given in Table 3-2.

This chapter presents a simplified model of the accelerated corrosion rates, which are present when co-firing biomass in power plants, combined with creep effects using the FE program Abaqus [215]. Initially creep effects were modelled on uniaxial test specimens. A simple superheater tube under closed-end conditions was then modelled. Initially the tube model was simulated with no damage effects; creep damage was then incorporated into the tube model, with corrosion effects being incorporated as a final step.

5.2.1. Creep Model

Creep damage was modelled based on the Kachanov, single variable creep damage equations [118,216], and implemented via the user defined subroutine CREEP in Abaqus. The multi-axial form of the creep damage equations have been shown previously in Chapter 2 as Equations 2-9, 2-10 and 2-11, and are repeated here as follows:

$$\frac{d\varepsilon_{ij}^c}{dt} = \frac{3}{2} A' \left(\frac{\sigma_{eq}}{1-\omega_c} \right)^n \frac{S_{ij}}{\sigma_{eq}} t^m \quad (5-1)$$

$$\frac{d\omega_c}{dt} = B' \frac{\sigma_r^\chi}{(1-\omega_c)^\phi} t^m \quad (5-2)$$

$$\sigma_r = \alpha\sigma_1 + (1-\alpha)\sigma_{eq} \quad (5-3)$$

where ε_{ij}^c is creep strain, t is time, ω_C is the creep damage variable, σ_{eq} is equivalent stress, σ_r is rupture stress, σ_I is maximum principal stress, S_{ij} is deviatoric stress and A' , m , n , B' , χ , ϕ and α are material constants. Failure is assumed to occur when the damage term reaches a value of 1. Material constants for these equations have been obtained from the work carried out by Hyde et al. [120] at 650 °C and are shown in Table 5.1.

Table 5.1: Material constants used in creep equations (obtained from Hyde et al. [4] for P91 at 650 °C).

A'	n	m	B'	ϕ	χ	α
1.092×10^{-20}	8.462	-4.754×10^{-4}	3.537×10^{-17}	7.346	6.789	0.215

5.2.2. Finite Element Model

A plain tube model has been developed in Abaqus making use of the axisymmetric geometry. A schematic of the geometry and loading applied can be seen in Figure 5.1. The analysis was carried out for an elastic-creep material model, where a uniform wall temperature was assumed. Future models could include plasticity effects and temperature gradients through the wall.

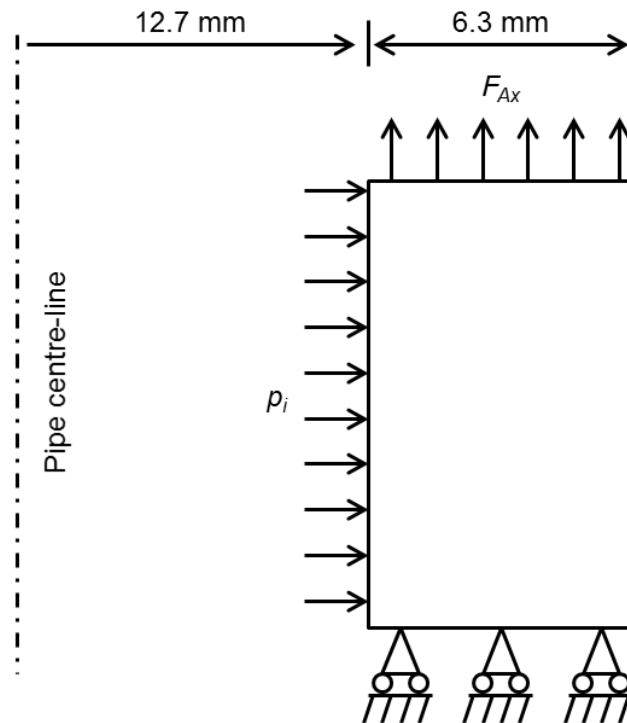


Figure 5.1: Dimensions and mechanical loading of P91 pipe.

Three different cases of internal pressures 10, 15 and 20 MPa were investigated, as this range captures typical operating pressures of in-situ tubes. The models were initially run with no creep damage or corrosion effects and results of hoop, axial and radial stress are compared with Lamé's equations, as follows:

$$\begin{bmatrix} \sigma_H \\ \sigma_A \\ \sigma_R \end{bmatrix} = \left(\frac{p}{\left(\frac{R_o}{R_i}\right)^2 - 1} \right) \begin{bmatrix} \left(1 + \left(\frac{R_o}{r}\right)^2\right) \\ 1 \\ \left(1 - \left(\frac{R_o}{r}\right)^2\right) \end{bmatrix} \quad (5-4)$$

where p is the internal pipe pressure, R_o is the outer radius of the pipe, R_i is the inner radius of the pipe, r is the radius at an arbitrary point through the wall thickness, σ_H is the hoop stress, σ_A is the axial stress and σ_R is the radial stress. Creep damage was then added to the model to investigate creep life without corrosion effects. Finally corrosion effects were added to the model, as described below.

5.2.3. Corrosion Model

Measurements of the oxide layer thickness were obtained from the experimental data. This oxide layer thickness was then related to the amount of substrate which was consumed in order to form the oxide scales, to determine the rate at which the substrate is corroded. This was done in a manner similar to that shown in Chapter 4. The PCM was not utilised during this calculation due to additional complexities of the corrosion mechanism when the base metal is an alloy.

The main oxides produced in this form of corrosion are Fe_2O_3 , Cr_2O_3 and a mixed FeCr spinel-type oxide. In this work the different forms of iron/chromium oxide are not differentiated, e.g. Fe_2O_3 and Fe_3O_4 are assumed to be the same, as are Cr_2O_3 and CrO. For the purposes of this calculation, attention was focused on the iron in the alloy and the associated oxides. This was done as (i) P91 consists predominantly of iron ($\approx 90\%$) and (ii) the relevant physical properties (i.e. molecular weights and densities, which are required for the model) of the different oxides are similar in value.

Again it was assumed that the accelerated corrosion proceeds via active oxidation as discussed in Chapter 2. For each time the iron chloride gas reacts with oxygen as per

reactions R2-3 and R4-3, in order for 1 mole of Fe₂O₃, for example, to form, 2 moles of Fe must be consumed from the healthy metal. Hence, the number of moles of Fe consumed was linked to the amount of oxide formed via the following expression:

$$\frac{dN_{Fe}}{dt} = 2 \frac{dN_{Fe_2O_3}}{dt} \quad (5-5)$$

where N_{Fe} and $N_{Fe_2O_3}$ are the number of moles of Fe consumed and the number of moles of Fe₂O₃ formed during reaction R2-3/R4-3, respectively. By using molecular weights, the mass of Fe removed was related to the amount of Fe₂O₃ formed, as follows:

$$\frac{1}{M_{Fe}} \frac{dm_{Fe}}{dt} = \frac{2}{M_{Fe_2O_3}} \frac{m_{Fe_2O_3}}{dt} \quad (5-6)$$

where m_{Fe} and $m_{Fe_2O_3}$ are the mass of the iron consumed and the mass of the oxide formed in the reaction, respectively. $M_{Fe_2O_3}$ is the molecular weight of Fe₂O₃. Hence, the rate of change of depth of substrate lost (l_{Loss}) was related to the rate of change of oxide layer thickness (l_{Ox}) as follows:

$$\frac{dl_{Loss}}{dt} = 2 \frac{M_{Fe}}{M_{Fe_2O_3}} \frac{\rho_{Fe_2O_3}}{\rho_{Fe}} \frac{dl_{Ox}}{dt} \quad (5-7)$$

Finally, an equation for l_{Loss} was obtained, as follows:

$$l_{Loss} = 2 \frac{M_{Fe}}{M_{Fe_2O_3}} \frac{\rho_{Fe_2O_3}}{\rho_{Fe}} l_{Ox} \quad (5-8)$$

Values for l_{Loss} were therefore obtained from the measured l_{Ox} values, as a function of time. A parabolic corrosion model, given by $l_{Loss} = a\sqrt{t}$, was hence used to describe the corrosion rate, where the constant a was identified using a least squares optimization technique:

$$a = \exp \left(\frac{\sum_{i=1}^n \ln l_{Loss,i} - 0.5 \sum_{i=1}^n \ln t_i}{n} \right) \quad (5-9)$$

where n is the amount of experimental data points used in the least squares calculation and t is time.

Corrosion was simulated here based on the Arbitrary Lagrangian Eulerian (ALE) adaptive meshing capability available in Abaqus/Standard and defined using the user subroutine UMESHMOTION. This capability allows the boundaries of the FE mesh to be moved between analysis increments [215]. This technique has previously been used in die wear prediction [217], fretting wear prediction [218], and in the corrosion modelling of stents [109].

In this method, material removal is simulated by the movement of nodes at the exterior of the mesh, simulating the incremental removal of material. As this method does not rely on element removal, it is less sensitive to mesh resolution. Additionally as the velocity of the node movement is determined via a user subroutine, it can be defined to depend on, for example, species concentrations and fluxes on the corrosion surface, as well as material stresses and strains in the vicinity of the surface [109].

Outer nodes of the oxide layer were defined as the nodes to be moved by UMESHMOTION, as shown in Figure 5.2. All elements in the tube and oxide were defined as the adaptive mesh domain, allowing for a high-quality mesh to be maintained through the analysis. The adaptive meshing technique proceeds via two steps. Initially, the surface nodes move in the local normal direction, to simulate material removal, as a purely Eulerian analysis. Secondly, the material quantities are re-mapped to the new positions via advection by solving the advection equations, for the material quantities, using the second order Lax-Wendroff method [215,218].

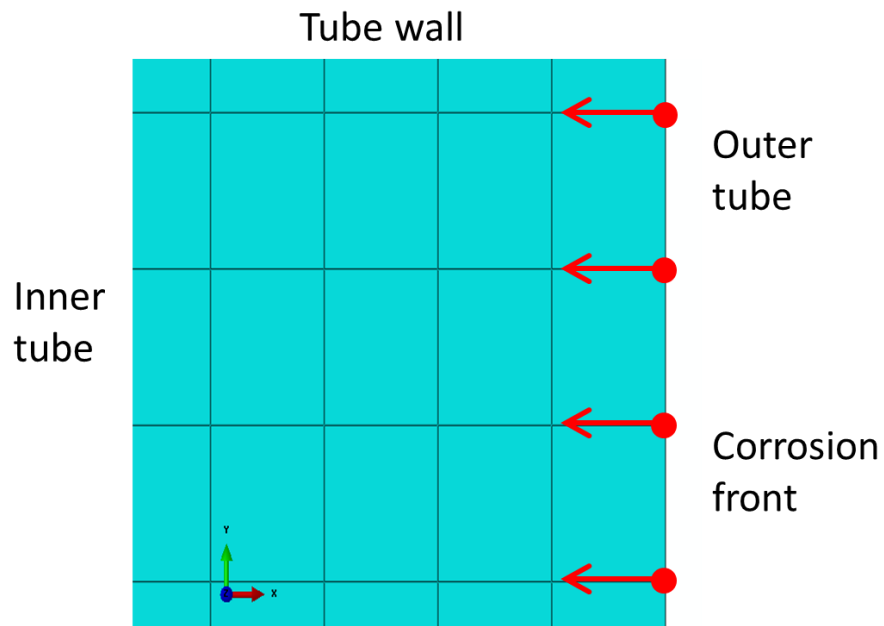


Figure 5.2: FE model showing direction of nodal movement.

This subroutine was then combined with the creep and tube models, resulting in a model showing a tube wall undergoing uniform corrosion with creep damage effects. A flowchart detailing the main processes within the finite element creep-corrosion methodology is shown in Figure 5.3. In this study, continuum, axisymmetric 4-node elements were used to model the pipe wall. A mesh convergence study was carried out with respect to von Mises stress and convergence was achieved to within 5% using 260 4-noded axisymmetric reduced integration elements.

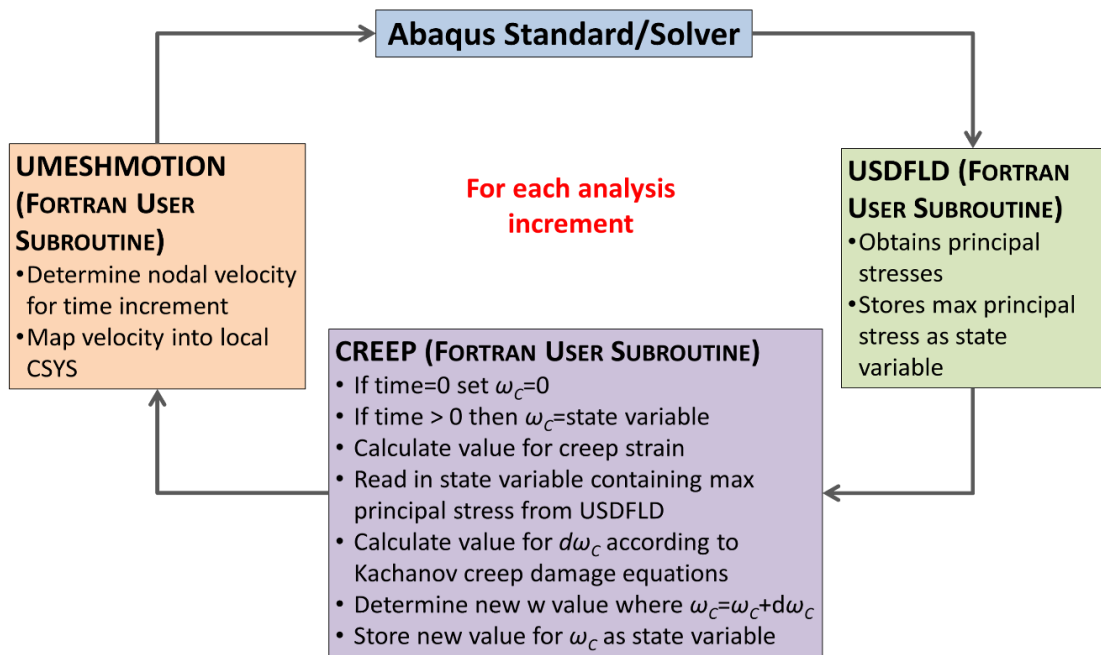


Figure 5.3: Flowchart detailing the user subroutines implemented in Abaqus.

5.3. Results

5.3.1. Experimental

SEM images and EDX element maps for the P91 samples tested at 540 °C for 1, 4, 7, 14, 21 and 28 days are presented and analysed in this section. From these images, valuable insight into the mechanism of the corrosion process and the complex, time-dependent structure of the corrosion layers is obtained.

SEM images of the samples' cross sectional areas are shown in Figure 5.4. Following 1 day of exposure, poorly-adhered multi-layers of oxides are visible, with voids formed above the substrate (Figure 5.4 (a)). These poorly-adhered multi-layers of oxides form due to high stresses in the oxides resulting in cracking and spalling [85,165]. Following 4 days exposure (Figure 5.4 (b)) the mixed oxide layer has travelled away from the substrate surface and now offers little protection against further corrosion. A second protective layer of oxide has formed close to the substrate surface and will slow the corrosion process.

The sample exposed for 7 days shows that the multi-layered oxide is again present far from the oxide layer. A second layer has also detached from the substrate and there is no evidence of the protective oxide layer (Figure 5.4 (c)). It is postulated that the

protective oxide layer has detached from the substrate; this delamination effect can occur due to stresses in the oxide scales [167].

Following 14 days of exposure (Figure 5.4 (d)) there is no evidence of a protective layer at the substrate surface but a number of layers which have detached from the substrate and moved away are visible. Similarly the sample exposed for 21 days (Figure 5.4 (e)) shows no evidence of protective oxide on the substrate surface; however, layers of oxide are visibly detached from the substrate. The sample exposed for 28 days is shown in Figure 5.4 (f). From this figure numerous scales of multi-layers of oxide which have detached from the substrate surface can be seen.

This is a more complex mechanism than was observed in Chapter 4, for pure iron. The different elements which are present in P91 result in the formation of different forms of oxides. These elements convert to oxide at varying distances from the substrate. Chromium, for example forms chromium oxide close to the substrate surface, with iron oxide typically forming further from the substrate than the chromium oxide. The addition of these elements to the base metal, make implementing the PCM significantly more complex. Numerous metal chlorides must be considered in this case in addition to the multiple layers of oxide which have formed.

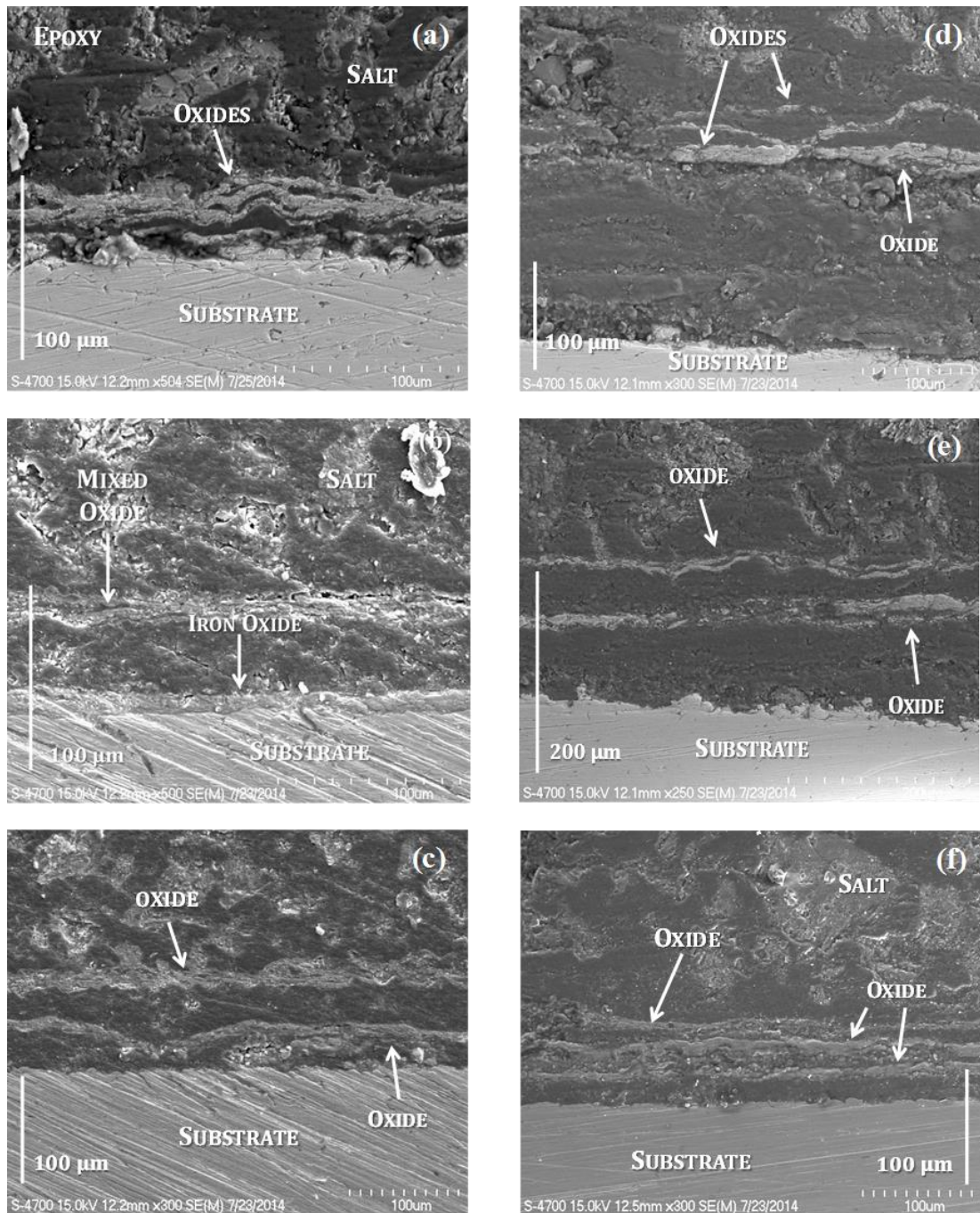


Figure 5.4: SEM images of P91 after exposure to synthetic salt at 540 °C for (a) 1 day; (b) 4 days; (c) 7 days; (d) 14 days; (e) 21 days; (f) 28 days.

The exfoliation process is attributed to growth stresses of the oxide, which cause crack initiation, as well as the formation of a chloride-rich layer at the metal-oxide interface [85]. Following deposition of the salt, Figure 5.5 (a), an oxide forms, via conversion of metal chlorides to metal oxides. The evaporating chromium-iron chlorides convert to oxides at different partial pressures, as shown in Figure 5.5 (b).

Chromium chloride converts to chromium oxide closer to the substrate, causing high growth stresses [167], which result in cracks forming in the oxide scale as shown in Figure 5.5 (c). These cracks lead to detachment of the oxide from the substrate, as depicted in Figure 5.5 (d). Following detachment of the initial oxide, a second oxide forms above the substrate in a similar manner (Figure 5.5 (e)). Growth stresses have been shown to cause repeated buckling of the individual layers resulting in voids forming between the layers [165,166].

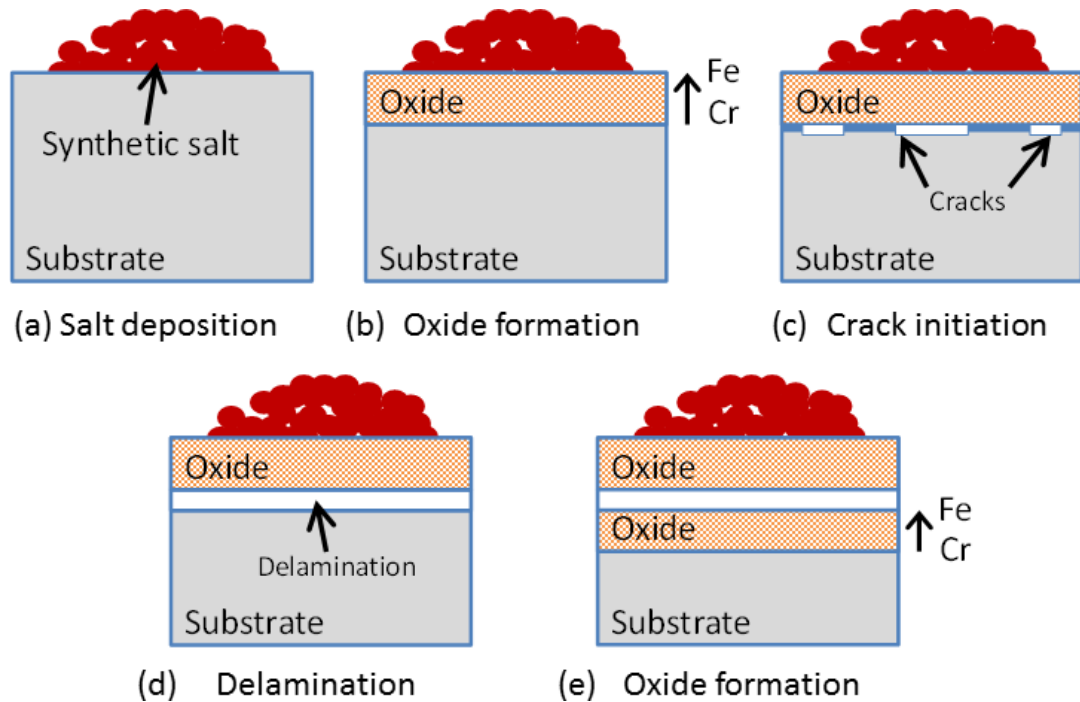


Figure 5.5: Schematic showing different stages of delamination process.

Chemical compositions of the samples are obtained via EDX analysis. Figure 5.6 shows the area of the 4 day sample which was analysed and the corresponding EDX element maps of Ca, S, O, Fe and Cr. Calcium and sulphur are clearly visible above the metal surface, as expected, due to their large contributions to the deposit layer (See Chapter 3 for deposit compositions).

From these maps a mixed Cr-Fe, multi-layered oxide, which has detached from the substrate surface, is visible. Additionally a layer of iron oxide exists close to the substrate surface with a thin layer of chromium oxide tightly bound to the substrate between the iron oxide layer and the substrate. The presence of oxygen in the scales confirm they are oxides, while the absence of oxygen from the substrate confirms that it is uncorroded.

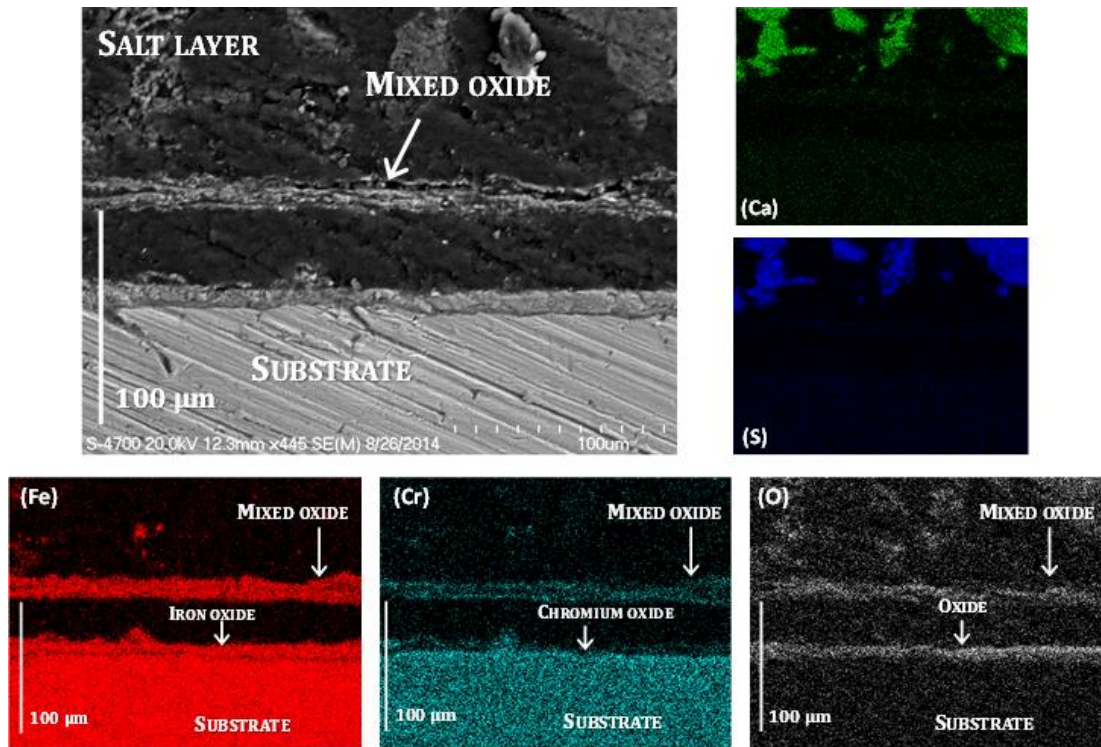


Figure 5.6: SEM image and EDX element maps of sample exposed to synthetic salt for 4 days.

The oxide scales were measured for each sample removed from the furnace and a plot showing the evolution of the oxide layer thickness, (l_{O_x}), with time is shown in Figure 5.7. Due to oxide spallation and fragmentation, obtaining accurate measurements for samples subjected to long term exposure is difficult. The corrosion evolution follows a similar trend to that reported in the literature [53]. The initial breakdown of the protective oxide results in a large oxide layer thickness following 1 day of exposure.

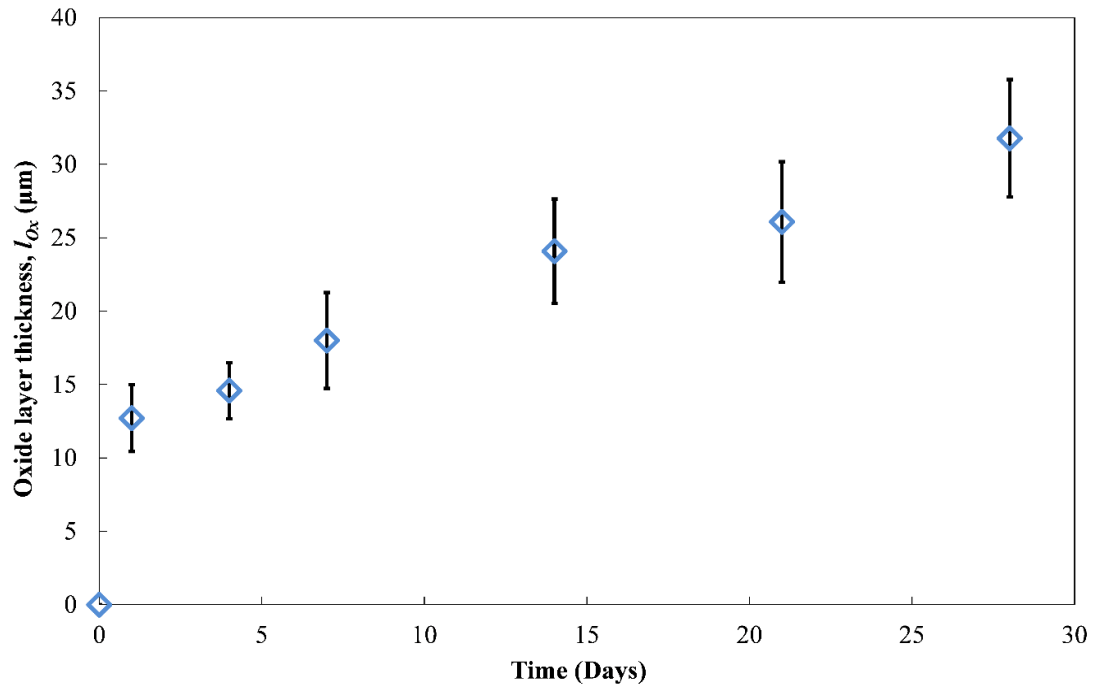


Figure 5.7: Thickness of oxide layer following exposure to synthetic salt.

Following this, the corrosion proceeds at a more uniform rate. The initial breakdown can be, at least partially, attributed to the formation of alkali chromates, depleting the protective oxide layer of chromium, as shown in reaction R2-13 in Chapter 2. The oxide layer thickness obtained during this testing indicates far greater levels of corrosion than those obtained with no exposure to harmful salts. Fournier et al. [101] report a maximum thickness of 2.80 μm following 36 days testing at 550 $^{\circ}\text{C}$ with no salt exposure; here a maximum thickness of 31.77 μm is obtained following 28 days testing at 540 $^{\circ}\text{C}$ with exposure to the synthetic salt.

5.3.2. Computational

Initial computational work focused on model validation of the individual user subroutines and tube model. The creep model was compared successfully with test data obtained from work by Hyde et al. [120] and the results are shown in Figure 5.8.

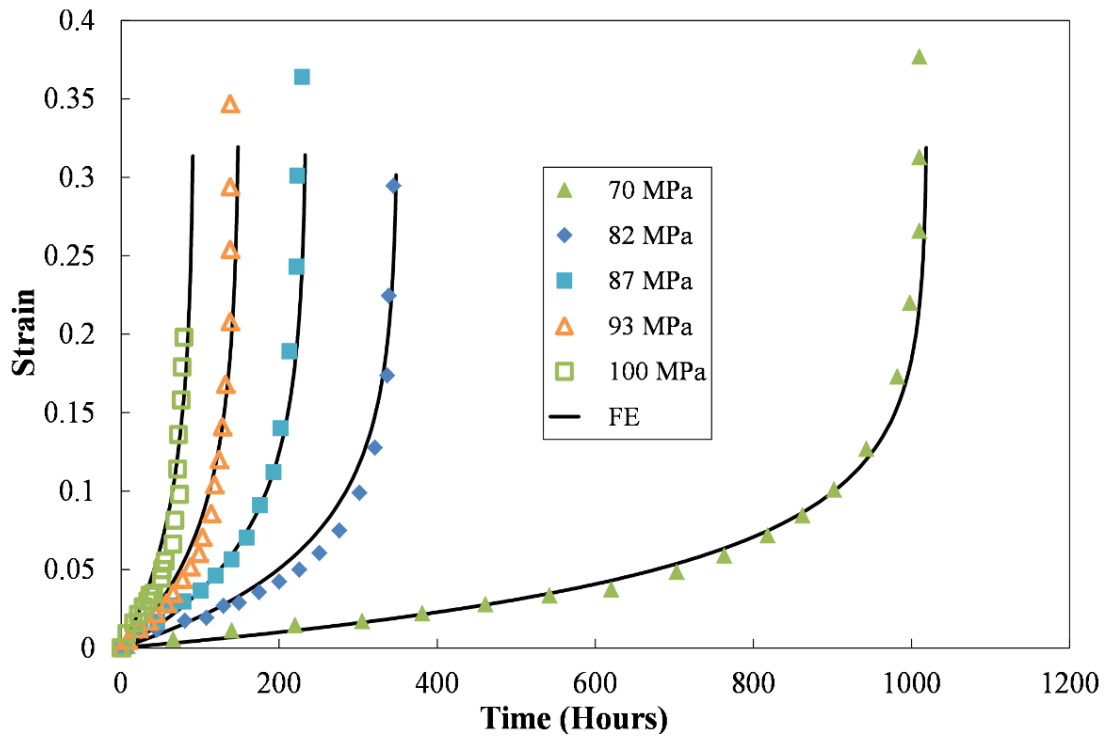


Figure 5.8: Creep curves obtained from F.E analysis compared with experimental data from Hyde et al. [4].

Values obtained for l_{Ox} were then converted to l_{Loss} via Equation 5-8 and the results are shown in Table 5.2. These results were then used to obtain the constant a from Equation 5-9. Figure 5.9 shows the depth of substrate, l_{Loss} which has been removed in order to form the oxide layers. These measurements were then compared with results of the adaptive meshing technique and MATLAB results from Equation (5-9), where the constant a was identified as 3.349, where t is in days and l_{Loss} is in μm . The results are shown to agree with those presented by Hyde et al. [120].

Table 5.2: Values for oxide layer thickness, l_{Ox} , and depth of substrate consumed, l_{Loss} .

<i>Days</i>	<i>1</i>	<i>4</i>	<i>7</i>	<i>14</i>	<i>21</i>	<i>28</i>
l_{Ox} (μm)	12.7	14.6	18.0	24.1	26.1	31.8
l_{Loss} (μm)	5.9	6.8	8.4	11.2	12.1	14.8

In addition to the parabolic equation, a bilinear fit was also considered for the model, as can be seen in Figure 5.9. While this initially appears to provide a more accurate prediction for l_{Loss} , following longer term exposure, the bilinear fit results in higher prediction for substrate consumed, as can be seen in Figure 5.10. Therefore, in order to maintain a conservative approach to corrosion predictions, the parabolic equation was used. The physical basis of the parabolic rate is that corrosion is controlled by diffusion of gas-phase corrosion products through the corrosion product layer [53], which is consistent with the active oxidation corrosion mechanism.

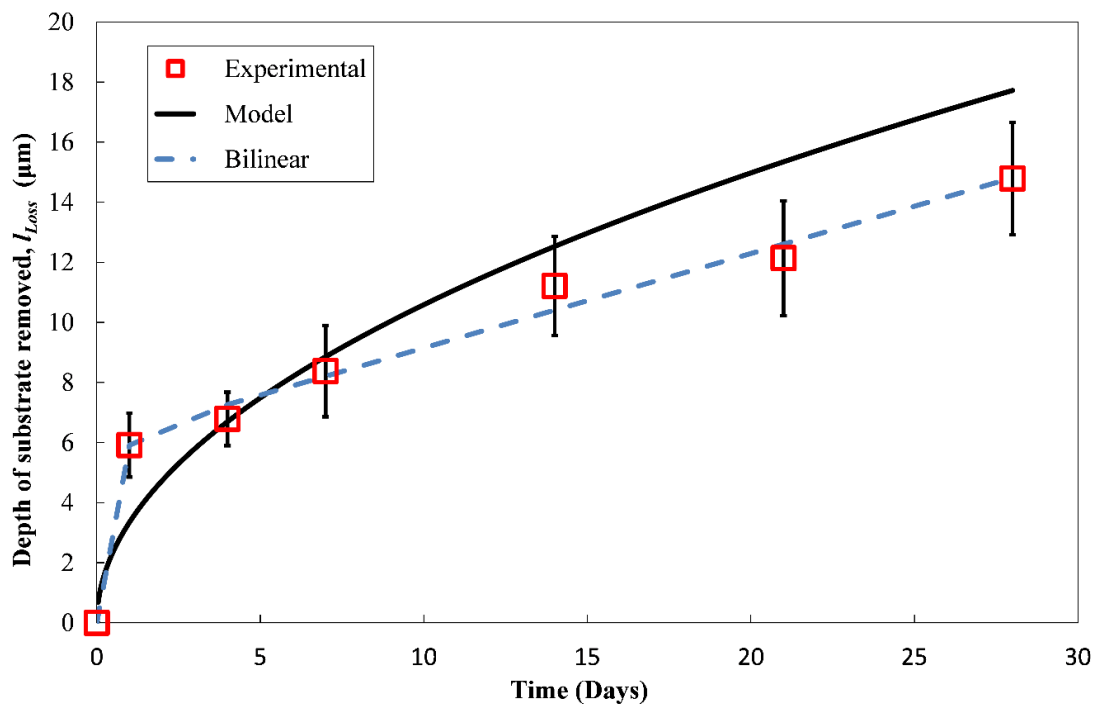


Figure 5.9: Depth of substrate removed following exposure compared with model and bilinear fit.

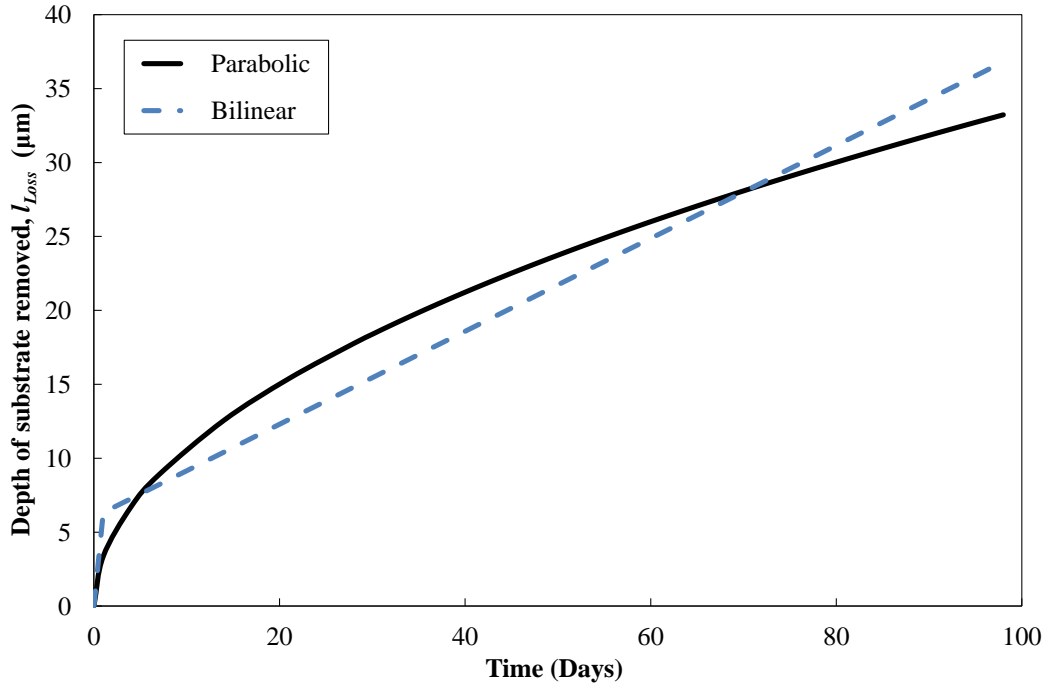


Figure 5.10: Comparison of bilinear rate vs parabolic rate for long term corrosion.

This work made use of a parabolic law for oxide layer growth assuming no initial wall loss as it is well established in literature [53,87,89,99,105,111,159,203,219–222] and regarded as state of the art. However, it is recognised that there is the potential for the longer term accuracy of these models to be improved by the addition of a constant of integration i.e. assuming non-zero initial wall loss. While this is not what is experimentally observed, it can improve the curve fit over longer times. This would change the equation used in this work to obtain the loss of wall thickness to the following:

$$l_{Loss} = a\sqrt{t} + c \quad (5-10)$$

where c is the constant of integration and all other values are as previously defined. A study was carried out to determine the extent to which this constant of integration would change the corrosion rate used in the model. Values for a and c of 5.8 and 2.7, respectively, were found following calibration.

Results comparing the model including the constant of integration with the traditionally used parabolic equation are shown in Figure 5.11. Figure 5.11 (a) shows a comparison of the two models with the experimental data also plotted. The constant of integration does appear to provide a better fit for the experimental data. When this was extrapolated for longer time periods (100 days), as shown in Figure 5.11 (b) the

difference was found to be relatively small (15% following 100 days) and does not appear to be increasing. As such it was deemed acceptable to continue to use the parabolic fit for this work. However the constant of integration could be incorporated in future work. When the length of time was increased from 100 to 1,000 days the increase was negligible (from 15% to 18%).

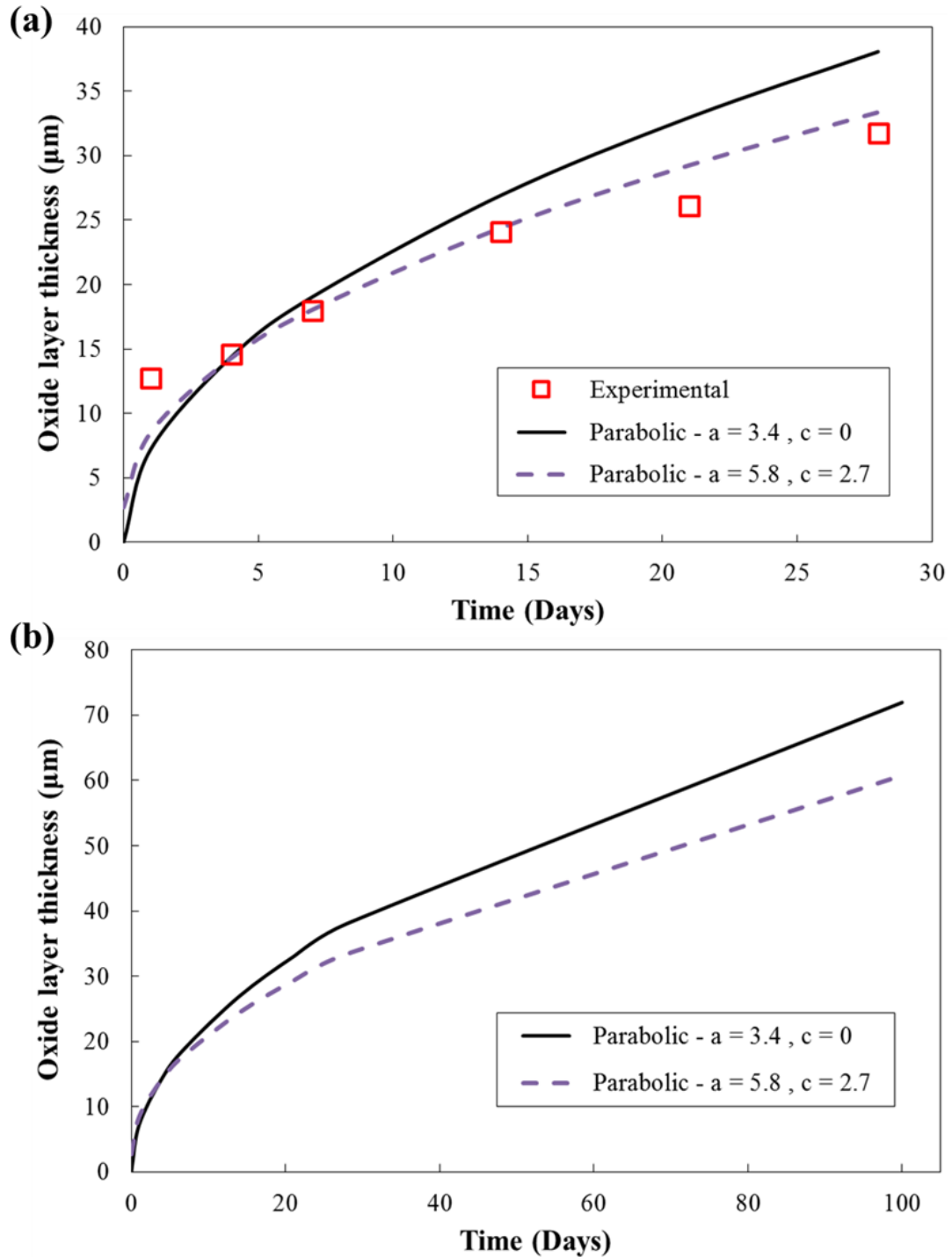


Figure 5.11 Comparison of parabolic fit vs fit with constant of integration added for (a) 30 days and (b) 100 days.

Initial FE analyses were carried out with no damage effects and results were compared to theoretical values obtained from Lamé's equations (Equation 5-4). The creep and corrosion effects were then added to the model and the effects on tube stresses and creep rupture life was investigated. The greatest change is with the hoop stress, which is initially highest at the tube interior but, following long-term creep and stress redistribution, becomes lowest at the interior of the tube.

Figure 5.12 (a) shows the evolution of hoop stress distribution in a pipe with an internal pressure of 15 MPa with increasing time. Initial elastic to steady-state stress redistribution was predicted to lead to reduced stress on the inside surface and increased stresses on the outside surface, e.g. for the case labelled 1,000 hours in Figure 5.12 (a). This stress redistribution occurred due to the time dependent creep deformation as described by Kraus [223] and has serious ramifications for the evaluation of the maximum stress in the tube.

Figure 5.12 (b) shows the hoop stress redistribution in a pipe with an internal pressure of 10 MPa with increasing time. The stress redistribution, results in the maximum hoop stress changing from the inner to outer tube wall was again evident. In addition to this increases in hoop stresses were found to occur with increases in time. This is attributed to the loss of healthy material from the tube wall due to corrosion. Corrosion of the tubes was hence shown to lead to a reduction of the load bearing capacity of the tubes resulting in early failure times.

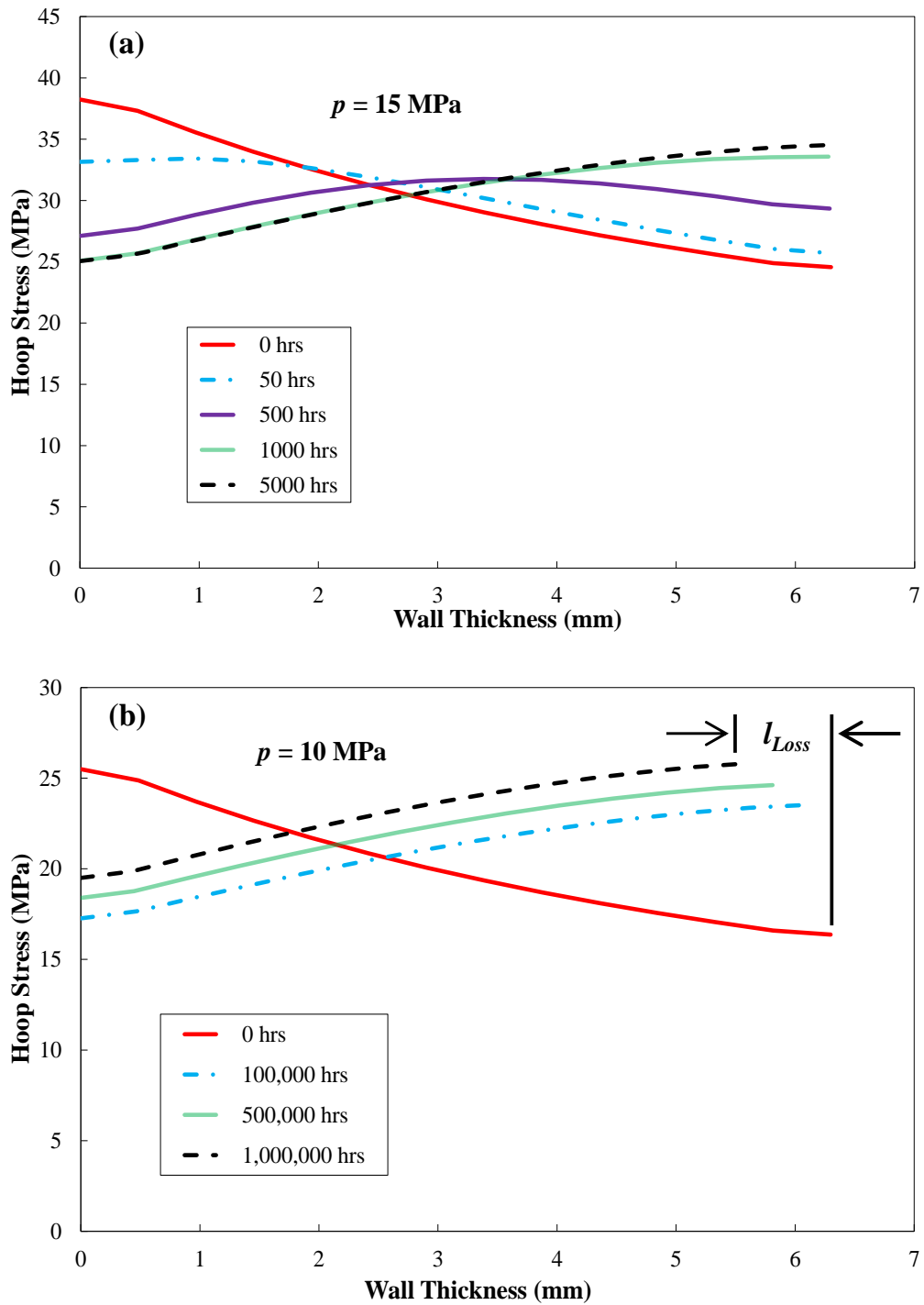


Figure 5.12: Hoop stress redistribution and increase with time at (a) 15 MPa and (b) 10 MPa.

The loss of wall thickness (l_{Loss}) is visible from Figure 5.12 (b). It is noted that the parabolic equation uses a calibrated value for a based on experimental data up to a maximum time period of 672 hours, while the model runs in to the millions of hours for the 10 MPa case. However, previous work has shown that exposure of 7 days in a furnace is sufficient to give reproducible and relevant information of the corrosion

tendency of steels [49]. Additionally, the more conservative parabolic rate has been chosen for modelling the evolution of l_{Loss} .

Figure 5.13 shows contour plots of the hoop stress at increasing time periods, for the tube subjected to an internal pressure of 20 MPa. The loss of tube wall material due to corrosion is evident from these plots. Additionally, the stress redistribution due to creep and the increase in hoop stress due to loss of wall thickness can be visually identified.

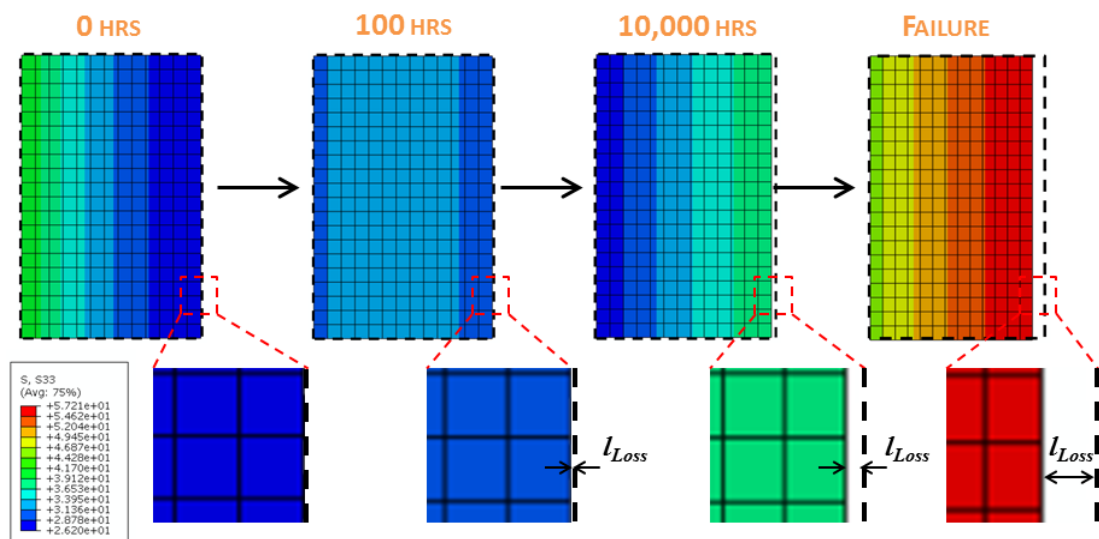


Figure 5.13: Abaqus plots for 20 MPa internal pressure showing hoop stress distribution and growing oxide layer with time.

Figure 5.14 shows the predicted damage evolution for the three load cases (internal pressure of 10, 15 & 20 MPa), up to failure, where failure occurs when damage reaches a value of 1. For the three cases, an effect of corrosion on life expectancy is visible. As expected, the longer the tubes are exposed, the greater the effect of corrosion, due to corrosion layer growth. The predicted life expectancy for the tubes subjected to both creep and creep-corrosion damage is shown in Table 5.3 for the three load cases.

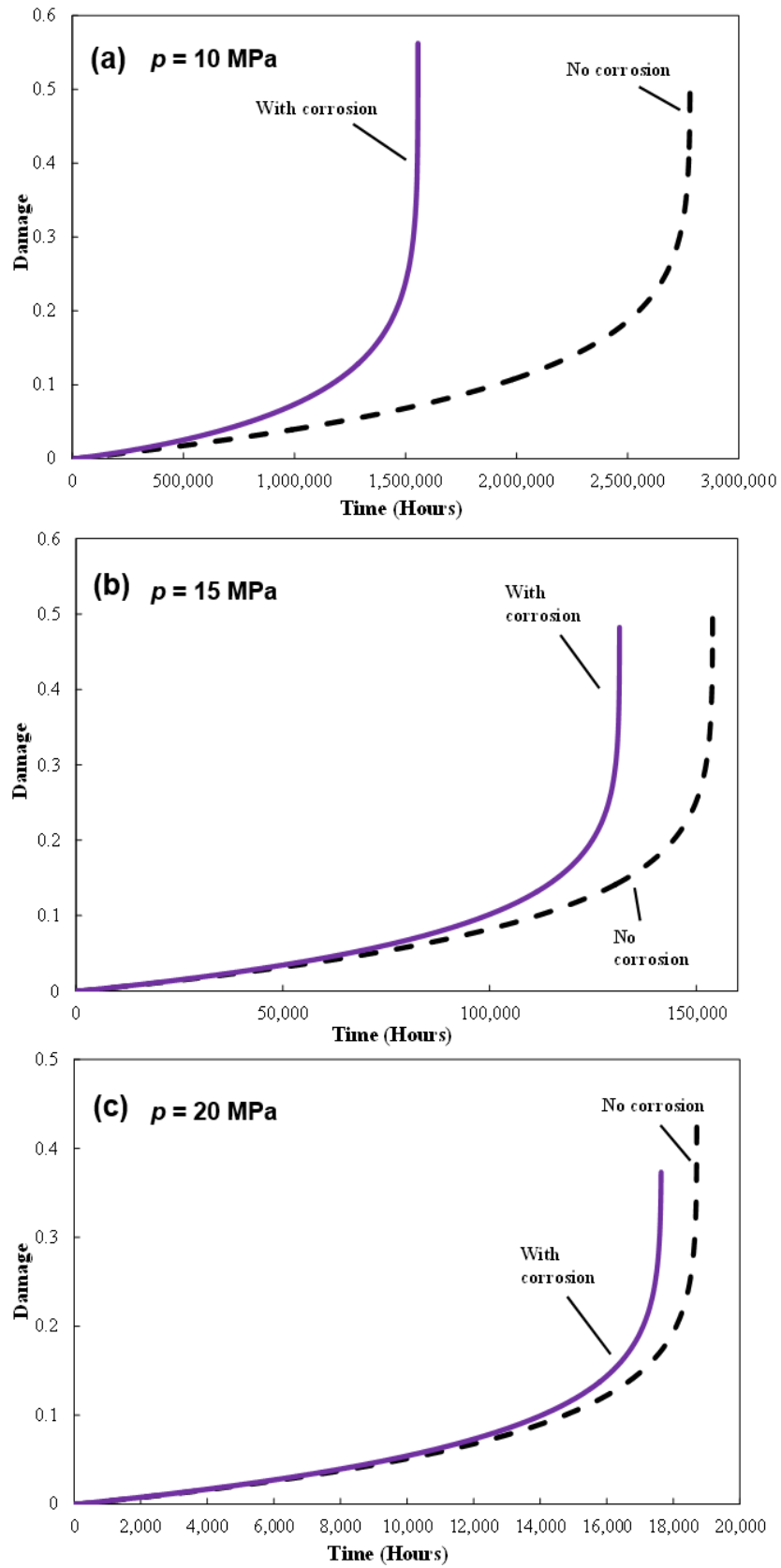


Figure 5.14: Damage curve for superheater tube with internal pressure of (a) 10 MPa, (b) 15 MPa, (c) 20 MPa.

Table 5.3: Time to failure for creep and creep corrosion cases (Creep constants taken at 650 °C from work by Hyde et al. [4]).

<i>Int. Pressure (MPa)</i>	<i>Creep (hrs)</i>	<i>Creep-Corrosion (hrs)</i>	<i>Decrease in life (%)</i>
<i>10</i>	2,880,000	1,556,000	44.0
<i>15</i>	153,900	131,400	14.6
<i>20</i>	18,700	17,600	5.7

The FE results were compared to rupture life predictions based on the Larson-Miller parameter given by:

$$P_{LM} = T(C_{LM} + \log t_R) \quad (5-12)$$

where P_{LM} is the Larson Miller parameter, T is temperature (K), t_R is time to rupture (hours) and C is a material specific constant. Results from accelerated creep tests carried out at a range of stresses (125 - 230 MPa) and a range of temperatures (566 - 649 °C) have been obtained from work carried out by Furtado et al., [224]. Based on these results and mean diameter hoop stress, rupture life predictions using the Larson-Miller parameter are compared with the Kachanov damage results in Figure 5.15. From this, it can be seen that the Larson-Miller model predicts similar life at higher stresses and significantly shorter rupture life at lower stresses.

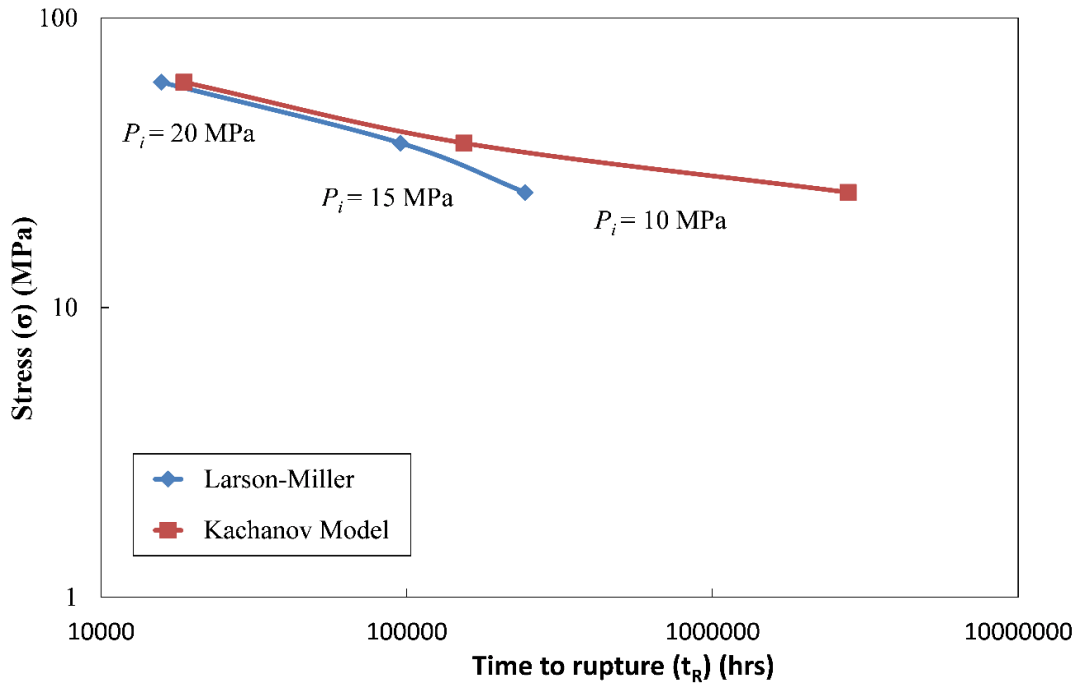


Figure 5.15: Comparison of creep rupture life predictions from the Kachanov model and the Larson-Miller parameter.

5.4. Discussion

The experiments performed for this chapter do not include the effect flue gas has on the deposit. However, previous work has shown that testing in air produces corrosion products similar to those in corrosive environments [49]. Potential future work could carry out tests in representative gaseous atmospheres. The extent of the internal attack, such as grain boundary degradation, has not been included in the oxide layer measurements, or investigated in the current study. This is an important area which has been investigated, as will be discussed in Chapter 6. Microstructural degradation can result in a significant loss of strength in a material and, hence, reduce the life expectancy of a tube.

It is noted that the predicted time to failure of the 10 MPa case is of the order of millions of hours. In reality other damage mechanisms, such as fatigue, steamside corrosion, erosion and over-heating can be expected to cause failure before this time. In addition to these damage mechanisms, superheater tubes typically operate at higher pressures than 10 MPa. It is included here to capture the typical range of operating

superheater tubes. Due to the extremely long life expectancy of the 10 MPa case, there is a large effect of corrosion on the predicted life expectancy (44%).

It is clear that the Larson-Miller and damage predictions are in reasonable agreement for higher stresses but the damage predicts significantly longer lives for the lower stresses. The Larson-Miller results are clearly generally conservative, the degree of conservatism increasing with decreasing stress.

Oxide scale exfoliation can be evaluated based on fracture mechanics of brittle thin layers. It is first necessary to consider the various stresses which can exist in the oxide layer. The stresses in an oxide can be described as a superposition of six individual stress terms [96], as discussed in Chapter 2. This equation is reproduced here as follows:

$$\sigma_{Total} = \sigma_{IntrGrwth} + \sigma_{GeomGrwth} + \sigma_{Therm} + \sigma_{Creep} + \sigma_{Microcracking} + \sigma_{Mechanical} \quad (5-10)$$

where $\sigma_{IntrGrwth}$ and $\sigma_{GeomGrwth}$ correspond to the stresses which occur during oxide growth and relate to the formation of new oxides within the oxide layer and to the surface geometry (e.g. curvature, roughness) respectively, σ_{Therm} which refers to the thermally induced stresses from the different thermal expansion coefficients of the oxides and the metal, σ_{Creep} and $\sigma_{Microcracking}$, which are stress relief mechanisms associated with oxide creep and oxide damage, respectively, and σ_{Mech} , which is stress applied via mechanical loading e.g. internal pressure. For this work, only growth and thermal stresses exist. Crack initiation, delamination and separation of oxide scales can be defined via a critical strain criteria as presented by Sabau et al. [97].

One possible approach for implementing oxide scale formation and exfoliation of the oxide scales in computational modelling is the use of extended finite element methods (XFEM), with a micro-cracking initiation criterion (e.g. see Grogan et al. [225]) and by the use of a surface-based cohesive zone model (SCZM) (e.g. see Grogan et al. [226]), for the delamination process. Potential future work could model the oxide scale formation and exfoliation based on the critical strain criteria via these mechanisms.

It should also be noted that the modelled corrosion rate did not include microstructural damage. The creep data used here corresponds to accelerated creep tests at 650 °C. At lower temperatures, such as those associated with the corrosion tests (540 °C) reported

here, the creep rupture life would increase, leading to increased corrosion effects, as demonstrated by the 10 MPa case shown in Table 5.3, for example. Similarly, it can be expected that the rate of corrosion will increase with increasing temperature.

5.5. Conclusions

The corrosion mechanism which occurs when P91 steel is exposed to a synthetic salt, representative of the deposit formed during co-firing a 70:30 peat woodchip mixture at high temperatures, was studied. SEM images and EDX element maps have provided a key insight into the corrosion process. Scales, consisting of multi-layered oxides are shown to form and detach from the substrate via repeated cracking and spalling of the oxides. These oxides lose both their protective properties against further corrosion, and load bearing capability due to the repeated cracking and subsequent detachment from the substrate. This results in an extremely high corrosion rate when compared to samples tested without exposure to salts.

A finite element methodology was presented for pipes under internal pressure. The effect of corrosion and creep damage on the stresses through the wall thickness and on the life expectancy of a tube are presented. Results have been compared between tubes subjected solely to creep damage and to creep-corrosion damage. The model shows that the longer the exposure time to the corrosive environment, the greater the effect on rupture life expectancy.

Following on from the testing carried out at 540 °C on P91, it was determined that a microstructural investigation was required to better understand the corrosion mechanism.

6. Microstructural Investigation into the Corrosion Response of P91 Steel

6.1. Introduction

This chapter presents results from a detailed microstructural study into the response of P91 to altered deposit compositions. Etching of samples allowed for a thorough investigation into the complex corrosion mechanism to be undertaken. A more thorough understanding of the effect of the material microstructure on the corrosion process was thus obtained. In particular the detrimental effect of impurities in the steel, such as inclusions, was shown. Results from FE analysis on the effect of differential thermal expansion coefficients between inclusions and base metal are presented.

Alkali chloride containing deposits have been known to cause accelerated corrosion via a mechanism known as active oxidation, which has been described previously in Chapter 2. During the oxidation process, stress accumulates in the oxide scale, which can be divided into three distinct processes: 1) growth stresses which are intrinsically induced during oxidation, 2) stress due to thermal mismatch and 3) phase transformation of the oxide layer [163]. This stress can then be relaxed via several mechanisms, such as spallation and cracking of the oxide scale [164].

P91 is a high temperature steel which provides high creep strength and resistance to thermal fatigue. It consists of a complex, hierarchical microstructure containing grains, packets, blocks and laths (sub-grains), with carbides dispersed along grain and sub-grain boundaries to prevent creep deformation [116,124,131]. Figure 6.1 shows the microstructure of P91 which is discussed in further detail in Chapter 2.

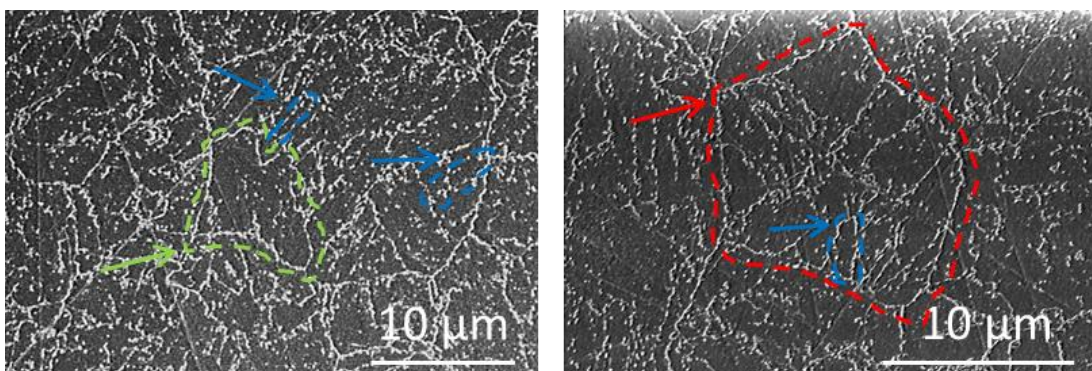


Figure 6.1: SEM images showing the hierarchical microstructure of P91. Red arrows point to prior austenite grains, green arrows point to packets and blue arrows represent blocks.

Impurities known as inclusions often form in steels during manufacturing due to chemical reactions with the environment and contamination. These inclusions are well known to act as pit nucleation sites [138–142] and also result in the loss of fatigue strength of a material [137,149]. The mechanism behind the pitting corrosion in a chlorine-containing environments is discussed in more detail in Chapter 2. It is generally accepted to occur through an initiation step and a propagation step involving the dissolution of the inclusion in a Cl-containing environment [140,145,148].

This chapter presents a detailed microstructural analysis of the response of P91 to two deposit compositions representative of different levels of co-firing. Experimental characterisation of the microstructural aspects of the corrosion process is presented. Inclusions in the metal are identified and the effect of these inclusions on pitting corrosion is investigated. Finite element modelling of the effect of inclusion composition on localised stresses is presented.

6.2. Methodology

6.2.1. Experimental

The experimental methodology adopted here is described in greater detail in Chapter 3. Synthetic salts representative of a 70% peat, 30% woodchip mixture and a 40% peat, 60% willow mixture, termed Salt A and Salt B as discussed in Chapter 3 are applied to P91 samples in a furnace at 600 °C for up to 28 days.

These samples were then fixed in epoxy, sectioned, ground, polished and etched to reveal the microstructure of the material. Samples were then analysed using optical microscopy, scanning electron microscopy (SEM) and energy dispersive X-ray spectroscopy (EDX).

6.2.2. Computational

The effect of the different thermal expansion coefficients (CTE) on localised stress concentrations at the inclusion-metal interface has been investigated via finite element (FE) models. A cylinder with a spherical inclusion located at its centre was modelled via an axisymmetric section of the cylinder wall, as shown in Figure 6.2. No

mechanical loading was applied during the modelling; all stresses occur as a result of thermal expansion and due to differences in the CTEs of the inclusion and metal. A temperature increase from 30 °C to 600 °C was applied via a change in the boundary temperature of the cylinder. A transient analysis was used in this study and the model ran until the temperature of the inclusion reached the outer boundary temperature. A mesh convergence study was carried out with respect to von Mises stress and plastic strain. A final mesh containing 7,000 4-node thermally-coupled elements achieved convergence to within 5%.

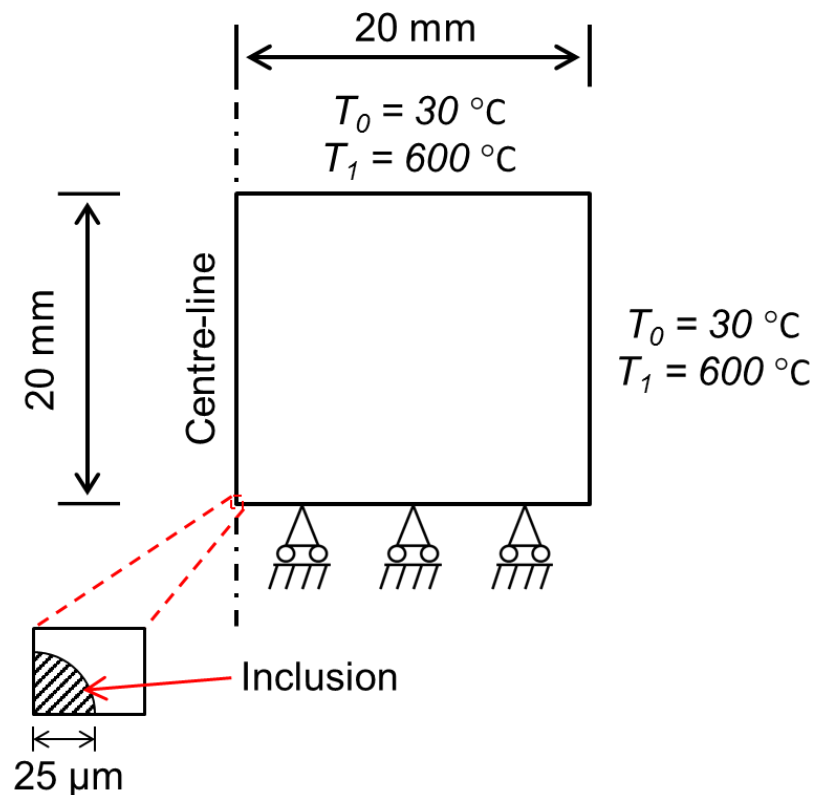


Figure 6.2: Dimensions and thermal loading of an axisymmetric FE model.

The effect of the different inclusion types was investigated by changing the thermal and mechanical properties applied in the model, based on data for different inclusions (Manganese sulphide (MnS), Aluminium oxide (Al_2O_3), and Titanium nitride (TiN)) presented in work by Melander [227], which can be seen in Table 6.1, along with material properties for P91 obtained from work by Yaghi et al. [228], where E is Young's modulus of the material, ν is Poisson's ratio, α is thermal expansion coefficient, ρ is density and σ_y is yield stress of a material.

The radius of the inclusion was assumed to be 25 μm for the purpose of this model, which is well above the previously-reported critical size for detrimental mechanical performance of materials ($> 10 \mu\text{m}$).

Table 6.1: List of material properties used in finite element model.

Material	E (GPa)	ν	α (1/K)	ρ (kg/m³)	σ_y (MPa)
MnS Inclusion	390	0.25	18×10^{-6}	3990	-
Al₂O₃ Inclusion	390	0.25	8×10^{-6}	3950	-
TiN Inclusion	320	0.19	9.4×10^{-6}	5220	-
P91 steel	125	0.3	1×10^{-5}	7860	400

6.3. Results

6.3.1. Experimental

6.3.1.1. Oxide layer analysis

In Figure 6.3 a sample exposed to salt A for 1 day is shown, upon which an oxide scale consisting of numerous layers is visible below the salt deposit. A number of cupola shapes can be clearly identified on the oxide scale, which is a common appearance associated with the active oxidation corrosion mechanism formed by the diffusing iron chloride gas. Additionally a tightly bound oxide is attached to the substrate, which is visibly darker than the substrate and second portion of oxide. This discolouration is due to the difference in atomic masses of the two distinct oxides and the substrate.

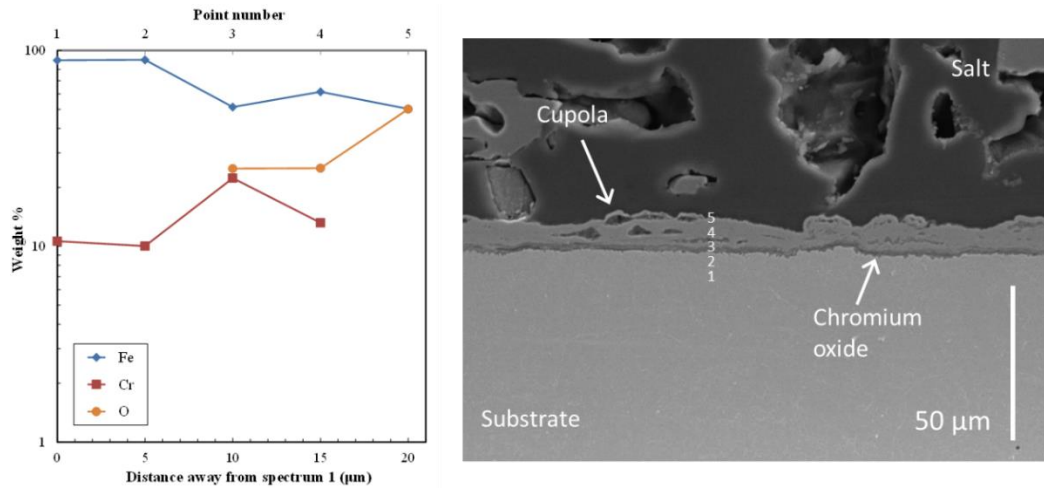


Figure 6.3: EDX point analysis and SEM image showing change in chemical composition through oxide and substrate surface, for salt A after 1 day.

EDX point analysis has been taken at 5 different points, through the depth of the sample, at 5 µm intervals as shown. As can be seen, no oxygen is present in the substrate. A large amount of chromium is measured at the oxide-substrate interface, on the oxide side (point 3), as expected due to chromium chloride being far less volatile than iron chloride; chromium oxide typically forms closer to the substrate. The chromium level drops with decreasing depth in the oxide (point 4), while at the surface of the oxide (point 5), where the sample is exposed to the salt, no chromium is detected and only iron oxide exists. Formation of the chromium oxide layer close to the substrate typically helps prevent further corrosion; however under these circumstances it can result in the formation of alkali chromates.

Figure 6.4 shows a montage of three SEM images of the surface of a sample exposed to salt A for 4 days at 600 °C, with two areas of higher magnification shown. The synthetic salt on this sample is separated from the substrate by a uniform solid oxide layer. There is very little evidence of cracking in this oxide scale. Thus it prevents the salt from reaching the substrate at any point. As a result of this, only a thin, tightly adhered oxide has formed beneath the upper oxide layer.

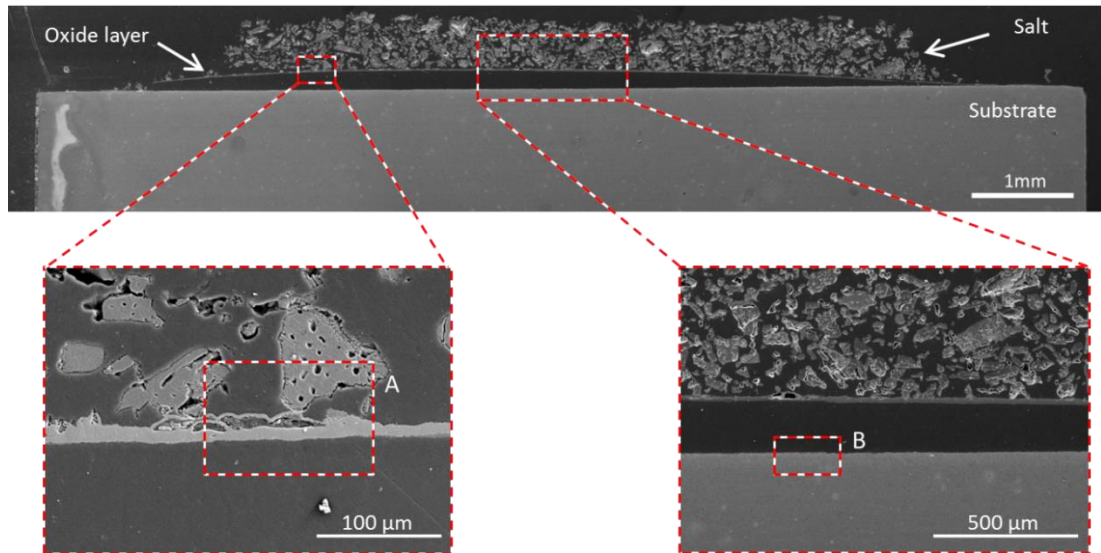


Figure 6.4: Montage SEM image showing entire surface of sample exposed for 4 days to salt A with two further magnified images showing oxide scale with areas analysed in Figure 6.5 identified.

Two images from the same sample are shown at a higher magnification in Figure 6.5 which show the tightly adherent oxide scale on the substrate surface, in addition to the uniform oxide layer and its structure. A number of cupola shapes can be identified on the oxide scale which has detached completely from the substrate. EDX point analysis was carried out on these locations with points taken through (a) the detached oxide scale and (b) the thin adherent oxide layer and the substrate itself.

On Figure 6.5 (a) the points at which EDX readings are obtained are shown, with points taken at location A of Figure 6.4, inset, a distance of 5 μm apart through the detached oxide scale. Two lines have been taken, which have been labelled L and R respectively. Both line traces display a similar trend with the oxide scale consisting primarily of iron oxide. The effect of delamination can be seen from the presence of chromium at point 3 on the L line, where point 3 corresponds to a point at the bottom portion of an oxide which has detached from the main oxide. Chromium is also detected at the bottom of the main oxide scale. This is expected as chromium oxide forms next to the substrate, and it is likely that growth stresses resulted in delamination [167].

Figure 6.5 (b) shows results for points taken through the tightly bound oxide scale, as shown in location B of Figure 6.4, inset, beneath the detached layer. As can be seen, the only oxide detected exists in the tightly adherent layer, with unoxidized metal

detected underneath. As well as oxygen, chlorine was also detected in this scale in the presence of iron and chromium, thus confirming the presence of iron-chromium chloride at the oxide-metal interface. Zahs et al. [85] have reported that bad adherence of the scale is caused by growth stresses and the formation of a chloride rich layer at the metal-oxide interface. The formation of chromium oxides will cause higher growth stresses as the evaporating chromium chlorides will convert to oxides at lower oxygen partial pressures than iron oxides and so will form closer to the substrate.

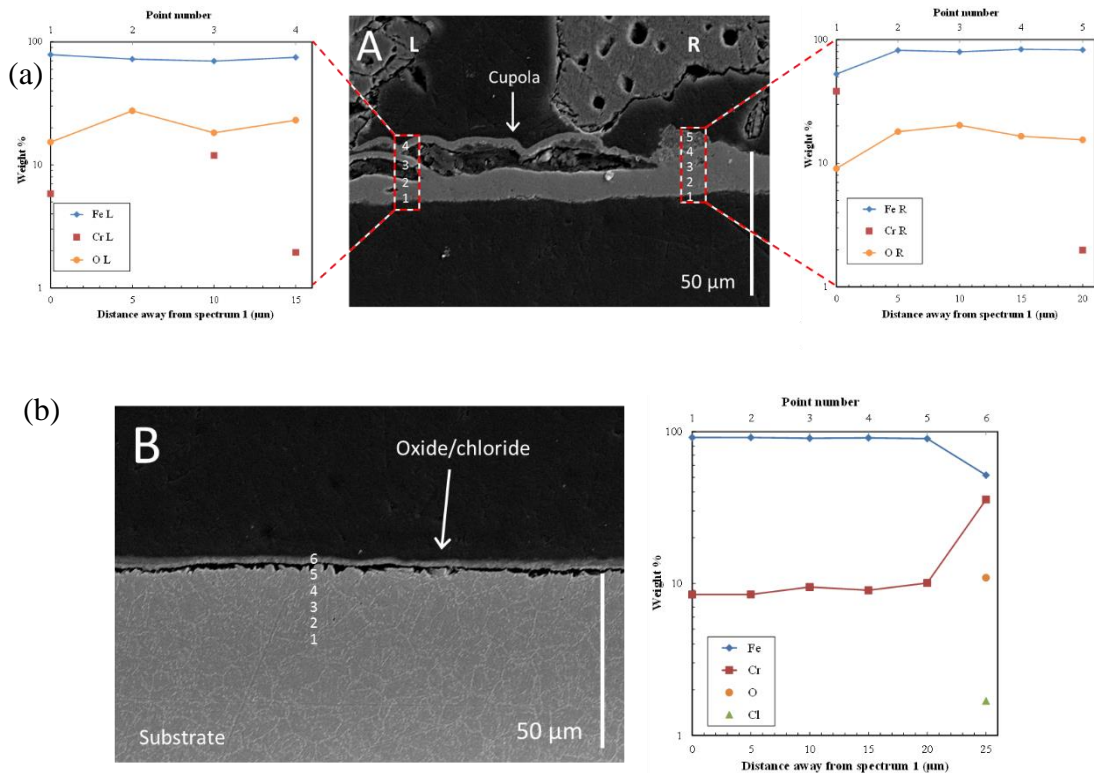


Figure 6.5: EDX point analysis and SEM image showing changing chemical composition through (a) oxide scale and (b) substrate surface, for salt A after 4 days.

In Figure 6.6 (a) a sample exposed to salt A for 7 days at 600 °C shows numerous layers of oxide, which have detached from the substrate. The multiple layers of oxides form due to repeated cracking and spallation of the oxide layers. A number of cupola shapes can be identified on the surface of the outermost oxide. Voids have formed between the layers due to repeating buckling of individual layers [166].

A sample exposed for 28 days to salt A is shown in Figure 6.6 (b); in this image we can see three distinct oxide layers. Two of these have detached significantly from the substrate and likely consist of primarily iron oxide with chromium oxide existing at

the point closest to the substrate, where detachment from the substrate would have occurred. This can be identified by the discolouration of the scale, due to the change in atomic masses.

The third oxide has formed very close to the substrate, and appears darker than the detached oxides. This likely consists of chromium oxide as, due to the relatively low volatility of chromium chloride (compared to iron chloride), it forms closer to the substrate. There is evidence of cracking in this oxide which is due to either growth stresses, or formation of chlorides at the oxide-metal interface. Furthermore it appears that these cracks lead to delamination from the unoxidized material, which results in a loss of the protective nature of the oxide.

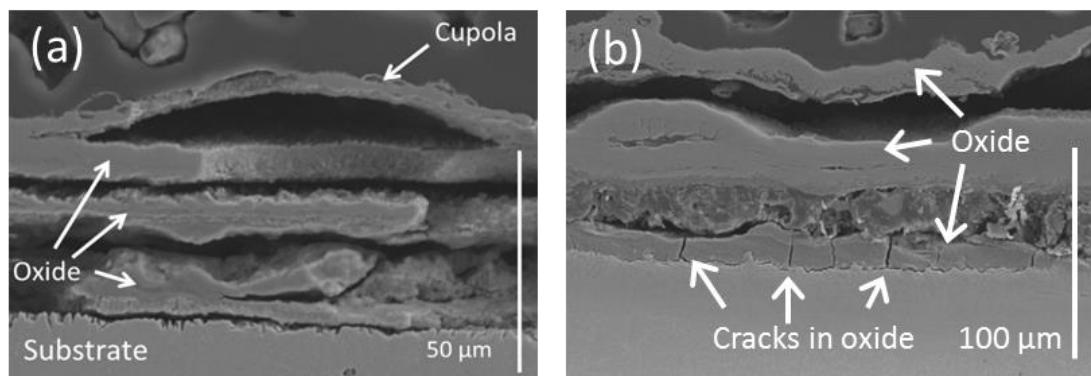


Figure 6.6: SEM images of sample exposed at 600 °C to salt A for (a) 7 days and (b) 28 days.

Figure 6.7 (a) shows the oxide scale which has formed over a sample following exposure to salt B for 7 days at 600 °C. This oxide appears close to the substrate and lacks the multi-layered appearance observed in samples exposed to salt A. Figure 6.7 (b) shows a sample exposed to salt B for 14 days. The oxide has detached from the substrate in this image; however it still consists of a single solid layer of oxide, with varying thickness along the sample. Again, the lack of multiple layers of oxide is evident in this image.

It is postulated that the lower chlorine content and higher potassium content of salt B may result in potassium chromate formation becoming the dominant form of corrosion; as opposed to the active oxidation mechanism, which is observed in the samples exposed to salt A. It is therefore proposed that there is a critical level of chlorine and potassium content for the deposit at which the dominant mechanism for corrosion changes from active oxidation, to alkali chromate formation.

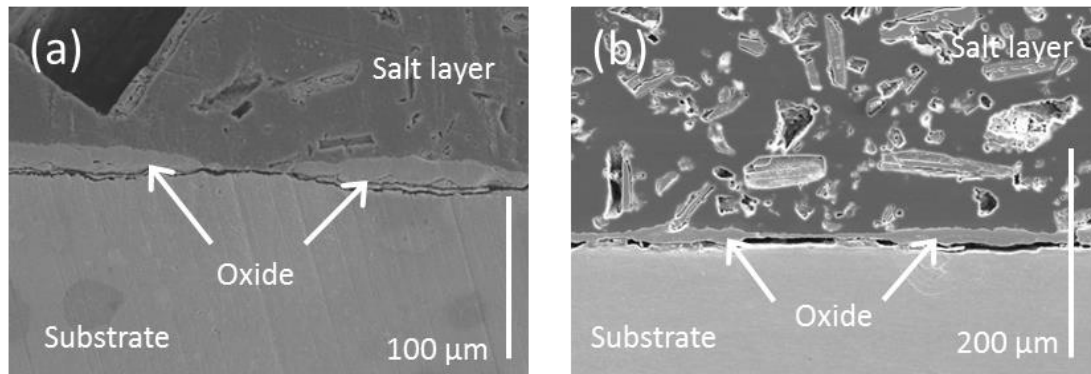


Figure 6.7: SEM images of sample exposed at 600°C to salt B for (a) 7 days and (b) 14 days.

Figure 6.8 shows EDX element maps taken from a region of oxide exposed for 14 days to salt A. The presence of Ca and S in the salt can be clearly identified. The high presence of oxygen in the detached layer clearly identifies it as an oxide, with Cr present closer to the metal surface, while the outer surface of the oxide consists primarily of Fe oxide. Furthermore there is clear evidence of oxidation of the substrate, as can be seen by the thin layer of oxygen which exists at the substrate surface.

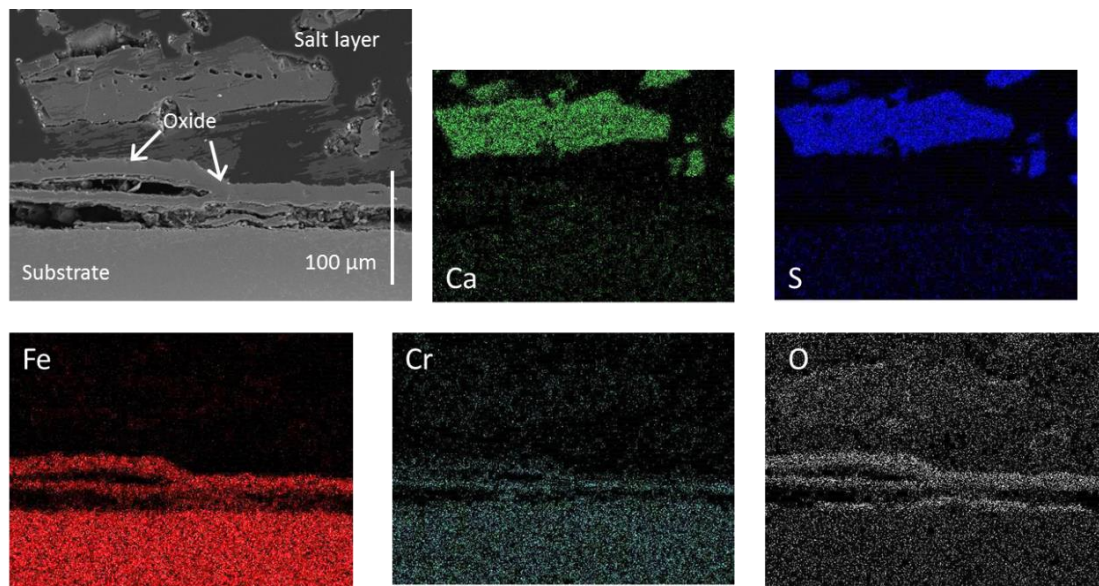


Figure 6.8: EDX element maps for sample exposed for 14 days to salt A.

Figure 6.9 (a) shows a sample of P91 exposed for 14 days from which cracks can be seen at the metal-oxide interface. These cracks are shown in further magnified images in Figure 6.9 (b) and (c). In Figure 6.9 (b) an area of oxide is shown which appears to have separated from the substrate. The detached surface of the oxide corresponds closely with the surface of the substrate, which is left intact. In Figure 6.9 (c) two SEM

images have been combined to provide a further magnified image of a portion of the sample. From this image multiple cracks can be seen, penetrating into the substrate.

It is postulated that these cracks may initiate from penetration of chlorine through grain boundaries resulting in the loss of material from either side of the boundary. These areas are then subjected to oxidation resulting in growth stresses, leading to crack initiation [167]. These cracks then propagate in a transgranular mode, resulting in the uniform detachment seen in Figure 6.9 (b). However, if these samples were mechanically loaded, for instance due to steam pressure, these cracks may propagate through the steel resulting in premature failure of tubes.

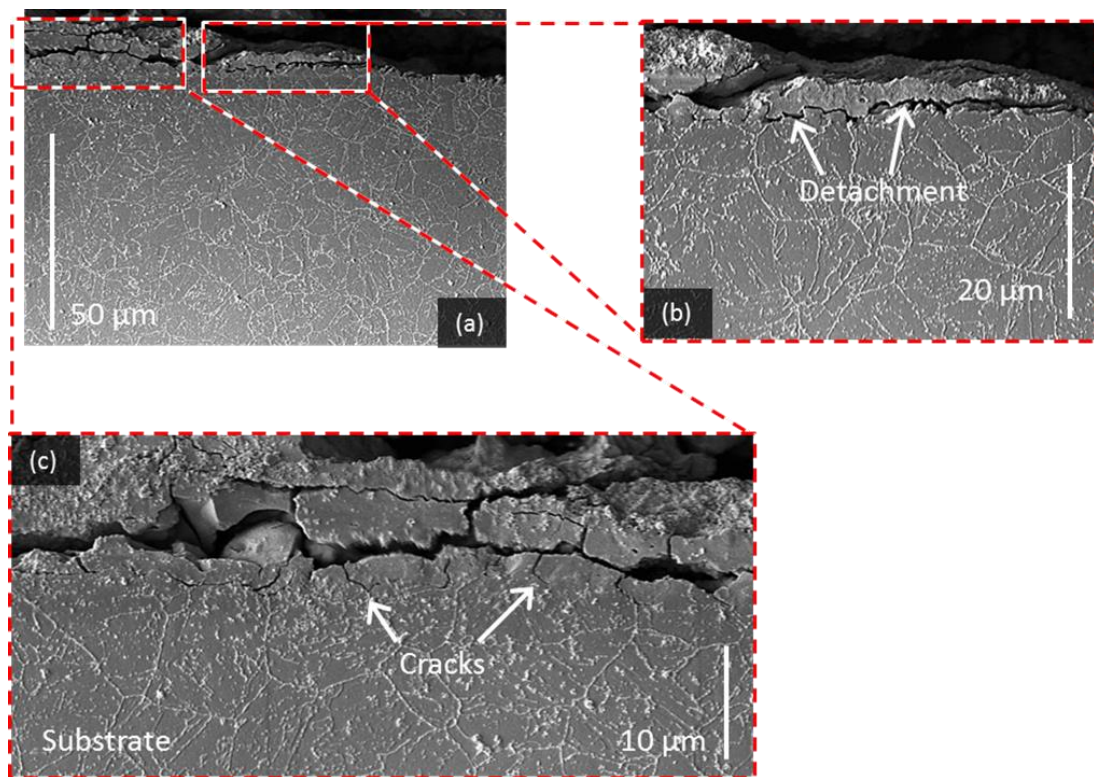


Figure 6.9: SEM images showing evidence of cracking at oxide/metal interface and cracks into metal following exposure to salt A for 14 days.

Figure 6.10 shows results of EDX point analysis taken along a section of a sample exposed to salt B for 21 days. The oxide layer is again located close to the substrate in a thick uniform scale, in contrast to the multi-layered oxides identified for salt A. The results of the point analysis show that oxide does not begin to form until point 3, which corresponds with the oxide-metal interface, with just chromium and iron being detected before this point. Point 3 contains sulphur and calcium in addition to iron,

chromium and oxygen. It appears as though small particles of the deposit may have travelled through a gap in the oxide scale to reach this point, as calcium and sulphur are large components of the deposit. The chromium level again decreases at the analysis reaches the top of the substrate, with the outermost point consisting entirely of iron oxide.

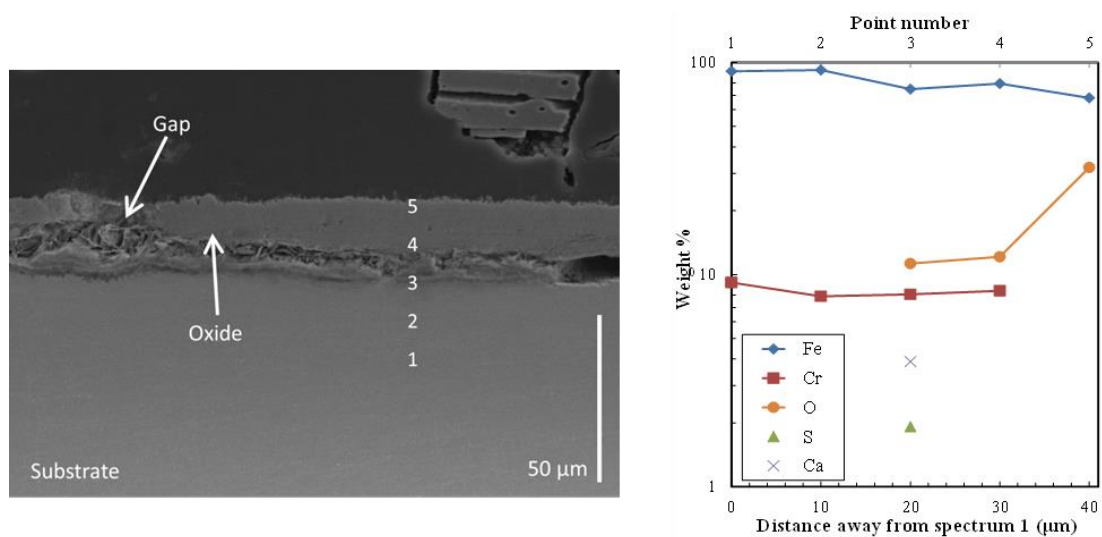


Figure 6.10: SEM image showing sample exposed to salt B for 21 days with EDX point analysis carried out for the 21 day sample.

6.3.1.2. Oxide Scale Measurements

Figure 6.11 shows a comparison of oxide layer thickness measurements obtained from testing P91 exposed to (a) salt A at 540 and 600 °C and (b) salt A and salt B at 600 °C. The oxide layer thickness increases with a temperature increase from 540 to 600 °C as expected. The 540 °C measurements presented have been discussed in detail in Chapter 5. The difference in corrosion rates between salt A and salt B shown in Figure 6.11 (b) is of interest and shows the importance of chlorine on the corrosion rate of metals.

From analysis of the oxide layers formed, the lower chlorine and higher potassium content of salt B resulted in the formation of a more protective oxide scale, controlled by the active oxidation mechanism. The higher chlorine content present in salt A leads to the formation of multiple layers of oxides which have detached from one another at multiple locations and the corrosion features, e.g. cupola shapes, which are typical for corrosion via active oxidation.

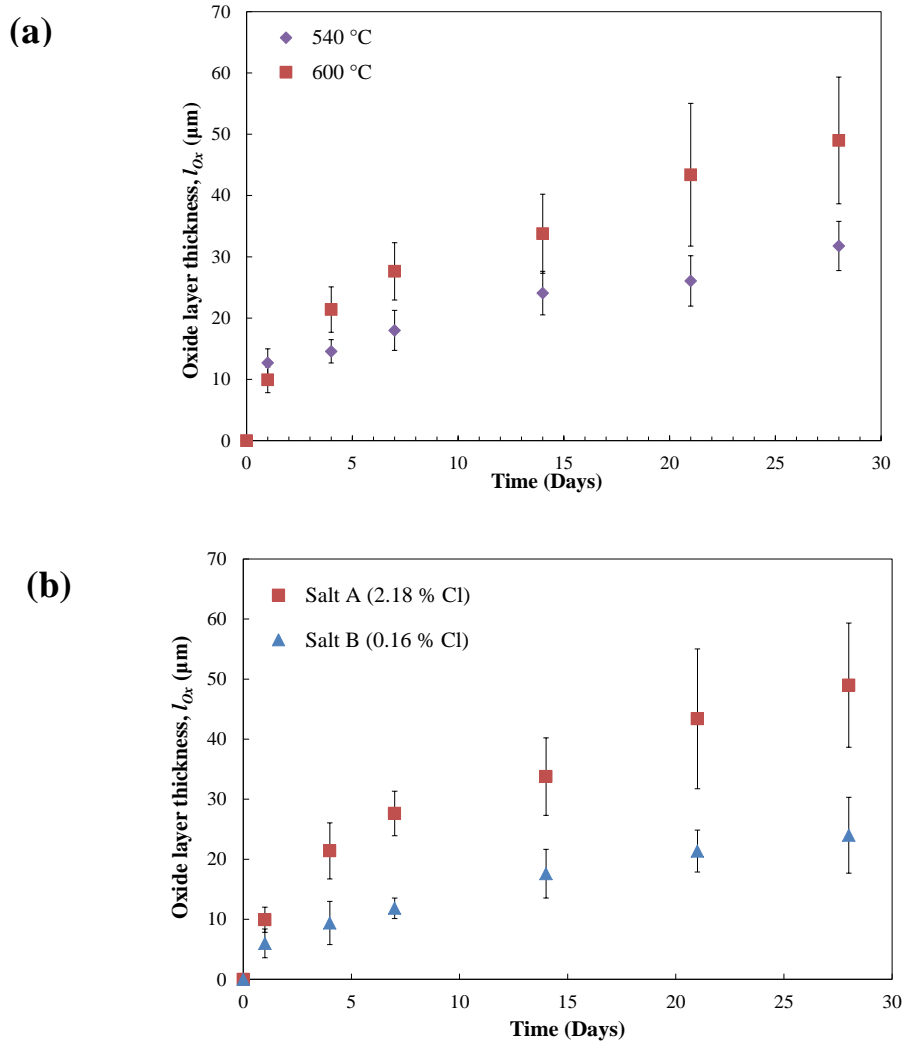


Figure 6.11: Oxide thickness measurements of P91 following exposure to (a) salt A at 540 and 600 °C and (b) salt A and salt B at 600 °C.

6.3.1.3. Inclusions and Pitting Corrosion

Figure 6.12 shows two inclusions clearly identified in the sample. The larger inclusion here was measured and found to have an exposed area approximately equal to $29 \mu\text{m}^2$, with an estimated maximum diameter of $6.2 \mu\text{m}$. It must be noted however, that this is just a two dimensional section of the inclusion which may vary in size and shape in the third dimension.

Results of EDX elemental analysis carried out on the inclusions are also shown in Figure 6.12. As can be seen there is an absence of chromium from all three sample locations, with locations 1 and 2 being classified as sulphates, primarily calcium sulphate. This is important as calcium sulphates, in particular, have been shown to

affect the corrosion resistance of steel, in particular pitting corrosion and cracking induced by stress corrosion [143,144]. The second inclusion is identifiable as an iron carbide inclusion. Subsurface inclusions are known to act as crack initiation sites in fatigue therefore the presence of the inclusions must be considered when looking at samples [149]

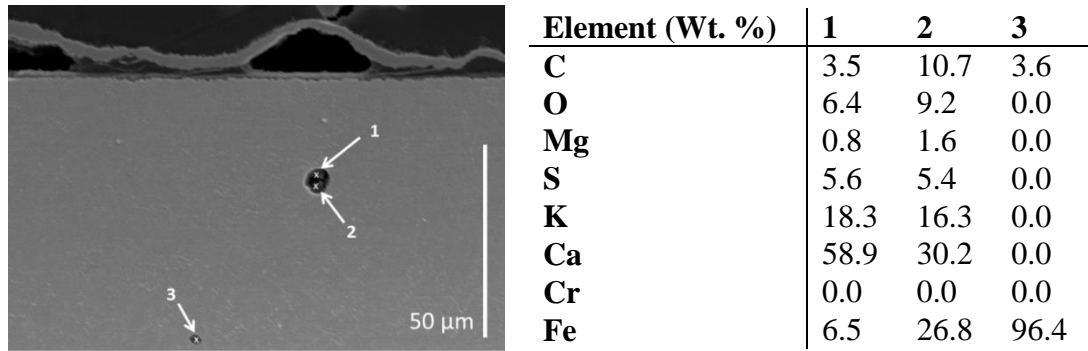


Figure 6.12: EDX point analysis of 2 inclusions located in sample.

Figure 6.13 (a) shows numerous inclusions which are clearly visible throughout the depth of the sample. The inclusions vary in size; however, due to the additional detrimental effect which occurs when inclusions are clustered, they are considered quite significant in terms of potential sites for crack nucleation [153]. Furthermore one inclusion is located close to the surface, which may lead to pit initiation, and related problems caused by pitting.

Figure 6.13 (b) shows a magnified image of an inclusion which was observed in a sample. Measurements of the area show that it has an approximate area of $304.89 \mu\text{m}^2$, with a maximum measured diameter of $23.05 \mu\text{m}$. This is above what is considered the critical inclusion size for affecting fatigue life ($> 10 \mu\text{m}$). It is possible that the area of this inclusion has been increased following etching, however it is unlikely to have resulted in a major difference in size.

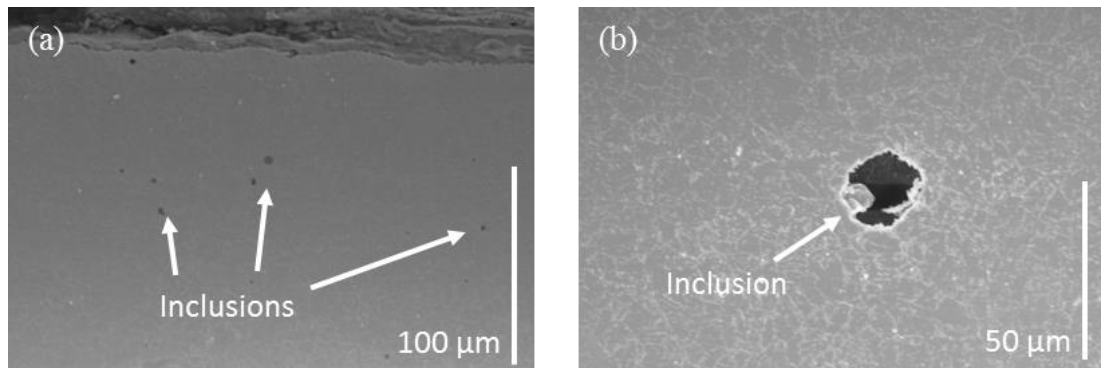


Figure 6.13: SEM images showing (a) numerous inclusions present in sample (b) image of large inclusion located in sample.

In Figure 6.14 a sample showing an oxide layer over the substrate following 7 days exposure to salt A is shown. Pitting corrosion and internal oxidation are also clearly visible in the image. Cracks are visible in the pit and along the oxide scale attached to the surface. EDX point analysis and mapping display the chemical composition of the sample. The depth of the pit was measured including the area identified as internal oxidation and found to be approximately 24.44 μm in depth.

The points for the EDX analysis were taken 30 μm apart. Point 1 shows that the first oxide scale, which has detached, consists primarily of iron oxide. The oxide which has formed a pit consists of a mixture of iron, chromium oxide, and a small amount of sulphur present. The third point analysed in the unoxidized metal, consists of just iron and chromium as expected. The presence of sulphur in the pit indicates that it likely began as an inclusion and formed a pit based on the mechanism previously discussed.

The maps confirm the large amount of oxygen present in the adherent oxide layer in addition to the pit. It also shows the lack of iron present in these areas, while the detached oxide consists primarily of iron oxide, with chromium oxide formed only at the bottom of the detached oxide. There is significant cracking of the oxide formed in the pit in addition to the oxide bound to the substrate; again this is thought to be due to growth stresses.

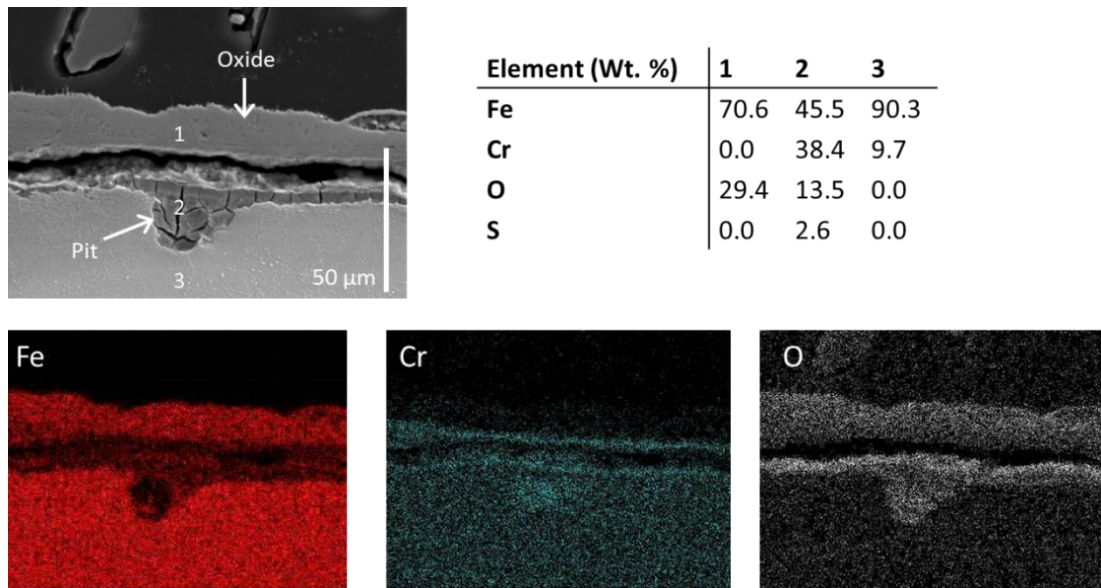


Figure 6.14: EDX element maps and point analysis following exposure for 7 days to salt A.

Figure 6.15 shows an inclusion at the oxide-metal interface, in the initial stages of pit formation. EDX point analysis and mapping have been carried out to determine the chemical composition at this location. Point 2 and 3 show significant chromium enrichment in the inclusion, while point 4 and 5 were found to contain bromine. Additionally micro-crevices are visible around the inclusion. This chromium enrichment and formation of micro-crevices are steps involved in the sequence of pitting corrosion previously discussed.

The presence of sulphur indicates that this inclusion consisted initially as a sulphide which is now being subjected to the corrosion process discussed previously. The pit depth reached approximately 27.3 μm . Point 7 and 8 display the chemical composition of unoxidized P91. It is noted that the peaks obtained from Mo and S from EDX analysis are similar and can be misread as one another by the EDX software, however due to the location of the point analysis in the pit, it is believed to be S.

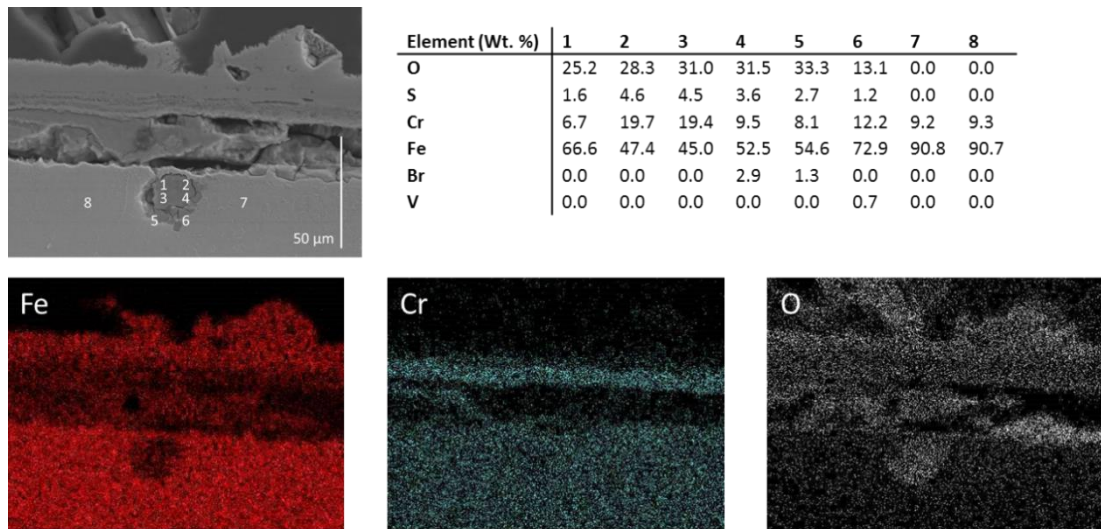
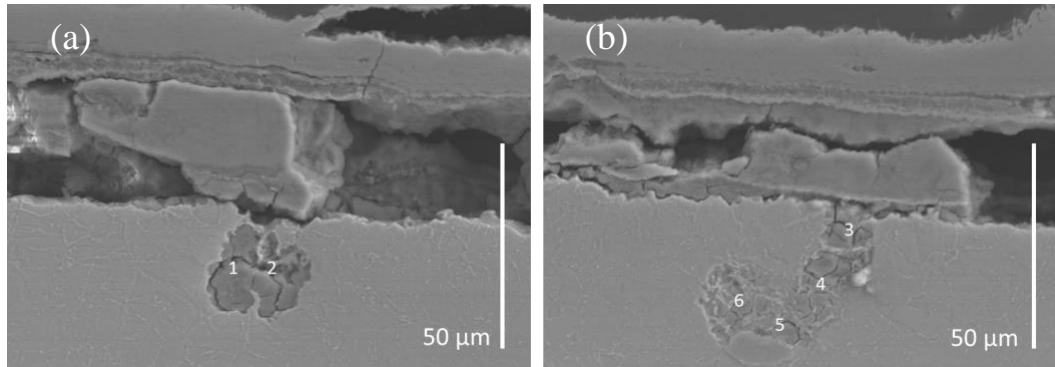


Figure 6.15: EDX element maps and point analysis showing pitting corrosion following exposure for 21 days to salt A.

Figure 6.16 (a) displays an inclusion which appears at the oxide-metal interface of a sample exposed to salt A at 600 °C for 21 days. Again chromium enrichment is measured at point 1, which has not occurred to the same extent at point 2. However both points confirm the presence of an oxide, which is likely to form a larger pit with further exposure. Figure 6.16 (b) meanwhile shows evidence of undercut pitting corrosion.

This is considered one of the most dangerous forms of pitting, as it appears to only affect a small area from the surface, but is actually extensive beneath the surface of otherwise unoxidized material. EDX analysis has been carried out on the area which appears to consist of corrosion products and the area has been confirmed to consist of oxide (EDX points 3-6). Chlorine has been identified at points 4 and 5 in the corrosion product, presumably in the form of chromium-iron chloride.



Element Wt %	1	2	3	4	5	6
O	39.5	14.6	26.5	11.3	11.9	3.2
S	5.3	1.4	3.5	0.5	0	0
Cl	0	0	0	0.7	0.4	0
Ca	0	1.1	0	0	0	0
Cr	29	11.2	18.3	13.7	12.8	9.5
Fe	26.2	71.8	51.8	73.8	74.9	86.7
V	0	0	0	0	0	0.6

Figure 6.16: EDX point analysis taken at a number of points in two examples of pitting corrosion observed in a sample exposed to salt A for 21 days at 600 °C.

6.3.2. Modelling

Results from finite element (FE) modelling using the general purpose, non-linear code Abaqus are presented in this section. Three different inclusion types were modelled based on varying elastic material properties, namely MnS, TiN and Al₂O₃ inclusions.

Figure 6.17 shows contour plots displaying the von Mises stress (MPa) distributions for the three inclusions in P91 steel, with the inclusions magnified. All three models display regions of stress concentration around the inclusion. The MnS inclusion is predicted to cause the highest stress concentration. This is attributable to this inclusion having the highest mismatch in CTE and elastic modulus with the P91 matrix. The second highest stress concentration is predicted at the Al₂O₃ inclusion. The Al₂O₃ inclusion has an equally large elastic modulus mismatch with P91 as MnS with a reduced CTE mismatch. The TiN modulus mismatch is slightly less than for Al₂O₃ and MnS, although the CTE mismatch is similar to Al₂O₃, the Poissons ratio mismatch is also greater. This highlights the importance of the CTE in producing stress concentrations at inclusions.

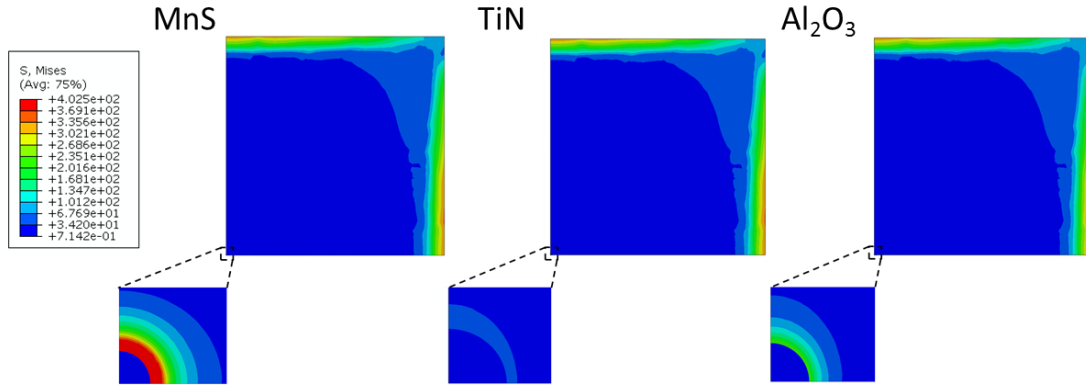


Figure 6.17: Contour plots showing the Mises stress (MPa) for MnS, TiN and Al₂O₃ inclusions in P91 steel following exposure to temperatures of 600 °C.

Figure 6.18 shows contour plots of predicted equivalent plastic strain distributions for the inclusions. For this model the inclusions have been assumed to be perfectly elastic. The outer edges of all samples display plastic strain; however the inclusion-metal interface is of most interest to this study. Plasticity is not predicted for the TiN and Al₂O₃ inclusion-metal interfaces. The stress concentrations at these points were less than the yield stress of P91. The higher plastic strain and stress concentrations are predicted at the MnS inclusion-matrix interface. Potential future work could include a study on a number of inclusions across the samples and investigate the effect of clusters of inclusions on stress distributions.

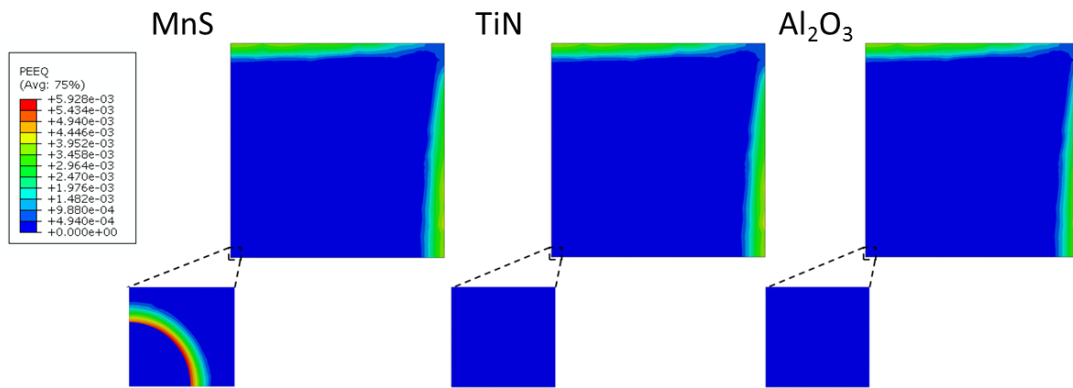


Figure 6.18: Contour plots showing the equivalent plastic strain for MnS, TiN and Al₂O₃ inclusions in P91 steel following exposure to temperatures of 600 °C.

6.4. Discussion

The results presented in this chapter illustrate the main corrosion phenomena which occur during biomass co-firing. The exact mechanism by which the process occurs is found to depend on the alkali and halide (e.g. potassium and chlorine) content in the deposit. If the chlorine content is high, then the corrosion process will proceed via the 'active oxidation' mechanism, such as in salt A in this work. In this mechanism, cupolas of oxide form which consist primarily of iron oxide at the outermost point of the scale, with chromium oxide forming close to the substrate.

Should the potassium level be high and the chlorine level low, then corrosion occurs at reduced rates due to the formation of alkali chromates, as opposed to active oxidation. The oxide layers observed on samples exposed to salt B do not display the typical characteristics of active oxidation (e.g. multiple layers of oxide, cupolas). Instead the oxide scale typically consists of one solid oxide layer, with perhaps a thinner oxide layer located between it and the substrate, indicating that active oxidation is not the dominant corrosion mechanism for salt B.

Cracking has been observed both in the chromium oxide, which has formed above the substrate and in unoxidized metal. These cracks have been shown to travel in a transgranular mode and result in the delamination of unoxidised metal, thus further reducing the load-bearing capability of tubes.

Comparison of results from tests carried out at 540 and 600 °C clearly show the effect of temperature, with higher corrosion rates observed at 600 °C. Salt A was also found to be more corrosive than salt B. This was expected as salt A has a higher Cl content, which results in the more damaging active oxidation corrosion process.

Numerous inclusions were identified throughout the samples tested. These are known to act as sites for crack nucleation which can lead to premature failure of tubes. Additionally, inclusions above 0.7 µm in size, which reach the sample surface in aggressive environments, are well known to act as sites for pitting corrosion [140].

Pitting corrosion has been observed at sites where inclusions are at the sample surface and have acted as pit initiation sites. Significant chromium enrichment was detected in the pits in addition to micro-crevices which are common features of pitting

corrosion initiated at inclusions. Undercutting pitting corrosion has also been identified in samples tested. The numerous different corrosion mechanisms detected during testing are shown schematically in Figure 6.19.

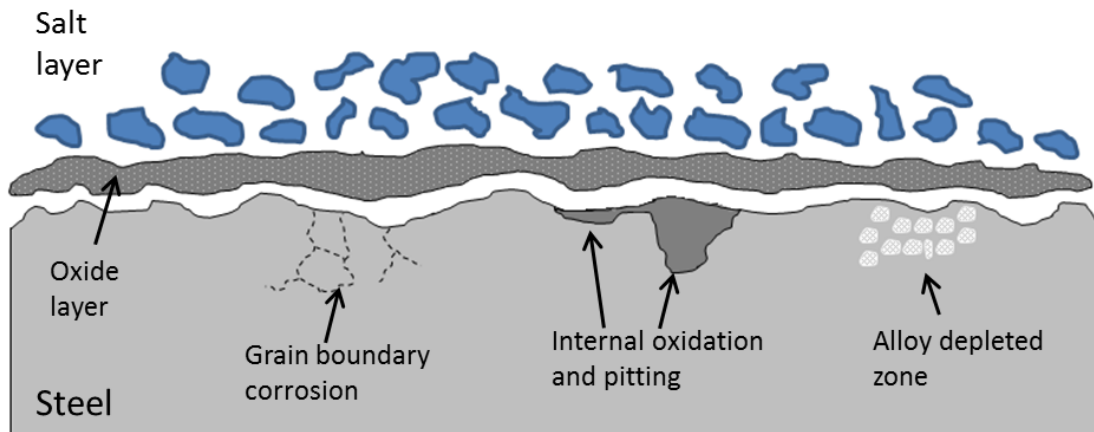


Figure 6.19: Schematic of sample cross section showing various corrosion mechanisms following corrosion testing (Adapted from [229]).

Regions of stress concentrations around inclusions, are clearly identifiable from the finite element modelling. This is particularly true for sulphide inclusions. The MnS inclusion modelled resulted in the formation of an area of localised plastic strain that is an important observation as regions of plastic strain are susceptible to cracking. It is also noted that only one relatively small inclusion was modelled, and it was located far away from the substrate surface and that if multiple inclusions were modelled the stress/strain concentrations would increase. These areas of localised stresses may result in increased corrosion rates, as the higher stress levels are known to result in multiple layers of non-protective oxides forming due to repeated cracking of the oxide [101].

6.5. Conclusions

A microstructural investigation into the rapid corrosion, which occurs during biomass co-firing has been undertaken. Samples of P91 have been exposed to two salts representative of different levels of co-firing. Inclusions were located throughout the metal samples following testing and their potential influence on stress levels in samples was modelled using the finite element program Abaqus. The following are the main conclusions drawn from this work:

- 1) The mechanism of corrosion during co-firing depends significantly on the chlorine and potassium content of the deposit formed. If the deposit has a high enough chlorine content, active oxidation will take place, with multiple detached layers forming over the substrate offering little protection against further corrosion. If the potassium content is high and chlorine content low then alkali chromates will form leading to a reduced rate of corrosion compared to that found during active oxidation.
- 2) Cracking has been observed in chromium oxide formed close to the substrate, due to growth stresses of the oxide. Additionally, cracking has been observed in unoxidized material, which is attributed to intergranular penetration of chlorine and subsequent oxidation.
- 3) Pitting corrosion which initiated at near-surface inclusions has been observed on a number of samples.
- 4) A large number of inclusions have been observed throughout the depth of the sample, which will act as sites for crack nucleation.
- 5) Finite element modelling of the inclusion-metal thermal mismatch demonstrated that sulphide inclusions cause the highest stresses and plastic strains at the inclusion-metal interface.

7. Microstructural Investigation into the Corrosion Response of 347SS

7.1. Introduction

This chapter presents results from a microstructural investigation into the accelerated corrosion of 347SS following exposure to two salts representative of deposits formed during different levels of biomass-peat co-firing. The methodology adopted in this chapter is similar to that of Chapter 6, which presented an analysis of P91 steel. The microstructural mechanisms of active oxidation are investigated. Comparisons are made between the corrosion rate and mechanism of 347SS to observations made for P91 in this chapter. Measurements of pits taken from in-situ tubes and laboratory test samples are presented. Finite element (FE) models were developed to investigate the effect of pitting corrosion on localised stresses in pressurised tubes.

347SS is an austenitic stainless steel with a fine grain microstructure containing small and uniformly distributed NbC precipitates. These precipitates help to pin grain boundaries, thus preventing or minimising grain coarsening. 347SS is widely used in operational plants, primarily due to its high steam-side corrosion resistance [127]. This high corrosion resistance is attributed to the Cr content (17 – 19%) and the fine grain structure, which promotes chromium diffusion along grain boundaries resulting in a protective Cr_2O_3 layer forming over the substrate. Figure 7.1 shows the microstructure of 347SS studied here. Further detail on the microstructure and material properties of 347SS are given in Chapter 2.

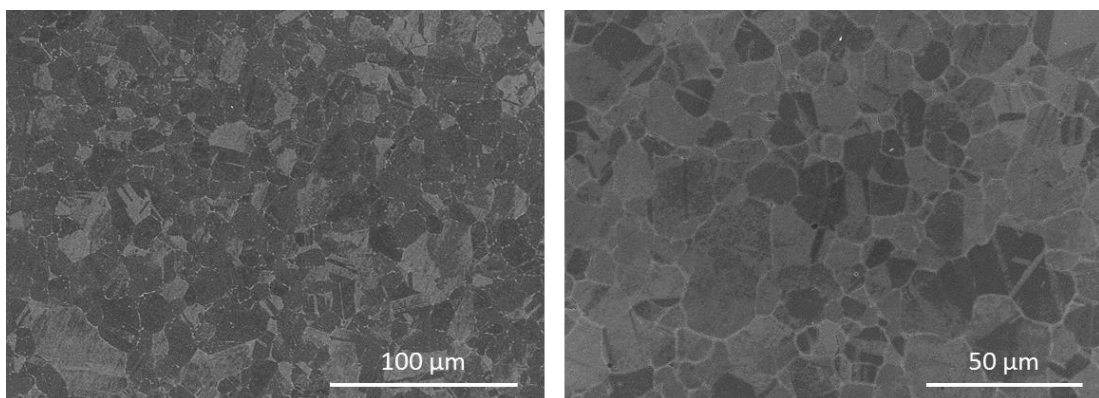


Figure 7.1: SEM images showing the microstructure of 347SS.

As for P91 in Chapter 6, a number of inclusions were experimentally detected during the study. Inclusions are well known to affect the fatigue strength of materials and can lead to pitting corrosion. The effect of inclusions on material performance is discussed in further detail in Chapter 2.

7.2. Methodology

7.2.1. Experimental

Samples were prepared in the same manner as described in Chapters 3 and 6. Synthetic salts representative of a 70% peat, 30% woodchip mixture and a 40% peat, 60% willow mixture, termed Salt A and Salt B were applied to 347SS samples in a furnace at 600 °C for up to 28 days. Samples were prepared as detailed previously revealing the material microstructure across a cross-sectional area of the samples.

For this study, a number of duplicate samples were placed in the furnace for 7, 14 and 21 days, respectively. Once removed from the furnace, the samples were (1) cleaned in an ultrasonic bath and (2) pickled using Vilella's reagent to remove any loose oxide on the substrate surface. This allowed for a comprehensive analysis of the sample surface. Further insight into the morphology of pits and surface inclusions was obtained from these samples. Samples were analysed using optical microscopy, scanning electron microscopy (SEM) and energy dispersive X-ray spectroscopy (EDX).

7.2.2. RepliSet samples

Replica samples were taken from in-situ tubes, which were in operation for approximately 22,100 hours (\approx 2.5 years) in Lough Ree power station, using the RepliSet system [202]. The RepliSet system is a non-destructive system for producing 3D replicas of surfaces to a resolution down to 0.1 μm [202]. The material of the tubes was 347SS, thus providing a direct comparison with our experimental tests. Lough Ree Power used pure peat as a fuel, therefore a lower corrosion rate is expected from these samples.

Samples were taken from five different sections of heat exchanger tubes along the tube banks. These tubes experience different levels of exposure to the ash formed during

combustion. Samples were analysed using white light interferometry, focusing on areas of the samples where pits were identified. Three areas from each section of tubing were analysed.

7.2.3. Computational

The effect of pitting corrosion on localised stress levels was investigated using the general purpose, non-linear finite element program Abaqus. This model is based on work carried out by Grogan et al. [108] at NUI Galway, which simulated pitting corrosion on bioabsorbable metallic stents. It is also similar to work carried out by Wenman et al., [104] which makes use of element deletion to model 2D stress corrosion cracking in heat exchanger tubes. This work applies the element deletion technique to a simple pressurised tube and investigates the effect of various pit sizes on stress distributions in the tube.

A region of the tube is defined as the exposed surface, which for the purposes of this work was applied to a section of outer of the tube, as shown in Figure 7.2. This area is intended to correspond to the region of largest deposits on heat exchanger tubes and consequently is the region where pits are most likely to form.

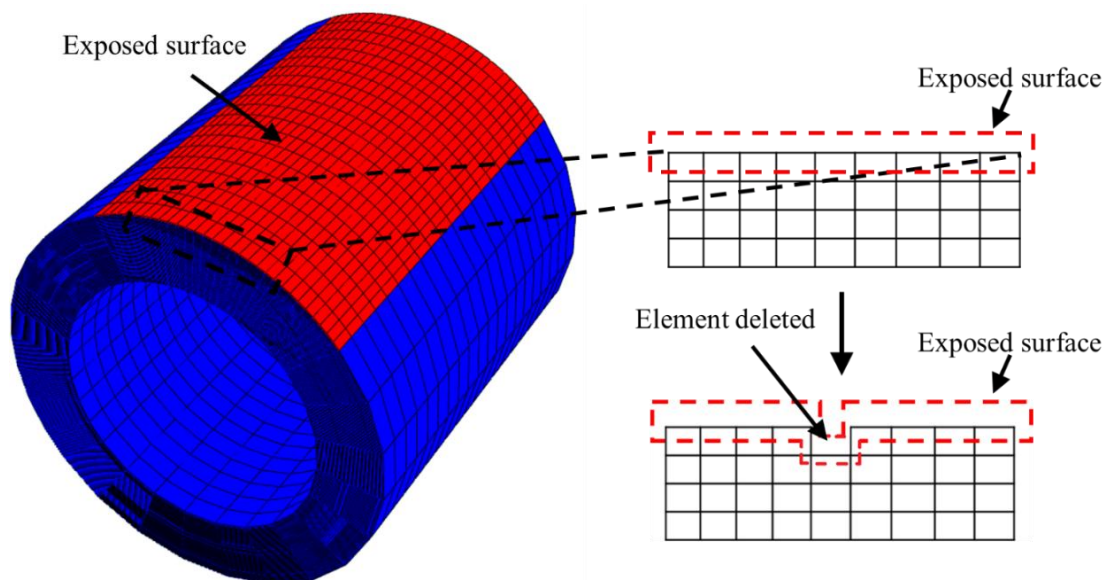


Figure 7.2 FE mesh showing exposed surface of tube and how element deletion leads to redistribution of the exposed surface.

Following definition of the exposed surface area, each element on the surface is assigned a random number, λ_e , based on a random number generator, via a Python

based pre-processor and a standard Weibull distribution. λ_e controls the heterogeneity of the pitting corrosion process. The probability of the value of λ_e lying in the range $[a, b]$ for each element is given by the following:

$$\Pr[a \leq \lambda_e \leq b] = \int_a^b \gamma(x)^{\gamma-1} e^{-(x)^\gamma} dx \quad (7-1)$$

where γ is a dimensionless distribution shape factor; increasing the value of γ provides a more symmetric Weibull distribution, leading to a narrower range of λ_e values being assigned, providing more homogeneous corrosion, with the condition that $x \geq 0$ and $\gamma > 0$. Based on this random distribution, damage is seeded for particular elements via the user subroutine VUMAT.

Damage is assigned to elements on the exposed surface based on the following damage evolution law:

$$\frac{dD_e}{dt} = \frac{\delta_U}{L_e} \lambda_e k_U \quad (7-2)$$

where k_U is a corrosion kinetic parameter, in units of hr^{-1} and δ_U and L_e are material and FE model characteristic lengths, in units of mm, as described in Ref. [230]. Once an element has reached a D_e of 1, it is deleted from the FE mesh and the connected elements inherit the value of its pitting parameter according to the following:

$$\lambda_e = \beta \lambda_n \quad (7-3)$$

where λ_n is the pitting parameter value in the recently deleted element and β is a dimensionless parameter that controls the acceleration of pit growth in the FE analysis [108]. Pits therefore continue to grow once the elements initially on the exposed surface are removed from the mesh.

The tube is meshed using approximately 70,000 linear reduced integration brick elements, with an element size of 126 μm . The size of the elements was chosen to closely replicate measured pit sizes from in-situ data and experimental testing. Although a smaller element size was desirable, the number of overall elements required to obtain this would increase the run-time of the model substantially. An internal pressure of 10 MPa was applied to the tube walls.

A simple rectangular specimen was modelled initially of measurements 2.5 x 2.5 x 0.75 mm. This was then partitioned along the top half of the sample and a fine mesh was generated at the surface of the sample, providing an element size of 7.5 μm and element length of 50 μm . This allowed for an accurate representation of pits witnessed on test samples.

7.3. Results

7.3.1. Experimental

7.3.1.1. Oxide layer analysis

This section presents SEM images for the 347SS samples exposed to salt A and salt B at 600 °C for 1, 4, 7, 14, 21 and 28 days. From these images, valuable information regarding the corrosion mechanism and the complex structure of the corrosion layers was obtained. Figure 7.3 shows SEM images of the sample cross-sectional areas exposed to salt A.

Following 1 day exposure, a thick, relatively uniform oxide scale was detached from the substrate (Figure 7.3 (a)). Although some voids are present in the scale, it is primarily solid. The sample exposed for 4 days (Figure 7.3 (b)), shows a similar structure with a relatively uniform layer present above the substrate, with voids noticeable through this layer.

Figure 7.3 (c) shows a sample exposed for 7 days; again a uniform oxide scale is visible detached from the substrate surface, with some intergranular corrosion detected. A number of cupolas are present on the surface of the oxide scale. A sample exposed for 14 days is shown in Figure 7.3 (d) where a large cupola is visible above the substrate, attached to a more uniform oxide scale. Again, voids can be identified in the uniform oxide scale. Additionally there appears to be some localised coarsening of the grains at the substrate surface.

A uniform oxide scale is again present above the sample exposed for 21 days, as shown in Figure 7.3 (e). Similarly, the sample exposed for 28 days shows that a uniform oxide scale has formed and detached from the substrate, as shown in Figure 7.3 (f).

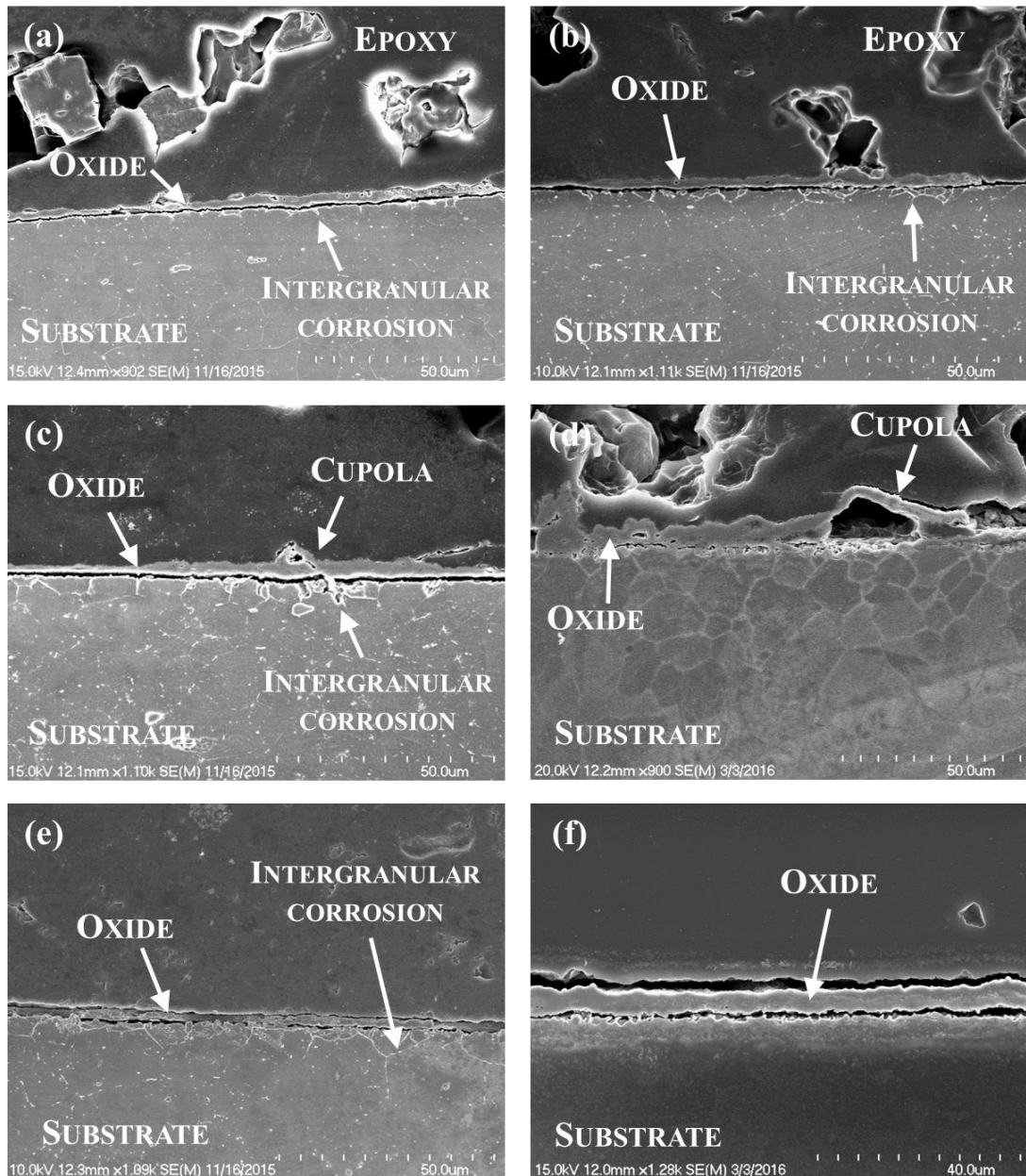


Figure 7.3: SEM images of 347SS after exposure to salt A at 600 °C for (a) 1 day; (b) 4 days; (c) 7 days; (d) 14 days; (e) 21 days; (f) 28 days.

SEM images of the samples exposed to salt B at 600 °C are shown in Figure 7.4. Figure 7.4 (a) shows the sample exposed for 1 day on which a uniform oxide scale has formed directly on the substrate. This oxide scale appears quite consolidated in nature and would help prevent against further corrosion. Similar oxide scales are observed for the samples exposed for 4, 7 and 14 days respectively (Figure 7.4 (b), (c) and (d)). These samples all display a uniform, non-porous oxide scale formed directly above the substrate.

Figure 7.4 (e) shows a sample exposed for 21 days. In this sample a uniform oxide scale again exists close to the substrate surface. The oxide scale appears to be separated from the substrate by a thin layer and cupolas of oxide are visible on the oxide scale. A sample exposed for 28 days is shown in Figure 7.4 (f). The oxide scale has now completely detached from the substrate and will likely offer no further protection against corrosion. The gap between substrate and oxide has likely grown larger following the addition of the epoxy. Additionally cupolas of oxide are again visible on the oxide surface.

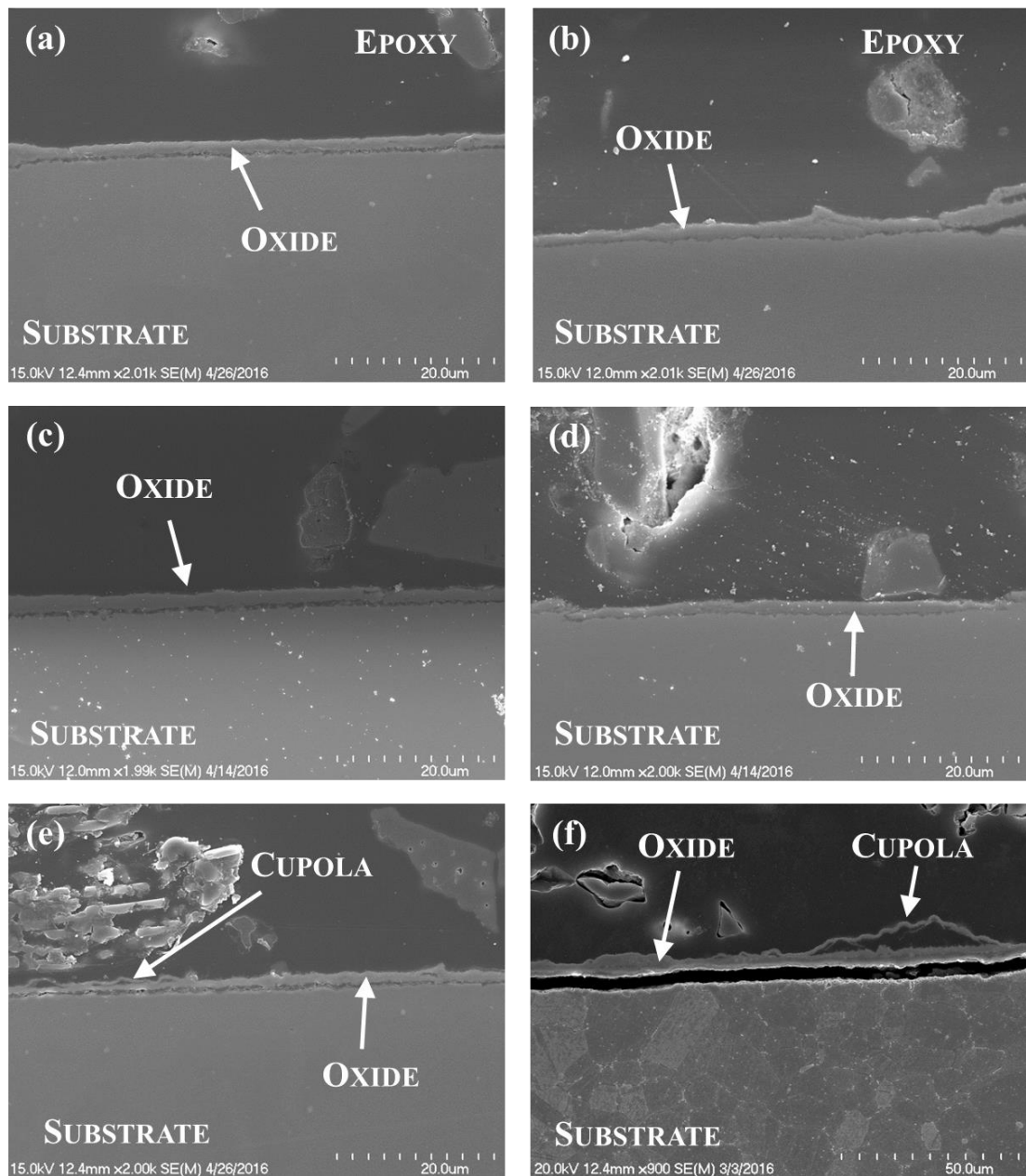


Figure 7.4: SEM images of 347SS after exposure to salt B at 600 °C for (a) 1 day; (b) 4 days; (c) 7 days; (d) 14 days; (e) 21 days; (f) 28 days.

Figure 7.5 shows another SEM image of a sample that was exposed to salt B for 28 days at 600 °C. The lower surface topography of the detached oxide is seen to correspond closely with the upper surface topography of the underlying substrate. This mechanism was also observed in the corrosion of P91 steel shown in Chapter 6. It was postulated that cracks may initiate from penetration of chlorine through grain boundaries. These grain boundaries then undergo oxidation, resulting in growth stresses that cause crack initiation. The cracks then propagate in a transgranular manner leading to the uniform detachment as shown in Figure 7.5, in a similar manner to that seen for P91, as discussed in Chapter 6.

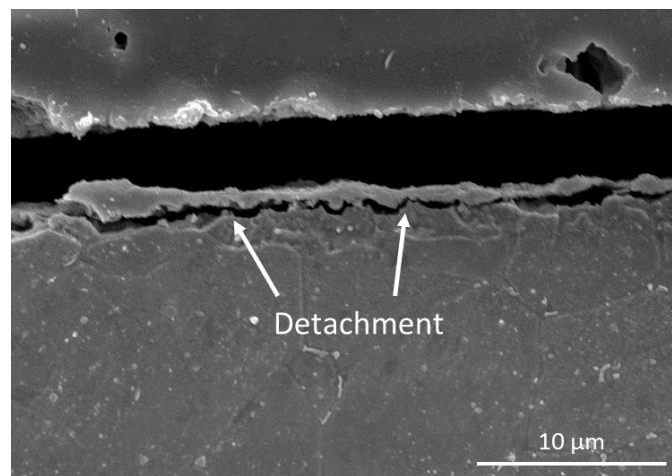


Figure 7.5: SEM image showing detachment of oxide scale from substrate following exposure to salt B for 28 days at 600 °C.

Two images showing buckling of oxide scales are shown in Figure 7.6 following exposure to salt B for (a) 7 days and (b) 28 days. As a consequence of this buckling, the oxide scale has detached significantly from the substrate surface. Buckling of oxide scales can typically occur due to growth stresses [166,165]. If the volume of the oxide is greater than that of the parent material the oxide will break the adhesion between oxide and substrate to relieve strain [87], as discussed in Chapter 2.

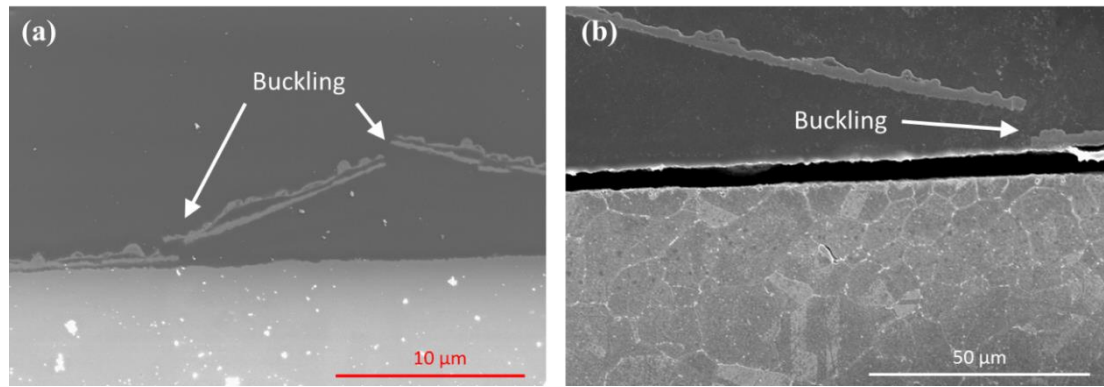


Figure 7.6: SEM images showing buckling of oxide scales following exposure to salt B for (a) 7 days and (b) 28 days.

7.3.1.2. Oxide Scale Measurements

Oxide scale measurements were taken via the procedure detailed in Chapter 3. Figure 7.7 (a) shows measurements of the oxide scale taken following exposure of 347SS to salt A and salt B at 600 °C for up to 28 days. The oxide layer thickness increases with a higher chlorine content, 2.18 % in salt A and 0.16 % in salt B as expected.

Figure 7.7 (b) compares the measured oxide layer thickness for 347SS with measurements taken from P91 steel, as presented in Chapter 6. The oxide layers measured on P91 steel were found to be significantly thicker (almost an order of magnitude) than those measured on 347SS. From comparison of the oxide layers formed over both samples, it appears that 347SS produces a more protective oxide layer. This forms closer to the substrate and primarily consists of a single solid oxide layer. By comparison, P91 formed multiple layers of oxide, which do not provide as much protection against further oxidation. This is attributed to the higher chromium content in 347SS, approximately 18 %, compared to P91, approximately 9 %.

Figure 7.7 (c) compares the results found here with a model presented by Nielsen et al. [53] where 347SS was exposed to pure KCl at 550 °C. As expected exposure to pure KCl resulted in a much higher corrosion rate, despite the lower temperature of the testing. Results are also shown from work carried out by Henriksen et al. [231], which displays the corrosion rate of a fine grained 347SS following exposure to no salt at 600 °C. There is a noticeable increase in corrosion rate due to exposure to both salt A and salt B.

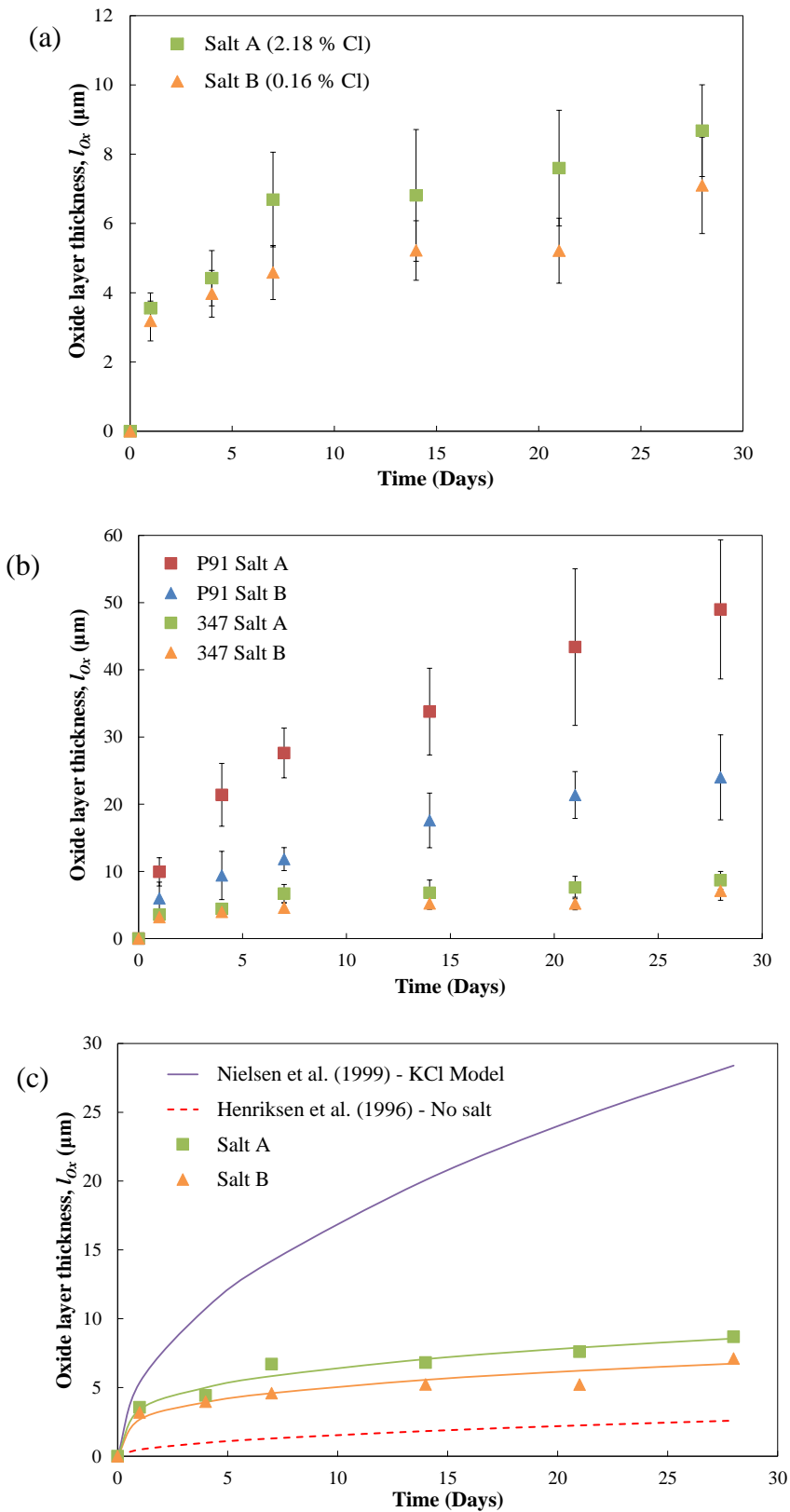


Figure 7.7: Oxide thickness measurements of 347SS (a) following exposure to salt A and salt B at 600 °C, (b) compared to measurements of P91 at 600 °C and (c) compared to a model of 347SS exposed to pure KCl presented by Nielsen et al. [53] and exposed to no salt, Henriksen et al., [231].

7.3.1.3. Intergranular corrosion

Localised intergranular corrosion was detected throughout the majority of samples tested. Figure 7.8 shows intergranular corrosion penetrating a sample exposed to salt A for 14 days at 600 °C. This intergranular penetration reached depths of 33.4 µm from the substrate surface, below the oxide scale that formed above the substrate.

This results in the weakening of alloys and an increased potential for cracking that can lead to early failure of materials. Intergranular corrosion can be extremely dangerous as it is not detectable with the naked eye and requires microscopic observation at high magnification.

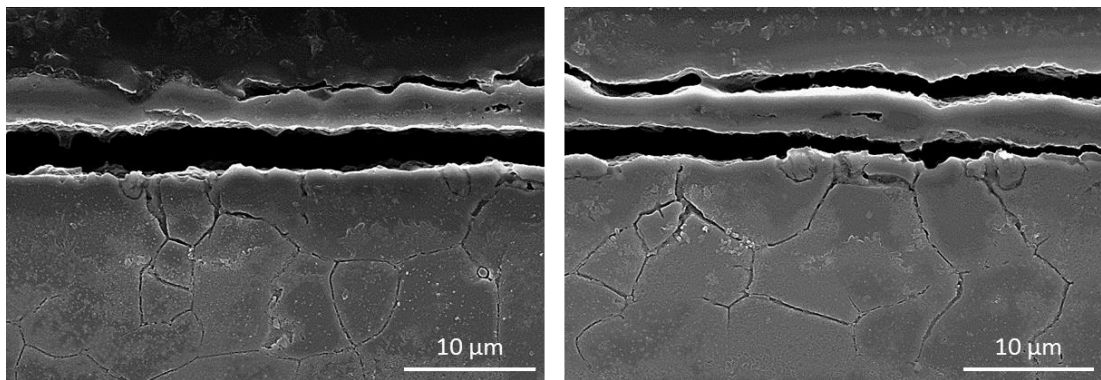


Figure 7.8: SEM images showing intergranular corrosion following exposure to salt A for 14 days.

7.3.1.4. Inclusions and Pitting Corrosion

Figure 7.9 shows two inclusions clearly identified in the sample. A cluster of inclusions are identified at the location shown in Figure 7.9 (a). The inclusion shown in Figure 7.9 (b) has an exposed area equal to approximately 25 µm². Additional inclusions were measured and have an area of approximately 35 µm². It is noted that this is just a two-dimensional slice of the inclusion and it may vary in size and shape in the third dimension.

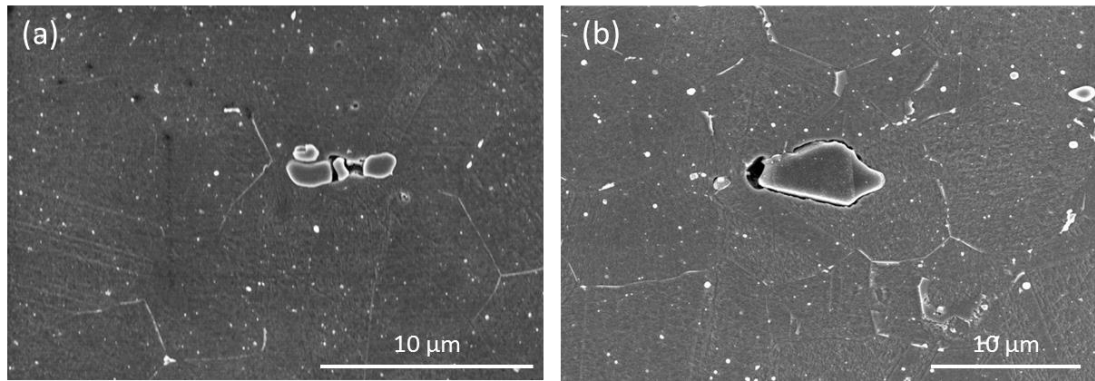


Figure 7.9: SEM images showing (a) a cluster of inclusions and (b) image of large inclusion located in sample.

As was discussed in Chapter 6, subsurface inclusions are well known to act as crack initiation sites. Therefore the presence of inclusions must be considered when looking at samples [149]. The importance of surface inclusions on pitting corrosion was also discussed in Chapter 6 [138–144]. The results shown in Chapter 6 provided evidence of pits initiating at surface inclusions. Figure 7.10 shows an example of an inclusion on the sample surface. EDX analysis of the inclusion showed that it consists of a large amount of oxygen, indicating that it is a mixed metal oxide. Oxide inclusions are less likely to form pits than sulphates as discussed in Chapters 2 and 6.

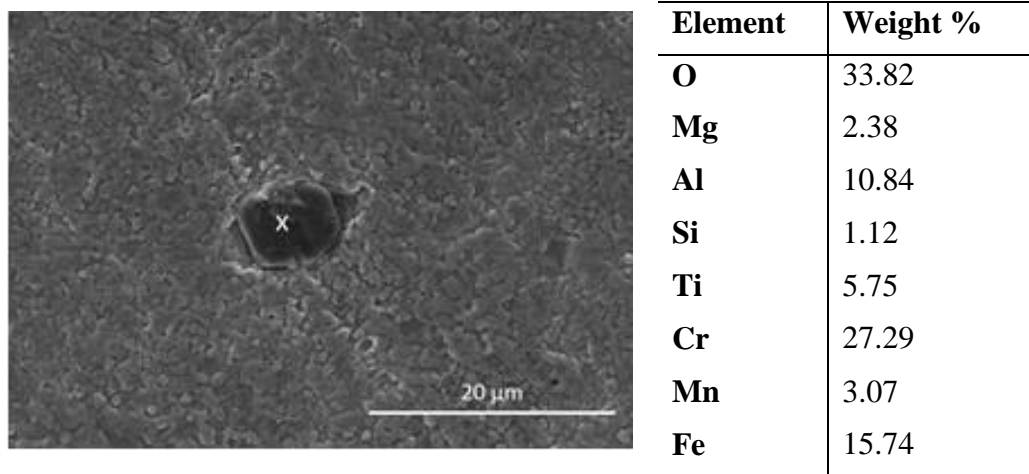


Figure 7.10: SEM and EDX analysis of inclusion identified on sample surface.

Localised areas of pitting corrosion exist on numerous samples analysed during this study. Two examples of pitting corrosion are shown in Figure 7.11 following exposure to salt A for (a) 1 day and (b) 14 days. These pits reach depths of approximately 4.0 and 6.7 μm , and areas of 14.7 and 37.6 μm^2 respectively. It is postulated that these pits formed from the dissolution of surface inclusions as discussed previously for P91.

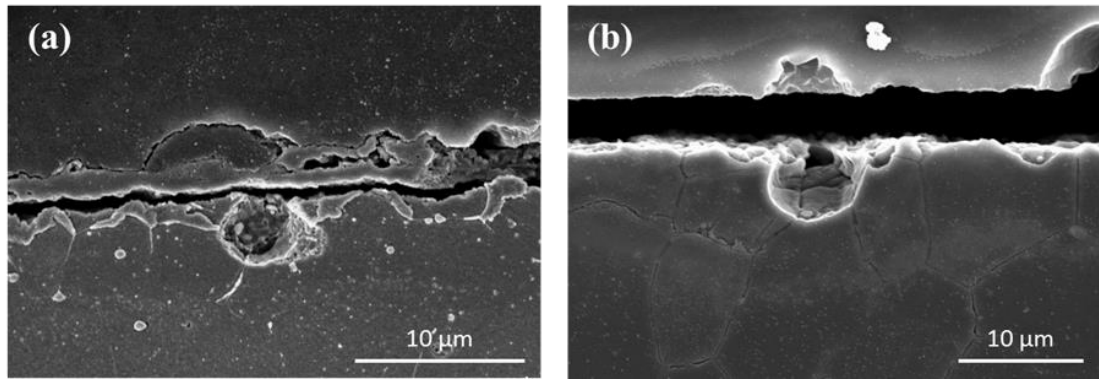


Figure 7.11 SEM images showing pitting corrosion on samples exposed to salt A for (a) 1 day and (b) 14 days.

Microscopic pits have been observed on all sample surfaces analysed. Figure 7.12 shows a pit following exposure to salt A for (a) 7 days and (b) 21 days. The pit following exposure for 7 days has an area of approximately 238 μm^2 .

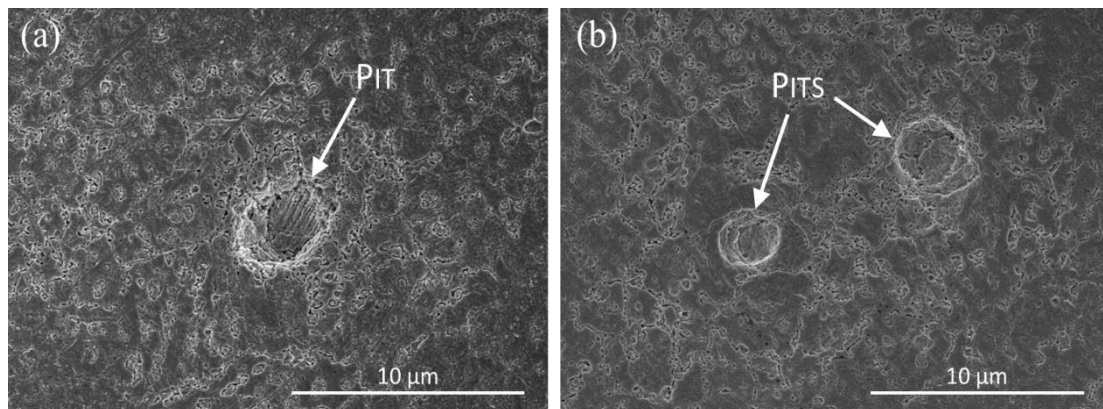


Figure 7.12: SEM images showing pitting corrosion on sample surface following exposure to salt A for (a) 7 days and (b) 21 days.

7.3.1.5. Surface profile

Further pits have been identified on the sample exposed to salt A for 14 days, as shown in Figure 7.13. On this sample a number of pits can be identified. The largest of these

Table 7.1: Maximum pit depths recorded from DEM images of sample surfaces.

	Salt A			Salt B		
	7 Days	14 Days	21 Days	7 Days	14 Days	21 Days
Pit depth (μm)	3.6	1.9	4.3	3.3	2.5	8.3

7.3.2. RepliSet samples

Figure 7.15 (a) shows a 2D surface profile of a RepliSet sample taken using white light interferometry; the corresponding 3D profile is presented as Figure 7.15 (b). Numerous pits are visible on these samples. In addition to the localised areas of pitting corrosion identified, the non-uniformity of the tube surface is evident from the surface profiles. It is evident that the entire tube surface has undergone corrosion, with the pitting corrosion most evident via surface analysis.

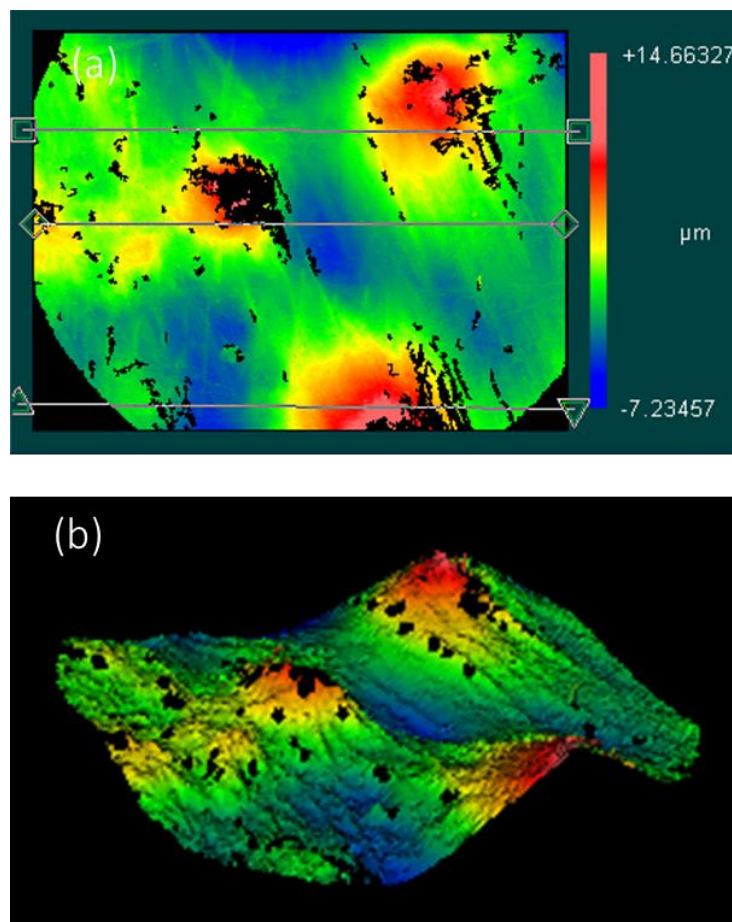


Figure 7.15: Surface profile of RepliSet sample taken from in-situ tubes showing corrosion pit profiles using white light interferometry in (a) 2D and (b) 3D profiles.

Table 7.2 and Table 7.3 show measurements of the root mean squared roughness (R_{RMS}), roughness average (R_a) and the maximum pit depth measured from the RepliSet samples taken from in-situ tubes.

Table 7.2: R_{RMS} , R_a and maximum pit depth measurements obtained from RepliSet samples of in-situ tubes. (a), (b) and (c) represent different sample locations on the tube banks.

Depth	SH1 – RHS			RH1 – Coil 1			RH1 – Coil 2		
	(a)	(b)	(c)	(a)	(b)	(c)	(a)	(b)	(c)
R_{RMS} (μm)	14.7	14.4	9.0	1.1	5.5	6.7	5.8	6.9	2.7
R_a (μm)	10.6	11.4	6.4	0.8	4.0	5.4	4.6	5.4	2.2
Max depth (μm)	107.5	85.5	100.4	10.5	45.3	47.8	40.8	52.1	40.9

Table 7.3: R_{RMS} , R_a and maximum pit depth measurements obtained from RepliSet samples of in-situ tubes. (a), (b) and (c) represent different sample locations on the tube banks.

Depth (μm)	SH1 – Coil 1			SH1 – Coil 2		
	(a)	(b)	(c)	(a)	(b)	(c)
R_{RMS} (μm)	2.7	4.2	3.3	2.9	2.9	2.3
R_a (μm)	2.0	3.2	2.6	2.3	2.4	1.7
Max depth (μm)	21.9	48.7	26.8	21.1	24.7	17.6

The locations from which the RepliSet samples were taken from in the plant are shown in Figure 7.16. For the reheater (RH) banks labelled RH1 – Coil 1 and Coil 2 the areas analysed were from the top portion of the tube walls. For the superheater (SH) banks labelled SH1 – Coil 1 and Coil 2 the areas analysed were taken from the bottom portion of the tube walls and SH1 – RHS was taken from the right hand side of SH1.

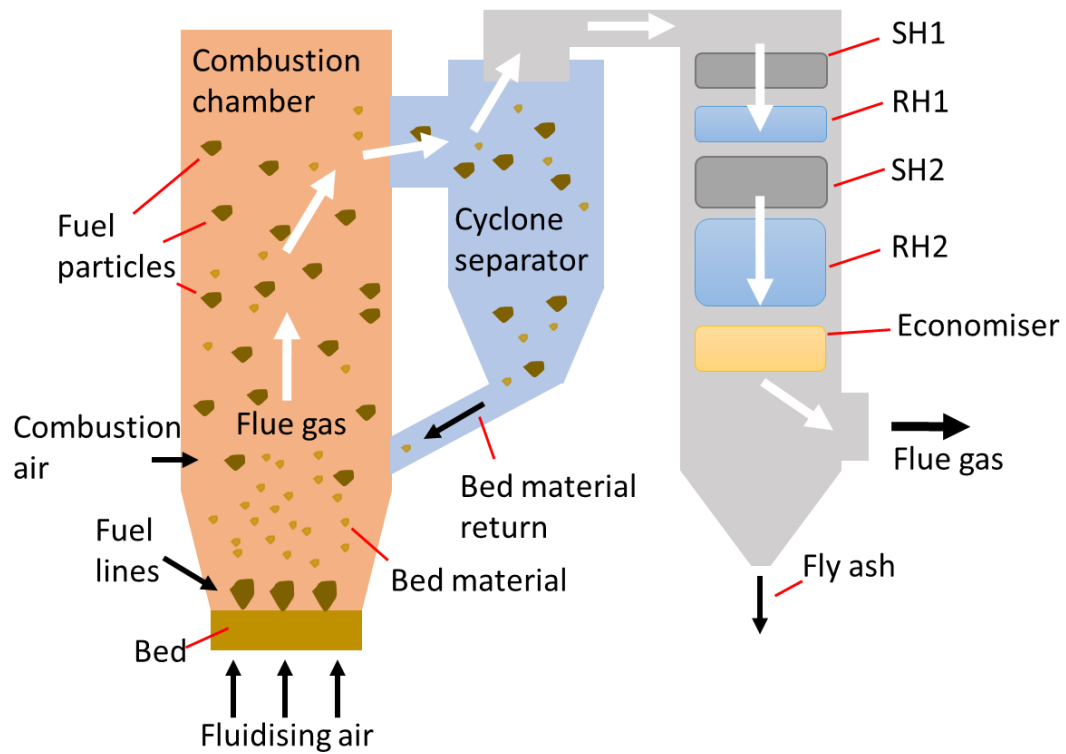


Figure 7.16 Schematic of plant showing location of tubes where RepliSet samples were taken from.

7.3.3. Modelling

Results from finite element (FE) modelling are presented in this section. Initially a test specimen was modelled in order to calibrate the corrosion sub-model to predict pits representative of those found during testing. Figure 7.17 shows the results of this model. The pitting corrosion is modelled via element deletion as discussed in Section 7.2.3. The morphology of the pits on the specimen surface can be clearly seen in Figure 7.17. A sectional view of the sample is also shown to highlight the pit depth through the sample. The maximum depth reached is 22.5 μm and is highlighted in Figure 7.17.

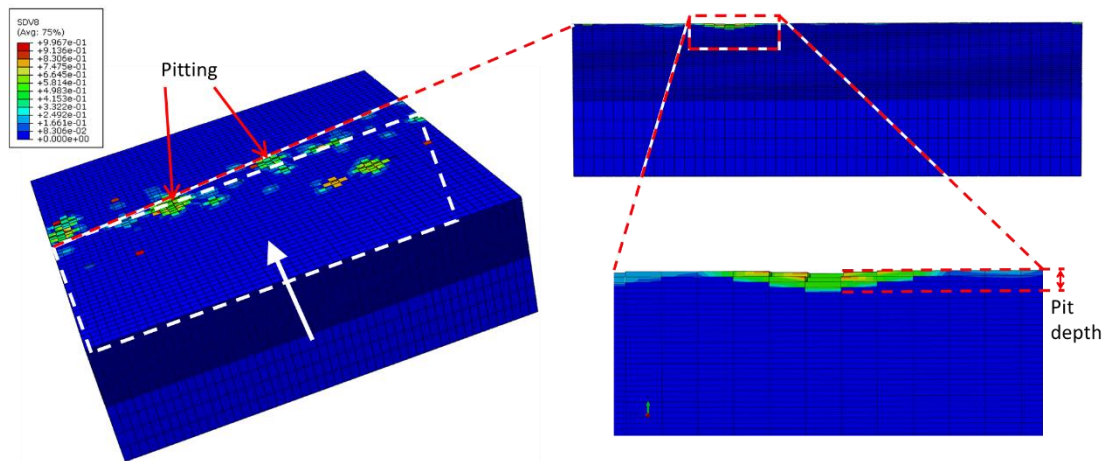


Figure 7.17: Images showing the pitting corrosion on the surface and through the cross section of a rectangular sample.

Based on results from this model parameters were calibrated to simulate growth of pits to a depth of 7.25 μm following 14 days of exposure. This rate was based on measurements of a pit exposed to salt A for 14 days, which measured 6.7 μm , as shown in Figure 7.11. The parameters obtained are shown as Salt A_{Pit} in Table 7.4. The rate Pit_{Accel} shown in Table 7.4 is an accelerated rate of pit growth, both in growth through the depth of the specimen and in terms of damage assigned to neighbouring elements, which simulates pit growth across the width of the sample. This was done to simulate an extreme case of pitting corrosion, which may develop if there is sufficient chlorine present in the deposit e.g. for extremely high levels of co-firing.

Table 7.4: Parameters used for the corrosion damage models used in this work.

	$k_U (\text{hr}^{-1})$	γ	β
Salt A_{Pit}	0.00288	0.2	0.6
Pit_{Accel}	0.02880	0.2	0.8

Figure 7.18 shows the damage distribution predicted for the exposed surface of the tube. Figure 7.18 (a) shows the initial stages ($t = 250$ days) of pit formation via the corrosion sub-model, a number of pits have formed on the surface of the tube and are beginning to grow. When the damage in an element reaches a value of 1 the element is deleted and its neighbouring elements are assigned damage. As more elements are

deleted the pits continue to grow in both depth and surface area as can be seen in Figure 7.18 (b) ($t = 700$ days). In addition to pit growth additional pits have begun to form on the surface of the tube.

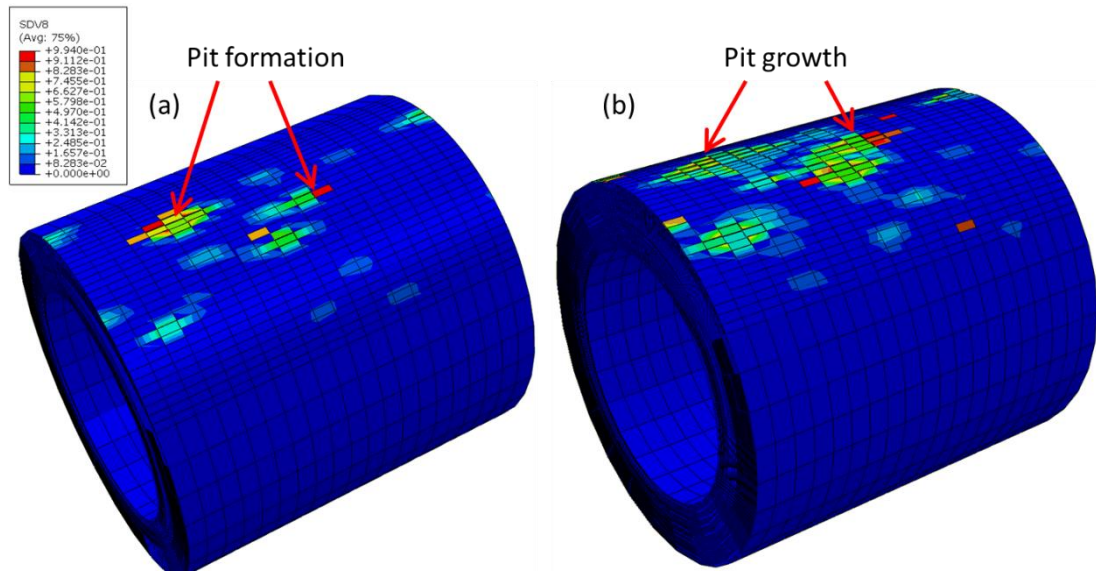


Figure 7.18: Image showing the evolution of damage and pitting of the model at (a) $t = 250$ days and (b) $t = 700$ days for corrosion rate Salt A_{Pit} .

The von Mises stress for a pressurised tube with pitting corrosion was compared to the corresponding stress for a tube without pitting corrosion at different rates using the following normalised stress:

$$\sigma_{vm}^{rel} = \frac{\sigma_{vm}^{pit}}{\sigma_{vm}^{nopit}} \quad (7-4)$$

Figure 7.19 (a) shows a comparison of this normalised pitting stress for the pitting rates given in Table 7.4. The figure also shows the predicted surface topographies for the corresponding two rates, the dashed line in both models represents the initial topography of the models. These topographies are shown graphically in Figure 7.19 (b), which shows a comparison of the wall thickness of the pressurised tube following corrosion at the two corresponding rates. As can be seen the higher β value in Pit_{Accel} has resulted in several of the pits joining together, while the higher k_U value has resulted in the pits reaching higher depths than that for Salt A_{Pit} . The more pits form the higher von Mises stress values reach compared with the model with no pitting. The

von Mises stress values for Salt A_{Pit} remain the same as the model with no pitting until it approximately $t = 500$ days. This is due to the fact that it takes approximately 238 days for the model to delete an element, as the elements are $126 \mu\text{m}$ in size, which is similar in size to the maximum pit depth found on the in-situ tubes of $107.5 \mu\text{m}$, as shown in Table 7.2.

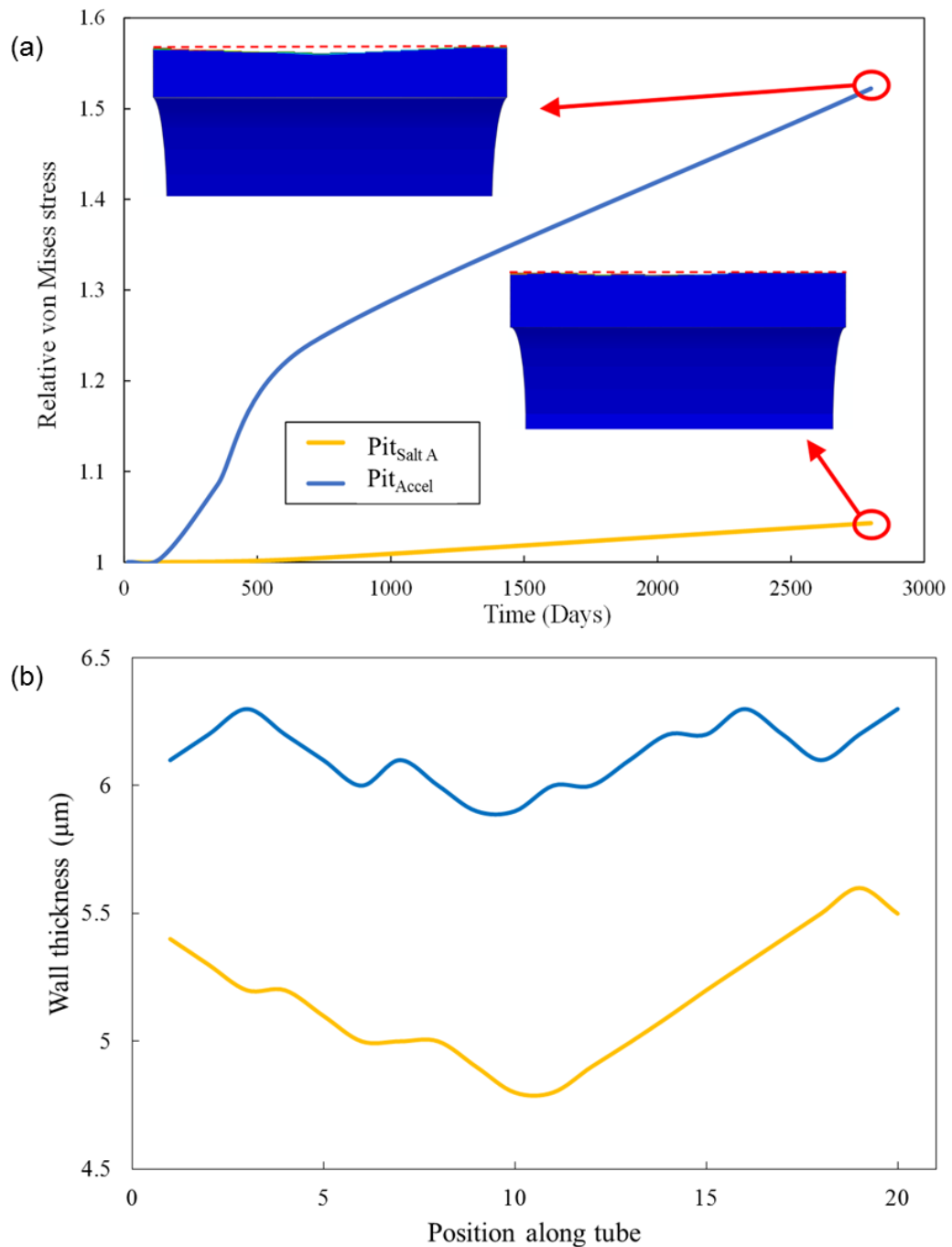


Figure 7.19: (a) Relative von Mises stress for pressurised tube with and without pitting corrosion at the two different rates and (b) respective wall thickness at points along the pressurised tube following corrosion.

7.4. Discussion

The results presented in this chapter illustrate the changing responses of different materials to salts representative of deposits formed during co-firing. The oxide layers that form on 347SS are significantly more protective than those formed on P91, as discussed in Chapter 6. There was evidence of localised active oxidation on the outer portion of the oxide scales on these samples, with the oxide primarily remaining a single layer. This is in contrast to P91 where multiple layers of oxide were typically found. The difference in oxide layer structure is attributed to the higher chromium content of 347SS compared to P91.

The different composition of the salts was found to have an effect on the structure of the oxide layer that formed on the substrate. The higher chlorine and lower potassium content in salt A has resulted in an oxide scale that has detached from the substrate following just 1 day of exposure. In contrast to this, the higher potassium and lower chlorine content in salt B has resulted in an oxide scale that is tightly attached to the substrate even after 21 days of exposure. This demonstrates the formation of a more protective oxide layer following exposure to salt B.

This is also consistent with the work presented for P91 in Chapter 6. The higher levels of potassium appear to have resulted in the preferential formation of potassium chromates following exposure to salt B. The higher chlorine levels in salt A appear to have resulted in the preferential formation of chromium chlorides, which convert to oxides further from the substrate than potassium chromates.

Delamination of the oxide scale on samples was identified at several locations. This delamination is attributed to cracks travelling in a transgranular mode, leading to oxidation of both sides of the sample. In addition to delamination, buckling of the oxide scale was identified at several samples. This buckling is attributed to the effects of growth stresses.

Salt A was found to be more corrosive than salt B, due to a higher chlorine content, resulting in the damaging active oxidation corrosion process. Comparison with results for P91 at 600 °C, from Chapter 6, showed that 347SS provides more protection against corrosion for both salt A and salt B. This corresponds with observations made regarding the structures of the oxide layers formed on both P91 (Chapter 6) and 347SS.

Corrosion rates from this study were compared with models presented by Nielsen et al., for 347SS exposed to pure KCl at 550 °C, and Henriksen et al., for 347SS exposed to no salt at 600 °C. The pure KCl resulted in a far higher corrosion rate than either of the synthetic salts tested here, despite the lower temperature. This is attributed to the higher chlorine content of KCl compared with the synthetic salts. Both synthetic salts did cause significantly higher corrosion rates than for the cases without salt, at the same temperature, 600 °C.

Localised intergranular corrosion was detected at several locations throughout the majority of 347SS samples tested. This is an extremely dangerous form of corrosion as it is not typically visible to the naked eye and requires examination of the affected area. Intergranular corrosion will result in weakening of the alloy and an increased potential for cracking. It can lead to galvanic corrosion and stress corrosion cracking, which can lead to early failure of tubes [232].

Numerous inclusions have been detected both at the surface and throughout the depth of the sample. Subsurface inclusions are known to have a detrimental effect under cyclic loading when greater than 10 μm^2 in size [153], and inclusions of up to 35 μm^2 have been measured at testing during this work.

Pitting corrosion has been observed at sites where inclusions are at the sample surface and have acted as pit initiation sites. It is postulated that these pits form in a manner similar to that observed in the pitting of P91 steel, with initiation and propagation steps. Pits have been measured to a maximum area of 1024 μm^2 , and reaching a depth of up to 6.7 μm . Digital elevation models (DEM) were presented to show the surface profile of a sample following exposure. From these images, it is clear that the entire surface is affected by the exposure. Maximum pit depths of up to 8.3 μm were recorded using the DEM profiles after 21 days exposure.

Surface profiles have been taken from replica samples of in-situ tubes. Pit depths of up to 107.5 μm in depth were measured from the material extracted from plants that were in operation for approximately two and a half years. If we assume a linear rate of pit growth, this provides a pit depth of 1.64 μm following 14 days. When compared with experimental results from pit growth this is in the order of magnitude of measured pits. It is however smaller than the smallest pit measured, however these experiments

were to simulate co-firing plants, while the plant data is from a plant which used only peat as a fuel source.

The effect of pitting corrosion on stress levels in pressurised tubes is evident from the results of the modelling shown. Stress levels increase with increasing pit size and depth. This shows just one aspect of how damaging pitting corrosion can be in relation to operational tube life expectancy. It must also be considered that pitting corrosion can lead to stress corrosion cracking.

7.5. Conclusions

A microstructural investigation into the accelerated corrosion of 347SS during biomass co-firing has been undertaken. Samples were exposed to salts representative of different levels of co-firing. Cross-sectional views were examined to determine the subsurface material degradation following exposure. Surface profiles of samples were obtained to determine the effect of corrosion on surface finishes. Replica samples of in-situ tubes were examined and pitting was identified as a primary form of damage on tube walls. Pitting corrosion was modelled using the finite-element program Abaqus and the effect of pitting on stress concentrations was investigated. The main conclusions found during this work are as follows:

- 1) The higher Cr content in 347SS compared to P91 has resulted in a single uniform oxide scale forming over the substrate. This scale offers significantly more protection than the multiple layers formed over P91.
- 2) A higher chlorine content in the salt resulted in higher corrosion rates.
- 3) Buckling of oxide scales was identified at several locations. This results in the loss of the protective nature of the oxides, leading to higher corrosion rates.
- 4) Localised intergranular corrosion has been detected at numerous locations on several samples. This will be detrimental for fatigue life of the metal.
- 5) Pitting corrosion was identified at near-surface inclusions on several samples. Sub-surface inclusions were also identified.

- 6) Pitting corrosion was found on replica samples of in-situ tubes taken from operational plants.
- 7) Finite element modelling of pitting corrosion has shown a detrimental effect on stress levels.

8. Discussion and Conclusions

8.1. Chapter Overview

This chapter summarises and discusses the findings of the work carried out during this research. A summary of the outcomes of the work presented in this thesis is given in Section 8.2. Ideas for future studies related to this work are provided in Section 8.3. Finally, overall conclusions are given in Section 8.4.

8.2. Discussion of Thesis

A comprehensive experimental and numerical characterisation of the impact of biomass-induced corrosion on high-temperature heat exchanger materials has been performed. Key contributions of this work include, experimentally: (i) the development of an experimental methodology to determine corrosion rates of metals, (ii) microstructural investigations into the corrosion mechanism of P91 steel and 347SS, (iii) comparison of the corrosion rates of P91 steel and 347SS, (iv) investigations into the impact of inclusions on pitting corrosion and (v) examination of samples from in-situ tubes.

Key contributions of this work computationally include: (i) the development of a physically based corrosion model for pure iron, (ii) an investigation of the effects of uniform corrosion on tube rupture life, (iii) a study of the potential of sub-surface inclusions to act as sites for localised stress concentrations and (iv) the development of a pitting corrosion model to investigate the effect on maximum stress levels in pressurised tubes.

An experimental methodology has been developed to determine the corrosion rates of candidate heat exchanger tube materials for thermal power plants. Two synthetic salts, representative of deposits formed during biomass co-firing, were applied to these materials, at representative temperatures. The results of the experiments were shown to be consistent with previously published experimental tests by other research groups. This test methodology was then applied through Chapters 4, 5, 6 and 7, to obtain corrosion rates and investigate the corrosion mechanism for different materials, deposit compositions and temperatures.

Elemental analysis of a range of biomass fuels and deposit samples was carried out and presented in Chapter 3. From these readings, fuel O:C ratios were obtained. This allowed for classification of fuel quality, as the lower the O:C ratio of a fuel the higher the HHV. From comparison of biomass fuels that underwent torrefaction the benefits of this technique on fuel quality were evident. This methodology provides the opportunity to analyse deposit compositions for various fuel-biomass mixtures. From these measurements, predictions into how corrosive a mixture is can be made from the Cl, Br, Na and K content of the deposit. Results are shown from three operational plants, which revealed higher levels of Cl, Br, Na and K in the deposit, during biomass combustion compared to conventional fossil fuel combustion.

Previously used models for the corrosion of metals due to biomass co-firing typically made use of an empirical factor to fit the model to experimental results. In order to develop a more physically-based model experiments were carried out on pure iron as detailed in Chapter 4. This provided the opportunity to investigate a corrosion mechanism at a fundamental level and develop a model based on this mechanism. The key physical phenomena associated with the biomass corrosion process were identified. These included the formation of initial oxides, detachment of oxides, fragmentation of oxide scales, followed by continued oxidation and fragmentation. Based on these experiments a novel porosity-based corrosion model (PCM) for active oxidation of iron was developed. The model was based on the rate-limiting step of the active oxidation process; outward diffusion of FeCl_2 . The model then used physical measurements of porosity and pore radius statistics in the oxide layer, as obtained from microscopy analysis of experimental test samples. The model was calibrated and validated against experimental measurements, and previously published, less physically based models.

The effect of the corrosion rate on the creep rupture life of tubes was identified as a key factor for determining the suitability of a biomass fuel for use in a co-firing plant. Experiments were carried out on P91 steel at 540 °C as presented in Chapter 5. This experimental test programme facilitated the characterisation of the P91 corrosion rate for the conditions investigated. A computational model for uniform corrosion based on a previously-published approach for corrosion of stents, was implemented for assessment of the effects of biomass corrosion on high temperature pipe integrity, based on this corrosion rate. The adaptive meshing corrosion models were combined

with creep damage models to simulate combined creep-corrosion damage in pressurised tubes. A detrimental effect of corrosion on creep life was demonstrated for P91 tubes. The corrosion mechanism observed for the P91 samples differed in a number of ways from that observed for pure iron. Experimental characterisation of P91 demonstrated the formation of scales consisting of multi-layered oxides which subsequently detached from the substrate, via repeated cracking and spalling of the oxides. These detached oxides no longer provided protection against further corrosion and additionally caused a loss in load bearing capability under mechanical loading. This highlighted the difficulty in expanding the physically based model to more complex materials, as the different elements in these metals would all react at different rates to the deposit. As a result of this, a far more complex model than that developed in Chapter 4 is required to capture this mechanism. This also highlighted the need for a greater understanding of the corrosion mechanism of P91 steel.

Detailed microstructural investigations into the accelerated corrosion of P91 and 347SS was undertaken as a result of this, and the results are shown in Chapters 6 and 7 respectively. The effect of chlorine and potassium content on how the corrosion mechanism proceeds was shown. It was found that a critical chlorine content exists in the salt, above which active oxidation is the primary corrosion mechanism. A critical potassium level also exists, above which active oxidation was not dominant, but rather alkali chromate formation was. Chromate formation offers protection against further corrosion in contrast to active oxidation, which offers minimal protection. Therefore lower chlorine salts and higher potassium salts lead to reduced corrosion rates and hence are beneficial. The corrosion rate of 347SS was found to be significantly lower than that of P91 (approximately an order of magnitude). This was attributed to the extra chromium content and finer grain structure of 347SS, which forms a protective initial oxide layer. Cracking and buckling was observed in oxide scales which formed close to the substrate, due to growth stresses of the oxide. Cracks were also identified in unoxidised material, which were attributed to intergranular penetration of chlorine and subsequent oxidation. Inclusions were identified throughout all of the samples, with near-surface inclusions acting as initiation sites for pitting corrosion. Localised intergranular corrosion was also observed during the corrosion of P91 and 347SS.

Sub-surface inclusions are known to have a deleterious effect on the fatigue life of materials. In order to investigate this FE models of the inclusion-metal interface were

developed. These models showed areas of localised stress concentrations at the interface, which was attributed to the thermal mismatch between the inclusions and base metal. Sulphide inclusions, were found to be particularly detrimental on microscale stress and strains at the interface.

Inclusions which reached the surface of the samples were identified as pit initiation sites during the experimental work. FE models were then developed to investigate the effect of pitting corrosion on stress levels in tube walls. These models clearly showed the more severe the pitting corrosion a tube was subjected to, the higher the stress levels in the tube.

8.3. Recommendations for Future Work

The work presented here provides a significant investigation into the response of materials to the accelerated corrosion which occurs during biomass co-firing. During the course of this work, several opportunities for further study were identified. In order to obtain a fully comprehensive understanding of the optimal materials to consider when operating biomass fuelled plants, further work is required. This section identifies a number of potential areas which could be investigated as a direct follow on from this research.

Samples could be exposed to deposits which have formed during the combustion of biomass in operational plants as opposed to synthetic salts which have been used here. Samples could be exposed in tube furnaces, where a gaseous atmosphere could be generated to simulate the flue gas to which materials would be exposed in operational plants. Furthermore a test-rig could be designed to replicate combustion in fluidised beds. A portion of tube could be placed in this test rig allowing for deposition rates and corrosion rates for a range of biomass fuels to be identified.

In order to obtain more homogeneous results for the elemental composition of fuel and deposit, samples should first be ground and sieved. This would remove any large particles of compounds which exist in the sample and not representative of the bulk deposit composition.

Combustion modelling software can be used to determine the alkali halide content of the deposit which would be produced for different biomass fuels. This could then be related to the corrosion potential of these fuels.

Computational fluid dynamics (CFD) programmes can be used to solve species transport equations to calculate the momentum and heat and mass transfer in a fluidised bed boiler [80,82]. This can be used to effectively model the evolution of combustion products, and obtain temperature distributions across regions of the plant of interest to operators, such as the heat exchanger regions. These models can be expanded to include deposit growth rates in addition to chlorine content of the deposits. These models could then provide information regarding the corrosion potential due to combustion conditions, metal temperature, deposit formation or chlorine content.

There is a significant opportunity for development of the porosity-based corrosion model (PCM) which was presented in chapter 4. A theoretical approach to pore growth, such as the random pore model [208,210], would allow for predictions of values of ε and \bar{r} . This will further reduce the need for experimental characterisation for the model, as ε and \bar{r} would no longer be required to be measured.

In order to apply the PCM to more complex alloys a number of additional chemical and gas transport aspects will need to be considered. Additional oxides and chlorides such as chromium oxide/chloride and mixed oxides/chlorides will need to be taken into consideration. The oxides will thus be more complex with a number of layers of different oxides expected. The partial pressures of these oxides, in addition to where they form and affect diffusion must be included. The role of inter-granular penetration of Cl_2 in the overall process and how this affects corrosion rates also presents opportunity for future study [166,209].

Chapter 5 presented a finite element model which incorporated corrosion and creep damage on a pressurised tube. This model did not include the effects of plasticity on tube performance. It also did not include the effects of temperature gradients through the tube wall and how this would affect the response of the material to long term creep damage. There is additionally the potential to carry out a range of long term creep tests to obtain material constants for a range of temperatures.

Pipe bends are well known to contain areas of stress concentrations, which can lead to early failure of tubes. Although finite element models of pipe bends have been developed previously [233], incorporating corrosion and creep damage into these models is considered an important area of future study.

An additional computational modelling technique is the use of extended finite element methods (XFEM) to model oxide scale formation and exfoliation. Oxide scale exfoliation can be evaluated based on the fracture mechanics of brittle thin layers. A critical strain criteria has been presented by Sabau et al. [97] for crack initiation, delamination and separation of oxide scales. Previous work carried out in NUI Galway for the delamination of composite plies has involved a micro-cracking initiation criterion (Grogan et al. [225]) and the use of a surface-based cohesive zone model (SCZM) (Grogan et al. [226]).

The effect of corrosion can be combined with fatigue models which have been developed in NUI Galway [114,123,124,234]. This would allow for a prediction of the effect of corrosion on flexible operations of power plants. The thermal cycling which occurs during flexible operations would likely result in further delamination of oxide scales due to the thermal stresses. This could potentially result in an accelerated corrosion rate which would result in a reduction in area of plant components resulting in earlier failure of components. In addition microstructural damage effects such as corrosion along grain boundaries and consumption of pinning carbides should be included in fatigue calculations as was discussed earlier in relation to creep damage.

Inclusions have been identified as areas of localised stress concentrations in Chapter 6. There is an opportunity to investigate the response of mechanically-loaded samples to inclusions of varying sizes via finite element modelling. Additionally the effect of clusters of smaller inclusions on stress distributions can be investigated. This would help identify critical sizes for inclusions to effect life expectancy of plant components.

In addition to being effected by the size of the inclusion it has been observed that the stress concentrations will be influenced by the shape of the inclusion. It has been proposed that the shape of inclusions may be more important than its material properties in some cases [235]. Future work could investigate the effect of different shaped inclusions on stress levels using finite-element modelling.

The pitting corrosion model presented in Chapter 7 could be expanded to more accurately model the corrosion rate measured, both experimentally and from in-situ data. This would require an intensive computational modelling program, involving extremely small element sizes and as a result extremely large number of elements in a mesh. This would also involve long runtimes of models, and would require the use of supercomputers.

8.4. Conclusions

This work has resulted in numerous useful observations relating to the corrosion of heat exchanger tubes during co-firing of biomass with traditional fuels in thermal power plants. A number of the key observations found during this research are summarised below:

- 347SS is more suitable than P91 as a material for heat exchanger tubes in co-firing plants, due to its higher Cr content.
- Stress caused by the formation of oxides results in buckling of oxide scales leading to an increase in corrosion rate, due to a loss of the corrosion resistant properties of the oxide.
- Inclusions found at the surface of the material act as initiation sites for pitting corrosion.
- Sub-surface inclusions were identified as sites of stress concentrations due to thermal mismatch with the metal.
- A high Cl content in the deposit formed during co-firing is more deleterious in terms of material loss than a high K content.
- Tube rupture life is greatly affected by the corrosion rate of tube walls.
- Experiments carried out based on the test methodology developed produced results representative of those seen in co-firing plants.

- Intergranular corrosion must be considered by plant operators when measuring corrosion of in-situ tubes, as it is difficult to detect without metallographic techniques.

References

- [1] Sustainable Energy Authority of Ireland, Energy Security in Ireland: A Statistical Overview, 2016.
- [2] M. Howley, M. Holland, D. Dineen, E. Cotter, Energy in Ireland 1990 – 2014, 2015.
- [3] Irish Wind Energy Association, Wind Energy Statistics, (2016). <http://www.iwea.com/windstatistics> (accessed April 19, 2016).
- [4] DCENR, Ireland's Transition to a Low Carbon Energy Future 2015-2030, 2016.
- [5] P. Murtagh, Bord na Móna signals end of peat harvesting by 2030, The Irish Times. (2015). <http://www.irishtimes.com/news/ireland/irish-news/bord-na-m%25C3%25B3na-signals-end-of-peat-harvesting-by-2030-1.2379624#.VhOeFBX1rI8.twitter>.
- [6] E.& N.R. Department of Communications, Draft Bioenergy Plan, 2014.
- [7] Sustainable Energy Authority of Ireland, Ireland's Energy Targets Progress, Ambition & Impacts, 2016.
- [8] S.E.A.I, Co-Firing with Biomass, 2004.
- [9] R. Saidur, E.A. Abdelaziz, A. Demirbas, M.S. Hossain, S. Mekhilef, A review on biomass as a fuel for boilers, *Renew. Sustain. Energy Rev.* 15 (2011) 2262–2289. doi:10.1016/j.rser.2011.02.015.
- [10] P. McKendry, Energy production from biomass (part 1): Overview of biomass, *Bioresour. Technol.* 83 (2002) 37–46. doi:10.1016/S0960-8524(01)00118-3.
- [11] L. Zhang, C. (Charles) Xu, P. Champagne, Overview of recent advances in thermo-chemical conversion of biomass, *Energy Convers. Manag.* 51 (2010) 969–982. doi:10.1016/j.enconman.2009.11.038.
- [12] T. Abbasi, S.A. Abbasi, Biomass energy and the environmental impacts associated with its production and utilization, *Renew. Sustain. Energy Rev.* 14 (2010) 919–937. doi:10.1016/j.rser.2009.11.006.

- [13] J. Parikh, S.A. Channiwalla, G.K. Ghosal, A correlation for calculating HHV from proximate analysis of solid fuels, 84 (2005) 487–494. doi:10.1016/j.fuel.2004.10.010.
- [14] M. Theis, B.-J. Skrifvars, M. Zevenhoven, M. Hupa, H. Tran, Fouling tendency of ash resulting from burning mixtures of biofuels. Part 2: Deposit chemistry, *Fuel*. 85 (2006) 1992–2001. doi:10.1016/j.fuel.2006.03.015.
- [15] Energy research Centre of the Netherlands, Phyllis2, database for biomass and waste, <https://www.ecn.nl/phyllis2>, (n.d.).
- [16] A. Demirbas, Estimating the Calorific Values of Lignocellulosic Fuels, *Energy Explor. Exploit.* 22 (2004) 135–144. doi:10.1260/0144598041475198.
- [17] D.H.F. Liu, B.G. Liptak, *Hazardous Waste and Solid Waste*, Taylor & Francis, 1999. <https://books.google.ie/books?id=5JNfFfSpHyoC>.
- [18] P. McKendry, Energy production from biomass (part 2): Conversion technologies, *Bioresour. Technol.* 83 (2002) 47–54. doi:10.1016/S0960-8524(01)00119-5.
- [19] B. Acharya, R. R Pradhan, A. Dutta, Qualitative and kinetic analysis of torrefaction of lignocellulosic biomass using DSC-TGA-FTIR, *AIMS Energy*. 3 (2015) 760–773. doi:10.3934/energy.2015.4.760.
- [20] M. Hupa, Ash-Related Issues in Fluidized-Bed Combustion of Biomasses: Recent Research Highlights, *Energy & Fuels*. 26 (2012) 4–14. doi:10.1021/ef201169k.
- [21] M. Sami, K. Annamalai, M. Wooldridge, Co-firing of coal and biomass fuel blends, *Prog. Energy Combust. Sci.* 27 (2001) 171–214. doi:10.1016/S0360-1285(00)00020-4.
- [22] M. Clancy, J. Bates, N. Barker, O. Edberg, J. Fitzgerald, R. Narkeviciute, et al., *BioEnergy Supply Curves for Ireland: 2010 - 2030*, 2012. http://www.seai.ie/Publications/Renewables_Publications_/Bioenergy/BioEnergy_Supply_Curves_for_Ireland_2010_-_2030.56271.shortcut.pdf.
- [23] M. Clancy, J. Scheer, *Energy Forecasts for Ireland to 2020* 2010, 2011.

www.seai.ie.

- [24] A. Demirbaş, Biomass resource facilities and biomass conversion processing for fuels and chemicals, *Energy Convers. Manag.* 42 (2001) 1357–1378. doi:10.1016/S0196-8904(00)00137-0.
- [25] A.V. Bridgwater, Catalysis in thermal biomass conversion, *Appl. Catal. A Gen.* 116 (1994) 5–47. doi:10.1016/0926-860X(94)80278-5.
- [26] N. Duffy, Investigation of Biomass Combustion in Grate Furnaces using CFD, National University of Ireland, Galway, 2012.
- [27] K.R.. Hein, J.. Bemtgen, EU clean coal technology—co-combustion of coal and biomass, *Fuel Process. Technol.* 54 (1998) 159–169. doi:10.1016/S0378-3820(97)00067-2.
- [28] T. Nussbaumer, Combustion and Co-combustion of Biomass: Fundamentals, Technologies, and Primary Measures for Emission Reduction, *Energy and Fuels.* 17 (2003) 1510–1521. doi:10.1021/ef030031q.
- [29] S. Van Loo, J. Koppejan, *The Handbook of Biomass Combustion and Co-firing*, Earthscan LLC, 2012. <https://books.google.ie/books?id=KE565zmFumQC>.
- [30] P. Basu, *Combustion and gasification in fluidized beds*, CRC Press, 2006. doi:10.1017/CBO9781107415324.004.
- [31] P. Chaibamrung, R. Maintenance, A. Optimization, E. Division, BASIC DESIGN OF CIRCULATING FLUIDIZED BED, (2012).
- [32] B.G. Miller, D.A. Tillman, *Combustion Engineering Issues for Solid Fuel Systems*, Elsevier, 2008. doi:10.1016/B978-0-12-373611-6.00013-6.
- [33] S.N. Oka, *Fluidized Bed Combustion*, Marcel Dekker Inc., New York, 2004.
- [34] E. Anthony, Fluidized bed combustion of alternative solid fuels; status, successes and problems of the technology, *Prog. Energy Combust. Sci.* 21 (1995) 239–268. doi:10.1016/0360-1285(95)00005-3.
- [35] E. Searcy, P. Flynn, E. Ghafoori, A. Kumar, The relative cost of biomass energy transport, *Appl. Biochem. Biotechnol.* 137–140 (2007) 639–652.

doi:10.1007/s12010-007-9085-8.

- [36] G. Forsberg, Biomass energy transport: Analysis of bioenergy transport chains using life cycle inventory method, *Biomass and Bioenergy*. 19 (2000) 17–30. doi:10.1016/S0961-9534(00)00020-9.
- [37] A.A. Khan, W. de Jong, P.J. Jansens, H. Spliethoff, Biomass combustion in fluidized bed boilers: Potential problems and remedies, *Fuel Process. Technol.* 90 (2009) 21–50. doi:10.1016/j.fuproc.2008.07.012.
- [38] A. Demirbas, Potential applications of renewable energy sources, biomass combustion problems in boiler power systems and combustion related environmental issues, *Prog. Energy Combust. Sci.* 31 (2005) 171–192. doi:10.1016/j.pecs.2005.02.002.
- [39] B.M. Jenkins, L.L. Baxter, T.R. Miles Jr, T.R. Miles, Combustion properties of biomass, *Fuel Process. Technol.* 54 (1998) 17–46.
- [40] S.E.A.I, Co-Firing with Biomass - A case study - The Edenderry Power Station, 2012.
- [41] M. Zevenhoven-Onderwater, J.-P. Blomquist, B.-J. Skrifvars, R. Backman, M. Hupa, The prediction of behaviour of ashes from five different solid fuels in fluidised bed combustion, *Fuel*. 79 (2000) 1353–1361. doi:10.1016/S0016-2361(99)00280-X.
- [42] W.A. LePori, C.B. Parnell, System and process for conversion of biomass into usable energy, US4848249 A, 1989. <https://www.google.com/patents/US4848249>.
- [43] M. Bartels, W. Lin, J. Nijenhuis, F. Kapteijn, J.R. van Ommen, Agglomeration in fluidized beds at high temperatures: Mechanisms, detection and prevention, *Prog. Energy Combust. Sci.* 34 (2008) 633–666. doi:10.1016/j.pecs.2008.04.002.
- [44] B.-J. Skrifvars, M. Hupa, E.J. Anthony, Mechanisms of Bed Material Agglomeration in a Petroleum Coke-Fired Circulating Fluidized Bed Boiler, *J. Energy Resour. Technol.* 120 (1998) 215–218.

<http://dx.doi.org/10.1115/1.2795038>.

- [45] M. Öhman, A. Nordin, B.-J. Skrifvars, R. Backman, M. Hupa, Bed Agglomeration Characteristics during Fluidized Bed Combustion of Biomass Fuels, *Energy & Fuels*. 14 (2000) 169–178. doi:10.1021/ef990107b.
- [46] E. Brus, M. Ohman, A. Nordin, Mechanisms of bed agglomeration during fluidized-bed combustion of biomass fuels, *Energy & Fuels*. 19 (2005) 825–832. doi:10.1021/ef0400868.
- [47] S. Enestam, D. Bankiewicz, J. Tuiremo, K. Mäkelä, M. Hupa, Are NaCl and KCl equally corrosive on superheater materials of steam boilers?, *Fuel*. 104 (2013) 294–306. doi:10.1016/j.fuel.2012.07.020.
- [48] K. Salmenoja, K. Makela, Corrosion in fluidized bed boilers burning potassium and chlorine containing fuels, *Tappi J.* 82 (1999) 161–166.
- [49] B.-J. Skrifvars, R. Backman, M. Hupa, K. Salmenoja, M. Westén-Karlsson, Corrosion of super-heater steel materials under alkali salt deposits. Part 2: SEM analyses of different steel materials, *Corros. Sci.* 52 (2010) 1011–1019. doi:10.1016/j.corsci.2009.11.026.
- [50] B.-J. Skrifvars, R. Backman, M. Hupa, K. Salmenoja, E. Vakkilainen, Corrosion of superheater steel materials under alkali salt deposits Part 1: The effect of salt deposit composition and temperature, *Corros. Sci.* 50 (2008) 1274–1282. doi:10.1016/j.corsci.2008.01.010.
- [51] H.J. Grabke, E. Reese, M. Spiegel, The effects of chlorides, hydrogen chloride and sulfur dioxide in the oxidation of steels below deposits, *Corros. Sci.* 37 (1995) 1023–1043.
- [52] R.M. Hatt, Fireside deposits in coal-fired utility boilers, *Prog. Energy Combust. Sci.* 16 (1990) 235–241. doi:10.1016/0360-1285(90)90032-X.
- [53] H.P. Nielsen, F.J. Frandsen, K. Dam-Johansen, Lab-Scale Investigations of High-Temperature Corrosion Phenomena in Straw-Fired Boilers, *Energy & Fuels*. 13 (1999) 1114–1121.
- [54] J. Lehmusto, D. Lindberg, P. Yrjas, B.-J. Skrifvars, M. Hupa, Studies on the

- Partial Reactions Between Potassium Chloride and Metallic Chromium Concerning Corrosion at Elevated Temperatures, *Oxid. Met.* 77 (2011) 129–148. doi:10.1007/s11085-011-9277-z.
- [55] Y. Shinata, F. Takahashi, K. Hashiura, NaCl-induced hot corrosion of stainless steels, *Mater. Sci. Eng.* 87 (1987) 399–405. doi:10.1016/0025-5416(87)90404-6.
- [56] H. Fujikawa, N. Maruyama, Corrosion behaviour of austenitic stainless steels in the high chloride-containing environment, *Mater. Sci. Eng. A.* 120–121 (1989) 301–306. doi:10.1016/0921-5093(89)90754-5.
- [57] J.. Harb, E.. Smith, Fireside corrosion in pc-fired boilers, *Prog. Energy Combust. Sci.* 16 (1990) 169–190. doi:10.1016/0360-1285(90)90048-8.
- [58] J. Pettersson, H. Asteman, J.-E. Svensson, L.-G. Johansson, KCl Induced Corrosion of a 304-type Austenitic Stainless Steel at 600°C; The Role of Potassium, *Oxid. Met.* 64 (2005) 23–41. doi:10.1007/s11085-005-5704-3.
- [59] H.P. Nielsen, F.J. Frandsen, K. Dam-Johansen, L.L. Baxter, The implications of chlorine-associated corrosion on the operation of biomass-fired boilers, *Prog. Energy Combust. Sci.* 26 (2000) 283–298.
- [60] D.A. Tillman, D. Duong, B. Miller, Chlorine in Solid Fuels Fired in Pulverized Fuel Boilers - Sources , Forms , Reactions , and Consequences : a Literature Review, *Energy & Fuels.* 23 (2009) 3379–3391.
- [61] M.A. Uusitalo, P.M.J. Vuoristo, T.A. Mäntylä, High temperature corrosion of coatings and boiler steels below chlorine-containing salt deposits, *Corros. Sci.* 46 (2003) 1311–1331. doi:10.1016/j.corsci.2003.09.026.
- [62] P. Mayer, A. V Manolescu, Influence of Hydrogen Chloride on Corrosion of Boiler Steels in Synthetic Flue Gas, *Corrosion.* 36 (1980) 369–373. doi:10.5006/0010-9312-36.7.369.
- [63] T. Jonsson, N. Folkesson, M. Halvarsson, J.E. Svensson, L.G. Johansson, Microstructural Investigation of the HCl-Induced Corrosion of the Austenitic Alloy 310S (52Fe26Cr19Ni) at 500 °C, *Oxid. Met.* (2014) 1–22.

doi:10.1007/s11085-013-9468-x.

- [64] S.C. Van Lith, F.J. Frandsen, M. Montgomery, T. Vilhelmsen, S.A. Jensen, Lab-scale Investigation of Deposit-induced Chlorine Corrosion of Superheater Materials under Simulated Biomass-firing Conditions . Part 1 : Exposure at 560 ° C †, *Energy & Fuels*. 59 (2009) 3457–3468.
- [65] J. Tomeczek, H. Palugniok, Kinetics of mineral matter transformation during coal combustion, *Fuel*. 81 (2002) 1251–1258. doi:10.1016/S0016-2361(02)00027-3.
- [66] B. Skrifvars, Ash and ash deposition for solid fuels, in: *Abo Akad.*, 2013.
- [67] J. Tomeczek, *Coal Combustion*, Krieger publishing company, Malabar, Florida, 1994.
- [68] Y.B. Yang, V.N. Sharifi, J. Swithenbank, L. Ma, L. I, J.M. Jones, et al., Combustion of a Single Particle of Biomass Combustion of a Single Particle of Biomass, *Energy*. (2008) 306–316. doi:10.1021/ef700305r.
- [69] S. Niksa, A.R. Kerstein, FLASHCHAIN theory for rapid coal devolatilization kinetics. 1. Formulation, *Energy & Fuels*. 5 (1991) 647–665. doi:10.1021/ef00029a006.
- [70] J.M. Vargas, D.D. Perlmutter, Interpretation of coal pyrolysis kinetics, *Ind. Eng. Chem. Process Des. Dev.* 25 (1986) 49–54. doi:10.1021/i200032a008.
- [71] P. Grammelis, E. Kakaras, Biomass Combustion Modeling in Fluidized Beds, *Energy Fuels*. 19 (2004) 292–297. doi:10.1021/ef049838o.
- [72] M. Asgaryan, Prediction of the remaining service life of superheater and reheater tubes in coal-biomass fired power plants, Cranfield University, 2013.
- [73] K.O. Davidsson, B.J. Stojkova, J.B.C. Pettersson, Alkali emission from birchwood particles during rapid pyrolysis, *Energy and Fuels*. 16 (2002) 1033–1039. doi:10.1021/ef010257y.
- [74] S. James G., *Handbook of Coal Analysis*, John Wiley & Sons, Hoboken, New Jersey, 2005.

- [75] A. Nordin, Chemical elemental characteristics of biomass fuels, *Biomass and Bioenergy*. 6 (1994) 339–347. doi:10.1016/0961-9534(94)E0031-M.
- [76] I. Obernberger, G. Thek, Physical characterisation and chemical composition of densified biomass fuels with regard to their combustion behaviour, *Biomass and Bioenergy*. 27 (2004) 653–669. doi:10.1016/j.biombioe.2003.07.006.
- [77] L.L. Baxter, Ash deposition during biomass and coal combustion: A mechanistic approach, *Biomass and Bioenergy*. 4 (1993) 85–102. doi:10.1016/0961-9534(93)90031-X.
- [78] H. Zhou, P.A. Jensen, F.J. Frandsen, Dynamic mechanistic model of superheater deposit growth and shedding in a biomass fired grate boiler, *Fuel*. 86 (2007) 1519–1533. doi:10.1016/j.fuel.2006.10.026.
- [79] H. Kaufmann, T. Nussbaumer, L. Baxter, N. Yang, Deposit formation on a single cylinder during combustion of herbaceous biomass, *Fuel*. 79 (2000) 141–151. doi:10.1016/S0016-2361(99)00137-4.
- [80] A. Leppänen, H. Tran, R. Taipale, E. Välimäki, A. Oksanen, Numerical modeling of fine particle and deposit formation in a recovery boiler, *Fuel*. 129 (2014) 45–53. doi:10.1016/j.fuel.2014.03.046.
- [81] J. Tomeczek, K. Waclawiak, Two-dimensional modelling of deposits formation on platen superheaters in pulverized coal boilers, *Fuel*. 88 (2009) 1466–1471. doi:10.1016/j.fuel.2009.02.023.
- [82] T. Gruber, R. Scharler, I. Obernberger, Application of an empirical model in CFD simulations to predict the local high temperature corrosion potential in biomass fired boilers, *Biomass and Bioenergy*. 79 (2015) 145–154. doi:10.1016/j.biombioe.2015.02.024.
- [83] D. Lundmark, C. Mueller, R. Backman, M. Zevenhoven, B.-J. Skrifvars, M. Hupa, CFD Based Ash Deposition Prediction in a BFBC Firing Mixtures of Peat and Forest Residue, *J. Energy Resour. Technol.* 132 (2010) 31003. doi:10.1115/1.4001798.
- [84] M.U. Garba, D.B. Ingham, L. Ma, R.T.J. Porter, M. Pourkashnian, H.Z. Tan, et

- al., Prediction of potassium chloride sulfation and its effect on deposition in biomass-fired boilers, *Energy and Fuels*. 26 (2012) 6501–6508. doi:10.1021/ef201681t.
- [85] A. Zahs, M. Spiegel, H.J. Grabke, Chloridation and oxidation of iron, chromium, nickel and their alloys in chloridizing and oxidizing atmospheres at 400–700°C, *Corros. Sci.* 42 (2000) 1093–1122.
- [86] A.J.B. Cutler, E. Raask, External corrosion in coal-fired boilers: Assessment from laboratory data, *Corros. Sci.* 21 (1981) 789–800. doi:10.1016/0010-938X(81)90089-5.
- [87] M.F. Ashby, D.R.H. Jones, *Engineering Materials 1, An introduction to their properties and applications*, Second Edi, Butterworth-Heinemann, 1996.
- [88] G.Y. Lai, *High-Temperature Corrosion and Materials Applications*, ASM International, 2007.
- [89] A.S. Khanna, *Introduction to High Temperature Oxidation and Corrosion*, ASM International, 2002.
- [90] N. Birks, G.H. Meier, F.S. Pettit, *Introduction to the High Temperature Oxidation of Metals*, Cambridge University Press, 2006.
- [91] M.G. Fontana, *Corrosion Engineering*, Tata McGraw-Hill, 2005.
- [92] K.R. Trethewey, J. Chamberlain, *Corrosion for Science and Engineering*, Longman, 1995. <https://books.google.ie/books?id=Ir8eAQAAIAAJ>.
- [93] M. Schütze, *Corrosion and environmental degradation*, Wiley-VCH, 2000.
- [94] A. Syed, *Fireside corrosion study of superheater materials in advanced power plants*, Cranfield University, 2011.
- [95] Pitting corrosion - Rolley alloys, (n.d.). <https://www.rolledalloys.ca/technical-resources/blog/pitting-corrosion> (accessed August 11, 2016).
- [96] M. Schütze, Modelling oxide scale fracture, *Mater. High Temp.* 22 (2005) 147–154. doi:10.1179/mht.2005.017.

- [97] A.S. Sabau, I.G. Wright, On the estimation of thermal strains developed during oxide growth, *J. Appl. Phys.* 106 (2009) 0–8. doi:10.1063/1.3157199.
- [98] R.W. Neu, H. Sehitoglu, Thermomechanical Fatigue , Oxidation , and Creep : Part I . Damage Mechanisms, *Metall. Trans.* 20A (1989) 1755–1767.
- [99] R.W. Neu, H. Sehitoglu, Thermomechanical fatigue, oxidation, and Creep: Part II. Life prediction, *Metall. Trans. A.* 20 (1989) 1769–1783. doi:10.1007/BF02663208.
- [100] V.V. Bolotin, a. a. Shipkov, Mechanical aspects of corrosion fatigue and stress corrosion cracking, *Int. J. Solids Struct.* 38 (2001) 7297–7318. doi:10.1016/S0020-7683(01)00002-6.
- [101] B. Fournier, M. Sauzay, C. Caës, M. Noblecourt, M. Mottot, a. Bougault, et al., Creep-fatigue-oxidation interactions in a 9Cr-1Mo martensitic steel. Part I: Effect of tensile holding period on fatigue lifetime, *Int. J. Fatigue.* 30 (2008) 649–662. doi:10.1016/j.ijfatigue.2007.05.007.
- [102] B. Fournier, M. Sauzay, C. Caës, M. Noblecourt, M. Mottot, a. Bougault, et al., Creep-fatigue-oxidation interactions in a 9Cr-1Mo martensitic steel. Part III: Lifetime prediction, *Int. J. Fatigue.* 30 (2008) 1797–1812. doi:10.1016/j.ijfatigue.2008.02.006.
- [103] B. Fournier, M. Sauzay, C. Caës, M. Noblecourt, M. Mottot, A. Bougault, et al., Creep-fatigue oxidation interactions in a 9Cr-1Mo martensitic steel . Part II : Effect of compressive holding period on fatigue lifetime, *Int. J. Fatigue.* 30 (2008) 663–676. doi:10.1016/j.ijfatigue.2007.05.008.
- [104] M.R. Wenman, K.R. Trethewey, S.E. Jarman, P.R. Chard-Tuckey, A finite-element computational model of chloride-induced transgranular stress-corrosion cracking of austenitic stainless steel, *Acta Mater.* 56 (2008) 4125–4136. doi:10.1016/j.actamat.2008.04.068.
- [105] J. Purbolaksono, a. Khinani, a. Z.Z. Rashid, a. a. a. Ali, N.F.F. Nordin, Prediction of oxide scale growth in superheater and reheater tubes, *Corros. Sci.* 51 (2009) 1022–1029. doi:10.1016/j.corsci.2009.02.025.

- [106] A. Turnbull, D.A. Horner, B.J. Connolly, Challenges in modelling the evolution of stress corrosion cracks from pits, *Eng. Fract. Mech.* 76 (2009) 633–640. doi:10.1016/j.engfracmech.2008.09.004.
- [107] A. Turnbull, L. Wright, L. Crocker, New insight into the pit-to-crack transition from finite element analysis of the stress and strain distribution around a corrosion pit, *Corros. Sci.* 52 (2010) 1492–1498. doi:10.1016/j.corsci.2009.12.004.
- [108] J.A. Grogan, B.J. O'Brien, S.B. Leen, P.E. McHugh, A corrosion model for bioabsorbable metallic stents., *Acta Biomater.* 7 (2011) 3523–33. doi:10.1016/j.actbio.2011.05.032.
- [109] J.A. Grogan, S.B. Leen, P.E. McHugh, Optimizing the design of a bioabsorbable metal stent using computer simulation methods., *Biomaterials.* 34 (2013) 8049–60. doi:10.1016/j.biomaterials.2013.07.010.
- [110] F. Biglari, K.M. Nikbin, Environmental creep intergranular damage and multisite crack evolution model for engineering alloys, *Comput. Mater. Sci.* 84 (2014) 267–277. doi:10.1016/j.commatsci.2013.12.020.
- [111] D. French, *Metallurgical Failures in Fossil Fired Boilers*, Wiley, 1993.
- [112] J. Larsson, *Evaluation of current methods for creep analysis and impression creep testing of power plant steels*, KTH Royal Institute of Technology, 2012.
- [113] L. Esposito, N. Bonora, Primary Creep Modeling Based on the Dependence of the Activation Energy on the Internal Stress, *J. Press. Vessel Technol.* 134 (2012) 61401. <http://dx.doi.org/10.1115/1.4006856>.
- [114] R.A. Barrett, *Experimental Characterisation and Computational Constitutive Modelling of High Temperature Degradation in 9Cr Steels Including Microstructural Effects*, National University of Ireland, Galway, 2016.
- [115] A.C.F. Cocks, M.F. Ashby, On creep fracture by void growth, *Prog. Mater. Sci.* 27 (1982) 189–244. doi:10.1016/0079-6425(82)90001-9.
- [116] F. Abe, Precipitate design for creep strengthening of 9% Cr tempered martensitic steel for ultra-supercritical power plants, *Sci. Technol. Adv. Mater.*

9 (2008) 13002. doi:10.1088/1468-6996/9/1/013002.

- [117] R.K. Penny, D.L. Marriott, Design for Creep, Springer Netherlands, 1995.
- [118] I. Kachanov, LM, Akad Naul, Akad. Nauk. SSSR. 8 (1958).
- [119] T.H. Hyde, W. Sun, A.A. Becker, J.A. Williams, Creep continuum damage constitutive equations for the base, weld and heat-affected zone materials of a service-aged 1/2Cr1/2Mo1/2V:21/4Cr1Mo multipass weld at 640°C, *J. Strain Anal. Eng. Des.* 32 (n.d.) 273–285. <http://cat.inist.fr/?aModele=afficheN&cpsidt=2810709> (accessed January 6, 2016).
- [120] T.H. Hyde, A.A. Becker, W. Sun, J.A. Williams, Finite-element creep damage analyses of P91 pipes, *Int. J. Press. Vessel. Pip.* 83 (2006) 853–863. doi:10.1016/j.ijpvp.2006.08.013.
- [121] I. Stephens, Ralph, A. Fatemi, R. Stephens, Robert, O. Fuchs, Henry, Metal Fatigue in Engineering, *J. Eng. Mater. Technol.* (2001) 472. doi:10.1115/1.3225026.
- [122] J. Lemaitre, R. Desmorat, Engineering Damage Mechanics: Ductile, Creep, Fatigue and Brittle Failures, Springer Berlin Heidelberg, 2006. <https://books.google.ie/books?id=SLyUINayQEoC>.
- [123] R. a. Barrett, P.E. O’Donoghue, S.B. Leen, An improved unified viscoplastic constitutive model for strain-rate sensitivity in high temperature fatigue, *Int. J. Fatigue.* 48 (2013) 192–204. doi:10.1016/j.ijfatigue.2012.11.001.
- [124] R.A. Barrett, T.P. Farragher, C.J. Hyde, N.P. O’Dowd, P.E. O’Donoghue, S.B. Leen, A Unified Viscoplastic Model for High Temperature Low Cycle Fatigue of Service-Aged P91 Steel, *J. Press. Vessel Technol.* 136 (2014) 21402. doi:10.1115/1.4025618.
- [125] F. Masuyama, History of power plants and progress in heat resistant steels, *ISIJ Int.* 41 (2001) 612–625.
- [126] M.F. Ashby, D.R.H. Jones, Engineering Materials 2 - An introduction to Microstructures, Processing and Design, Second, Butterworth-Heinemann,

Oxford, 2013. doi:10.1016/B978-0-08-096668-7.00014-0.

- [127] S.M.S.T. GmbH, Dmf 347 Hfg, (2008) 24. http://www.smst-tubes.com/fileadmin/media/pdf_datasheets/smst_booklet_347HFG_2008.pdf.
- [128] R.W. Swindeman, M.L. Santella, P.J. Maziasz, B.W. Roberts, K. Coleman, Issues in replacing Cr-Mo steels and stainless steels with 9Cr-1Mo-V steel, *Int. J. Press. Vessel. Pip.* 81 (2004) 507–512. doi:10.1016/j.ijpvp.2003.12.009.
- [129] ASTM, Standard Specification for Seamless Ferritic Alloy-Steel Pipe for High-Temperature Service, (2015).
- [130] ThyssenKrupp Materials International, Material data sheet P91, 2011.
- [131] J.S. Dubey, H. Chilukuru, J.K. Chakravarty, M. Schwienheer, A. Scholz, W. Blum, Effects of cyclic deformation on subgrain evolution and creep in 9-12% Cr-steels, *Mater. Sci. Eng. A.* 406 (2005) 152–159. doi:10.1016/j.msea.2005.06.029.
- [132] P.J. Ennis, a. Czyrska-Filemonowicz, Recent advances in creep-resistant steels for power plant applications, *Sadhana.* 28 (2003) 709–730. doi:10.1007/BF02706455.
- [133] J. Hald, Microstructure and long-term creep properties of 9-12% Cr steels, *Int. J. Press. Vessel. Pip.* 85 (2008) 30–37. doi:10.1016/j.ijpvp.2007.06.010.
- [134] C.G. Panait, W. Bendick, a. Fuchsmann, a. F. Gourgues-Lorenzon, J. Besson, Study of the microstructure of the Grade 91 steel after more than 100,000 h of creep exposure at 600 °C, *Int. J. Press. Vessel. Pip.* 87 (2010) 326–335. doi:10.1016/j.ijpvp.2010.03.017.
- [135] Aperam, AISI 347/347H Technical Properties, Sao Paulo Brazil, n.d.
- [136] J.-O. Nilsson, Prediction of Properties in Type 347 Austenitic Stainless Steel after Long-Term Service at High Temperatures, *Mater. Sci. Forum.* 539–543 (2007) 4920–4925. doi:10.4028/www.scientific.net/MSF.539-543.4920.
- [137] S. Rhode, V. Kain, V.S. Raja, G.J. Abraham, Factors affecting corrosion behavior of inclusion containing stainless steels: A scanning electrochemical

- microscopic study, *Mater. Charact.* 77 (2013) 109–115. doi:10.1016/j.matchar.2013.01.006.
- [138] T.L.S.L. Wijesinghe, D.J. Blackwood, Real time pit initiation studies on stainless steels: The effect of sulphide inclusions, *Corros. Sci.* 49 (2007) 1755–1764. doi:10.1016/j.corsci.2006.10.025.
- [139] C. Donik, I. Paulin, M. Jenko, Influence of MnS inclusions on the Corrosion of Austenitic Stainless steel.pdf, *Mater. Technol.* 44 (2010) 67.
- [140] R. Ke, Initiation of Corrosion Pits at Inclusions on 304 Stainless Steel, *J. Electrochem. Soc.* 142 (1995) 4056. doi:10.1149/1.2048462.
- [141] M. Elboujdaini, R.W. Revie, Metallurgical factors in stress corrosion cracking (SCC) and hydrogen-induced cracking (HIC), *J. Solid State Electrochem.* 13 (2009) 1091–1099. doi:10.1007/s10008-009-0799-0.
- [142] G.S. Frankel, Pitting Corrosion of Metals A Review of the Critical Factors, *J. Electrochem. Soc.* 145 (1998) 2186–2198.
- [143] T. V. Shibaeva, V.K. Laurinavichyute, G.A. Tsirlina, A.M. Arsenkin, K. V. Grigorovich, The effect of microstructure and non-metallic inclusions on corrosion behavior of low carbon steel in chloride containing solutions, *Corros. Sci.* 80 (2014) 299–308. doi:10.1016/j.corsci.2013.11.038.
- [144] I.I. Reformatskaya, I.G. Rodionova, Y.A. Beilin, L.A. Nisel'son, A.N. Podobaev, The effect of nonmetal inclusions and microstructure on local corrosion of carbon and low-alloyed steels, *Prot. Met.* 40 (2004) 447–452. doi:10.1023/B:PROM.0000043062.19272.c5.
- [145] G.S. Eklund, Initiation of Pitting at Sulfide Inclusions in Stainless Steel, *J. Electrochem. Soc.* 121 (1974) 467. doi:10.1149/1.2401840.
- [146] S.E. Lott, The Role of Inclusions on Initiation of Crevice Corrosion of Stainless Steel, *J. Electrochem. Soc.* 136 (1989) 973. doi:10.1149/1.2096896.
- [147] M.P. Ryan, D.E. Williams, R.J. Chater, B.M. Hutton, D.S. McPhail, Why stainless steel corrodes., *Nature.* 415 (2002) 770–774. doi:10.1038/415770a.

- [148] D.E. Williams, M.R. Kilburn, J. Cliff, G.I.N. Waterhouse, Composition changes around sulphide inclusions in stainless steels, and implications for the initiation of pitting corrosion, *Corros. Sci.* 52 (2010) 3702–3716. doi:10.1016/j.corsci.2010.07.021.
- [149] X. Xie, L. Zhang, M. Zhang, J. Dong, K. Bain, Micro-Mechanical Behavior Study of Non-Metallic Inclusions in P / M Disk, *Mater. Sci.* (2004).
- [150] D. Hull, *Fractography: Observing, Measuring and Interpreting Fracture Surface Topography*, Cambridge University Press, 1999. <https://books.google.ie/books?id=71n2ZTCt4iIC>.
- [151] H.K.D.H. Bhadeshia, R. Honeycombe, *Steels Microstructure and Properties*, Third edit, Butterworth-Heinemann, Oxford, 2006.
- [152] W.W. Bose Filho, A.L.M. Carvalho, P. Bowen, Micromechanisms of cleavage fracture initiation from inclusions in ferritic welds, *Mater. Sci. Eng. A.* 452–453 (2007) 401–410. doi:10.1016/j.msea.2006.10.096.
- [153] R. Prasannavenkatesan, J. Zhang, D.L. McDowell, G.B. Olson, H.J. Jou, 3D modeling of subsurface fatigue crack nucleation potency of primary inclusions in heat treated and shot peened martensitic gear steels, *Int. J. Fatigue.* 31 (2009) 1176–1189. doi:10.1016/j.ijfatigue.2008.12.001.
- [154] T.P. Gabb, J. Telesman, P.T. Kantzos, J.W. Smith, P.F. Browning, Effects of High Temperature Exposures on Fatigue Life of Disk Superalloys, *Superalloys*. (2004) 3–6.
- [155] M. Montgomery, A. Karlsson, O.H. Larsen, Field test corrosion experiments in Denmark with biomass fuels Part 1: Straw-firing, *Mater. Corros.* 53 (2002) 121–131. doi:10.1002/1521-4176(200202)53:2<121::AID-MACO121>3.0.CO;2-R.
- [156] A. Zahs, M. Spiegel, H.J. Grabke, The influence of alloying elements on the chlorine-induced high temperature corrosion of Fe-er alloys in oxidizing atmospheres, *Mater. Corros.* 50 (1999) 561–578.
- [157] H. Asteman, M. Spiegel, Investigation of the HCl (g) attack on pre-oxidized

- pure Fe, Cr, Ni and commercial 304 steel at 400°C, *Corros. Sci.* 49 (2007) 3626–3637. doi:10.1016/j.corsci.2007.03.028.
- [158] J.-M. Abels, H.-H. Strehblow, A surface analytical approach to the high temperature chlorination behaviour of inconel 600 at 700 °C, *Corros. Sci.* 39 (1997) 115–132. doi:10.1016/S0010-938X(96)00112-6.
- [159] F.H. Stott, C.Y. Shih, The influence of HCl on the oxidation of iron at elevated temperatures, *Mater. Corros.* 51 (2000) 277–286.
- [160] N. Folkesson, L.-G. Johansson, J.-E. Svensson, Initial Stages of the HCl-Induced High-Temperature Corrosion of Alloy 310, *J. Electrochem. Soc.* 154 (2007) C515. doi:10.1149/1.2754174.
- [161] J. Robertson, J.E. Forrest, Corrosion of carbon steels in high temperature acid chloride solutions, *Corros. Sci.* 32 (1991) 521–540. doi:http://dx.doi.org/10.1016/0010-938X(91)90105-X.
- [162] S.C. Cha, M. Spiegel, Local reactions of KCl particles with iron, nickel and chromium surfaces, *Mater. Corros.* 57 (2006) 159–164. doi:10.1002/maco.200503903.
- [163] A.G. Evans, D.R. Mumm, J.W. Hutchinson, Mechanisms controlling the durability of thermal barrier coatings, *Prog. Mater. Sci.* 46 (2001) 505–553.
- [164] A.M. Limarga, D.S. Wilkinson, G.C. Weatherly, Modeling of oxidation-induced growth stresses, *Scr. Mater.* 50 (2004) 1475–1479. doi:10.1016/j.scriptamat.2004.03.001.
- [165] H.J. Grabke, M. Spiegel, A. Zahs, Role of Alloying Elements and Carbides in the Chlorine-Induced Corrosion of Steels and Alloys, *Mater. Res.* 7 (2004) 89–95.
- [166] N. Folkesson, T. Jonsson, M. Halvarsson, L.-G. Johansson, J.-E. Svensson, The influence of small amounts of KCl(s) on the high temperature corrosion of a Fe-2.25Cr-1Mo steel at 400 and 500°C, *Mater. Corros.* 62 (2011) 606–615. doi:10.1002/maco.201005942.
- [167] T. Hussain, A.U. Syed, N.J. Simms, Trends in fireside corrosion damage to

- superheaters in air and oxy-firing of coal/biomass, *Fuel*. 113 (2013) 787–797. doi:10.1016/j.fuel.2013.04.005.
- [168] Y. Shinata, Accelerated oxidation rate of chromium induced by sodium chloride, *Oxid. Met.* 27 (1987) 315–332. doi:10.1007/BF00659274.
- [169] G.J. Janz, C.B. Allen, J.R.J. Downey, R.P.T. Tomkins, *EUTECTIC DATA: Safety, Hazards, Corrosion, Melting Points, Compositions, and Bibliography*, Troy, NY, United States, 1976.
- [170] S.C. Cha, M. Spiegel, Local reactions of KCl particles with iron, nickel and chromium surfaces, *Mater. Corros.* 57 (2006) 159–164. doi:10.1002/maco.200503903.
- [171] D. Lindberg, R. Backman, P. Chartrand, M. Hupa, Towards a comprehensive thermodynamic database for ash-forming elements in biomass and waste combustion — Current situation and future developments, *Fuel Process. Technol.* 105 (2013) 129–141. doi:10.1016/j.fuproc.2011.08.008.
- [172] R. Backman, M. Hupa, E. Uppstu, Fouling and corrosion mechanisms in the recovery boiler superheater area, *Tappi J.* 70 (1987) 123–127. <http://cat.inist.fr/?aModele=afficheN&cpsidt=7383608> (accessed August 27, 2015).
- [173] L.-G. Johansson, J.-E. Svensson, E. Skog, J. Pettersson, C. Pettersson, N. Folkesson, et al., Critical Corrosion Phenomena on Superheaters in Biomass and Waste-Fired Boilers, *J. Iron Steel Res. Int.* 14 (2007) 35–39. doi:10.1016/S1006-706X(08)60048-5.
- [174] P.D. Miller, H.H. Krause, J. Zupan, W. Boyd, Corrosive Effects of Various Salt Mixtures Under Combustion Gas Atmospheres, *Corrosion*. 28 (1972) 222–225. doi:10.5006/0010-9312-28.6.222.
- [175] S.C. Okoro, M. Montgomery, F.J. Frandsen, K. Pantleon, High temperature corrosion during biomass firing: improved understanding by depth resolved characterisation of corrosion products, *Mater. High Temp.* 32 (2015) 92–101. doi:10.1179/0960340914Z.00000000081.

- [176] P. Viklund, R. Pettersson, A. Hjörnhede, P. Henderson, P. Sjövall, Effect of sulphur containing additive on initial corrosion of superheater tubes in waste fired boiler, *Corros. Eng. Sci. Technol.* 44 (2009) 234–240. doi:10.1179/174327809X419203.
- [177] S.C. Okoro, M. Montgomery, F.J. Frandsen, K. Pantleon, High Temperature Corrosion under Laboratory Conditions Simulating Biomass-Firing: A Comprehensive Characterization of Corrosion Products, (2014).
- [178] J. Pettersson, J.-E. Svensson, L.-G. Johansson, KCl-Induced Corrosion of a 304-type Austenitic Stainless Steel in O₂ and in O₂ + H₂O Environment: The Influence of Temperature, *Oxid. Met.* 72 (2009) 159–177. doi:10.1007/s11085-009-9153-2.
- [179] J. Pettersson, N. Folkesson, L.G. Johansson, J.E. Svensson, The effects of KCl, K₂SO₄ and K₂CO₃ on the high temperature corrosion of a 304-type austenitic stainless steel, *Oxid. Met.* 76 (2011) 93–109. doi:10.1007/s11085-011-9240-z.
- [180] S. Karlsson, J. Pettersson, L.-G. Johansson, J.-E. Svensson, Alkali Induced High Temperature Corrosion of Stainless Steel: The Influence of NaCl, KCl and CaCl₂, *Oxid. Met.* 78 (2012) 83–102. doi:10.1007/s11085-012-9293-7.
- [181] J. Lehmusto, B.-J. Skrifvars, P. Yrjas, M. Hupa, Comparison of potassium chloride and potassium carbonate with respect to their tendency to cause high temperature corrosion of stainless 304L steel, *Fuel Process. Technol.* 105 (2013) 98–105. doi:10.1016/j.fuproc.2011.12.016.
- [182] M.K. Hossain, A.C. Noke, S.R.J. Saunders, Oxidation of a Ni-Cr-Al alloy at 850°C in air containing HCl gas, *Oxid. Met.* 12 (1978) 451–471. doi:10.1007/BF00612090.
- [183] Y.S. Li, Y. Niu, M. Spiegel, High temperature interaction of Al/Si-modified Fe-Cr alloys with KCl, *Corros. Sci.* 49 (2007) 1799–1815. doi:10.1016/j.corsci.2006.10.019.
- [184] C. Pettersson, J. Pettersson, H. Asteman, J.E. Svensson, L.G. Johansson, KCl-induced high temperature corrosion of the austenitic Fe-Cr-Ni alloys 304L and Sanicro 28 at 600 °C, *Corros. Sci.* 48 (2006) 1368–1378.

doi:10.1016/j.corsci.2005.05.018.

- [185] T. Jonsson, J. Froitzheim, J. Pettersson, J.-E. Svensson, L.-G. Johansson, M. Halvarsson, The Influence of KCl on the Corrosion of an Austenitic Stainless Steel (304L) in Oxidizing Humid Conditions at 600 °C: A Microstructural Study, *Oxid. Met.* 72 (2009) 213–239. doi:10.1007/s11085-009-9156-z.
- [186] N. Israelsson, K. Hellström, J.-E. Svensson, L.-G. Johansson, KCl-Induced Corrosion of the FeCrAl Alloy Kanthal ® AF at 600 °C and the Effect of H₂O, *Oxid. Met.* 83 (2014) 1–27. doi:10.1007/s11085-014-9506-3.
- [187] N. Hiramatsu, Y. Uematsu, T. Tanaka, M. Kinugasa, Effects of alloying elements on NaCl-induced hot corrosion of stainless steels, *Mater. Sci. Eng. A.* 120–121 (1989) 319–328. doi:10.1016/0921-5093(89)90757-0.
- [188] T.S. Sidhu, S. Prakash, R.D. Agrawal, Hot corrosion studies of HVOF NiCrBSi and Stellite-6 coatings on a Ni-based superalloy in an actual industrial environment of a coal fired boiler, *Surf. Coatings Technol.* 201 (2006) 1602–1612. doi:10.1016/j.surfcoat.2006.02.047.
- [189] J. Stringer, High Temperature Corrosion Issues in Energy-Related Systems, *Mater. Res.* 7 (2004) 1–9.
- [190] K. Natesan, J.H. Park, Fireside and steamside corrosion of alloys for USC plants, *Int. J. Hydrogen Energy.* 32 (2007) 3689–3697. doi:10.1016/j.ijhydene.2006.08.038.
- [191] S. Srivastava, K. Godiwalla, M. Banerjee, Fuel ash corrosion of boiler and superheater tubes, *J. Mater. Sci.* 2 (1997) 835–849. <http://link.springer.com/article/10.1023/A:1018585129341>.
- [192] T. Dudziak, T. Hussain, N.J. Simms, a. U. Syed, J.E. Oakey, Fireside corrosion degradation of ferritic alloys at 600°C in oxy-fired conditions, *Corros. Sci.* 79 (2014) 184–191. doi:10.1016/j.corsci.2013.11.005.
- [193] A.U. Syed, N.J. Simms, J.E. Oakey, Fireside corrosion of superheaters: Effects of air and oxy-firing of coal and biomass, *Fuel.* 101 (2012) 62–73. doi:10.1016/j.fuel.2011.03.010.

- [194] B.S. Lutz, G.R. Holcomb, G.H. Meier, Determination of the Initiation and Propagation Mechanism of Fireside Corrosion, *Oxid. Met.* (2015). doi:10.1007/s11085-015-9559-y.
- [195] S. Shamanna, H.H. Schobert, Fireside corrosion of selected alloys by ash recovered from coal-water slurry combustion, *Fuel Process. Technol.* 53 (1997) 133–156. doi:10.1016/S0378-3820(97)00045-3.
- [196] P. Viklund, R. Pettersson, HCl-Induced High Temperature Corrosion of Stainless Steels in Thermal Cycling Conditions and the Effect of Preoxidation, *Oxid. Met.* 76 (2011) 111–126. doi:10.1007/s11085-010-9227-1.
- [197] Anon, OLYMPUS Stream Motion Image analysis software. Germany: Olympus Soft Imaging Solutions GmbH, (n.d.).
- [198] H.H. Corporation, P. No, INSTRUCTION MANUAL FOR MODEL S-4800 FIELD EMISSION, (2002).
- [199] F. Jappe Frandsen, Utilizing biomass and waste for power production—a decade of contributing to the understanding, interpretation and analysis of deposits and corrosion products, *Fuel.* 84 (2005) 1277–1294. doi:10.1016/j.fuel.2004.08.026.
- [200] T. Zhang, N.M. Harrison, P.F. McDonnell, P.E. McHugh, S.B. Leen, Micro–macro wear–fatigue of modular hip implant taper-lock coupling, *J. Strain Anal. Eng. Des.* . 49 (2014) 2–18. doi:10.1177/0309324713502175.
- [201] N. Stojilovic, Why can't we see hydrogen in X-ray photoelectron spectroscopy?, *J. Chem. Educ.* 89 (2012) 1331–1332. doi:10.1021/ed300057j.
- [202] Struers, Repliset, (2010). <http://www.struers.ie/resources/elements/12/264392/Repliset> brochure English.pdf.
- [203] D.O. Albina, N.J. Themelis, Theory and experience on corrosion of waterwall and superheater tubes of waste-to-energy facilities, Dpartment of Earth and Environmental Engineering Fu Foundation School Of Engineering and Applied Science Columbia University, 2005.

- [204] R.B. Bird, W.E. Steward, E.N. Lightfoot, *Transport Phenomena* 2nd Edition, 2001.
- [205] E.L. Cussler, *Diffusion, Mass Transfer in Fluid Systems*, Third, Cambridge, 2009.
- [206] H. Rashidi, H. Ale Ebrahim, B. Dabir, Application of random pore model for synthesis gas production by nickel oxide reduction with methane, *Energy Convers. Manag.* 74 (2013) 249–260. doi:10.1016/j.enconman.2013.04.044.
- [207] J.M. Smith, *Chemical Engineering Kinetics*, 2nd Edition, 2nd ed., McGraw-Hill, 1970.
- [208] D.D. Bhatia, S.K. and Perlmutter, A random pore model for fluid-solid reactions 2 Diffusion and Transport effects.pdf, *AIChE J.* 27 (1981) 247–254.
- [209] M. Montgomery, S. a. Jensen, U. Borg, O. Biede, T. Vilhelmsen, Experiences with high temperature corrosion at straw-firing power plants in Denmark, *Mater. Corros.* 62 (2011) 593–605. doi:10.1002/maco.201005856.
- [210] D.D. Bhatia, S.K. and Perlmutter, A random pore model for fluid-solid reactions 1 Isothermal kinetic control, *AIChE J.* 26 (1980) 379–385.
- [211] K. Zarrabi, Estimation of boiler tube life in presence of corrosion and erosion processes, *Int. J. Press. Vessel. Pip.* 53 (1993) 351–358. doi:10.1016/0308-0161(93)90087-A.
- [212] R. Viswanathan, S.R. Paterson, H. Grunloh, S. Gehl, Life Assessment of Superheater/Reheater Tubes in Fossil Boilers, *J. Press. Vessel Technol.* 116 (1994) 1–16. <http://dx.doi.org/10.1115/1.2929553>.
- [213] T.H. Hyde, A.A. Becker, W. Sun, A. Yaghi, A. Thomas, P. Seliger, Finite Element Creep Failure Analyses of P91 Large Tensile Cross-Weld Specimens Tested At 625 O C, in: *5th Int. Conf. Mech. Mater. Des.*, 2006: pp. 1–12.
- [214] K. Sawada, M. Fujitsuka, M. Tabuchi, K. Kimura, Effect of oxidation on the creep rupture life of ASME T23 steel, *Int. J. Press. Vessel. Pip.* 86 (2009) 693–698. doi:10.1016/j.ijpvp.2009.03.001.

- [215] Anon., Abaqus analysis manual v6.12, (2012).
- [216] D.R. Hayhurst, Creep rupture under multi-axial states of stress, *J. Mech. Phys. Solids*. 20 (1972) 381–382. doi:10.1016/0022-5096(72)90015-4.
- [217] C. Wang, J. Chen, Z.C. Xia, F. Ren, Die wear prediction by defining three-stage coefficient K for AHSS sheet metal forming process, *Int. J. Adv. Manuf. Technol.* 69 (2013) 797–803. doi:10.1007/s00170-013-5069-8.
- [218] T. Zhang, P.E. McHugh, S.B. Leen, Computational study on the effect of contact geometry on fretting behaviour, *Wear*. 271 (2011) 1462–1480. doi:10.1016/j.wear.2010.11.017.
- [219] T.F.J. Quinn, Computational methods applied to oxidational wear, *Wear*. 199 (1996) 169–180. doi:10.1016/0043-1648(95)06856-2.
- [220] S. Mrowec, A. Stokłosa, Calculations of parabolic rate constants for metal oxidation, *Oxid. Met.* 8 (1974) 379–391. doi:10.1007/BF00603388.
- [221] H.H. Uhlig, R.W. Revie, Corrosion and corrosion control: an introduction to corrosion science and engineering, Wiley, 1985. <https://books.google.ie/books?id=cM5RAAAAMAAJ>.
- [222] F. Gesmundo, F. Viani, The parabolic rate constant for the high-temperature oxidation of pure or slightly alloyed nickel and the defect structure of nickel oxide, *Solid State Ionics*. 6 (1982) 33–42. doi:10.1016/0167-2738(82)90093-5.
- [223] H. Kraus, Creep analysis, John Wiley & Sons Canada, Limited, 1980. <http://books.google.ie/books?id=IqYeAQAAIAAJ>.
- [224] H.C. Furtado, L.H. De Almeida, I. Le May, Damage and remaining life estimation in high temperature plant with variable operating conditions, *OMMI*. 5 (2008) 1–10.
- [225] D.M. Grogan, S.B. Leen, C.M. Ó Brádaigh, An XFEM-based methodology for fatigue delamination and permeability of composites, *Compos. Struct.* 107 (2014) 205–218. doi:10.1016/j.compstruct.2013.07.050.
- [226] D.M. Grogan, C.M. Ó Brádaigh, S.B. Leen, A combined XFEM and cohesive

- zone model for composite laminate microcracking and permeability, *Compos. Struct.* 120 (2015) 246–261. doi:10.1016/j.compstruct.2014.09.068.
- [227] A. Melander, A finite element study of short cracks with different inclusion types under rolling contact fatigue load, *Int. J. Fatigue.* 19 (1997) 13–24. doi:http://dx.doi.org/10.1016/S0142-1123(96)00045-X.
- [228] A.H. Yaghi, T.H. Hyde, A.A. Becker, J.A. Williams, W. Sun, Residual stress simulation in welded sections of P91 pipes, *J. Mater. Process. Technol.* 167 (2005) 480–487. doi:10.1016/j.jmatprotec.2005.05.036.
- [229] D. Bankiewicz, Corrosion behaviour of boiler tube materials during combustion of fuels containing Zn and Pb, *Abo Akademi*, 2012.
- [230] D. Gastaldi, V. Sassi, L. Petrini, M. Vedani, S. Trasatti, F. Migliavacca, Continuum damage model for bioresorbable magnesium alloy devices - Application to coronary stents., *J. Mech. Behav. Biomed. Mater.* 4 (2011) 352–65. doi:10.1016/j.jmbbm.2010.11.003.
- [231] N. Henriksen, O. Hede Larsen, R. Blum, Lifetime evaluation of superheater tubes exposed to steam oxidation, high temperature corrosion and creep, in: *Int. Conf. Power Plant Chem. Technol.*, Kolding, Denmark, 1996: p. 6.1-6.23.
- [232] A.J. Sedriks, *Corrosion of stainless steel*, Second edition, John Wiley and Sons, Inc., New York, NY (United States), United States, 1996. http://www.osti.gov/scitech/servlets/purl/378109.
- [233] J.P. Rouse, W. Sun, T.H. Hyde, a. Morris, W. Montgomery, A Method to Approximate the Steady-State Creep Response of Three-Dimensional Pipe Bend Finite Element Models Under Internal Pressure Loading Using Two-Dimensional Axisymmetric Models, *J. Press. Vessel Technol.* 136 (2013) 11402. doi:10.1115/1.4025720.
- [234] T.P. Farragher, S. Scully, N.P. O’Dowd, S.B. Leen, Thermomechanical Analysis of a Pressurised Pipe Under Plant Conditions, *J. Press. Vessel Technol.* 6 (2013) 119–128.
- [235] Z. Szklarska-Smialowska, E. Lunarska, The effect of sulfide inclusions on the

susceptibility of steels to pitting, stress corrosion cracking and hydrogen embrittlement, *Mater. Corros.* 32 (1981) 478–485. doi:10.1002/maco.19810321103.